RE-250

POLARIMETRIC MEASUREMENTS OF
SIMULATED LUNAR SURFACES

May 1966

GPO PRICE $ _____

CFSTI PRICE(S) $ _____

Hard copy (HC) _____

Microfiche (MF) _____

ff 653 July 65

Grumman

RESEARCH DEPARTMENT

GRUMMAN AIRCRAFT ENGINEERING CORPORATION

BETHPAGE NEW YORK

Grumman Research Department Report RE-250

POLARIMETRIC MEASUREMENTS OF SIMULATED LUNAR SURFACES

by

W. G. Egan

L. L. Smith

G. C. McCoyd

Geo-Astrophysics Section

May 1966

Final Report on Contract NAS 9-4942

Approved by: *Richard H. Scheuing*
for Charles E. Mack, Jr.
Director of Research

FOREWORD

This is the final report of "Polarimetric Measurements of Simulated Lunar Surfaces," an investigation conducted under Contract No. NAS 9-4942. Contained herein are the results of Phase IV and other work provisions of Proposal B.

The NASA-supported program "Polarimetric Measurements of Simulated Lunar Surfaces" has as its objective the seeking of an understanding of the causes of the moon's unique polarimetric properties by:

1) Laboratory simulation of observed characteristics
2) Detailed correlation of factors producing the observed laboratory polarization characteristics
3) Investigation of the application of electromagnetic theory to the development of a model reproducing all observed detailed polarization characteristics

The program consisted of four phases:

I. Investigation of Natural Specimens
II. Investigation of Pulverized Specimens
III. Investigation of Contrived Models
IV. Analysis of Lunar and Laboratory Data

The authors wish to acknowledge the continuing efforts of H. B. Hallock, J. Grusauskas, and D. R. Lamberty in perfecting the polarimetric analyzer and recording data. We wish also to give thanks to C. Bartollota, C. Krolik, and D. Schlaijker, for their assistance.

We are also grateful to the following individuals for discussions in relation to the pursuit of the program: J. Halajian, Dr. N. Milford, J. Reichman, Dr. M. Sidran, and F. Spagnolo.

The study was conducted under the cognizance of the Space Science Office with Mr. Robert Runnels of the Meteoroid and Optics Branch, Space Physics Section, serving as Technical Representative.

ABSTRACT

An experimental study (Phases I, II, and III) and a theoretical study (Phase IV) of the polarimetric properties of simulated lunar surfaces were undertaken. They consisted of: I) polarimetric investigation in visual light (0.54μ) of natural specimens having a good photometric match to the moon; II) polarimetric investigation in visual light of pulverized specimens from Phase I to determine particle size effects; III) polarimetric investigation of contrived models combining the results of Phases I and II in blue (0.48μ), green (0.54μ) and infrared (1.0μ) wavelengths; and IV) theoretical analysis of lunar and laboratory data.

The over-all conclusion of the experimental program is that the polarization properties of the lunar surface can be produced by a suitable material with a particulate coating of itself. Thus, the surface properties could yield information on the underlying matter and ultimately give information as to the choice of good landing areas for the Apollo mission.

Phase IV has confirmed the existence of a correlation between albedo and polarization on a theoretical basis.

TABLE OF CONTENTS

LIST OF ILLUSTRATIONS

LIST OF TABLES

SUMMARY AND INTRODUCTION

A considerable quantity of observational data has existed on the polarimetric properties of the lunar surface (Ref. 1), but these data were not adequately utilized until now in an attempt to search for a satisfactory model of the lunar surface. Furthermore, there now exist a number of reasonable photometric models such as Hapke's theoretical photometric function (Ref. 2), his revised photometric function (Ref. 3), Gehrels' suspended particle model (Ref. 4) and a number of natural and contrived photometric models developed at Grumman by Halajian et al. (Refs. 5 through 9).

The objective of the present program was to determine lunar surface models that reproduce both the photometric and polarimetric properties of the moon. The logical starting point for such a search was the models that have proven to be satisfactory in laboratory photometric investigations. Thus, an attempt was made to develop laboratory simulation of lunar polarization using various combinations of the natural photometric models. The program at Grumman utilizes a large scale photometer developed for this purpose.

The program is not concerned exclusively with obtaining a "model" of the lunar surface or a specific material. Rather, it seeks the general properties of materials that produce the polarization characteristics observed for the lunar surface. A completely theoretical approach is ruled out because a rigorous analytical treatment of the problem must include multiple scattering of electromagnetic radiation, the effect of surface and particle geometry, the influence of the complex index of refraction of the surface, and the spectral content of the light used. Such considerations have eluded detailed analysis except for specific simplified models like isolated single spheres, ellipsoids, or long cylinders. Therefore, an experimental program was indicated and was pursued in this work.

Phase I of the program consisted of polarimetric measurements on seven natural specimens possessing good photometric characteristics. The significant parts of their polarimetric curves were determined in integrated visual light, and compared with Lyot's lunar data, with additional reference to the work of Hapke, Coffeen, and Gehrels.

1

The objective of the experiments was the determination of the percent polarization and the position of the plane of polarization of light scattered from various natural specimens. These properties were determined as a function of phase angle for two simulated lunar longitudes and latitudes, and a comparison was made with the corresponding lunar observations.

The results of Phase I described herein are summarized under the section Lunar Implications in Table 9 and the graphs of Fig. 36. As a result of Phase I, it was found that Volcanic Ash Nos. 1 and 4 and Coral No. 1 possessed average properties that could vary sufficiently in detail to permit them to be considered as polarimetric models of the lunar surface.

The previously reported models such as those of Lyot, Dollfus, Gehrels, Hapke, and Wehner are not unique. This was borne out by the recent Luna 9 photographs. However, it appears that there is a commonality that exists among models such that we may use all the data on hand (photometric, thermal, and mechanical) to evaluate appropriate polarimetric models that conform to the requirements.

The investigation of Phase II was undertaken to lay the basis for a subsequent analytical approach. Thus, the polarization properties of materials were investigated as a function of particle size, albedo and porosity, since current theories of polarization indicate some of these properties as significant parameters.

Apparently, to obtain the proper polarimetric signature consistent with a good photometric signature, the coarse structure (which can only be observed on a large scale photometer such as the Grumman unit) producing proper shadowing for photometry must be modified in some way. This modification could occur from an overcoat of powder. It appears from the present work that certain overcoat particle size ranges produce the proper signature based an a least squares curve fit of percent polarization. The laboratory data of Phase II has been analysed in terms of lunar maria (Crisium) and highland (Clavius) curves. The best fit to Mare Crisium was obtained with Furnace Slag No. 4 particles less than 37 microns, Volcanic Ash No. 4 between 37 and 88 microns, Volcanic Ash No. 1 greater than 0.21 mm, the spongelike slag obtained at NASA, and the Ash from Vesuvius. For Clavius, Furnace Slag No. 4 less than 1 micron, Volcanic Ash No. 4 between 1 and 37 microns, and Volcanic Ash No. 1 less than 1 micron were best fits.

This surface coating is not ruled out by the resolution of 2 mm given by the Luna 9 photographs. A powder thin enough to be consistent with the Luna 9 pictures would not effect the bearing strength of the underlying "rock". It appears possible to draw certain inferences about the limits to be placed on the thermal inertia constant, γ, based on a two layer model of the lunar surface. A two layer thermal model of the lunar surface has been analyzed (Ref. 21), and it is applied to a high γ (porous) upper layer and a low γ under layer. The particle size limits in such a layer can be inferred from the present work, to be between 1 micron and somewhat over 0.21 mm depending upon material.

A spongelike slag obtained at NASA/MSC appeared to yield the improper inversion angle and minimum.

Phase III was then undertaken so that the polarimetrically promising models of Phase I, which also were good photometrically by original selection, could be modified by sprinkling with the powders of Phase II to obtain a close match to lunar data in integrated and B, G, I light. Five required good models were obtained. An extra model, embodying the slag obtained at NASA/MSC was modified to produce a good polarimetric model. Comparison to the lunar colorimetric curves of Gehrels reveals that Models 5 (Volcanic Ash No. 4 topped with particles of itself $\leq 1\mu$) and 6 (Volcanic Ash No. 1 topped with particles of itself $\leq 1\mu$) are the closest matches to Mare Crisium, with Model 6 being the over-all best match. Model 1 (Slag, Spongelike, topped with 0.088 to 0.21 mm particles of Volcanic Ash No. 1) is a fair match to Crisium. The highest polarization occurs on all samples in the region where the albedo is lowest; the increase in albedo in the Infrared lowers the polarization, similar to the lunar observations. The dependence of the location of the polarization maximum in relation to the maximum percent polarization cannot be determined for each sample from our data, but the general over-all trend is towards higher phase angles for higher maxima below about 130 degrees phase angle. The inversion angle tends towards higher phase angles for decreased maximum polarization. No clear trend is seen for the negative minimum percent polarization.

In essence, as a result of Phase III, a satisfactory photometric and polarimetric model may be constructed, by combining a large scale photometric model that produces the shadowing necessary for good photometry, with a powder that produces the scattering and refraction properties necessary for good polarization. The

3

results are consistent with present knowledge of the lunar surface. It remains to reconcile thermal, mechanical, and radar observations of the lunar surface. It appears possible that a high γ dust layer at the order of 1 mm thick $[\gamma = (K\rho c)-1/2$ of the order of a few thousand] on top of the underlying material could explain some of the observed lunar thermal observations.

The fundamental conclusion of Phase III is that the polarization properties of the lunar surface can be produced by a suitable particulate coating of the underlying material. This particulate coating could be the result of the deterioration of the underlying material into dust by micrometeorite bombardment, and the resulting powder possibly adheres to the lunar surface by high vacuum bonding. Thus, the surface properties could yield information on the underlying matter and ultimately give information as to the choice of good landing areas for the Apollo mission.

The final part of the effort, Phase IV, consisted of an analysis of lunar and laboratory data. An examination was made of the principal factors contributing to the polarization characteristics of certain known and controllable models, such as that of Gehrels' and the contrived Grumman photometric models. A comparison was made between the polarimetric properties of these models, the bulk and powdered form of the natural specimens, and experimentally contrived models to those of the moon. By observing polarimetric changes produced by certain physical changes in the models, an attempt was made to identify the outstanding physical and geometric factors contributing to the lunar polarimetric signature. One result was a confirmation of the existence of a correlation between polarization and albedo based on the contrived Grumman polarimetric model.

Additional investigations of material properties are required to define the scientific and engineering properties that yield the proper lunar polarimetric and photometric signatures. Typical investigations could be differential thermal analysis and x-ray diffraction. This should be supplemented by extension of infrared investigations to longer wavelengths, the investigation of luminescence as it affects albedo and polarization, investigation of incremental color changes as an index of lunar landing characteristics, and the investigation of simulated solar wind effects on the best contrived models. In addition, the theoretical work on polarimetric models should be continued.

TEST EQUIPMENT

Description

The test equipment used for Phase I is essentially that described in Ref. 9, with further modifications described in a forthcoming report (Ref. 10). The modifications were carried out under a Grumman-supported program. This equipment is the only type of precision polarimeter available that permits laboratory measurements to be made on the total area of large size samples up to 4 inches in diameter in integrated visible light and also spectral light. Previously reported laboratory equipment has been designed for small scale polarimetry on areas of a fraction of an inch in diameter.

Type 6199 photomultipliers were used for the polarimetric observations in integrated visible light in Phases I, II and III. Spectral measurements were made on these photomultipliers and others under a Grumman program to check the agreement of the actual photocathode responses with the published values. There appears to be a serious doubt as to whether proper caution was exercised by previous observers in assuming that the manufacturer's published data were correct (Ref. 11).

The 60° photometer was converted into a polarimeter after the initial equipment status report was written (Ref. 9), permitting measurements up to a phase angle of 130°. However, for this 60° polarimeter, the viewing angle is 60°, while for measurements with the 0° polarimeter, it is 0° for a horizontal sample table. By comparing the measurements made with the 0° and 60° polarimeters in Phase I, the effect of simulated lunar longitude was obtained, because of the change in viewing angle of the sample in the plane of vision.

For simulated lunar latitude in Phase I, the 60° polarimeter was used, with the sample normal tilted 30° out of the plane of vision in a plane perpendicular to the plane of vision. Larger angles were not used because the powder samples would slide off the sample table.

The subassembly, consisting of two rhodium front surface mirrors reflecting the source illumination of the sample, was modified for Phase I to permit measurements from phase angles as small as 3°. Initially, the mirrors were aligned mechanically. However, in an attempt to reduce extraneous polarization effects that appear as residual polarization of the source, the two mirrors were realigned with an autocollimator for the measurements of

Phase I. Also, the original ground glass depolarizers were replaced by ground quartz depolarizers, permitting more light to pass.

The light source, increased from a 625 watt to a 1 kilowatt tungsten iodine lamp, was modified for Phase I to operate from a regulated power supply to permit a more constant light output.

To decrease the noise level, the photomultiplier resistor bank carbon resistors were replaced with thin film, low noise resistors, and the carbon potentiometers in the signal input circuits were replaced by precision wire wound potentiometers.

The operation of the equipment was periodically checked by measurements on a piece of plate glass filling the field of view; its percent polarization can be computed.

Plane of polarization measurements for Phase I were obtained by making a measurement on a black aluminite metal plate filling the field of view and comparing it to the sample being measured. This was accomplished by placing the metal plate in a fixed position on the sample table, rotating the polaroid through 360° , and recording the resulting sine curve. This sine curve represents the polaroid position in the polarimeter, and the plate locates the reference direction. Thus, when the sample to be checked is placed on the sample table, the corresponding sine curve displacement relative to the reference is proportional to the displacement of the plane of polarization. This procedure may be understood better by referring to the Appendix I (Test Procedure). For subsequent work, the procedures were the same as outlined, with the exception that a secondary standard was substituted for the aluminite plate for absolute measurements of the plane of polarization.

Subsequently, the test equipment described for Phase I was improved under a Grumman-supported program for Phase II. During the calibration and measurements of Phase I, there appeared to be a residual non-uniform 1 percent polarization in the collimated light beam illuminating the sample. There also appeared to be an additional 1 percent residual polarization in the 60° polarimeter above the zero degree polarimeter. In addition, there was an apparent rotation of the observed plane of polarization with phase angle.

As a result of extensive observations, measurements, and analyses of the equipment, these effects were appreciably reduced, eliminated or clarified.

Phase II Source Polarization

The collimated light from the source was analyzed on the sample table with a test jig using a 6199 end window photomultiplier prior to Phase II. Initially, the jig utilized a plastic polaroid, but this was replaced by a glass sandwich HN-22 polaroid for higher precision. It was then found that there was an over-all positive asymmetric polarization bias from the source. By a process of elimination, it was found that the largest contributor to the polarization was the tungsten-iodine 1000 watt lamp itself. Two ground quartz diffuser discs in front of the lamp were found to be inadequate to remove the residual polarization. But by following the two diffuser discs with an opal glass, the polarization was reduced to a small value. The source lens was found to be non-contributory to the average residual polarization following checks with a frosted incandescent lamp. The rhodium mirrors were realigned following replacement of one that had some pin holes in it. The field stop in the source was opened up to smear out the nonuniformities in the field and allow more light through. This also increased the beam divergence from $\frac{1}{2}°$ to $2°$. The result was a nearly symmetrical beam with a residual polarization of about 1 percent at the center. However, the planes of the residual polarization of the source were not exactly parallel or perpendicular to the plane of vision at the four cardinal points as they should be if the source were perfect; they were found at varying intermediate angles. The situation was improved by realigning the source field stop and replacing the tungsten-iodine lamp with a frosted one. This was done prior to Phase III.

Phase II Photometer-Polarimeter Polarization

The zero degree polarimeter was checked for residual polarization prior to Phase II by placing a frosted lamp behind a ground glass and located where the photomultiplier would be. The collimated light from this arrangement was examined on the sample table with the test jig. The residual polarization was found to be of the order of $+\frac{1}{4}$ of a percent due mainly to the residual polarization of the source used. An alternate method was used to recheck the over-all polarization of both polarimeters following the measurements. This consisted of using a frosted incandescent lamp under a 2-inch square plate of opal glass covered by a mylar diffusing screen as the source being observed by the polarimeters. The polarization of this configuration was measured on the polarimeter by rotating the polaroid; then the source was rotated $90°$ about the viewing direction and the polarization remeasured. This rotation of the source was done to check that no residual polarization existed in the source.

However, in Phase I, the 60° polarimeter was observed to have a residual polarization of about 1 percent above that of the zero degree polarimeter. After other variables had been eliminated, the 7-element, 12-inch f/2.5 Aero Ektar field lens was found to have a small separation at the center of one of the three cemented elements. This lens was replaced with another, and the residual polarization was then found to be about ¼ percent.

The test equipment used for Phase II was further improved under a Grumman supported program for Phase III. The source in Phase II had produced a symmetrical beam with +1 percent residual polarization at the center. In addition, there was inadequate signal for good polarimetric observations at I (1.0μ) wavelength. The polarimeters had a residual polarization of +¼ percent.

Source Polarization

The source was modified prior to Phase III in a number of ways subsequent to the completion of Phase II. The clear 1000 watt source lamp was replaced with a frosted envelope lamp to reduce the lamp residual polarization. The source field stop was slightly off the optical axis, and by suitably realigning it, the source over-all residual polarization was reduced to 0.2 percent at the center with good symmetry around the periphery of the 3-inch diameter illuminated sample area.

Color filters, to permit B, G, and I photometry, previously had been mounted close to the 1000 watt source lamp. As a result, the filters were heated excessively, causing a change in their spectral response as well as frequent breakage. For polarization, large 6 ½-inch square filters were obtained and mounted in a frame in front of the source lens housing closely perpendicular to the optical axis. The residual polarization of the filters was of the order of a tenth of a percent.

An increased capacity blower was installed on the source housing which permitted the lamp to be operated at rated value.

For the I (1.0μ) measurements, HR infrared polaroids were used because the usual HN-22 polaroids cease to be effective beyond 0.7μ.

8

Calibration

Phase I

To interpret the data properly it is necessary to determine the effect of the equipment (lamp, mirrors, diffusing screens, field stops, collimating lens plus the photometer) on the observed percent polarization and plane of polarization.

As the source arm could not be positioned to allow the lamp to shine directly on either photometer, the percent polarization from a glass plate (index 1.52) placed on the sample table was measured for phase angles 5°, 10°, 15°, 20° with the 0° photometer, and phase angle 5° with the 60° photometer. A piece of black flock (cloth with a reflectance of below 0.1 percent) was placed under the glass to eliminate reflections from the sample table. Applying Fresnels' equations for reflected light and allowing for multiple reflections from the two glass surfaces, it was found that the observed polarization from the equipment itself can be accounted for by assuming that the incident beam is + 2 percent polarized. The result from the 60 photometer appeared to show an additional + 1 percent residual polarization above that measured with the 0 photometer.

The percent polarization due to the source alone was measured by placing a small photometer on the sample table and rotating the polaroid by hand; the result was approximately + 1 percent polarization at the center of the incident beam and + 1½ percent polarization at the edge.

The instrumental effect on the measured angle of the plane of polarization in Phase I was determined by observing the diffuse reflected light from a black aluminite metal plate. The plate was ordinary sheet aluminum that had been chemically treated to produce a black finish. The plane remained fixed to within 0.4° for phase angles greater than 55° for the 60° polarimeter. For angles less than 55°, there was a gradual rotation of the plane of polarization as the phase angle approached 0°. When the specular reflection from the glass plate was measured, the plane of polarization remained fairly constant for phase angles greater than 60°, but gradually rotated reaching $\Delta\theta \sim 4°$ for a phase angle of 20°.

The +2 percent instrumental polarization could possibly be reduced through realignment of the optical elements of the system, but only the central region of the lens would have 0% polarization

9

ideally. By virtue of the refraction process with lenses, the outer regions would produce either positive or negative polarization, which would average out to 0% over the entire field. The additional polarization read by the 60° photometer above the 0° photometer for a fixed phase angle is probably mainly the result of residual polarization in the polarimeter.

The sample data presented in the Phase I report were not corrected for instrumental errors pending a more complete evaluation of these effects, and the establishment of an adequate standard for percent polarization and plane of polarization.

Phase II

Percent Polarization

The percent polarization calibration of the over-all system for Phase II is twofold: first, the residual polarization of the source assembly (the lamp, diffusers, lens, and two rhodium front surface mirrors) is checked at the position of the sample table with the 6199 photomultiplier test jig; second, the residual polarization of the two polarimeters is checked by the techniques mentioned previously under Description, and by reflection from a 1-inch thick glass plate using the source beam.

The residual polarization of the source must be checked over the entire 3-inch diameter field viewed by the polarimeters at the same voltage applied to the lamp for observations. During the measurements of Phase II, a lamp voltage lower than the rated was used to prevent the photomultipliers from saturating. The higher available lamp intensity at rated voltage is necessary for Phase III for measurements in the I (1.0 μ) region, where the filter assembly cuts the light down considerably. The lower lamp voltage, as well as the combination of two diffusers and an opal glass, redden the source somewhat. The system color response was determined by the use of narrow band interference filters and was found to be centered at a wavelength of 0.55μ for the lamp voltage used. When albedos were measured, a still lower voltage was used for comparison to the magnesium carbonate block for the same reason. The color response of the system at this lower voltage was measured and found to be centered at 0.56μ.

The polarimeter jig with the 6199 photomultiplier was checked for residual polarization with an unpolarized light source (frosted bulb plus diffusers) and found to have about a tenth of a percent.

10

Rotation of Plane of Polarization

Calibration curves were run with a 1-inch thick glass plate held in the incident beam by another jig prior to Phase II. This jig served to locate the front surface of the glass plate exactly on the axis of rotation of the source. It was found that the source was still not sufficiently depolarized to permit the application of Fresnel's equations to the glass plate to check percent and plane of polarization. Hence, as additional depolarizer was inserted into the same beam below the mirrors. This depolarizer consisted of another opal glass and a frosted mylar diffuser. Agreement was then obtained for the position of the plane of polarization within a fraction of a degree when a simultaneous calibration was made to monitor the gain of the potentiometer recorder used in the measurements.

Phase III

Percent Polarization

Calibrations of the polarimeter were made as described in Phase II for percent polarization, with the exception that the lamp was operated at a rated voltage of 120 V, producing a system color response centered at 0.54μ as compared to 0.55μ for Phase II. Albedo measurements were made as before with a system color response centered at 0.56μ because of the lower voltage (28V) necessary on the source lamp so as not to saturate the photomultipliers.

The 6199 photomultipliers used for the B (0.48μ), G (0.54μ), and Visual (0.54μ) measurements were operated at 820 V. The 7102 photomultipliers used for the I (1.0μ) measurements were operated at 1100 V. The voltages were determined experimentally to produce the best average signal to noise ratios for the respective photomultiplier tubes.

A more detailed discussion of the technique mentioned will be reported in a forthcoming Grumman sponsored analysis of photometric and polarimetric procedures (Ref. 10).

PHASE I - NATURAL SPECIMENS

Purpose

Phase I determines the specimens that are polarimetrically promising in integrated visual light relative to the repro- duction of observed polarimetric properties of the lunar surface. Significant parts of the polarimetric curves are determined and correlated to lunar data. The data taken are interpreted primarily in terms of Lyot's lunar observations, with reference to observations of Gehrels. Phase I indicates the specimens to be investigated with the more refined spectral observations of Phase III.

Test Specimens

The light scattered from the contractually required speci- mens was analyzed polarimetrically for the percent polarization and position of the plane of observation. The following natural specimens were investigated:

1. Furnace Slag No. 1 furnished by NASA (Fig. 2)
2. Furnace Slag No. 4 (Fig. 8)
3. Volcanic Ash No. 1 (Fig. 13)
4. Volcanic Ash No. 4 (Fig. 18)
5. Coral No. 1 (Fig. 23)
6. Copper Oxide Powder
7. Silver Chloride Powder

The additional furnace slag specimen (No. 4) was included because Phase II required pulverization of the Furnace Slag No. 1, and it was believed that it would be undesirable to pulverize and thus destroy that particular specimen. Hence, the other slag was used as a substitute.

The properties of percent polarization and position of the plane of polarization are determined as a function of phase angle for simulated lunar longitude and simulated lunar latitude.

Standard Polarimetric Curve and Data Presentation

Currently, the best data for the polarization of integrated lunar light appears to be that of Lyot (see Fig. 1). The average polarization is given by the median curve, B, with the inversion angle, the maximum, and minimum as shown; curves D and E correspond to regions of the lunar surface of strongest and

weakest polarization, respectively. Lyot's standard curve appears on all of the curves that have been obtained at Grumman for Phase I so that a comparison can be easily made. It is to be strongly emphasized that the Lyot curves are _averaged_ for visual integrated light over the lunar surface, and that averages can be misleading if interpreted incorrectly. Comparison to the lunar data of Gehrels et al. or to that of the Russian workers will be made in the Discussion of Results subsection as appropriate.

Note that the lunar percent polarization is independent of lunar latitude and longitude for features with the same albedo (Ref. 13). Also, the plane of polarization of lunar light is either in the plane of vision (for small phase angles) or normal to the plane of vision (for large phase angles) (Refs. 4, 12, and 13).

Experiments

Percent Polarization

The percent polarization as a function of phase angle for the seven samples is presented in Figs. 2 through 35 and Tables 1 through 5. The data can be analyzed conveniently for all samples in five sections:

1. Reproducibility of 0° polarimeter
2. Reproducibility of 60° polarimeter
3. Effect of Sample Orientation
4. Effect of Simulated Lunar Longitude
5. Effect of Simulated Lunar Latitude

Thus, the data are presented for each sample in terms of comparison graphs, along with the average Lyot curve for the percent polarization.

Plane of Polarization

The plane of polarization for the above seven samples was analyzed as a function of phase angle referenced to the aluminite and is presented in Tables 6 through 8. The data are in three parts:

1. Relative Plane of Polarization: 0° Polarimeter, 0° Latitude
2. Relative Plane of Polarization: 60° Polarimeter, 0° Latitude
3. Relative Plane of Polarization: 60° Polarimeter, 30° Latitude

The data are discussed in each part.

Discussion of Test Results

Percent Polarization

Reproducibility of 0° Polarimeter

Consider Figs. 3, 9, 14, 19, 24, 29, and 33, which are summarized in Table 1. Generally, the average increase in the observed percent polarization of 1.3 percent for phase angles between 0° and 25° and 1.2 percent for phase angles between 25° and 68° appears to be the result of the realignment of the two 45° front surface mirrors on the polarimeter source arm between the observations. Initially, the mirrors were aligned mechanically, but prior to the latest measurements, an autocollimator was used to achieve precise alignment. The magnitude of the discrepancy in the incremental percent polarization depends upon the sample. The question arises: "Does the finding of the discrepancy indicate that the equipment is now reading correctly?" We must refer to the calibration made with the glass plate (see appendix), corrected for rear surface reflection, backing material and source residual polarization as required. It appears that there possibly is a small residual positive polarization that has raised the curves at low phase angles, a portion or all of which may be due to the approximately 2 percent residual polarization of the source perpendicular to the plane of vision. It appears that the curves are most sensitive at the low phase angles with respect to residual polarization effects, whereas at large angles, these effects are much smaller. However, over a period of one week, the reproducibility of data is of the order of $\frac{1}{2}$ percent.

Thus, the question of exactly where the inversion angle is located and whether copper oxide or silver chloride may have an inversion angle depends upon a more precise calibration of the polarimeter at small phase angles. Procedures are being evolved to permit the more precise checking of the residual polarization of the source with a portable polarimeter, and the use of a glass plate standard to check residual polarization of the polarimeter-photometer unit.

14

TABLE 1

Reproducibility of Data - 0° Polarimeter: Incremental Percent Polarization Relative to Data Taken at the Earliest Date.*

Sample	Phase Angle Range	
	0°-25°	25°-68°
Furnace Slag No. 1	+1.0	+1.0
Furnace Slag No. 4	+ .7	+1.7
Volcanic Ash No. 1	+2.3	+2.5
Volcanic Ash No. 4	**$\left\{\begin{array}{l}-1.5\\+2.0\end{array}\right.$	**$\left\{\begin{array}{l}-1.5\\+2.0\end{array}\right.$
Coral No. 1	+0.8	0.0
Copper Oxide	+4.5	+4.0
Silver Chloride	+0.6	0.0
Average	+1.3	+1.2

*See Figs. 3, 9, 14, 19, 24, 29, and 33, respectively.

**The two values shown are the result of comparisons between different data, the first figure denotes comparisons of data taken on 3/1/65 and 3/22/65; the second figure compares 9/22/65 and 10/26/65 (see Fig. 19).

Reproducibility of the 60° Polarimeter

Consider Figs. 4, 10, 15, 20, 25, and 30, which are summarized in Table 2. Here we observe that the increased percent polarization is largest at the smallest phase angles, which agrees with the results from the 0° polarimeter. The average increases of +1.9 percent and 1.0 percent at phase angles of 0° to 25° and 25° to 68°, respectively, are to be compared to +1.3 percent and +1.2 percent for the 0° polarimeter. It appears that at the lowest phase angles, the 60° polarimeter has a small residual polarization of a fraction of a percent above the 0° polarimeter, which may be due to the flexure of the large polarimeter frame. At the highest phase angles, sample depolarization is apparently large enough so that effects of

mirror reorientation are negligible. However, the reproducibility of the data is of the order of $\frac{1}{2}$ percent except for Furnace Slag No. 1, which consists of pebbles and appears strongly orientation sensitive.

TABLE 2

Reproducibility of Data - 60° Polarimeter:
Incremental Percent Polarization Relative
to Data Taken at the Earliest Date.*

Sample	Phase Angle Range		
	0°-25°	25°-68°	68°-130°
Furnace Slag No. 1	+1.0	-1.0	-3.0
Furnace Slag No. 4	+1.3	-0.2	** $\begin{cases} -2.0 \\ +2.0 \end{cases}$
Volcanic Ash No. 1	+2.3	+3.1	+3.7
Volcanic Ash No. 4	+1.7	+1.0	+1.0
Coral	+0.5	0.0	+0.8
Copper Oxide	+4.5	+3.0	-0.5
Average	+1.9	+1.0	+0.3

*See Figs. 4, 10, 15, 20, and 30, respectively.

**The two values shown are the result of comparison
  between different dates, the first figure denotes
  comparison of data taken on 8/19/65 and 10/27/65;
  the second figure compares 10/27/65 and 11/3/65
  (see Fig. 10).

Effect of Sample Orientation

Only two samples with fixed physical structure were used to investigate sample orientation effect. With powders and particles, the orientation is not very meaningful. The results for Furnace Slag No. 1 and Coral No. 1, which are shown graphically in Figs. 5 and 26 and tabulated in Table 3, are differences between measurements taken as the samples are rotated 90° about the normal to their surface. It appears that sample orientation has almost negligible effect at low phase angles but a large effect at large

phase angles for these samples. This is initially attributed to shadowing effects of the samples, which are greatest at largest phase angles.

TABLE 3

Effect of Sample Orientation* - 60° Polarimeter:
Incremental Percent Polarization Relative
to the Standard Sample Position Data.**

Sample	Phase Angle Range		
	0°-25°	25°-68°	68°-130°
Furnace Slag No. 1	-0.5	-0.5	-2.5
Coral No. 1	0.0	0.0	-0.3
Average	-0.3	-0.3	-1.4

*See Text.

**See Figs. 5 and 26, respectively.

Effect of Simulated Lunar Longitude

The effect of simulated lunar longitude is obtained by the intercomparison of the observations taken between October 25 and October 27 from the 0° and 60° polarimeters. The results are presented in Figs. 6, 11, 16, 21, 27, 31, and 34 and summarized in Table 4. It must be remembered that at low phase angles, the discrepancy could be due to a residual polarization in the 60° polarimeter above that which could exist in the 0° polarimeter. Thus, the average observed effect of +0.4 percent at small phase angles could be, in part or all, due to residual polarization in the 60° polarimeter. At large phase angles, it is seen that the effect is negligible; this probably is the result of factors such as source residual polarization and depolarization effects of the sample.

Effect of Simulated Lunar Latitude

The effect of simulated lunar latitude is the result of the comparison of data taken between October 25 and October 29 on the 60° polarimeter only, and hence residual differences between two polarimeters do not enter. The results are depicted in Figs. 7, 12, 17, 22, 28, 32, and 35, and summarized in Table 5. At low

TABLE 4

Effect of Simulated Lunar Longitude -
Incremental Percent Polarization for a 60° Viewing Angle
Relative to the Data Taken for a 0° Viewing Angle.*

Sample	Phase Angle Range	
	0°-25°	25°-68°
Furnace Slag No. 1	0	0.0
Furnace Slag No. 4	+0.4	-0.8
Volcanic Ash No. 1	+0.6	+0.2
Volcanic Ash No. 4	+0.5	-0.3
Coral No. 1	+0.5	+0.9
Copper Oxide	+0.5	-0.2
Silver Chloride	+0.6	+0.5
Average	+0.4	+0.0

*See Figs. 6, 11, 16, 21, 27, 31, and 34, respectively.

TABLE 5

Effect of Simulated Lunar Latitude of 30° -
Incremental Percent Polarization Relative to 0° Simulated Lunar
Latitude, both Orientations Being at 60° Simulated Lunar Longitude.*

Sample	Phase Angle Range		
	0°-25°	25°-68°	68°-130°
Furnace Slag No. 1	-0.3	-1.0	-1.5
Furnace Slag No. 4	+0.5	+1.0	+7.0
Volcanic Ash No. 1	-0.3	-0.3	-0.6
Volcanic Ash No. 4	0.0	0.0	+0.2
Coral No. 1	-0.5	-0.6	-1.2
Copper Oxide	0.0	-0.5	-0.5
Silver Chloride	0.0	-1.5	-5.0
Average	-0.1	-0.4	-0.2

*See Figs. 7, 12, 17, 22, 28, 32, and 35, respectively.

phase angles, the average amounts to a polarization increment of -0.1 percent. For particular samples, especially very rough ones where shadowing could cause an appreciable effect on albedo larger variations appear at small phase angles (see Ref. 12).

At large phase angles, the effect on the percent polarization is varied, depending upon the sample, but in a consistent direction for a particular sample with increase of phase angle. Furnace slag No. 4 is particularly exceptional, and the effect is probably the result of a reflecting particle oriented in a direction to produce a strong polarization at large phase angles. The silver chloride also is exceptional, and this may be due to some dielectric property that produces a strong polarization at large phase angles.

Plane of Polarization

Zero Degree Polarimeter

The observations made on the position of the plane of polarization are listed in Table 6 referenced to the aluminite at a phase angle of 68°. This angle of 68° was chosen as the largest possible angle that could be used to check the 0° polarimeter. At phase angles below about 40°, the reference plate begins to produce an observed rotation of the plane of polarization, and thus is inadequate at smaller phase angles. The largest phase angle on the 0° polarimeter is 68°, and hence, it was selected. It can be seen that the plane of polarization is perpendicular to the plane of vision within a few tenths of a degree at phase angles of 68° and 35°, as expected (Ref. 13). Coral appears to be an exception, but this is primarily due to the low polarization resulting in a low signal to noise ratio, and decreased accuracy. For a phase angle of 5°, the plane of polarization is parallel to the plane of vision within a few degrees for the samples with distinct inversions - furnace slag No. 1, volcanic ashes Nos. 1 and 4, and coral No. 1. With this polarimeter, furnace slag No. 4 has an inversion, but the direction of displacement of the plane of polarization cannot be determined with the limited angular data. Note (see next two sections) that furnace slag No. 4 does not have an inversion when observed with the 60° polarimeter either in 60° simulated longitude or 30° simulated latitude. The silver chloride and copper oxide planes of polarization are not exactly perpendicular to the plane of vision, presumably due to the lower accuracy at the low polarization

TABLE 6

Plane of Polarization (Relative):
0° Polarimeter, 0° Latitude
$\Delta\theta$ (degrees) referred to 68° Aluminite Reference

Sample	Phase Angles (Degrees)		
	68°	35°	5°
Furnace Slag No. 1 11/16/65	+.3	+.1	-85.1 (?)
Furnace Slag No. 4 11/16/65	-.2	+.2	* $\begin{Bmatrix} -86.5 \\ +93.5 \end{Bmatrix}$ (?)
Volcanic Ash No. 1 11/16/65	+.1	+.2	-86.8 (?)
Volcanic Ash No. 4 11/16/65	+.4	+.3	-87.7 (?)
Coral No. 1 11/15/65	+.3	+1.5	-87.6 (?)
Copper Oxide 11/16/65	+.1	-.5	-10.0 (?)
Silver Chloride 11/15/65	-.3	-.3	-19.7 (?)
Average	+0.1	+0.2	

*Uncertainty due to limited data.

values existing at the phase angle of 5°. Data of questionable accuracy due to very low signal to noise ratio are followed by the symbol (?). However, a more basic question has arisen. That is whether there is a gradual shift in the plane of polarization near the inversion angle, either in one direction or the opposite, or whether there is an abrupt change. If there is a gradual change, this requires highly sensitive measurements to be made near the inversion.

Sixty Degree Polarimeter (0° Latitude)

The data from these measurements are tabulated in Table 7 referenced to the aluminite at a phase angle of 128°, which was chosen as the largest possible angle (see above).

It appears that there is an angular instrumental effect that increases with phase angle; this effect appears to be the result of the flexure of the polarimeter frame. The effect appears to

TABLE 7

Plane of Polarization (Relative):
60° Polarimeter, 0° Latitude
$\Delta\theta$ (degrees) referred to 128° Aluminite Reference

Sample	Phase Angles (Degrees)				
	128°	95°	68°	35°	5°
Furnace Slag No. 1 11/11/65	- .1	- .3	-1.5	-1.2	-69.6 (?)[*]
Furnace Slag No. 4 11/12/65	+1.0	+1.0	+ .8	+ .1	-10.9 (?)[*]
Volcanic Ash No. 1 11/12/65	+1.4	+1.2	+1.1	+ .3	-75.8 (?)[*]
Volcanic Ash No. 4 11/12/65	+1.1	+1.1	+1.2	+ .4	-80.5 (?)[*]
Coral No. 1 11/12/65	+1.3	+1.6	+1.3	+ .6	none
Copper Oxide 11/12/65	+ .8	+1.0	+ .6	-1.0	-2.7 (?)[*]
Silver Chloride 11/15/65	+1.0	+ .7	+ .7	- .6	- 7.8 (?)[*]
Average	+0.9	+0.9	+0.6	-0.2	

[*]For a discussion of the symbol (?), see the previous section for the 0° polarimeter.

begin at a phase angle of about 40° and increases to a value of about 1° at a phase angle of 128°. Below about 40°, the instrumental accuracy is of the order of about 1°.

It is observed that furnace slag No. 1 and volcanic ash Nos. 1 and 4 have inversions; (i.e., passes through 0° polarization and goes negative) the plane of polarization is within a degree of being perpendicular to the plane of vision above the inversion and approximately parallel to the plane of vision below the inversion as expected (Ref. 13). The inaccuracy at the 5° phase angle is the result of a low signal to noise ratio from the resultant low polarization.

The coral No. 1, copper oxide, and silver chloride do not have an inversion from these data; it appears that this is the

result of the equipment accuracy limitations at small phase angles, resulting from the residual polarization of the source (see text: Test Equipment).

Sixty Degree Polarimeter (30° Latitude)

These data are shown in Table 8 referenced to the aluminite at a phase angle of 128° and 0° latitude (viewing angle of 60°) (see discussion above for the selection of 128°).

TABLE 8

Plane of Polarization (Relative):
60° Polarimeter, 30° Latitude
$\Delta\theta$ (degrees) referred to 128° Aluminite Reference
at 0° Latitude

Sample	Phase Angles (Degrees)				
	128°	95°	68°	35°	5°
Furnace Slag No. 1 11/15/65	+ .8	+1.0	+1.1	+ .8	-45.7
Furnace Slag No. 4 11/12/65	0	- .6	- .4	0	- 1.2
Volcanic Ash No. 1 11/12/65	+1.7	+ .4	- .2	- .8	-80.2 (?)
Volcanic Ash No. 4 11/12/65	- .5	- .8	- .2	+ .7	-87.7
Coral No. 1 11/15/65	+1.9	+1.9	+1.8	+1.1	none
Copper Oxide 11/12/65	+1.5	+1.4	+1.8	+2.0	+ 1.5
Silver Chloride 11/15/65	+ .4	+ .4	+ .5	+2.0	+ 4.3
Average	+0.8	+0.5	+0.6	+0.8	———

The comments of the previous section on instrumental effects do not clearly apply for this set of observations, as indicated by the averages (i.e., there is no definite trend indicated between consecutive phase angle observations). The analysis of the

flexure effects are complicated by the tilting of the sample so that the normal to the average surface makes an angle of 30° to the plane of vision.

From these data, we find that the furnace slag No. 1, and volcanic ash Nos. 1 and 4 have inversions within the experimental errors, with the plane of polarization behaving as expected for larger phase angles, but not quite parallel to the plane of vision for 5° phase angle, particularly in the case of furnace slag No. 1. This is basically a problem of low signal resulution.

Essentially, the remaining samples lack an inversion, probably for the same reasons outlined in the previous section (i.e., residual polarization of the source).

Lunar Implications

On the basis of the data obtained for the percent polarization of the various samples as a function of phase angle, which is summarized in Table 9 and Fig. 36, we may infer the appropriateness of particular samples as possessing properties characteristic of the lunar surface.

It appears that the following materials possess average properties that could vary sufficiently in detail, depending upon the particular sample of material, to permit them to be considered:

- Volcanic Ash No. 1

- Volcanic Ash No. 4

- Coral No. 1

Figures 36a and b show that the locations of the maxima on the curves of the aforementioned materials do not occur at exactly 100°, as on the Lyot curve. The location of the maximum could possibly be affected by the albedo, or by the geometrical or physical properties of the material. The maxima might thus be slightly shifted by varying one of these parameters to achieve exact agreement.

Two other materials could be considered as having appropriate properties when combined with a suitable nonpolarizing material of varying albedo as a function of phase angle that would serve

TABLE 9

Preliminary Correlation to Lunar Data

Sample	% P min	% P max	Inversion Angle	Angle of Min.	Angle of Max.	Geometric Albedo	Lat. Indep.	Long. Indep.
Lyot (Lunar standard)	-1.2	7.6	23.5	11	102	.11	yes	yes
Furnace Slag No. 1**	~-.5	47	~16	~5	130	.10	yes	yes
Furnace Slag No. 4	0 (?)	39	possible	--	130	.10	no	no
Volcanic Ash No. 1*	~-1.5	20	~18	8	115	.11	yes	yes
Volcanic Ash No. 4*	-1.0	17	~17	~8	113	.14	yes	yes
Coral No. 1*	~-0.5(?)	5	~13	~9	81	.16	yes	yes
Copper Oxide**	~-1.0(?)	>75	possible	~6	>130	.07	yes	yes
Silver Chloride	0 (?)	>42	possible	--	>130	.13	no	yes

*Promising for Lunar Simulation.
**Promising for Lunar Simulation when modified by combining with nonpolarizing material.

to reduce the maximum percent polarization and shift the maxima to smaller angles:

- Furnace Slag No. 1

- Copper Oxide

Because of the lack of the required independence of latitude and/or longitude for furnace slag No. 4 and silver chloride, these do not appear to possess the properties required in the form observed.

Data obtained from the position of the plane of polarization do not specifically conflict with the conclusions drawn from the percent polarization characteristics.

There is no essential disagreement with the results of Lyot, Dollfus, Hapke, or Coffeen (see Ref. 13 through 16). Volcanic ash has previously been shown to be satisfactory on small scale photometers (Refs. 13 and 16). Proton bombardment as investigated by Hapke, Dollfus, and Wehner (Refs. 15, 17, and 18) has not as yet been used, nor have dust or "fairy castle" models. However, coral No. 1, furnace slag No. 1, and copper oxide have emerged as new possible lunar models on the basis of the present program.

The integrated visual light, "V," as used in the measurements in this investigation, is the result of the combination of the S-11 photosensitive surface of the 6199 photomultiplier and the spectral output of the tungsten-iodine lamp.

The common properties that are exhibited by all polarimetrically satisfactory materials observed in this investigation are: roughness (nonspecular); nontransparency of materials; nonhomogeneity of materials for the most part (the homogeneity, or isotropy of the copper oxide has not been determined); and general scale of roughness much greater than the wavelength of light.

Conclusions

As a result of Phase I, we may draw certain preliminary conclusions, subject to further experimental verification and theoretical corroboration. For this investigation, materials were chosen that were photometrically promising.

The main conclusion of Phase I is that it appears that the average polarimetric properties of a surface do not uniquely define the surface material or configuration. As a matter of fact, it appears that a number of small surfaces may be combined in an infinite number of ways to produce the required average polarization characteristics of the lunar surface. This will be elaborated in Phase IV.

The surface commonality that exists on the basis of the investigation of Phase I indicates that clearly defined limits cannot be set for lunar particle sizes, porosity, roughness, homogeneity, or complex index of refraction. In other words, previously reported models such as those of Lyot, Dollfus, Gehrels, Hapke, and Wehner (see Refs. 4, 13-15, and 17-18) are not unique.
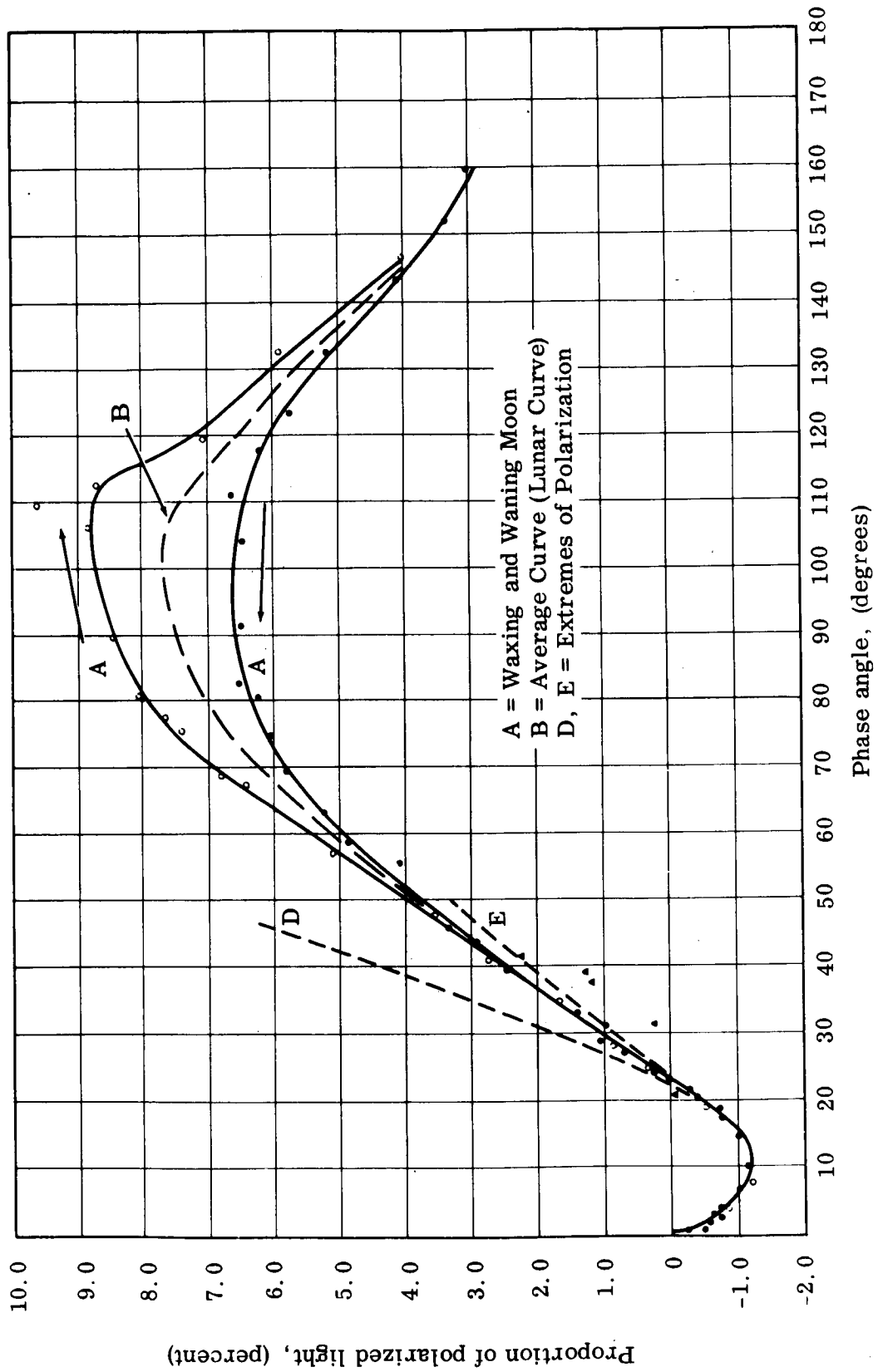
Fig. 1 Polarization Curve of the Moon (Lyot-1929)

A = Waxing and Waning Moon
B = Average Curve (Lunar Curve)
D, E = Extremes of Polarization

Phase angle, (degrees)

Proportion of polarized light, (percent)
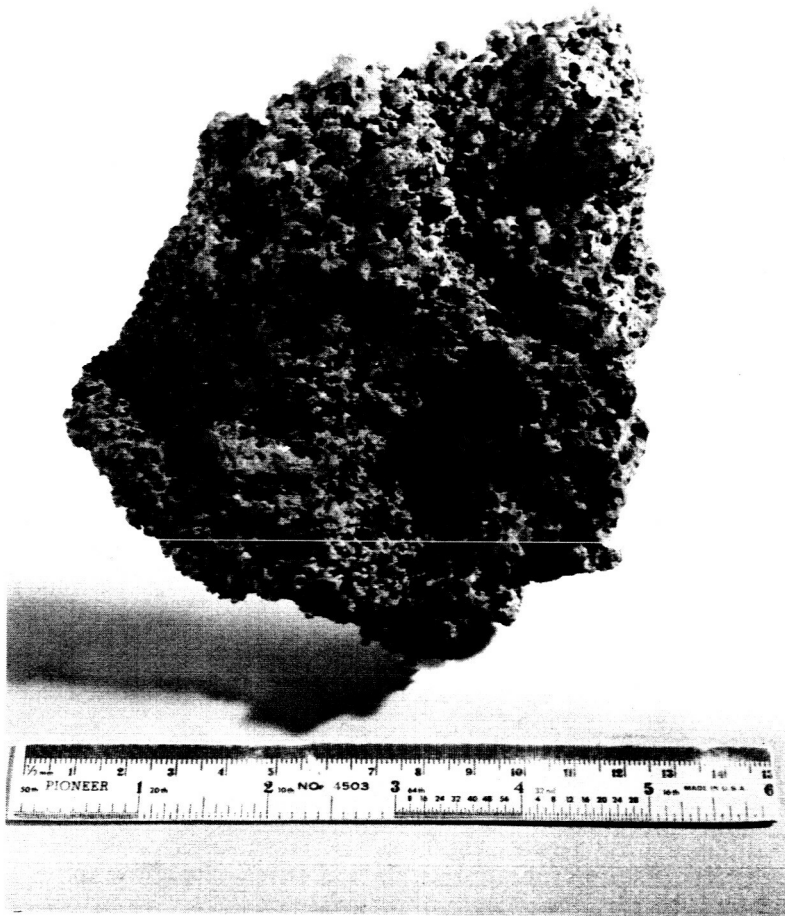
Fig. 2 Furnace Slag No. 1
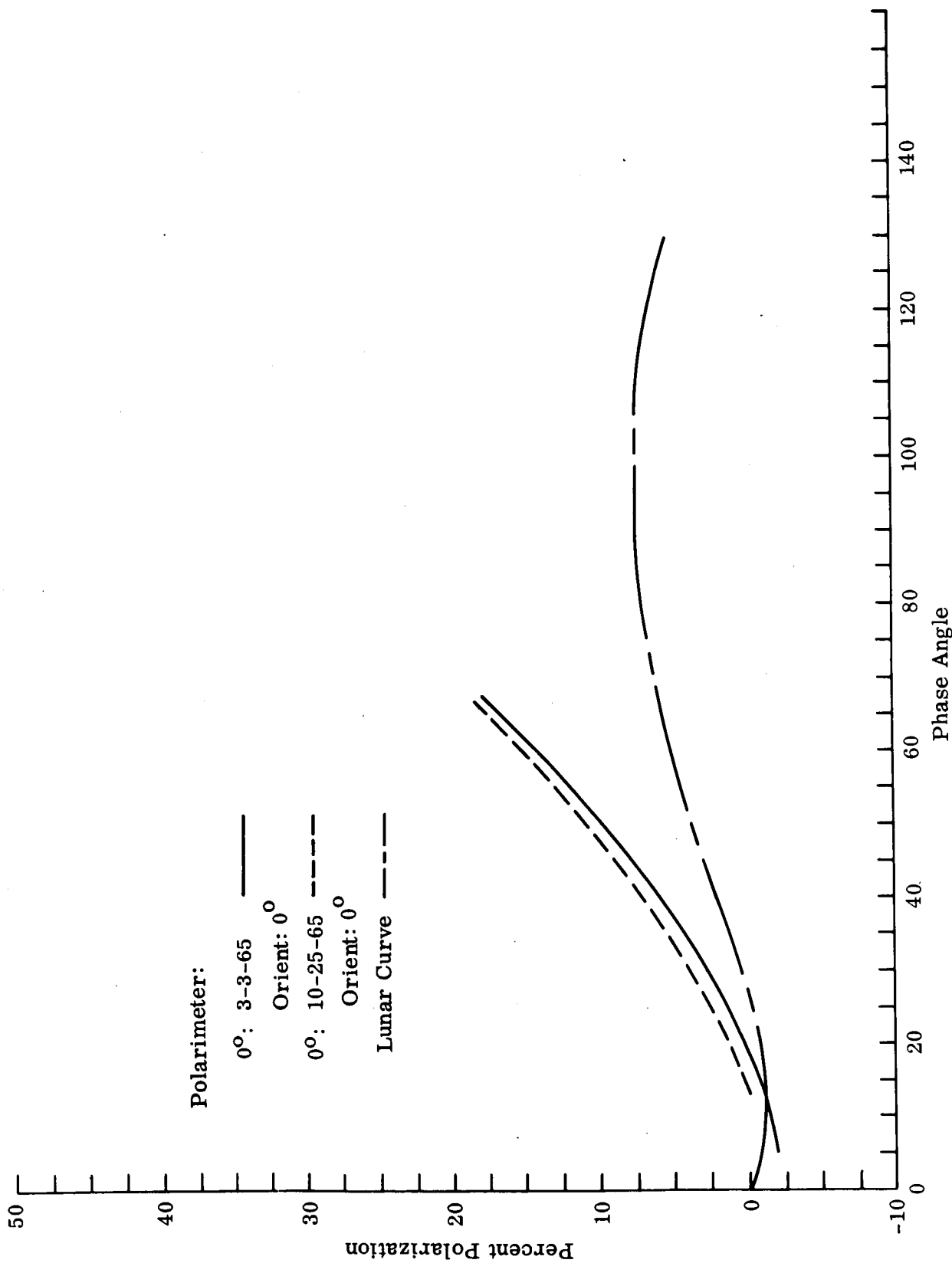
Fig. 3 – Furnace Slag No. 1: Comparison of Percent Polarization Observations on Different Dates – 0° Polarimeter
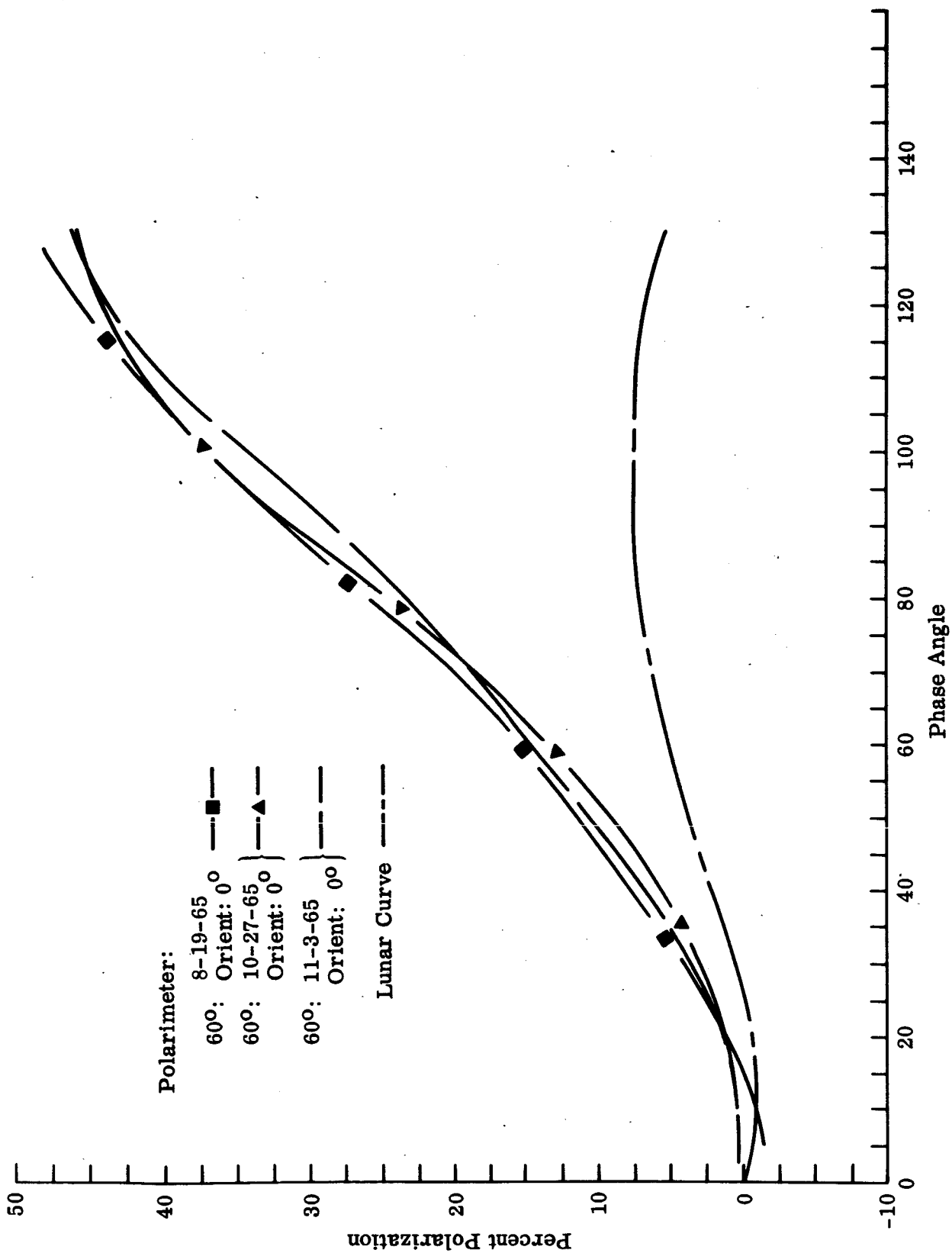
Fig. 4 – Furnace Slag No. 1: Comparison of Percent Polarization Observations on Different Dates – 60° Polarimeter
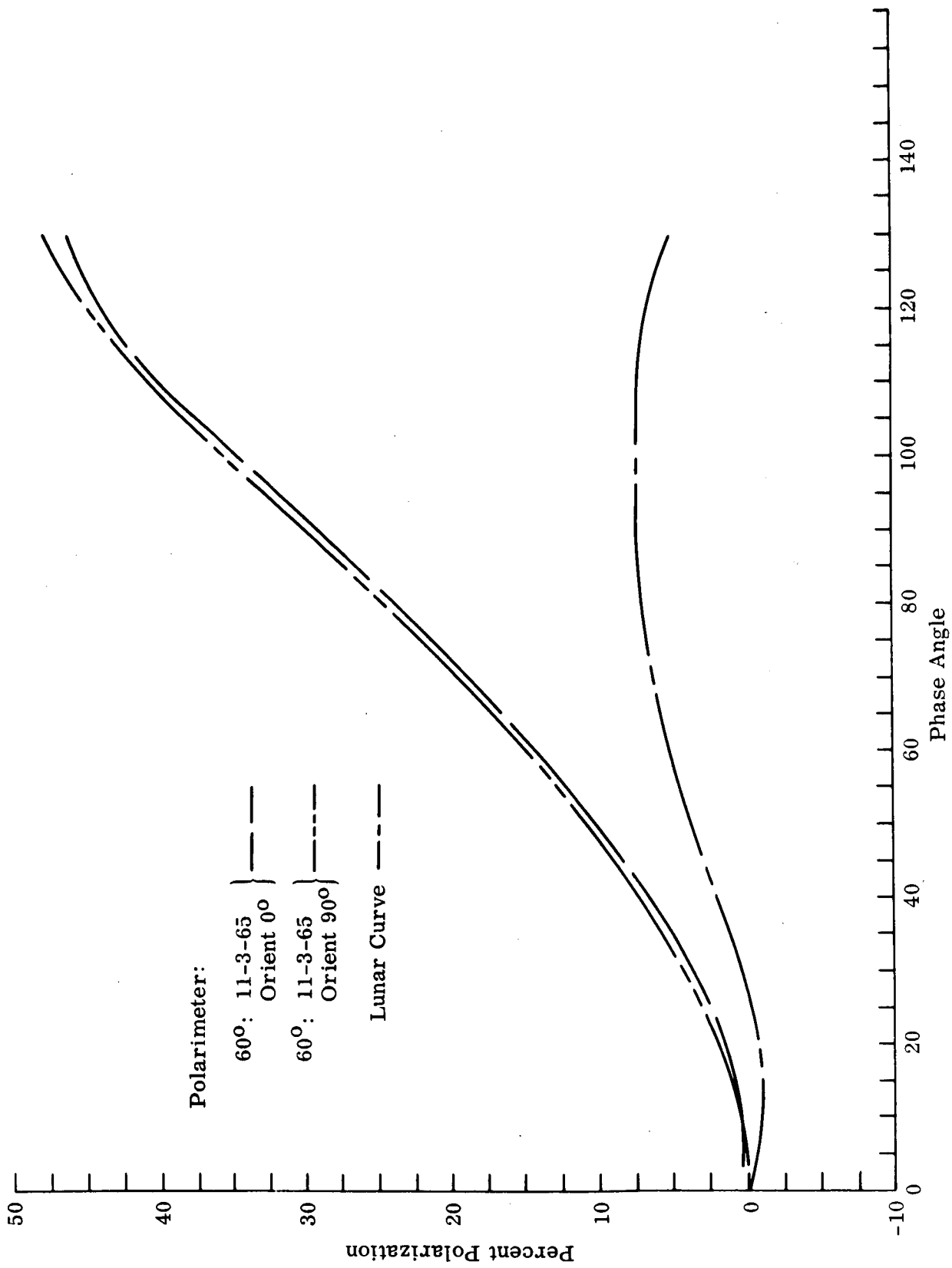
Fig. 5 – Furnace Slag No. 1: Sample Orientation Effect on Observed Percent Polarization
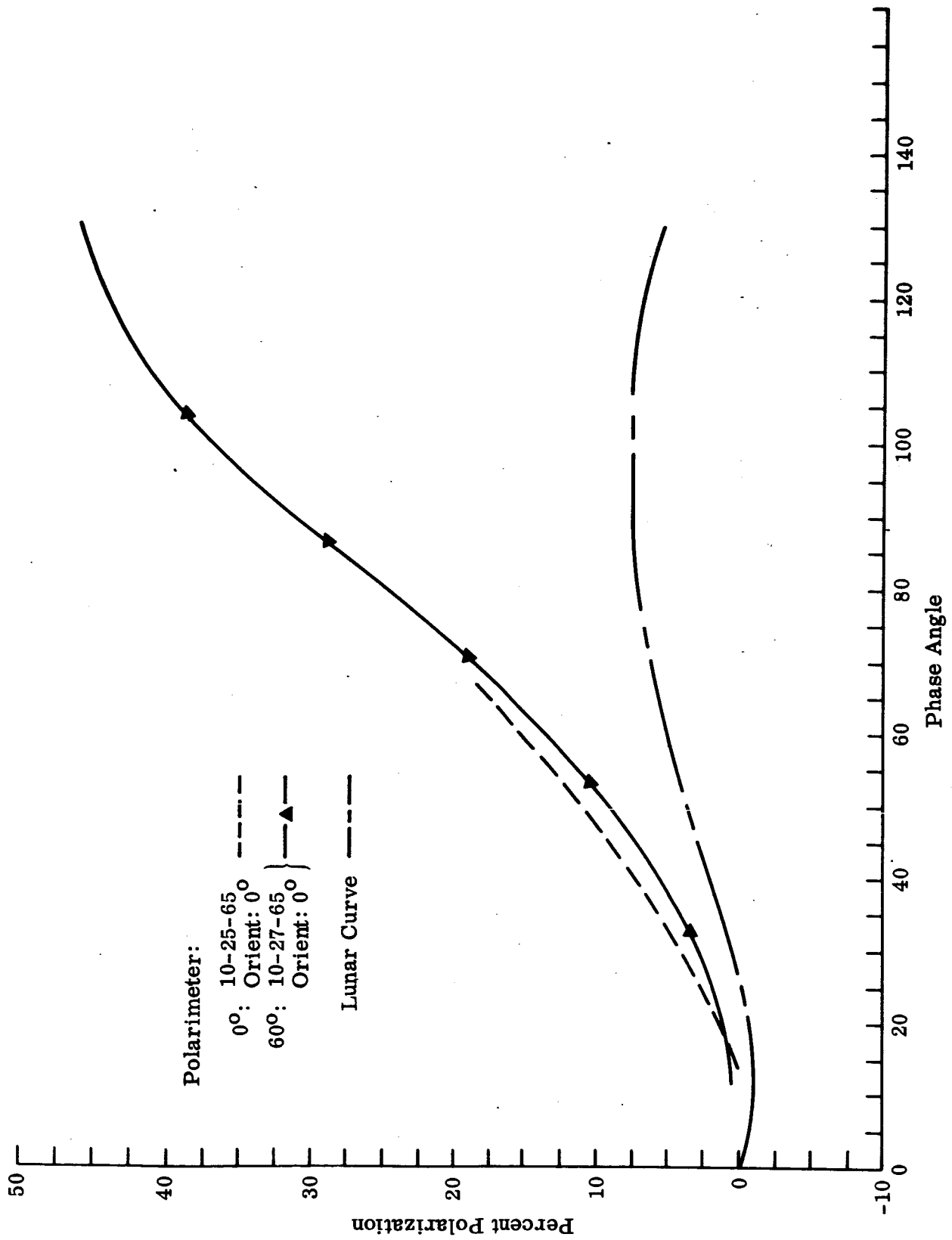
Fig. 6 – Furnace Slag No. 1: Simulated Lunar Longitude Effect on Percent Polarization
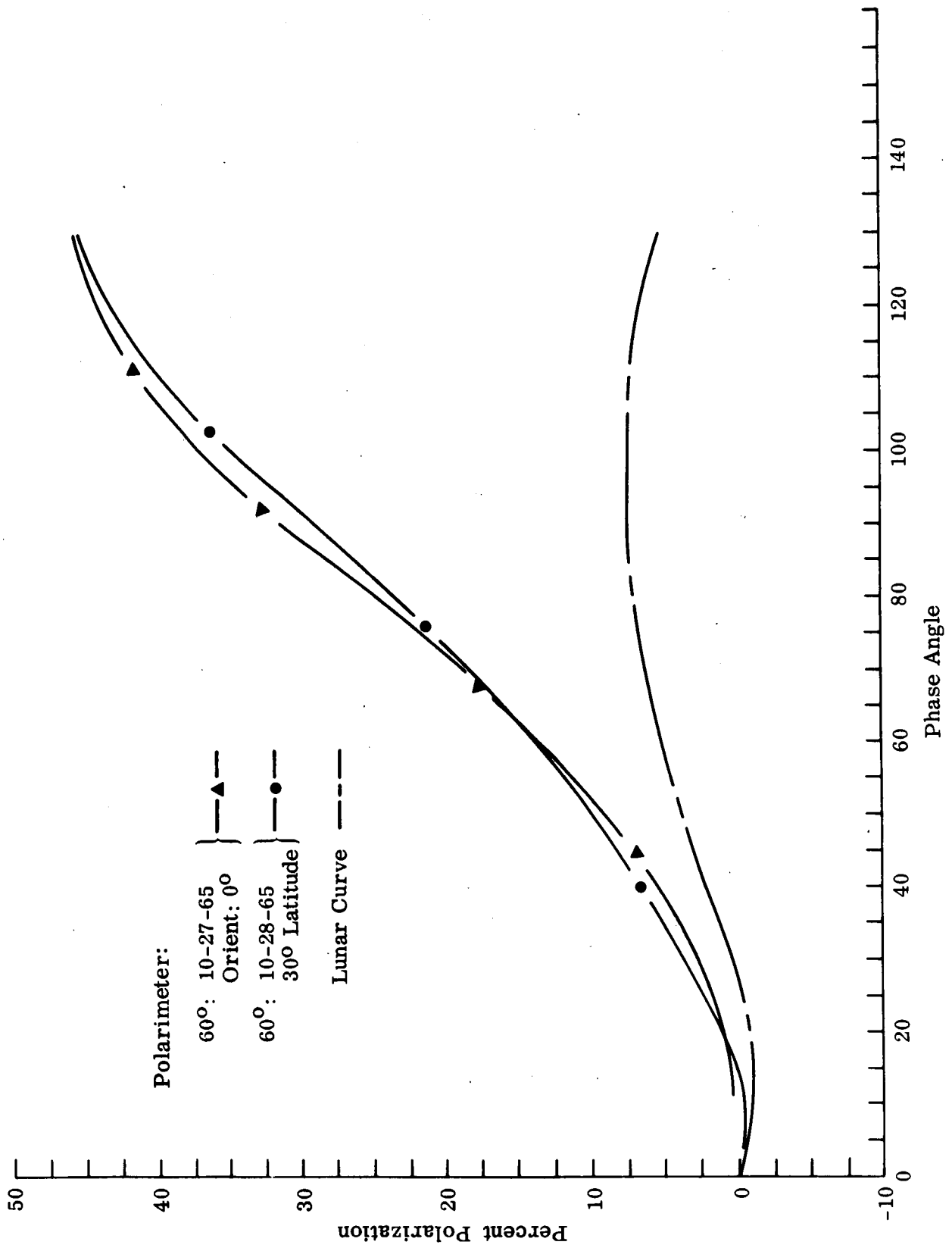
Fig. 7 - Furnace Slag No. 1: Simulated Lunar Latitude Effect on Percent Polarization
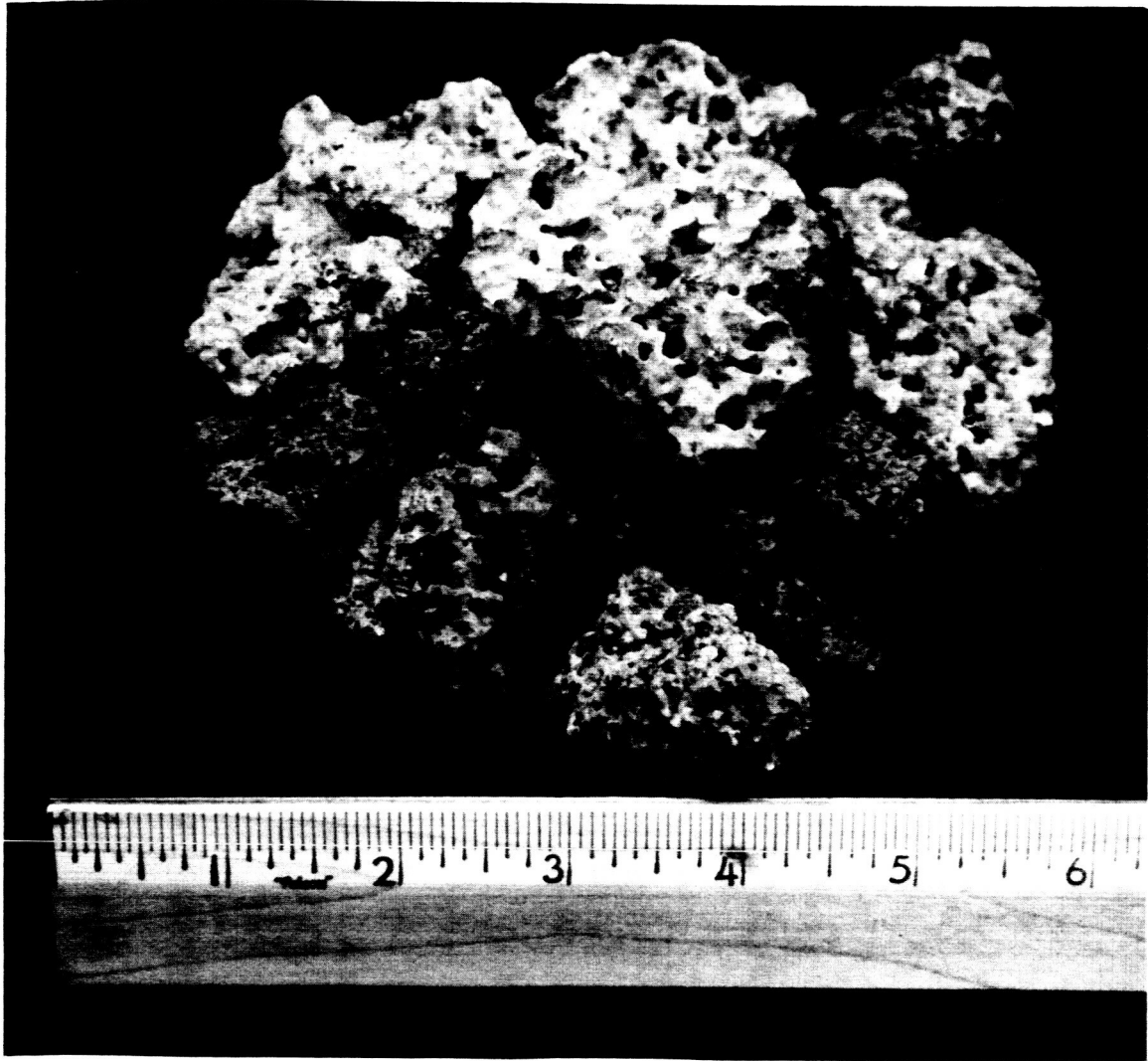
Fig. 8   Furnace Slag   # 4
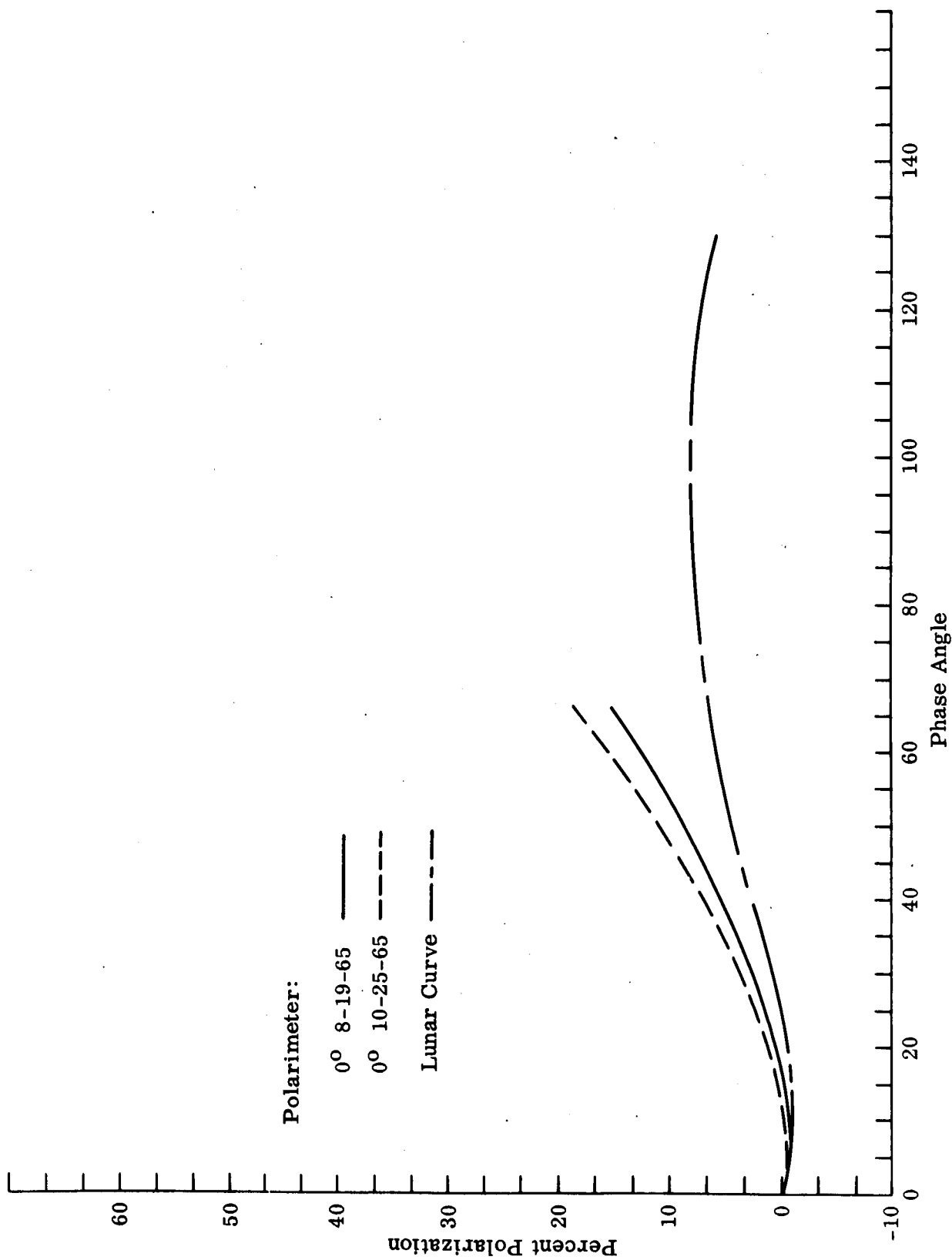
Fig. 9 – Furnace Slag No. 4: Comparison of Percent Polarizations on Different Dates – 0° Polarimeter
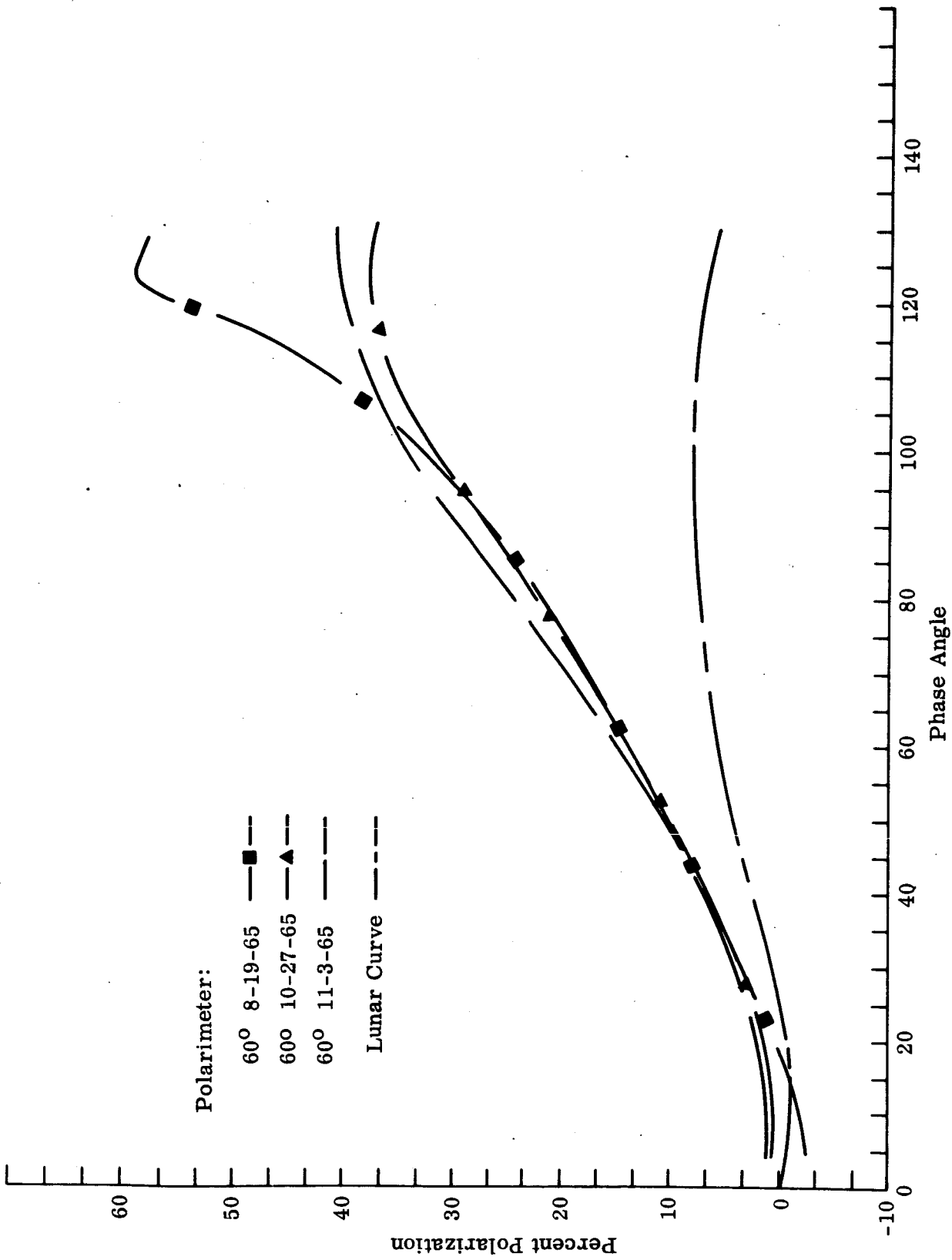
Fig. 10 – Furnace Slag No. 4: Comparison of Percent Polarization Observations on Different Dates – 60° Polarimeter

35
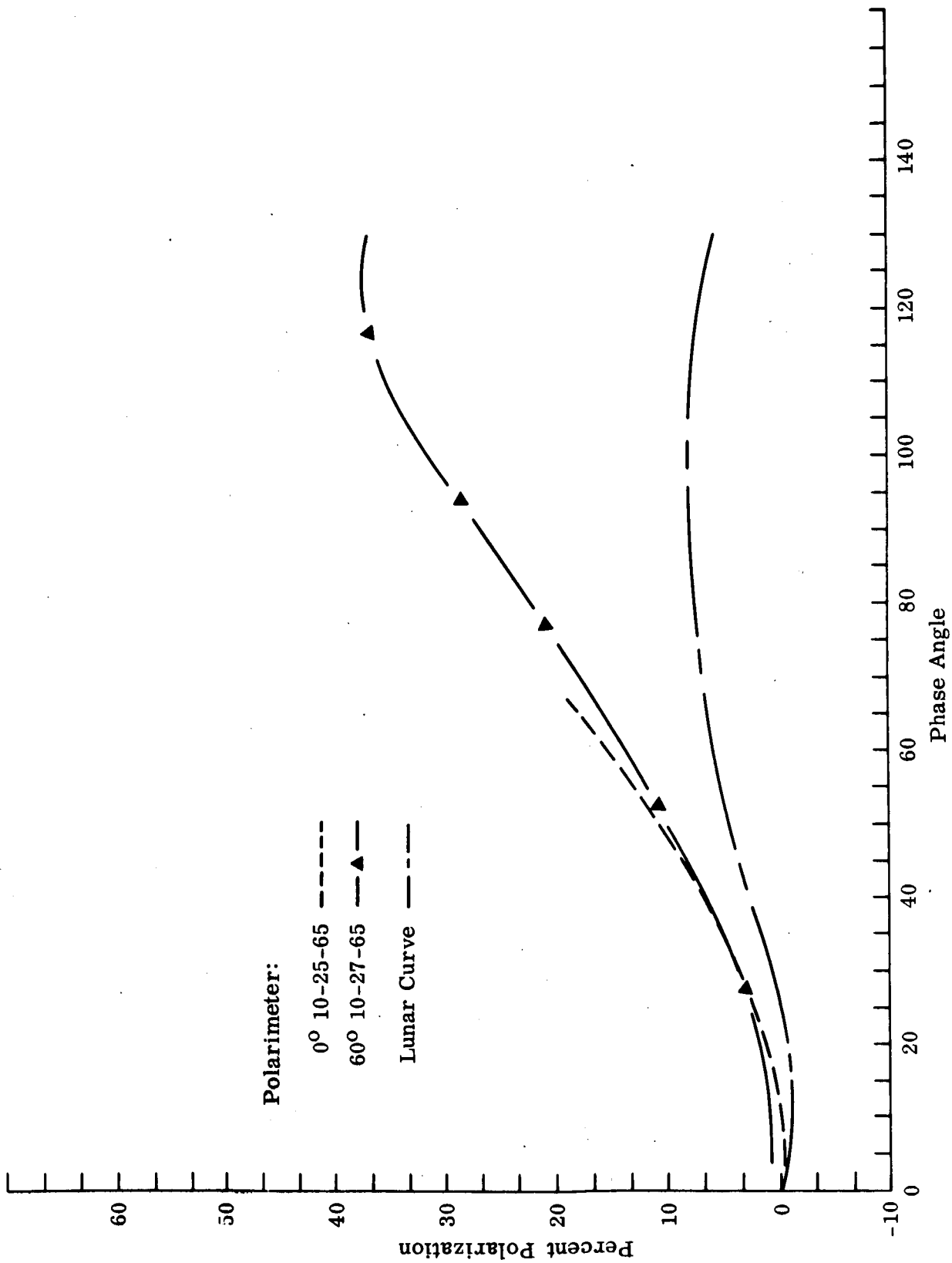
Fig. 11 - Furnace Slag No. 4: Simulated Lunar Longitude Effect on Percent Polarization
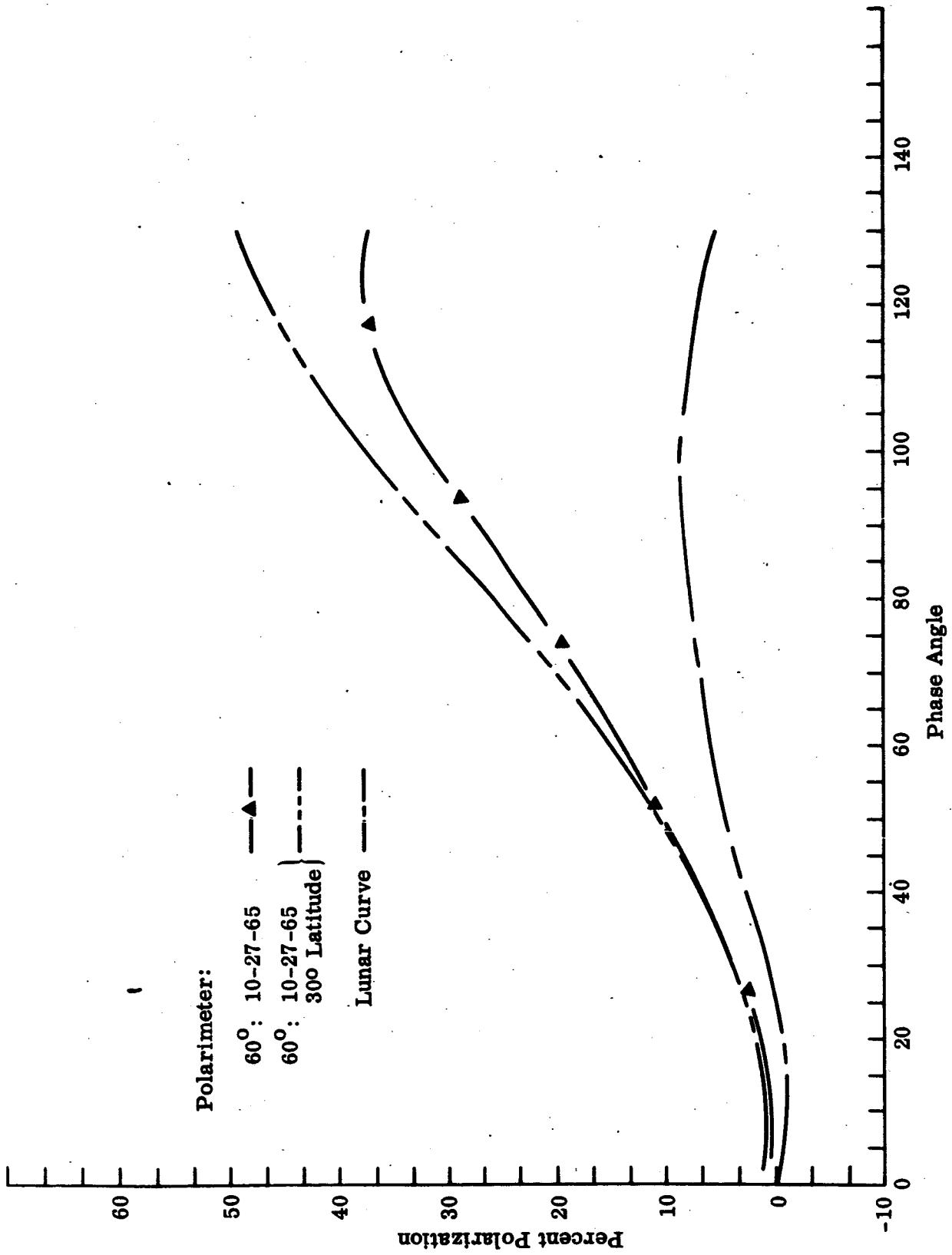
Fig. 12 -- Furnace Slag No. 4: Simulated Lunar Latitude Effect on Percent Polarization

Phase Angle

Percent Polarization

Polarimeter:

60°: 10-27-65

60°: 10-27-65
30° Latitude

Lunar Curve
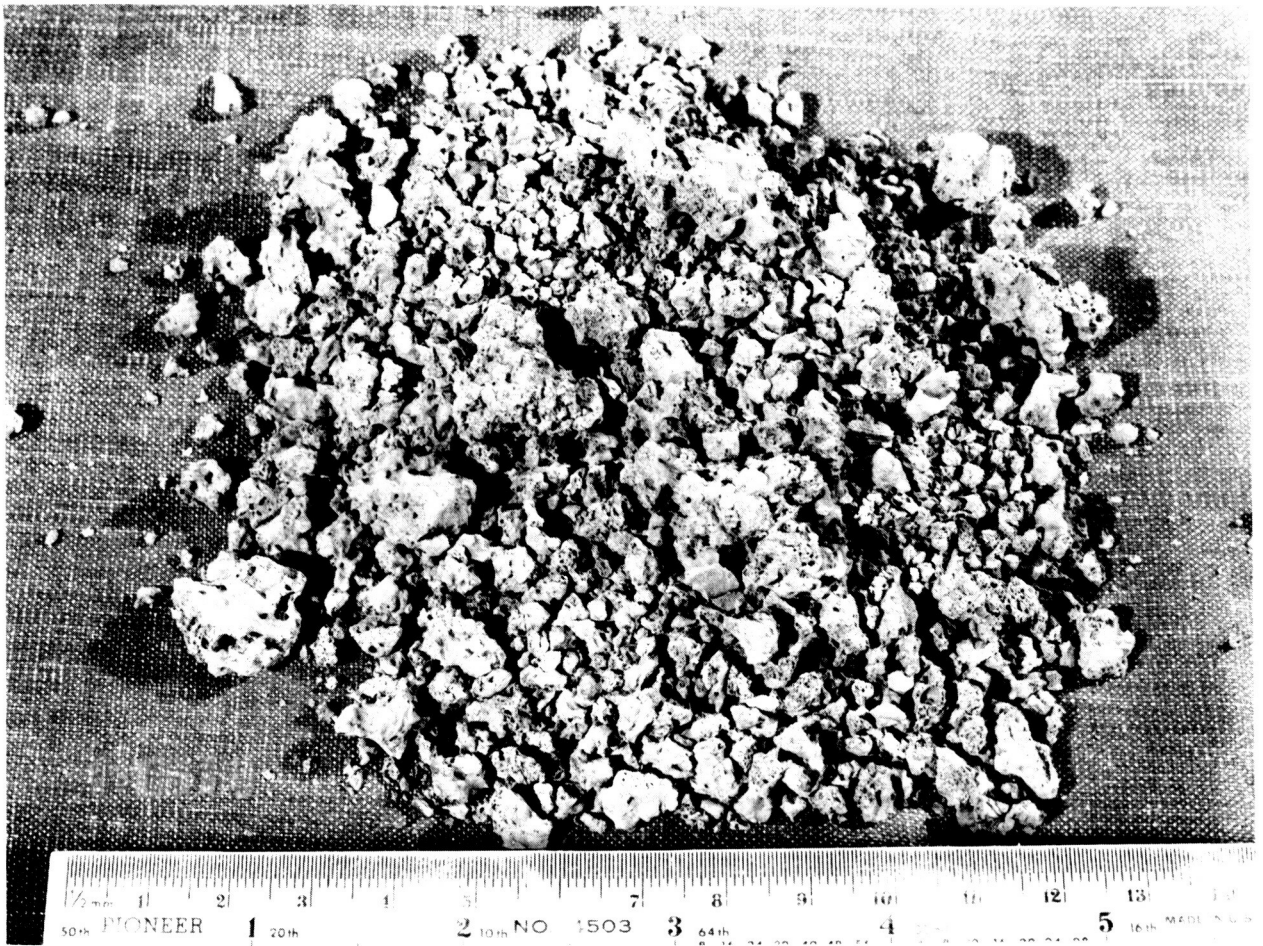
Fig. 13   Volcanic Ash No. 1
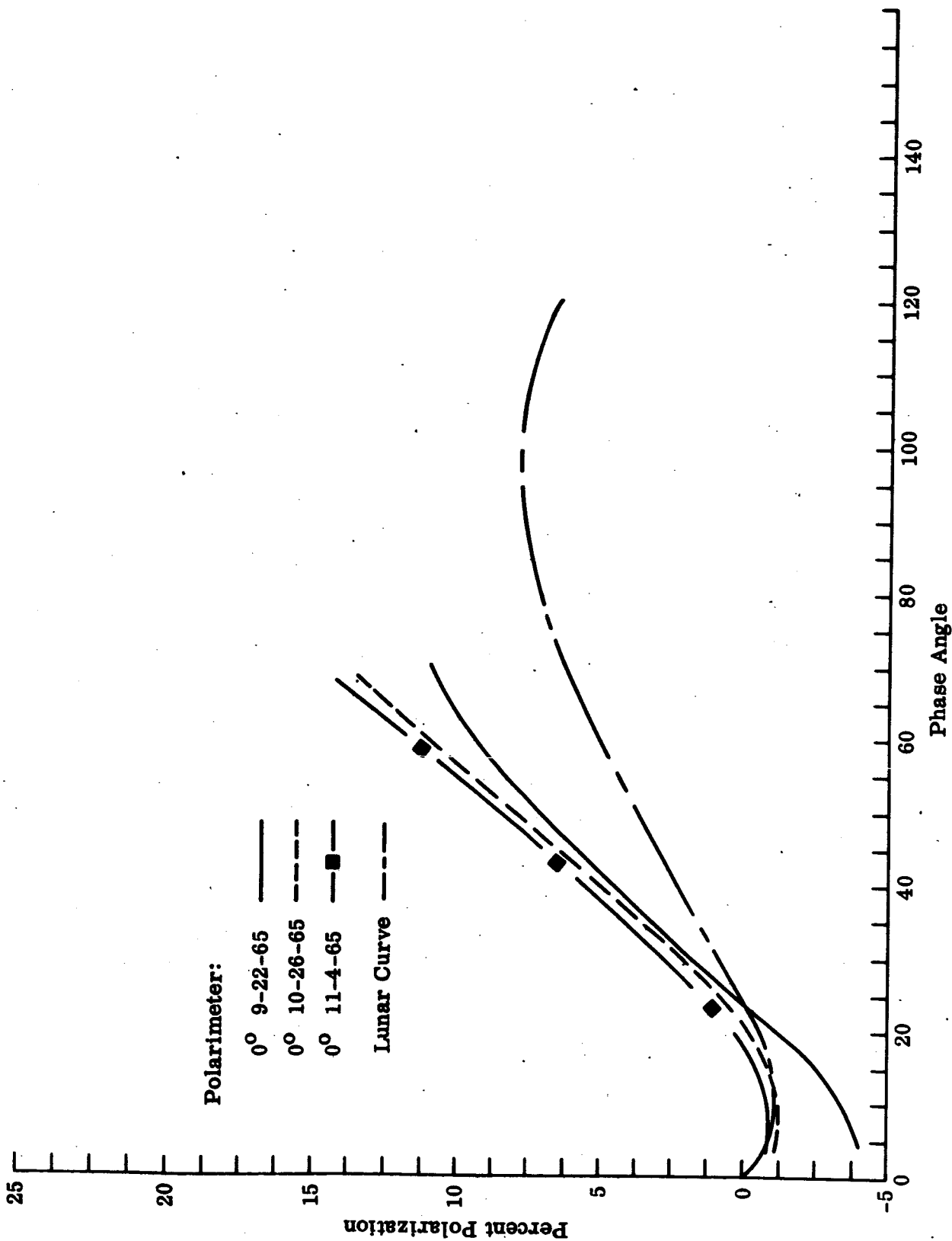
Fig. 14 – Volcanic Ash No. 1: Comparison of Percent Polarization Observations on Different Dates – 0° Polarimeter
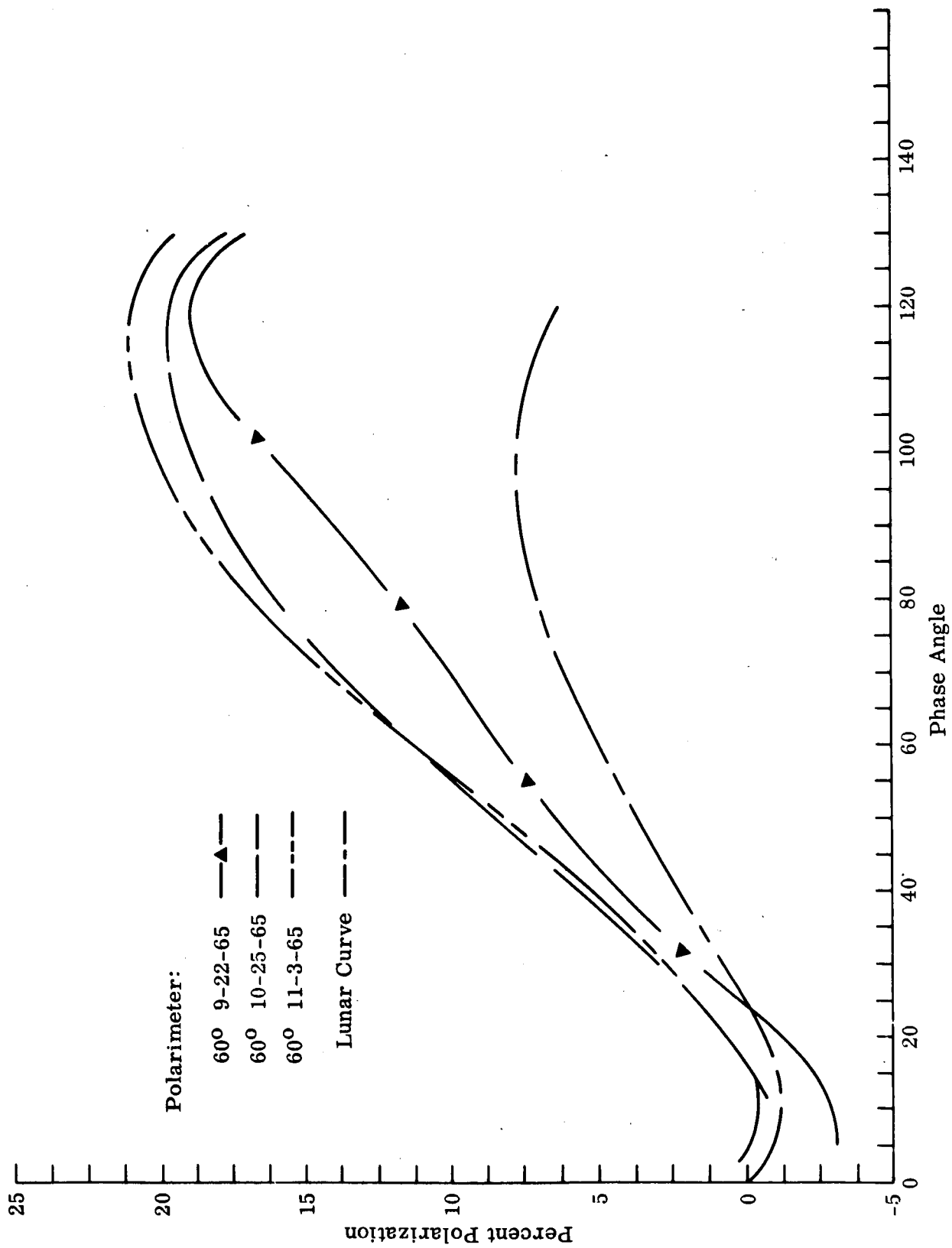
Fig. 15 – Volcanic Ash No. 1: Comparison of Percent Polarization Observations on Different Dates –
60° Polarimeter
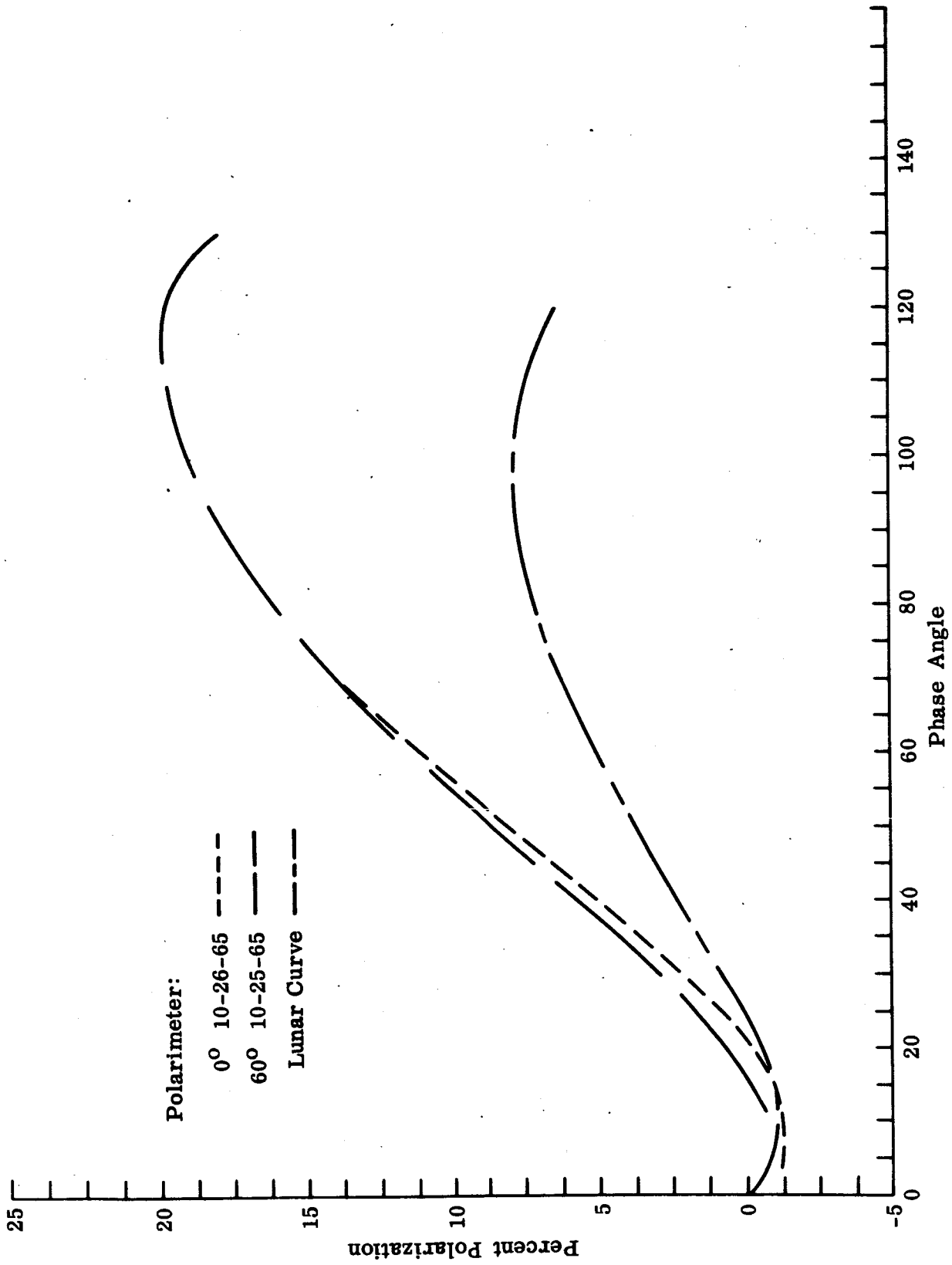
Fig. 16 – Volcanic Ash No. 1: Simulated Lunar Longitude Effect on Percent Polarization
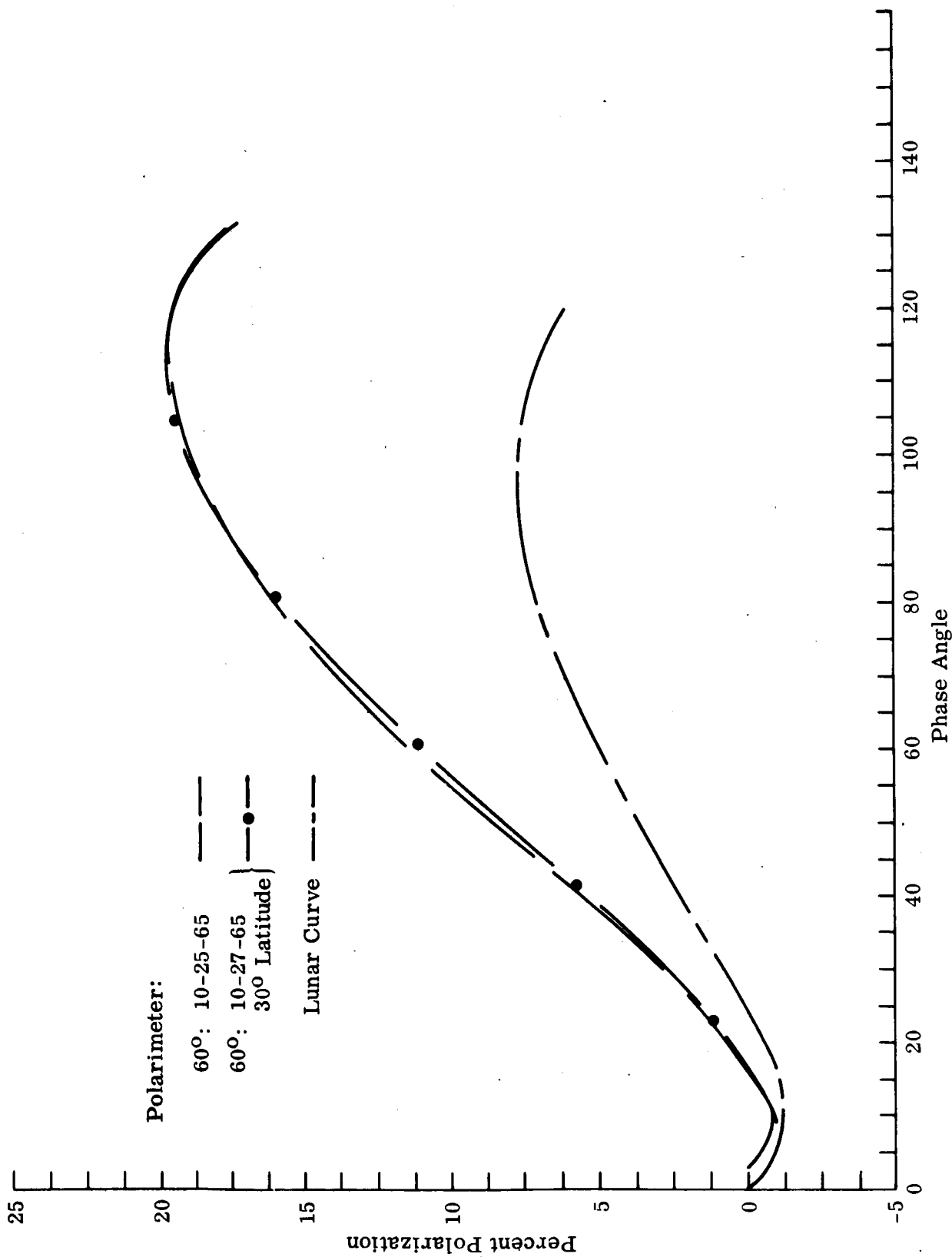
Fig. 17 – Volcanic Ash No. 1: Simulated Lunar Latitude Effect on Percent Polarization

Polarimeter:

60°: 10-25-65

60°: 10-27-65
30° Latitude

Lunar Curve

Percent Polarization

Phase Angle

Fig. 18 Volcanic Ash No. 4

43

Fig. 19 – Volcanic Ash No. 4: Comparison of Percent Polarization Observations on Different Dates – 0° Polarimeter

Polarimeter:

0° 3-1-65

0° 9-22-65

0° 10-26-65

Lunar Curve

Phase Angle
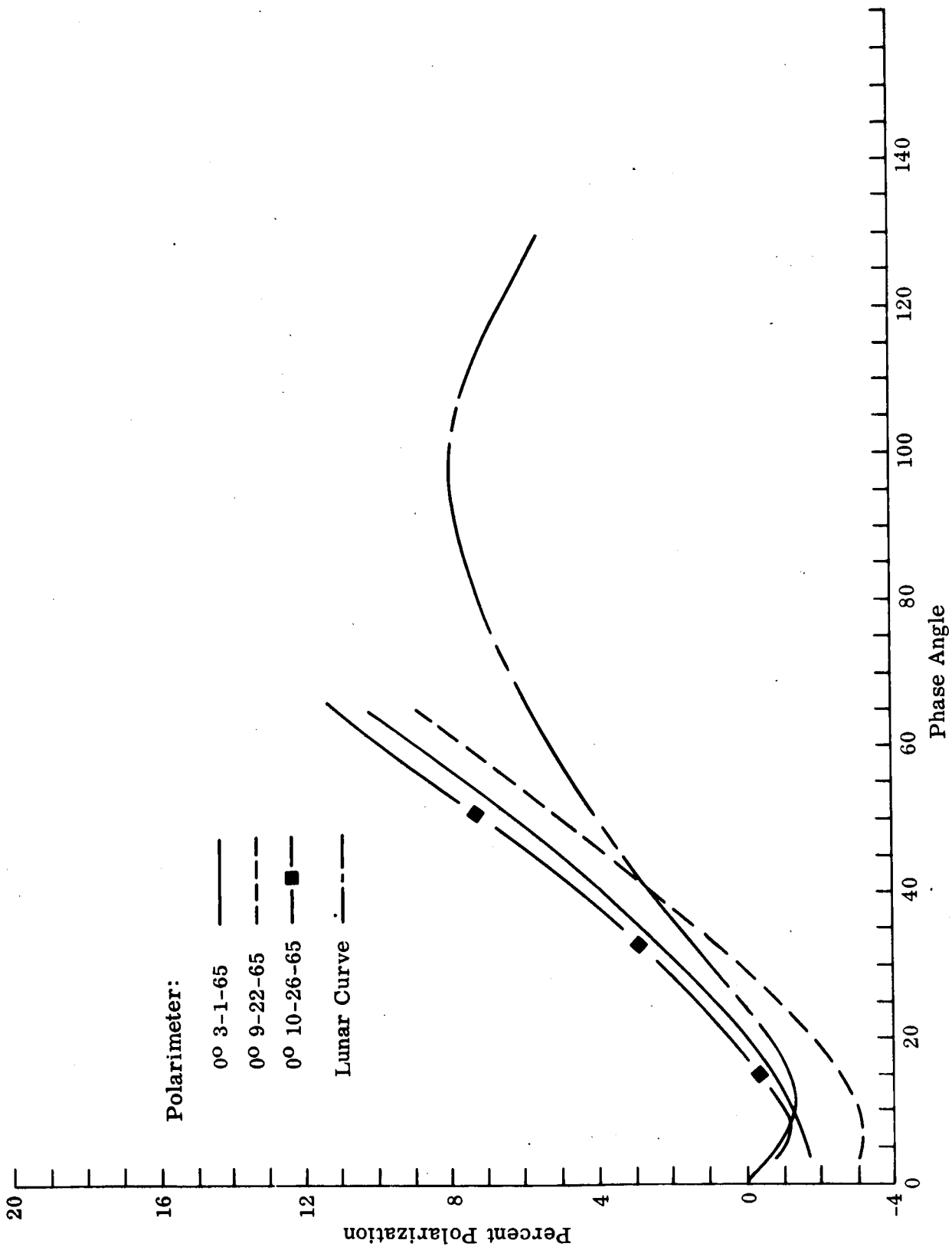
Percent Polarization
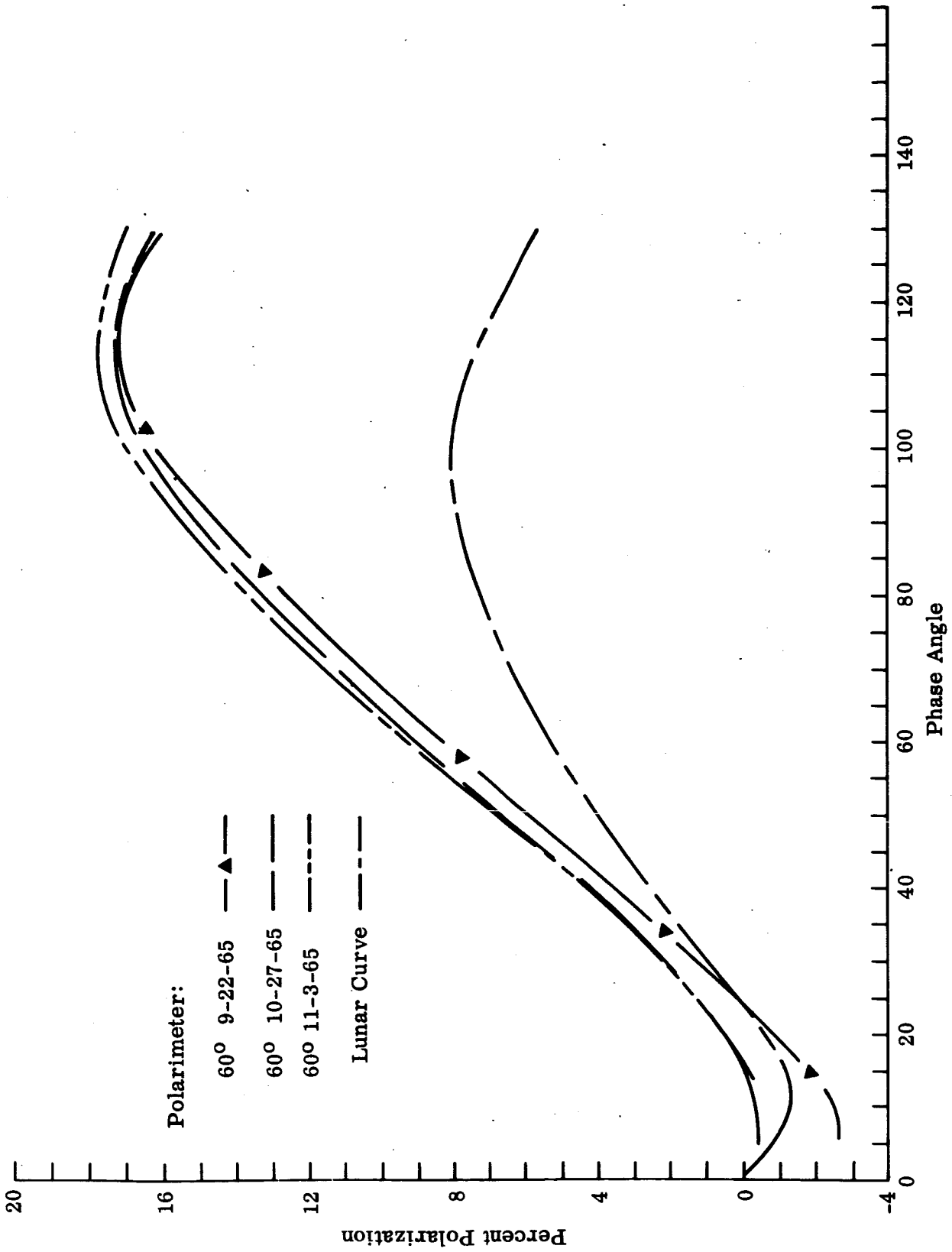
Fig. 20 – Volcanic Ash No. 4: Comparison of Percent Polarization Observations on Different Dates – 60° Polarimeter

Fig. 21 – Volcanic Ash No. 4 – Simulated Lunar Longitude Effect on Percent Polarization

Polarimeter:

0° 10-26-65 ■

60° 10-27-65

Lunar Curve

Percent Polarization

Phase Angle
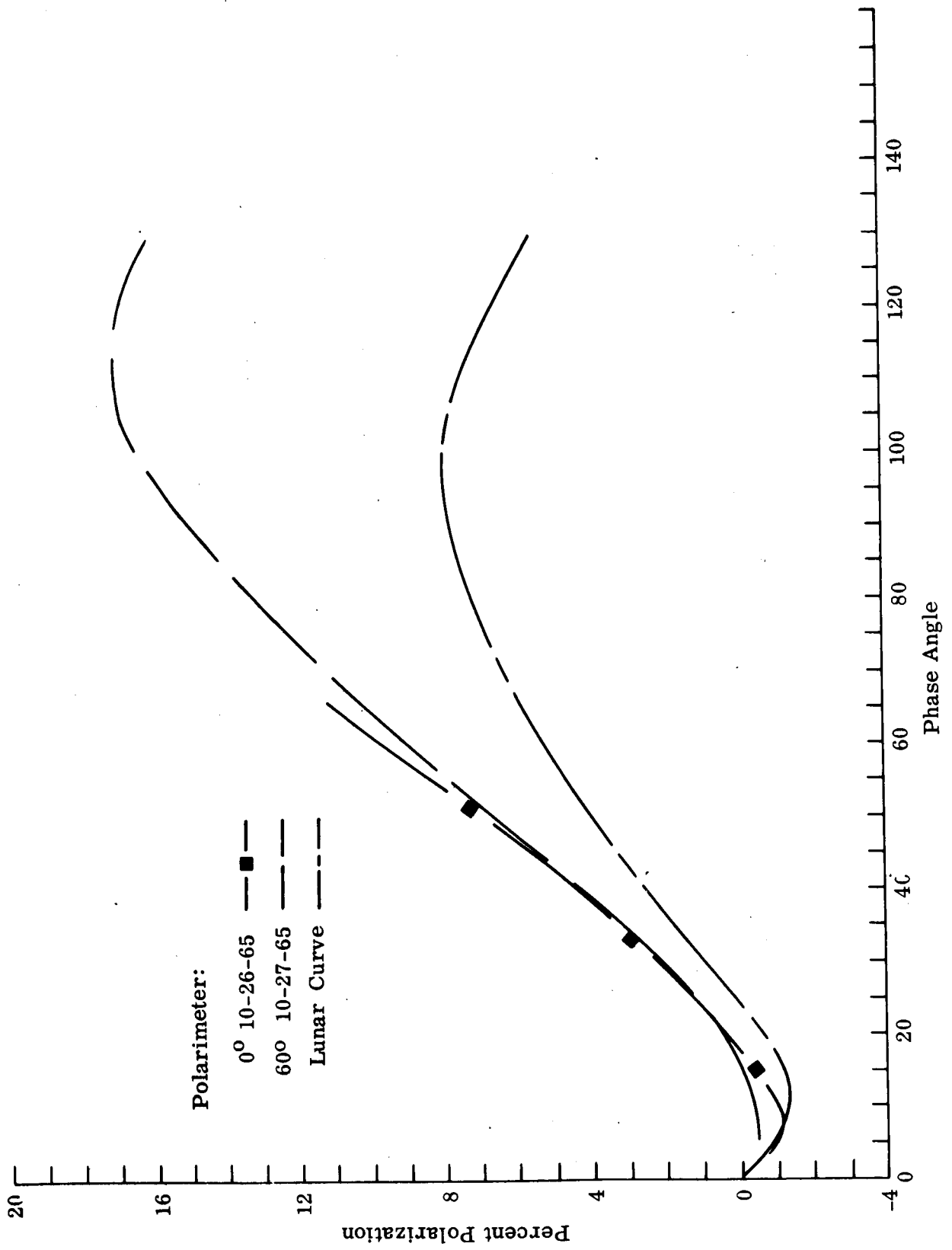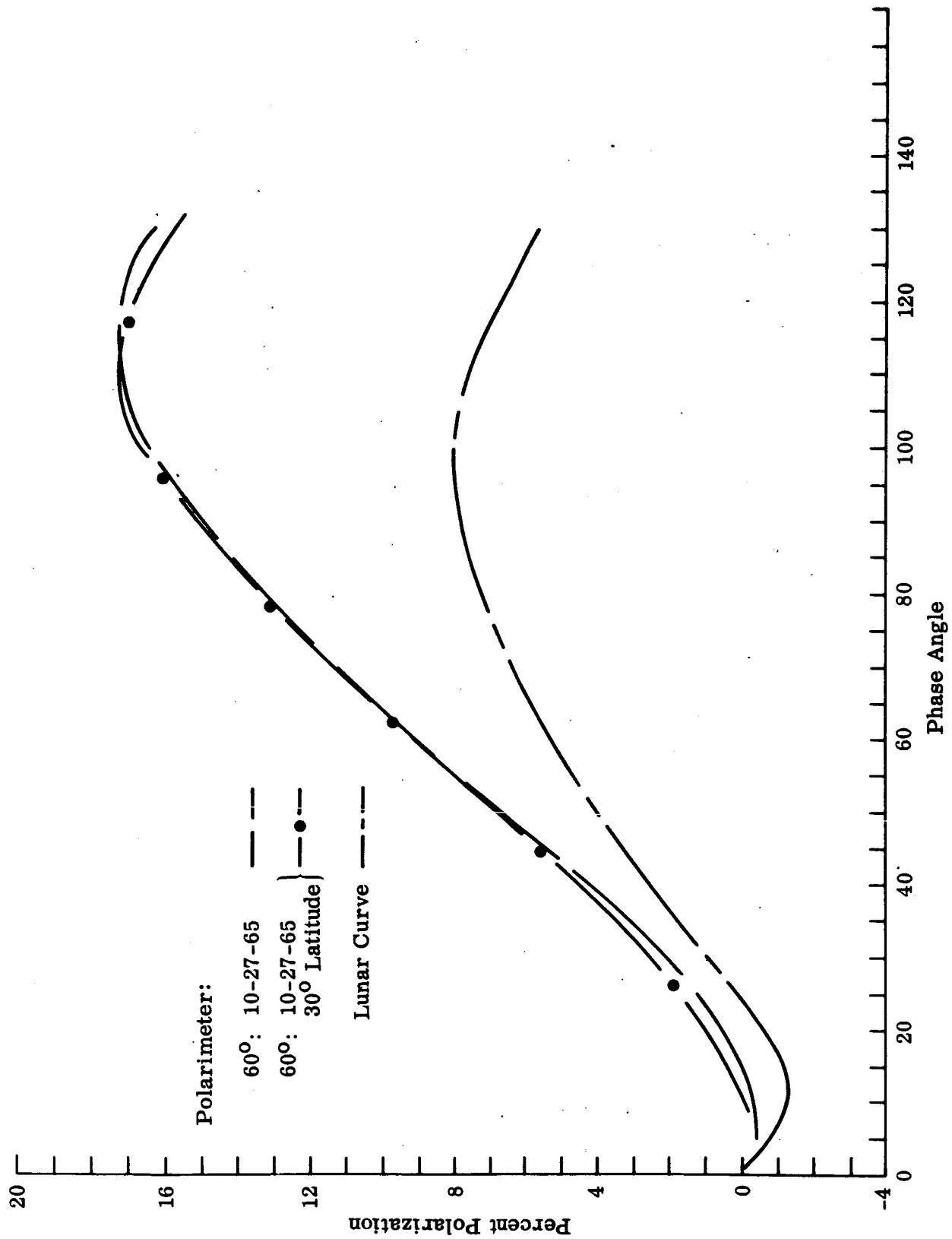
Fig. 22 – Volcanic Ash No. 4: Simulated Lunar Latitude Effect on Percent Polarization

47

Fig. 23 Coral No. 1

48
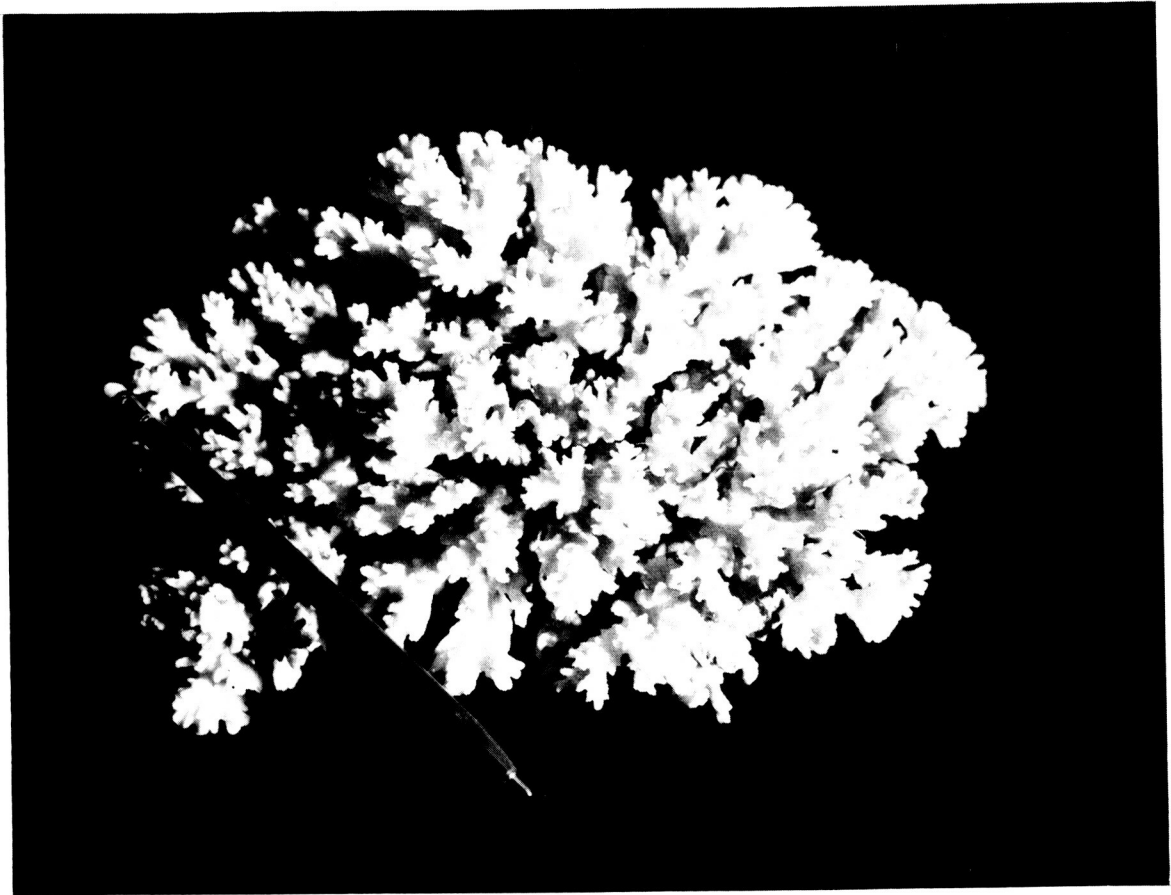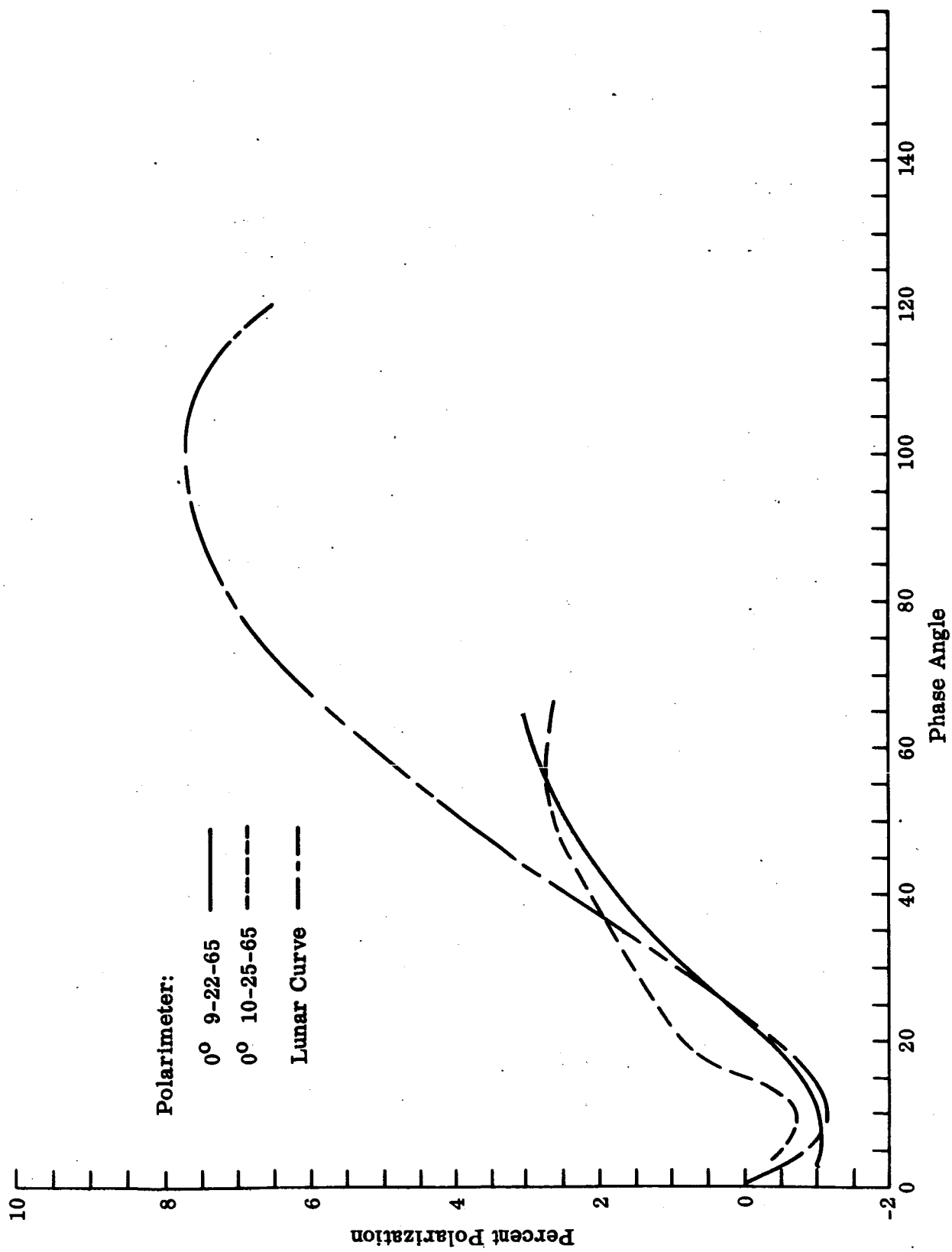
Fig. 24 – Coral No. 1-Comparison of Percent Polarization Observations on Different Dates – 0° Polarimeter
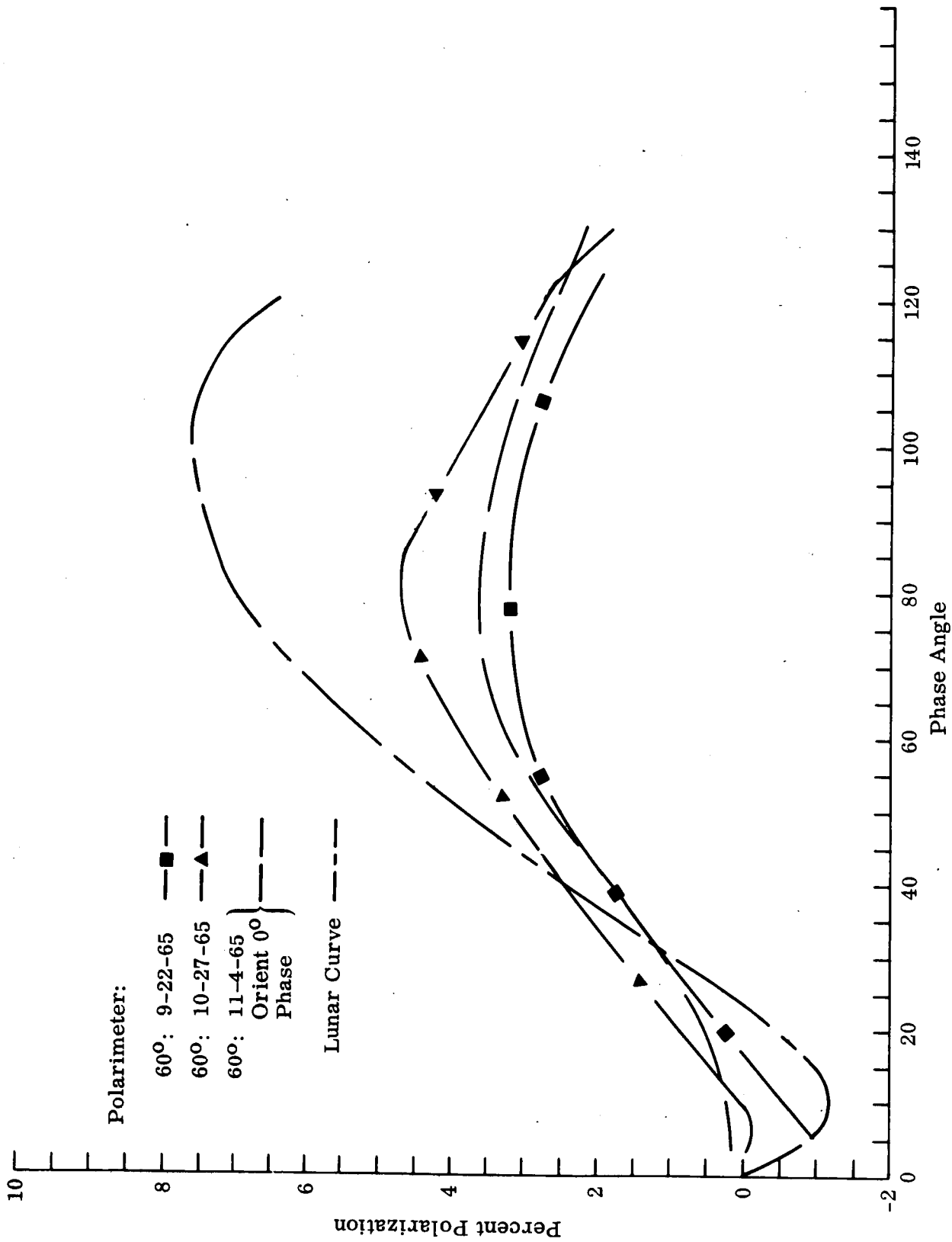
Fig. 25 - Coral No. 1: Comparison of Percent Polarization
Observations on Different Dates - 60° Polarimeter
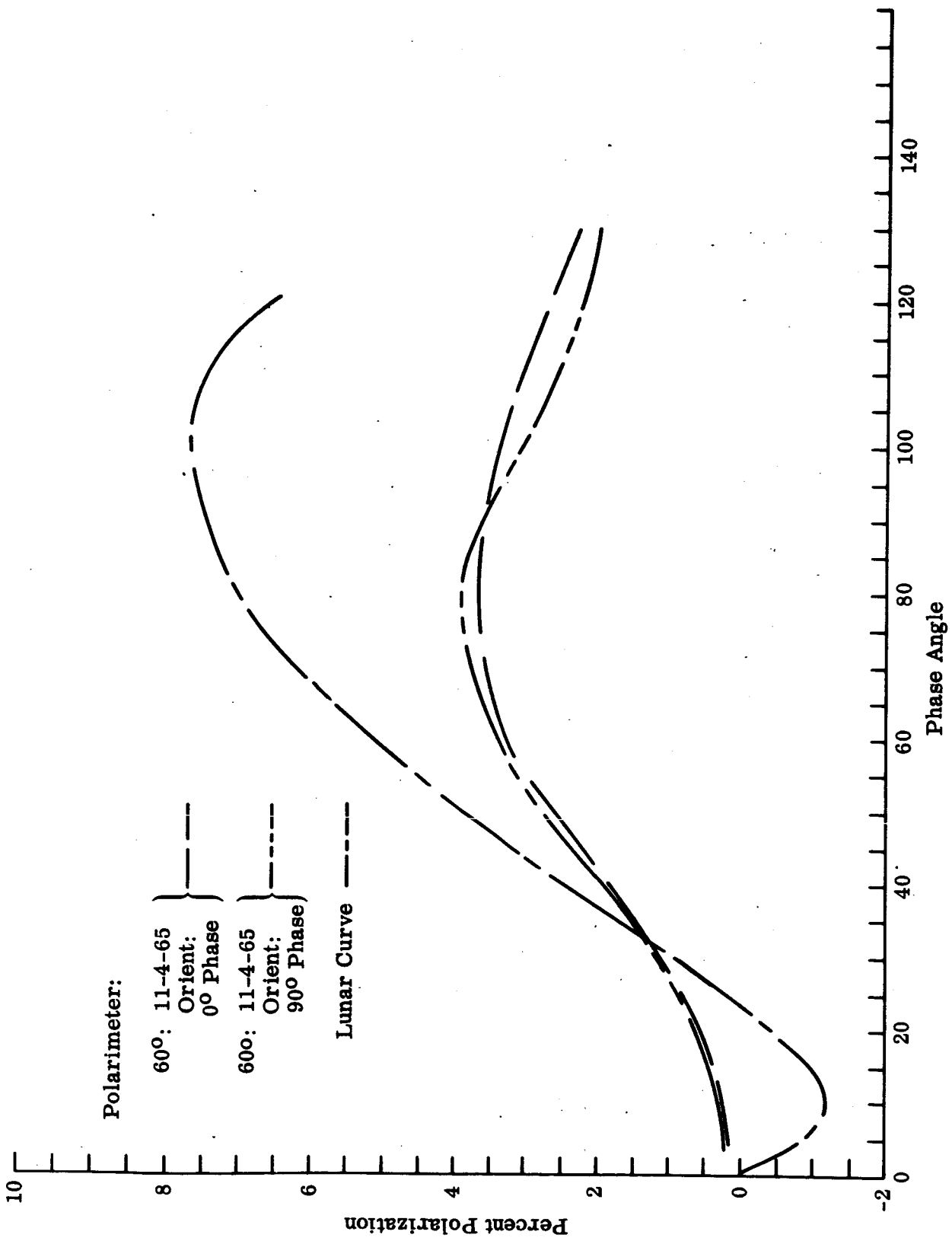
Fig. 26 – Coral No. 1: Sample Orientation Effect on Observed Percent Polarization

Polarimeter:

60°: 11-4-65 } Orient:
0° Phase

60o: 11-4-65 } Orient:
90° Phase

Lunar Curve

Phase Angle

Percent Polarization
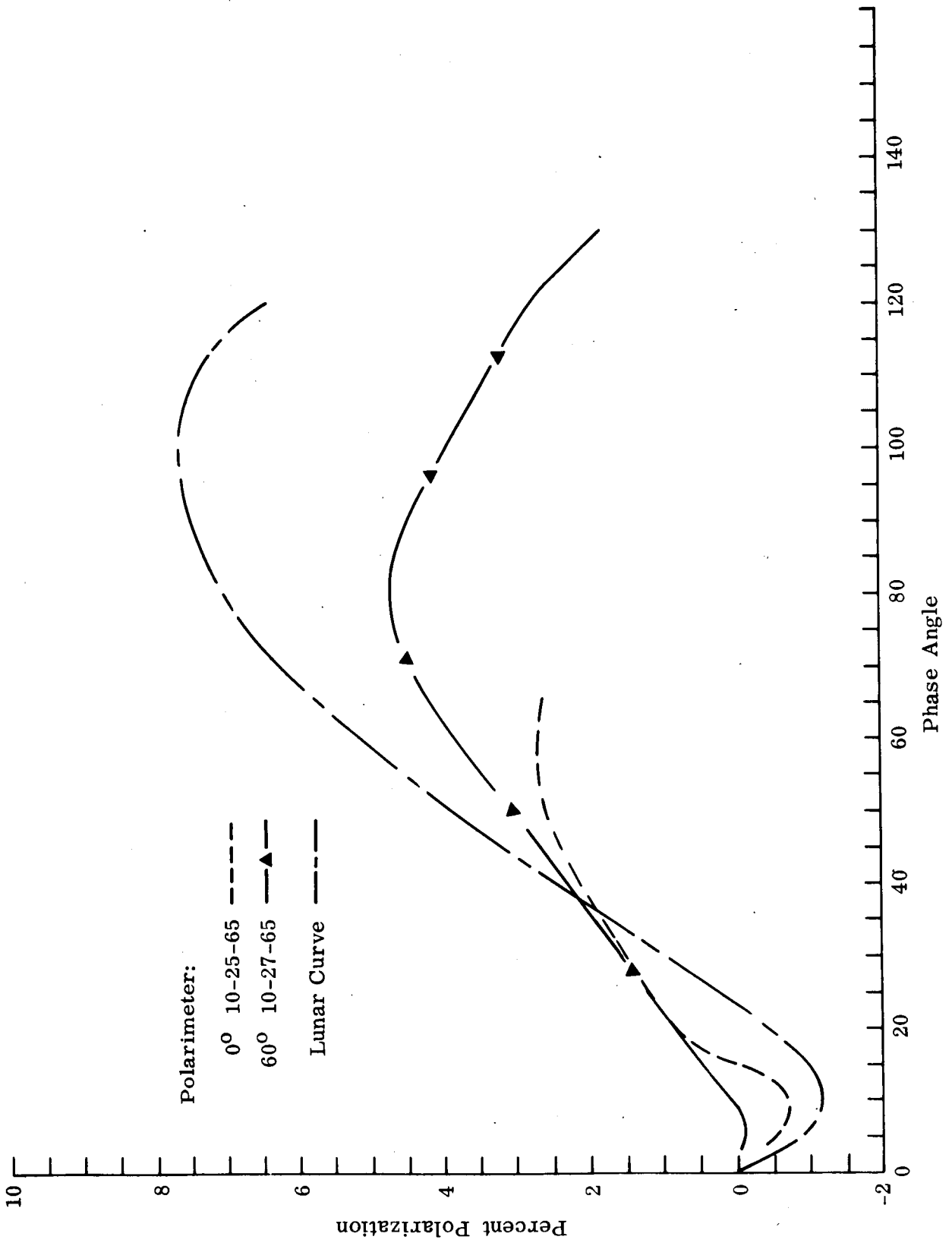
Fig. 27 – Coral No. 1: Simulated Lunar Longitude Effect on Percent Polarization
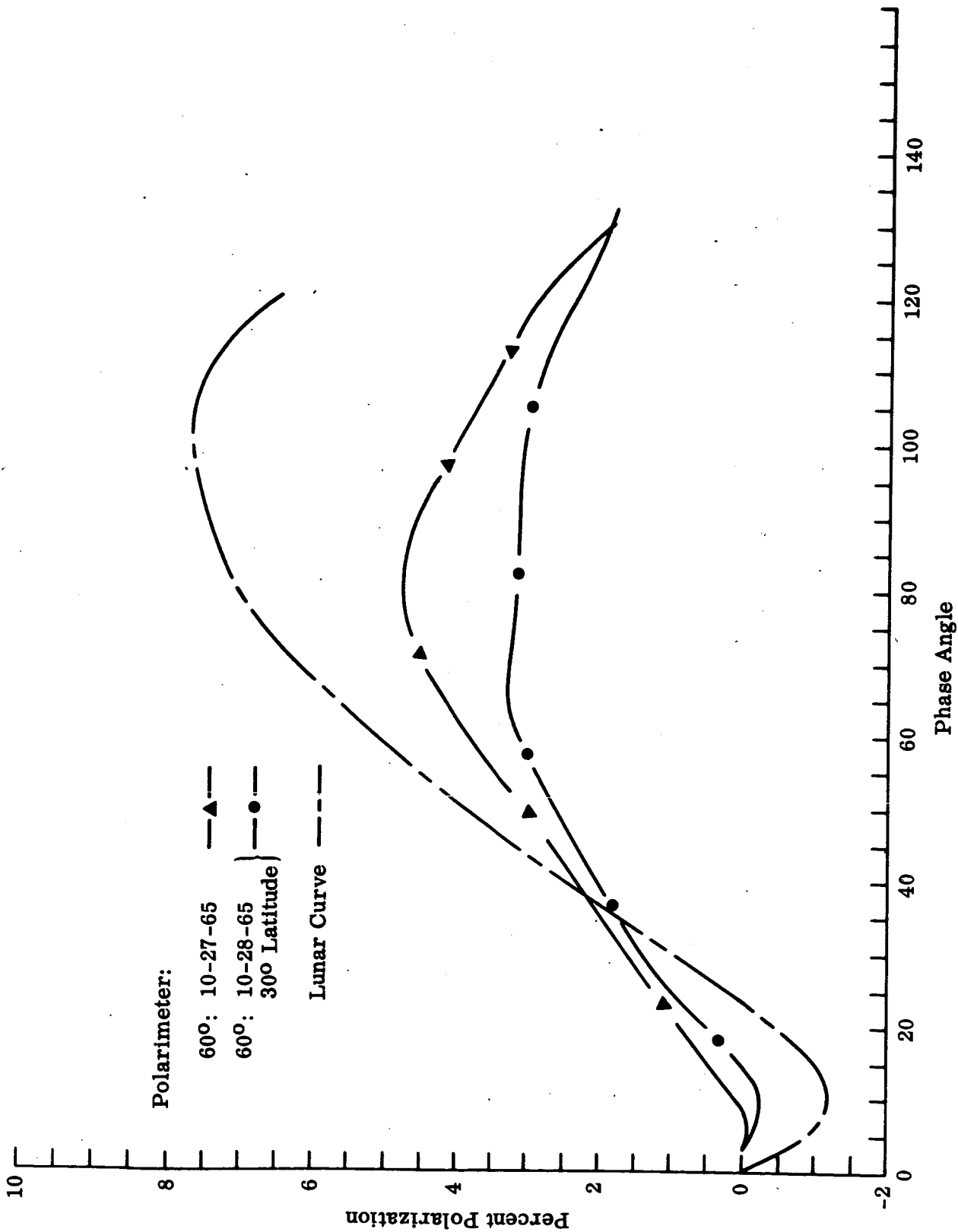
Fig. 28 – Coral No. 1: Simulated Lunar Latitude Effect on Percent Polarization
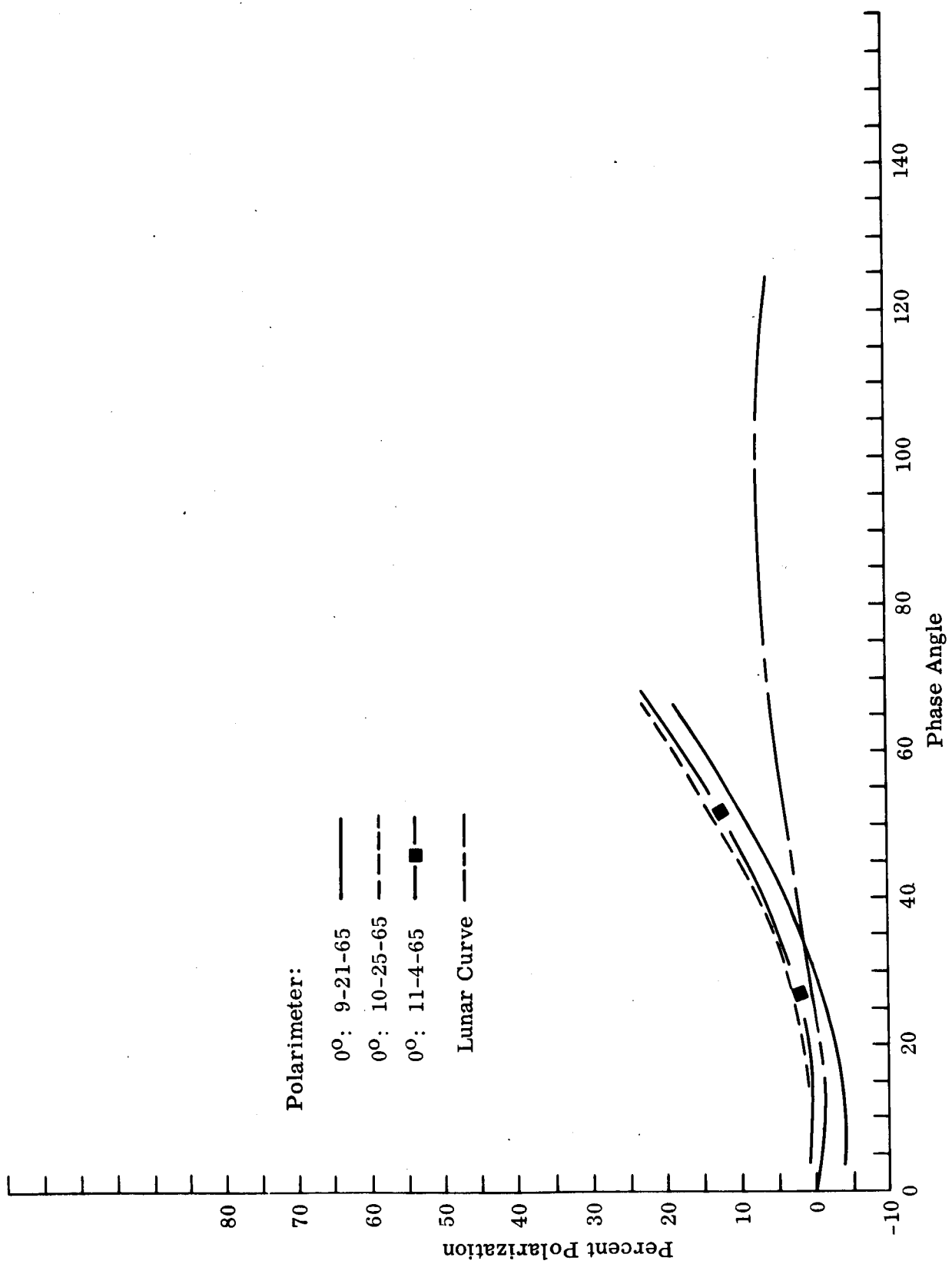
53

Fig. 29 – Copper Oxide: Comparison of Percent Polarization Observations on Different Dates – 0° Polarimeter

Polarimeter:

0°: 9-21-65 ——
0°: 10-25-65 – – –
0°: 11-4-65 ■
Lunar Curve — —

Phase Angle

Percent Polarization
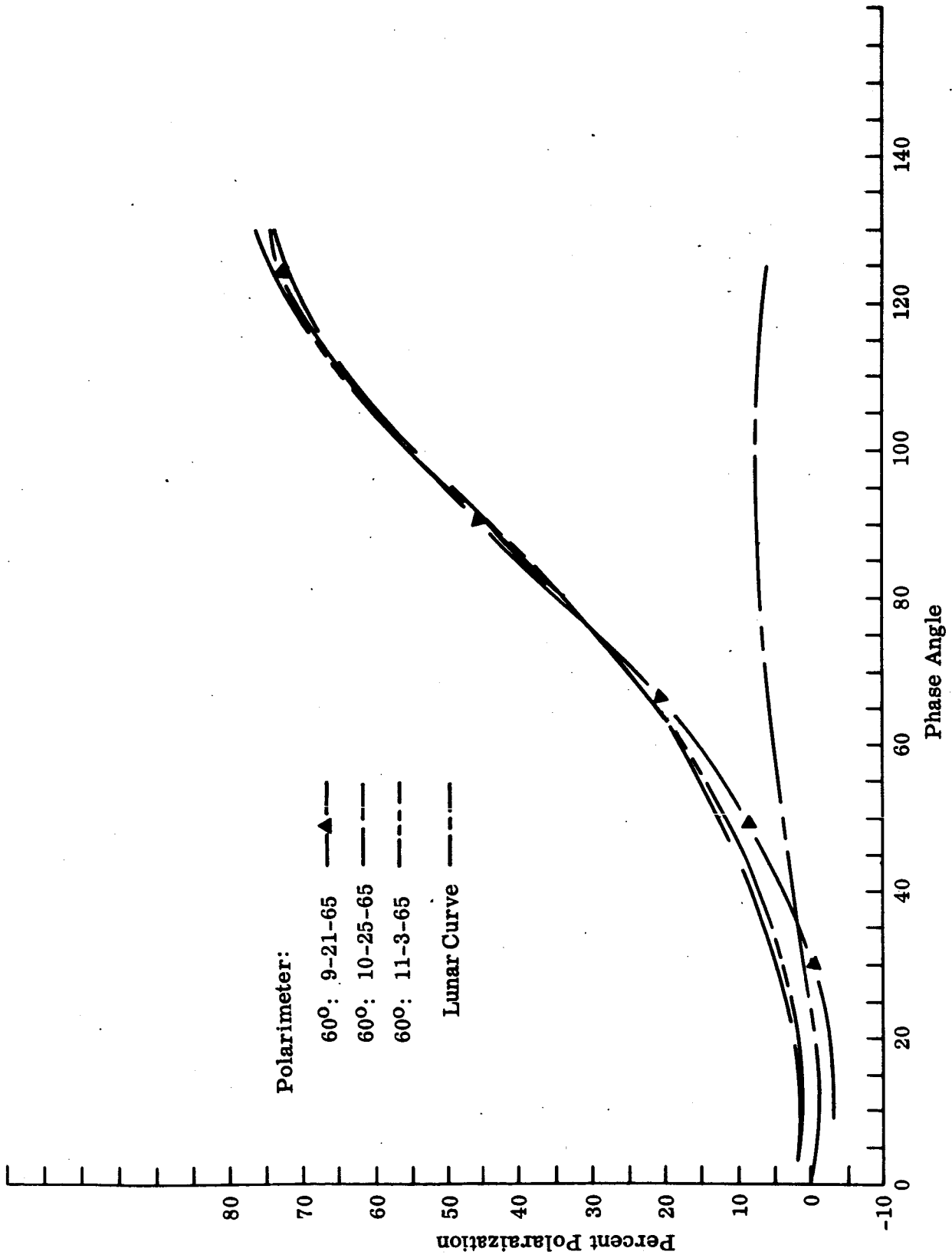
Fig. 30 – Copper Oxide: Comparison of Percent Polarization Observations on Different Dates –
60° Polarimeter

55
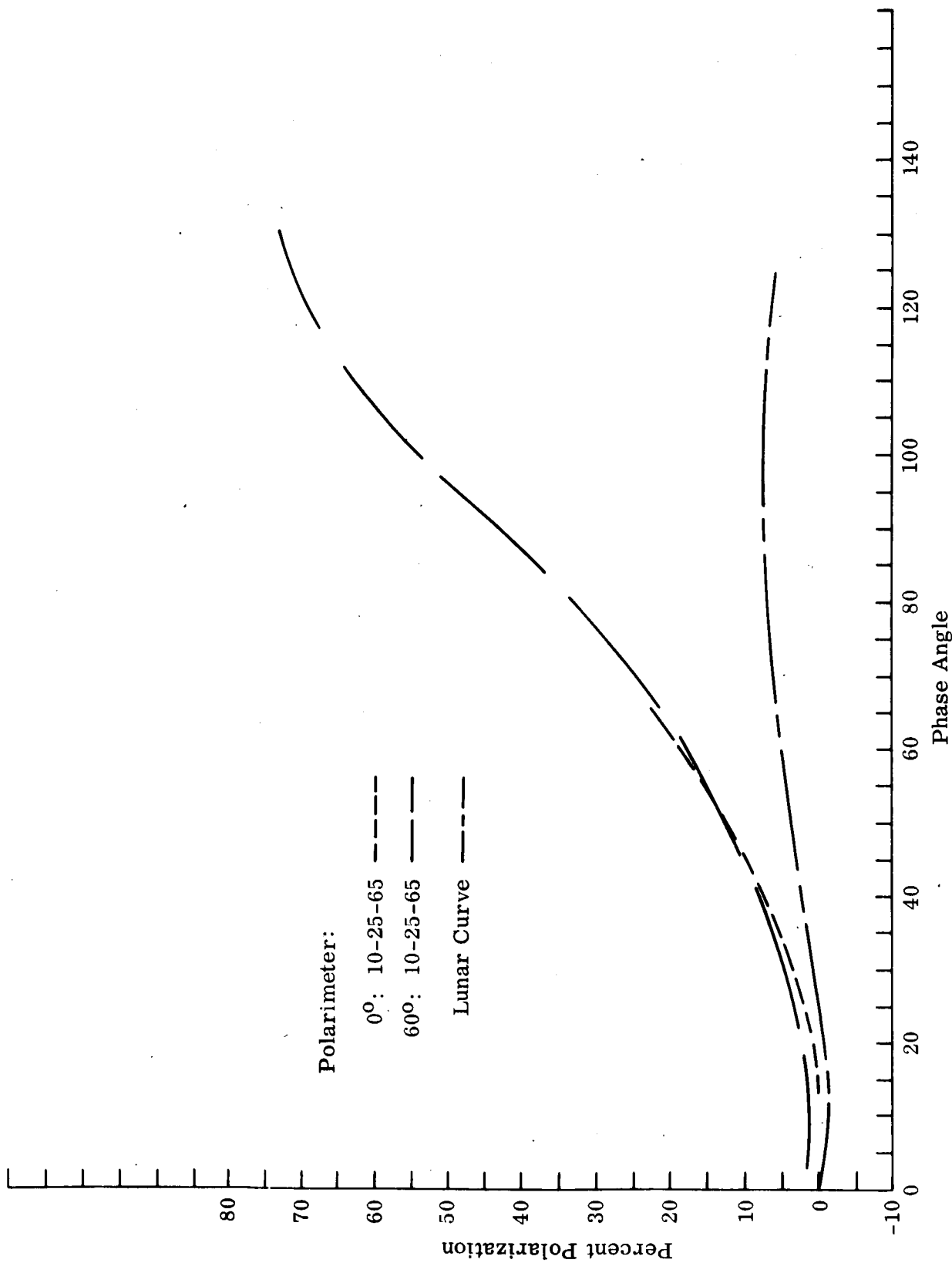
Fig. 31 - Copper Oxide: Simulated Lunar Longitude Effect on Percent Polarization

Polarimeter:

0°: 10-25-65 ――――

60°: 10-25-65 ――――

Lunar Curve ――――
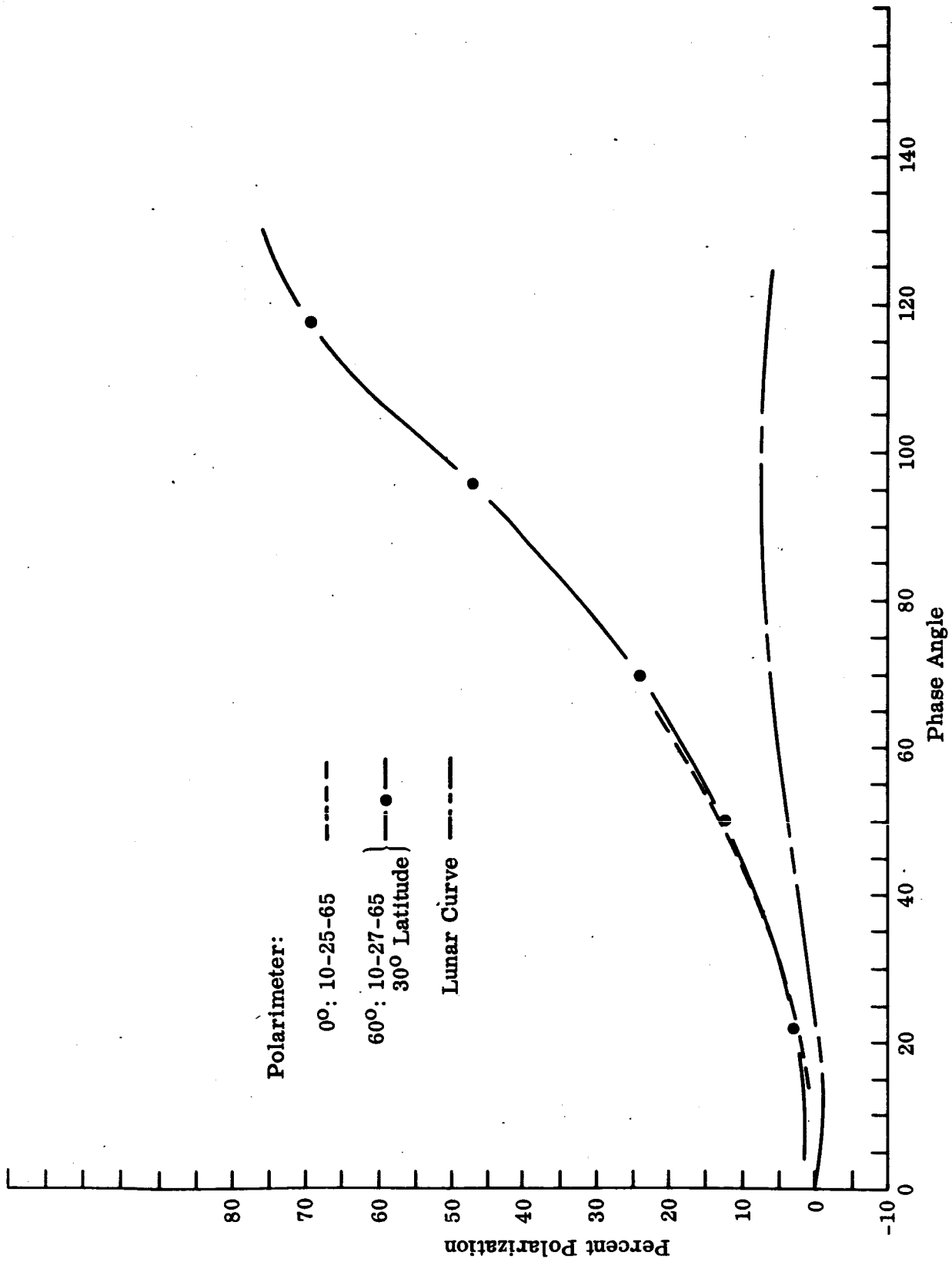
Fig. 32 – Copper Oxide: Simulated Lunar Latitude Effect on Percent Polarization
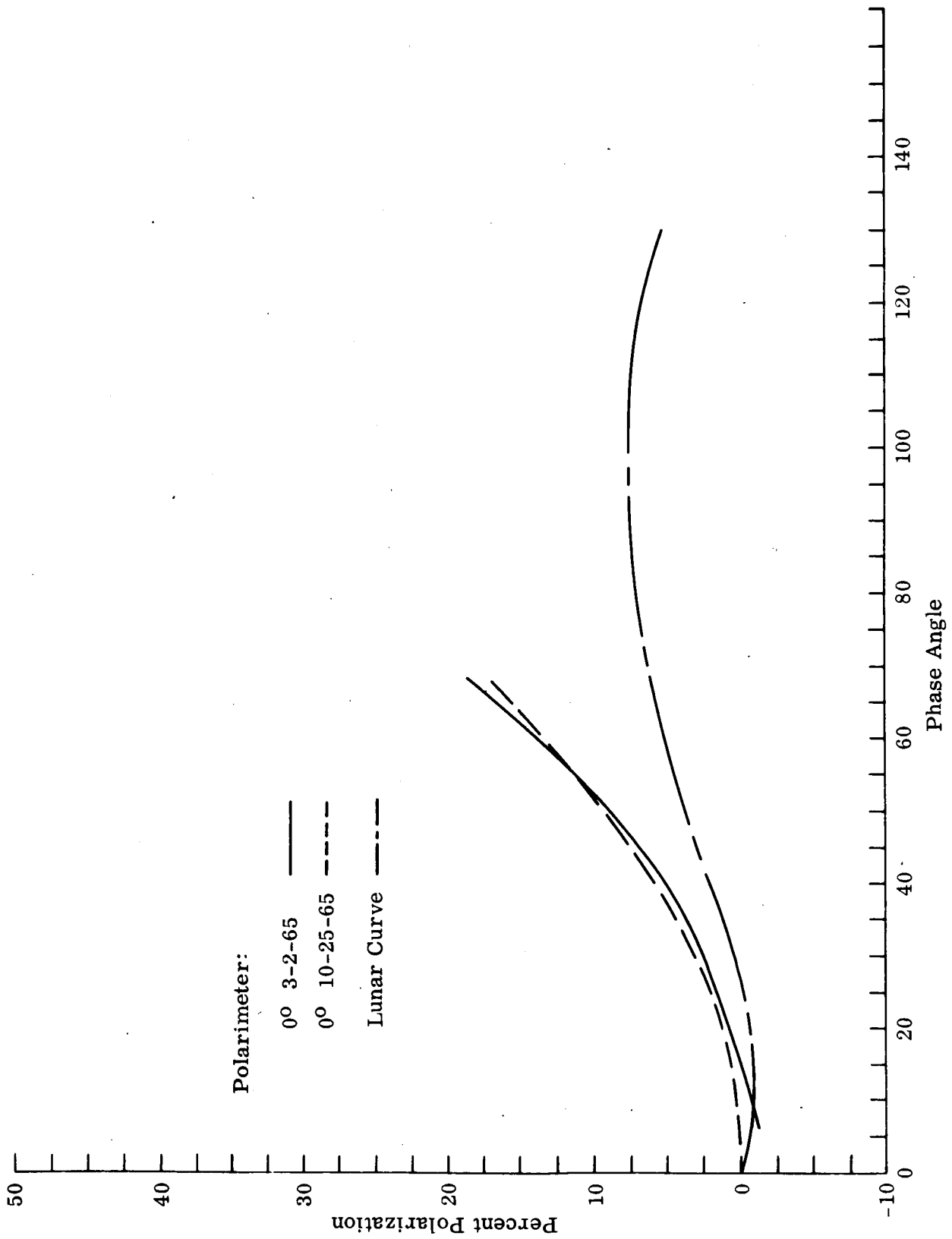
Fig. 33 – Silver Chloride: Comparison of Percent Polarization Observations on Different Dates – 0° Polarimeter
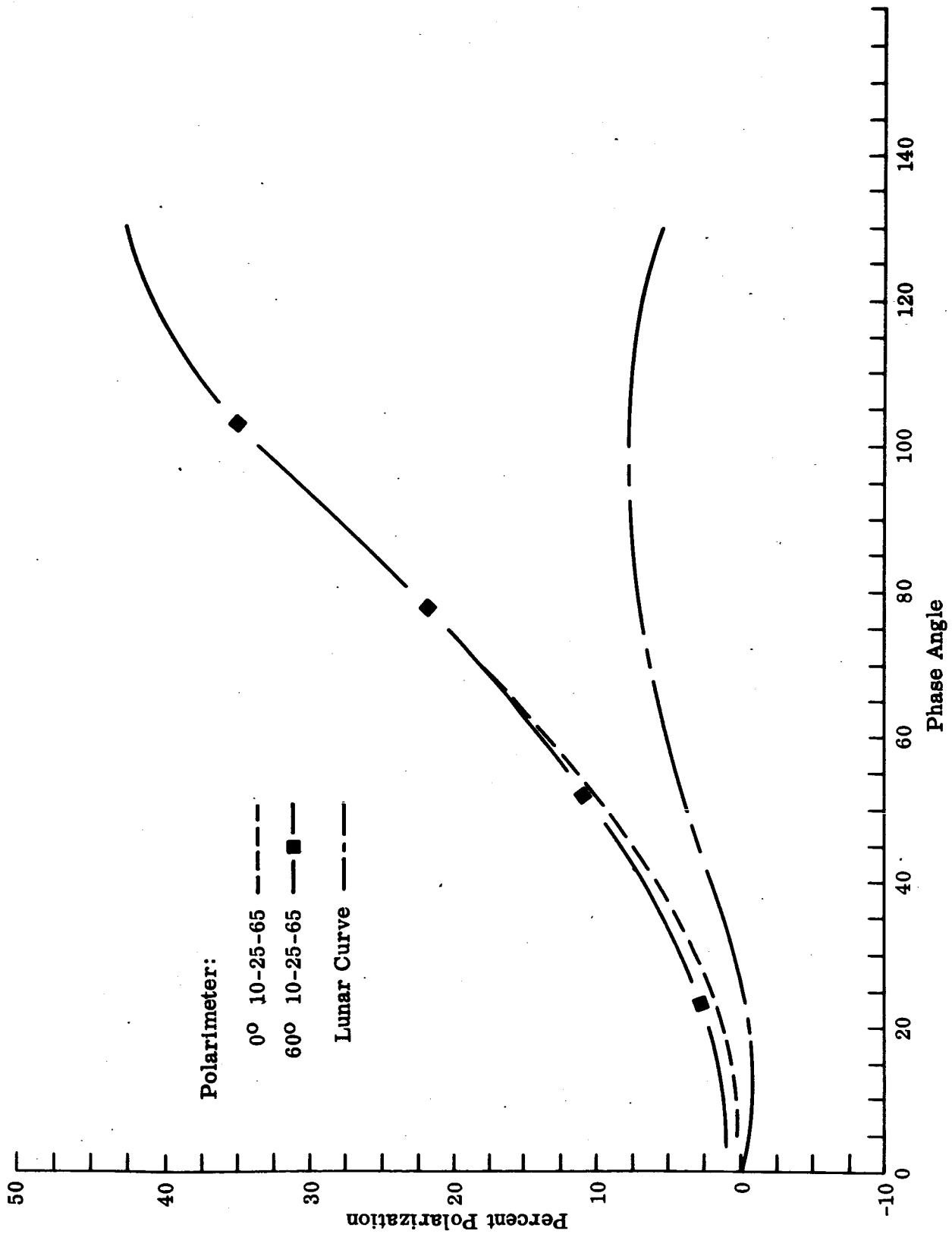
Fig. 34 – Silver Chloride: Simulated Lunar Longitude Effect on Percent Polarization
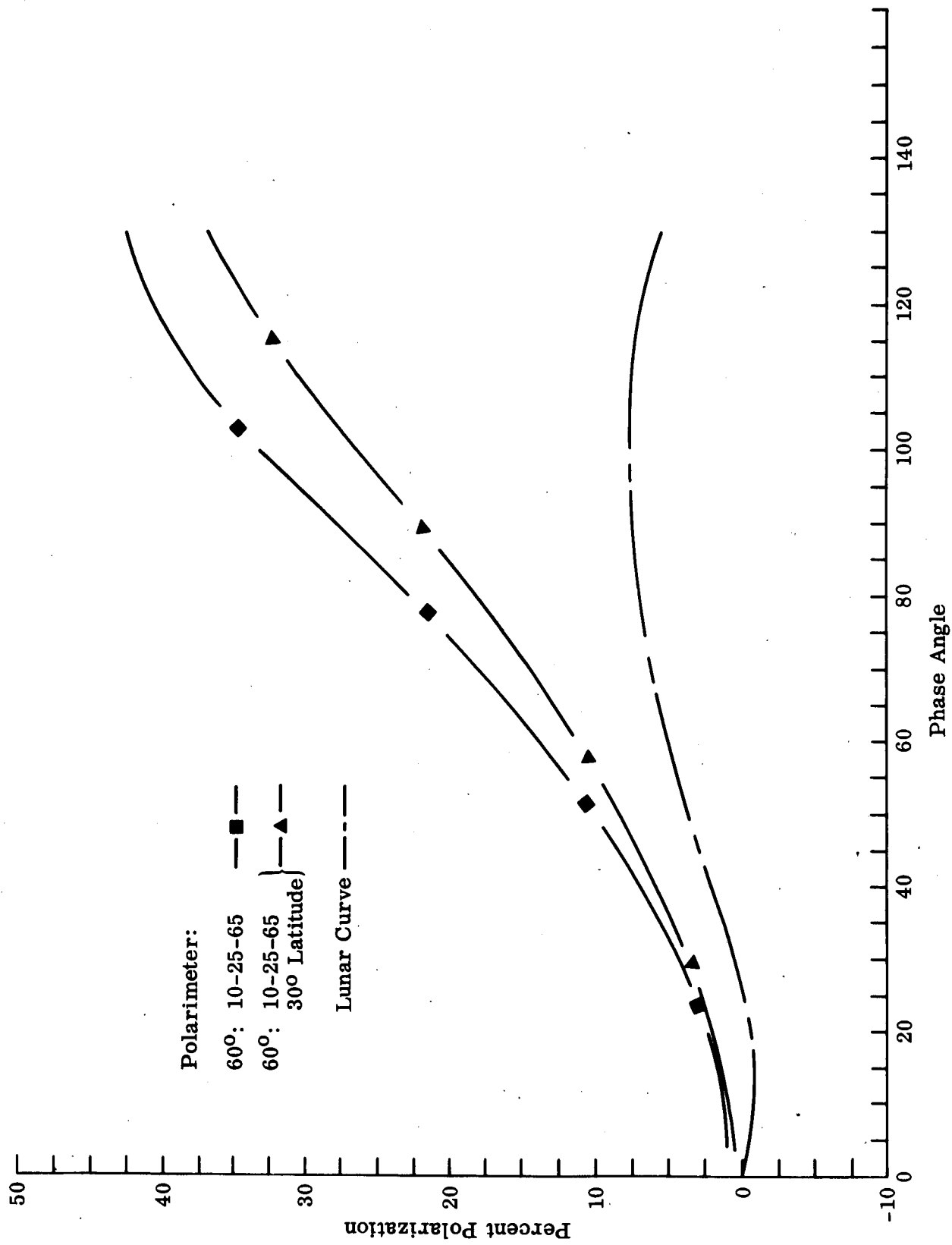
Fig. 35 – Silver Chloride: Simulated Lunar Latitude Effect on Percent Polarization
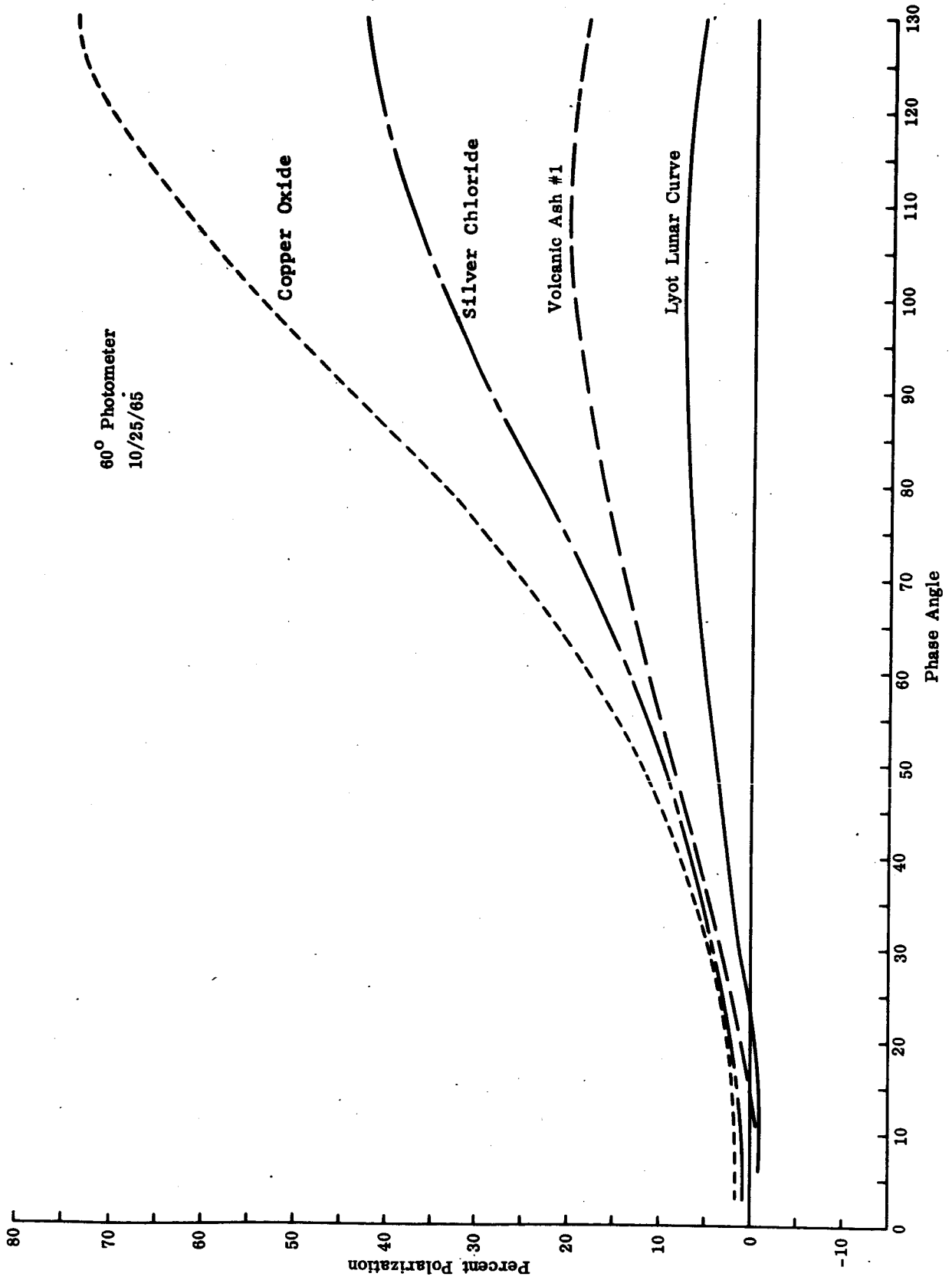
Fig. 36a   Summary Comparison of Percent Polarization Curves: Copper Oxide,
Silver Chloride, Volcanic Ash No. 1, and Lyot Lunar Curve.

61
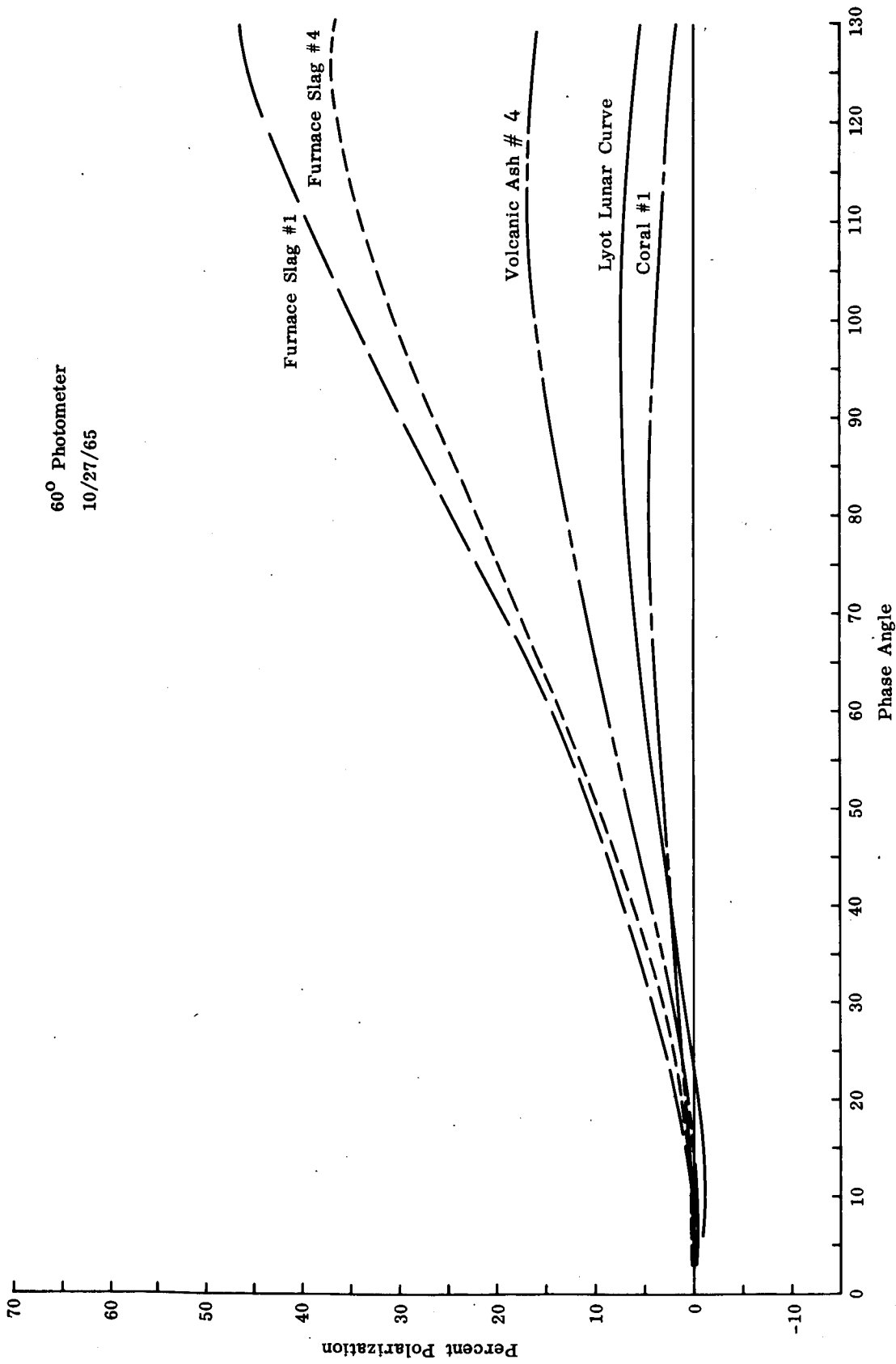
Fig. 36b   Summary Comparison of Percent Polarization Curves: Furnace Slag
Nos. 1 and 4, Volcanic Ash No. 4, Coral No. 1, and Lyot Lunar Curve.

62

PHASE II — PULVERIZED SPECIMENS

Purpose

Phase II has the objective of laying the basis for an analytical approach to the polarization properties of materials. Since current theories of polarization indicate that particle size, albedo and porosity are significant parameters, these were investigated. Materials were those of Phase I, whether or not they proved satisfactory polarization models, plus some additional ones.

Test Specimens

The light scattered from the contractually required specimens was analyzed polarimetrically for the per cent polarization and position of the plane of polarization. The following pulverized specimens were investigated:

Volcanic Ash No. 4 and Furnace Slag No. 4 in the following sizes:

a) 2.83 mm to 6.35 mm

b) 1.19 mm to 2.83 mm

c) 0.50 mm to 1.19 mm

d) 0.21 mm to 0.50 mm

e) 0.088 mm to 0.21 mm

f) 0.037 mm to 0.088 mm

g) $\leq$ 0.037 mm

h) $\leq$ 1 μ

(It is to be noted that Furnace Slag No. 4 was substituted for Furnace Slag No. 1 in order that the sample not be destroyed as mentioned under Phase I.)

Coral, Silver Chloride, Copper Oxide and Volcanic Ash No. 1 in the following sizes:

a)   0.088 mm to 0.21 mm

b) $\leq$ 1μ

The properties of percent polarization and position of the plane of polarization are determined as a function of phase angle and simulated lunar longitude in integrated visual light (0.55μ).

In addition, Vesuvius Ash, and two furnace slags furnished by NASA/MSC were checked for polarization, and a sample of Loyt's volcanic ash was examined microscopically.

Standard Polarimetric Curves and Data Presentation

Although the best data in integrated lunar light seem to be that of Lyot (Ref. 13), it appears that, as lunar and laboratory data become more refined, as in Phases II and III, a range of values should be considered to differentiate the lunar maria from the highlands. The best detailed regional lunar polarization data appears to be that of Gehrels, Coffeen and Owings (Ref. 4). The Russian observations appear to be inaccurate because of a large residual polarization in the instrumentation (see Ref. 1). Since Gehrels et al., made spectral observations, a comparison will be made of the integrated visual data of Phase II and their G(0.54μ) data as the closest approximation. The two areas that had the most complete lunation curve, including the maximum, with the greatest extremes in polarization were Mare Crisium and Clavius. Other curves depicted slightly higher maximum polarization, but because of problems in the observation of certain lunar phase angles, the curves were incomplete. Crisium and Clavius are representative of lunar maria and highlands (a crater floor) with corresponding low and high albedos, and high and low polarization respectively. The curves are shown in Fig. 37, together with the curve of Lyot formerly used (Ref. 19). The maxima are seen to be 12.5 and 5.8 percent compared to 7.7 percent of Lyot. The minimum of Clavius is -0.9 and that of Crisium and Lyot is -1.2 percent. The inversion angles also differ: Mare Crisium 23.7°, Lyot (average) 23.5°, and Clavius 25.0°. The phase angle at maxima of Lyot (average) and Crisium are the same (102°), but the brighter Clavius has its maximum at 91°.

By refining the data analysis on the basis of these curves, it may be possible to determine, from polarization observations, the characteristics of a typical maria and highland surface.

It should be pointed out that the curves for Mare Crisium and Clavius are averages of observations for positive and negative phase angles in Gehrels et al. (Ref. 4).

As mentioned in Gehrels' paper, the polarization observed in 1963 was higher, compared to observations in 1959, presumably due to lunar luminescence. This is also inferred from their visual brightness measurements showing brighter areas in 1956 or 1959 (when the sun was active in producing a high level of ionizating radiation), compared to 1963 and 1964. Hence, the albedos used in this report are averages of the two values obtained at those times.

According to Gehrels (Ref. 4) the existence of lunar luminescence could be inferred from not only the albedo data but from the polarization data, where the polarization is lower in 1956 and 1959 indicating a non-polarizing (luminescence) component in the polarization observation.

To explain the reduced polarization, it is not necessary to require the luminescent light to be unpolarized. In fact, as long as the per cent polarization of the luminescent light is smaller than the per cent polarization of the non-luminescent light, the addition of luminescence will reduce the observed polarization percentage. This will be elaborated upon in Phase IV.

Sample Preparation

The larger size particles were obtained by coarse pulverization in a rock crusher and sieving. The finer particles (below about 0.21 mm), other than silver chloride and coral, were obtained by stainless steel ball milling the larger particles, and sieving. The smallest particles were obtained by subjecting the particles below 0.037 mm to processing by a Helme Fluid Energy Mill (Fig. 38). The Fluid Energy Mill is a device that converts a compressed gas into an energy exchange mechanism that causes the particles of a material to be thrown together with such velocities as to cause them to break up into micron and submicron particles. The fineness of the grind depends upon the gas pressure used, the nozzle adjustments, and the number of times the particles are fed through the machine. Dry nitrogen was used as the grinding medium.

The coral was reduced in size in a porcelain mortar and pestle (so as not to contaminate the surface with metallic particles from a ball mill), and subsequently ground in the fluid energy mill.

The larger sizes of silver chloride were obtained as a powder. The smallest size was obtained as a precipitate of silver chloride from a silver nitrate solution using hydrochloric acid, and dried in a thin layer. An alternative larger powder sample was ground up to a 2 to 3 micron size in the fluid energy mill, before it clogged the mill. Silver chloride is ductile and is not readily ground. The particles obtained from the mill were examined in a dispersed form under a microscope for proper required sizes (see Fig. 39).

This Figure 39 shows that there is still evidence of non-dispersed agglomerates of particles (visible in Fig. 3a). Figures 3a, b, c, d, f, and h are "bright field" illumination, wherein the collimated light from the source impinges directly upon the upper surface of the specimen, and the specimen is viewed in reflected light. Figures 39e and g are "dark field," wherein they are illuminated obliquely, resulting in their being visible by refracted and obliquely reflected light. The advantage of the dark field illumination is that one may gain some insight into the transparency and refraction properties of a substance by microscope observation. There was no problem with obtaining particles 1 micron or less of the Volcanic Ashes, Furnace Slag, Coral or Copper Oxide (Figs. 39a, b, c, d, and h). The silver chloride precipitate agglomerates, but the individual particles are well below a micron in size (Fig. 39e). The silver chloride that resulted from the fluid energy mill grind (sizes from 3 to 8 microns) is shown in Figs. 39f and g under bright and dark field illumination. Agglomeration is evident. Because of the non-dispersed effect of the silver chloride precipitate layer, the 3-8 micron silver chloride powder was also examined for polarization as an extra sample.

Samples were carefully dispersed over the sample area on the polarimeter, covering the backing board completely in the viewing area.

The finest particles tended to agglomerate because of the high strength of the surface forces.

Some additional specimens, not required by the contract, were examined. These were:

(a)   Ashes from the side of the cone of Vesuvius, obtained by one of the authors (W.G. Egan) June 1, 1965.

(b)   Two furnace slag samples, obtained by one of the authors (W.G. Egan) at the NASA/MSC astronaut simulation pit on March 16, 1965; one was sponge-like and the other appeared rusty, suggesting iron.

(c)   Ashes of Vesuvius, April 14, 1908, used in the Lyot Configuration, (Ref. 13, 109 - Thesis p. 120), Curve E, Albedo 0.166; this sample was kindly furnished to one of the authors (W.G. Egan) by Prof. A. Dollfus, May 1965.

Experiments

Percent Polarization

The percent polarization as a function of phase angle for the six required and 4 additional samples is presented graphically in Figs. 40 through 63 and Table 10.

The data can be analyzed conveniently for the contractually required specimens in five sections:

1. Effect of Albedo
2. Effect of Particle Size
3. Effect of Porosity
4. Effect of Material
5. Effect of Simulated Lunar Longitude

The remaining samples (Vesuvius Ash, two Furnace Slags furnished by NASA/MSC and Lyot Volcanic Ash) are examined in percent polarization and albedo for the first three and microscopically for the last.

Thus, the percent polarization data are presented for each of the observed samples in terms of comparison graphs, along with the curves for Mare Crisium and Clavius.

Plane of Polarization

The plane of polarization for the above six required samples was analyzed as a function of phase angle, referenced to the secondary polaroid standard, which was aligned to the plane of vision determined by the glass plate. The data are presented in Table 11.

Discussion of Test Results

Effect of Albedo

A relationship between albedo and polarization has been observed for the lunar surface (see, for instance, Lyot (Ref. 13); the lower the albedo, the higher the maximum observed polarization. This may be conveniently seen for the laboratory observations by reference to Table 10 which is essentially a summary of the graphical information contained within Figs. 40 through 63, but which has

Table 10

DATA ANALYSIS

PERCENT POLARIZATION

Furnace Slag No. 4

	Size Range	Average Albedo	Percent Porosity	Maximum %	Maximum Angle	Minimum %**	Minimum Angle	Inversion** Angle	Apparent Density g/cm³	Real Density g/cm³
a)	2.83 to 6.35 mm	.085	65*	41	117°	-0.8	10°	18.5°	1.59*	4.4*
b)	1.19 to 2.83 mm	.080	56*	40	116	-0.9	9	17.5	1.97*	4.8*
c)	0.50 to 1.19 mm	.075	60*	46	117	-1.0	8?	17.0	1.82*	4.9*
d)	0.21 to 0.50 mm	.070	58*	47	122	-1.0	9?	18.5	1.90*	4.6
e)	0.088 to 0.21 mm	.070	60*	46	123	-0.9	9	17.0	1.78*	4.3*
f)	0.037 to 0.088 mm	.095	65*	20	109	-0.9	9	17.5	1.60*	4.5*
g)	≤ 0.037 mm	.105	68*	14	111	-0.7	9	18.5	1.44*	4.3*
h)	≤ 1μ mm	.140	76	9	115	-0.8	11?	23.0	1.00	4.2

Volcanic Ash No. 1

	Size Range	Average Albedo	Percent Porosity	Maximum %	Maximum Angle	Minimum %**	Minimum Angle	Inversion** Angle	Apparent Density g/cm³	Real Density g/cm³
	0.088 to 0.21 mm	.150	67	8.4	93.5	-1.4	10	24.5	1.10	3.3
	≤ 1μ	.175	80	5.8	99.0	-1.2	10	25.0	0.50	2.5

Volcanic Ash No. 4

	Size Range	Average Albedo	Percent Porosity	Maximum %	Maximum Angle	Minimum %**	Minimum Angle	Inversion** Angle	Apparent Density g/cm³	Real Density g/cm³
a)	2.83 to 6.35 mm	.135	71*	16.6	104	-1.4	2.5?	21.0	0.85*	2.72*
b)	1.19 to 2.83 mm	.125	64*	17.6	106	-1.3	6?	21.5	1.00*	2.94*
c)	0.50 to 1.19 mm	.120	60*	18.1	106	-1.4	6?	23.0	1.16*	3.05*
d)	0.21 to 0.50 mm	.125	53*	17.5	113	-1.7	10	23.5	1.38*	3.05*
e)	0.088 to 0.21 mm	.125	55*	16.0	109	-1.5	11	22.5	1.31*	3.00*
f)	0.037 to 0.088 mm	.130	59*	13.4	107	-1.3	11?	22.5	1.20*	2.82*
g)	≤ 0.037 mm	.165	73*	6.7	92	-1.2	9	20.5	0.80*	2.93*
h)	≤ 1μ	.195	75	4.8	105?	-1.0	12	24.0	0.70	2.80

Coral No. 1

	Size Range	Average Albedo	Percent Porosity	Maximum %	Maximum Angle	Minimum %**	Minimum Angle	Inversion** Angle	Apparent Density g/cm³	Real Density g/cm³
	0.088 to 0.21 mm	.54	53	>2.4	>125°	<-0.5	4.5°	29.0°	1.24	2.7
	≤ 1μ	.71	81	>1.4	>125	<-0.4	7	27.5	0.53	2.8

Copper Oxide

	Size Range	Average Albedo	Percent Porosity	Maximum %	Maximum Angle	Minimum %**	Minimum Angle	Inversion** Angle	Apparent Density g/cm³	Real Density g/cm³
	0.088 to 0.21 mm	.04	72	75.5	125	-0.8	7	17.5	1.74	6.2
	≤ 1μ	.06	73	66	121	-0.7	7.5	14.5	1.71	6.2

Silver Chloride

	Size Range	Average Albedo	Percent Porosity	Maximum %	Maximum Angle	Minimum %**	Minimum Angle	Inversion** Angle	Apparent Density g/cm³	Real Density g/cm³
	0.088 to 0.21 mm	.09	63	>69	>125	-0.9	5	15.0	2.22	6.0
	3 to 8μ	.09	67	>35	>125	-0.8	5	17.0	1.85	5.6
	≤ 1μ	.12	-	48	120	-0.9	12	26.5	-	-

Miscellaneous Samples

	Size Range	Average Albedo	Percent Porosity	Maximum %	Maximum Angle	Minimum %**	Minimum Angle	Inversion** Angle	Apparent Density g/cm³	Real Density g/cm³
	Vesuvius Cinders	.13	-	~15	~118	-1.2	10	22.5	-	-
	Slag (Sponge-like)	.11	-	>24	>125	-0.8	3	15	-	-
	Slag (with rust)	.08	-	>47	>125	-0.9	6	15	-	-

Lunar Comparison

	Size Range	Average Albedo	Percent Porosity	Maximum %	Maximum Angle	Minimum %**	Minimum Angle	Inversion** Angle	Apparent Density g/cm³	Real Density g/cm³
	Clavius	.268	-	5.8	91	-0.9	11	25.0	-	-
	Crisium	.137	-	12.5	102	-1.2	11	23.7	-	-
	Lyot (average)	.11	-	7.7	102	-1.2	11	23.5	-	-

* From Ref. 6

** Corrected for + 1/4% instrumental error.

been corrected for the residual polarization of +0.25% found in the 0° and 60° polarimeters. The albedos measured are to an accuracy of ±0.01, which is consistent with the values given in Halajian (Ref. 6).

Consider, for example Furnace Slag No. 4 (curves in Figs. 49 through 51). For the smallest particle sizes, the albedo is highest, and the maximum polarization the smallest. Through an intermediate range of particle sizes up from 0.21 mm to 0.50 mm, the polarization increases as the albedo decreases; then, going to larger particles, the polarization decreases as the albedo increases.

It appears that as the particles are made finer, they become transparent. This was verified by microscope observations (see Fig. 39). It is then expected that the refracted component of the incident light (negative polarization) becomes stronger relative to the reflected component (positive polarization). Thus, as observed, one would expect the negative component to counterbalance a larger part of the positive component and reduce the maximum positive polarization observed for the intermediate size particles.

However, for the largest particles of furnace slag, an anomalous effect occurs. Because of a white surface coating on some of the slag particles (not extending to the interior), the albedo increases for larger particle sizes. This increased albedo could lower the polarization by multiple reflection effects, but can be misleading as to porosity inferences (see following discussions on Particle Sizes and Porosity).

The Volcanic Ash No. 4 (Figs 41 through 44) shows the same tendency for maximum polarization as a function of particle size for the smaller particles. However, on both the Volcanic Ash No. 4 and Furnace Slag No. 4, (and also the moon - see Table 10) as the albedo decreases, the maximum moves to larger phase angles, contrary to the theoretical analysis of Hapke (Ref. 20) who assumes a nonpolarizing component given by the Schoenberg reflection formula for a diffusely-reflecting sphere.

Copper oxide (Fig. 57) with the lower albedo as compared to the silver chloride (Fig. 56), does not clearly have the higher polarization. This is probably due to metallic silver particles formed when the silver chloride was exposed to light, possibly causing a large scattered positive polarization component.

Coral (Fig. 55), being quite translucent in the smaller particles, has a low positive polarization. The coral is presumed to be mainly calcium carbonate.

Volcanic Ash No. 1 (Fig. 59), having a lighter brownish color, has a lower polarization because of the higher albedo.

In an over-all comparison, there appears to be no clear relationship between the inversion point or the minimum polarization and albedo on these samples.

Effect of Particle Size

There appears to be a relationship between albedo and particle size; this was pointed out by Halajian (Ref. 6) for Furnace Slag No. 4 and Volcanic Ash No. 4. Our work indicates this to be true for small particle sizes, but an extraneous effect appears for larger particle sizes. Because of a white coating on some of the largest furnace slag specimens, the albedos of the large particles measured higher than would be expected if the particles were homogeneous between the surfaces and the interior.

Thus, the relationship of higher albedo for smaller particle sizes holds only below about 0.50 mm particles.

The inversion angle appears to be greatest for medium size particles (excluding the below 1 micron particles) of Volcanic Ash No. 4. The negative minimum shows a similar effect in both volcanic and No. 4 and Furnace Slag No. 4.

Effect of Porosity

Referring to Table 10, it is seen that the porosity and albedo appear to follow the same trend for the smaller particles below about 0.50 mm in size for Volcanic Ash No. 4 and Furnace Slag No. 4. For the larger sizes, there is the previously mentioned misleading surface effect that causes an increase in albedo for Furnace Slag No. 4.

Thus, the trend of increasing porosity [and decreasing apparent density (see Ref. 6)],with increasing albedo, only occurs for particles below about 0.50 mm. The real densities do not vary appreciably.

Effect of Material

The primary effect of the material is in respect to the complex index of refraction. For transparent or translucent materials (low

imaginary component of the complex index of refraction, the magnitude of the positive maximum is decreased. The real component along with the complex portion, the particle size, and the particle shape possibly influence the inversion and the negative minimum.

Longitude Independence

Referring to Figs. 45 and 46 (Volcanic Ash No. 4), Figs. 52 and 53 (Furnace Slag No. 4), and Volcanic Ash No. 1 (Fig. 59), there appears to be a slightly higher average positive percent polarization on the 60 degree polarimeter.

Within the experimental errors, no longitude dependence is discerned for coral (Fig. 55), silver chloride (Fig. 56), or copper oxide (Fig. 57).

Miscellaneous Samples

Vesuvius cinders - these samples (Fig. 60) of cinders (about 3 mm average diameter) were picked up by one of the authors (W.G. Egan) within about 1000 feet of the top of the volcano. Of course they have been subject to weathering and erosion, but they were thought to offer some promise in lunar simulation based on the work of Lyot on smaller samples (see Fig. 64a, b). The Lyot sample (furnished by Prof. A. Dollfus) was one of the two sizes of Vesuvius Ash that were combined to reproduce the average lunar polarization curve. There are particles of approximately 210 (Fig. 64a,b) macrons as well as those of a few microns in size This assortment would be expected to give a resulting polarization made up of a "weighted" average of the particles in that range. The smallest particles are somewhat translucent.

It is interesting to compare the bright and dark field photographs of copper oxide powder (Figs. 64c, d). In bright field illumination (Fig. 64c) the copper oxide is opaque, but in dark field (Fig. 64d) the copper oxide looks like speckled glass with many reflecting or diffracting facets.

However, small particles of coral (Fig. 64e) look like rock candy under the microscope.

Volcanic Ash No. 1 (Fig. 64f) appears as an assortment of light and dark brown transparent grains.

The observed polarization on the Vesuvius Cinders is depicted in Fig. 61).

Furnace slags - these samples (Fig. 62) of blast furnace slag were picked up by one of the authors (W.G. Egan) during a visit to NASA/MSC on March 16, 1965. They were obtained from the pit used for astronaut lunar simulation. One sample was dark, sponge-like in appearance, and light in weight. The other sample was also dark but denser, and appeared to be dispersed with iron, giving it a rusty appearance. The observed polarizations are shown in Fig. 63.

Plane of Polarization

The observations made on the position of the plane of polarization are listed in Table 11 referenced to the secondary polaroid standard, which has been aligned to the plane of vision as determined by the glass plate reference. Polaroid alignment to the glass plate was made at 128° and 68° phase angles on the 60° and 0° polarimeters. The accuracy of alignment was checked through the range of smaller phase angles for both polarimeters, and alignment was to within a fraction of a degree.

In the observations listed in Table 11 the angular displacement of the plane of polarization follows the convention in the Appendix of Ref. 1. Angles greater than 90 degrees are considered negative to make the data easily readable (i.e., $\theta_r = -95°$ is identical to $\theta_r = +85°$).

Referring to Table 11, we may draw the following conclusions:

1. There is general agreement between the inversion angle determined from the corrected percent polarization data and the plane of polarization data;

2. The angular shift in the plane of polarization from 0° to 90° at inversion is more rapid with the 60° polarimeter as compared to the 0° polarimeter;

3. There is a general negative drift in the 0° position of the plane of polarization as observed with the 0° polarimeter with decreasing phase angle; the 60° polarimeter does not show this. Hence, a possible instrumental effect is suggested as an explanation.

Table 11

PLANE OF POLARIZATION OBSERVATIONS

FURNACE SLAG NO. 4

Particle Size	Zero Degree Polarimeter				60 Degree Polarimeter			
	Date	Inversion Angle	Phase Angle	θ_r	Date	Inversion Angle	Phase Angle	θ_r
2.83 to 6.35 mm	2/4/66		68°	-2°	2/4/66		128°	0°
			21	-8.5			59	-1
		18.5°	15	-78.5			24	-8
			11	-83		18.5°	10	-91.5
			9	-84			7	-94
1.19 to 2.83 mm	2/4/66		68	+2.5	2/4/66		128	-1
			36.5	+1			62.5	-1
			28	-1.5			32.5	-1.5
		17.5	21	-13.5			24	-2
			14	-83.5		17.5	14	-93
			7.5	-80.5			7	-92
0.50 to 1.19 mm	2/5/66		68	-1.5	2/5/66		128	-1
			29.5	-2.5			63	-0.5
			21	-7.5			20	-3.5
		17.0	19	-20		17.0	11.5	-88
			15	-85.5			6	-90
			11	-84.5				
0.21 to 0.50 mm	2/5/66		68	-0.5	2/5/66		128	0
			24	+0.5			57	0
			20	-4			28	+0.5
		18.5	15.5	-65			21	+0.5
			6	-77.5		18.5	12	-97.5
							7.5	-89.5
0.088 to 0.21 mm	2/5/66		68	0	2/5/66		128	0
			23	-1			58.5	-0.5
			19.5	-4			21.5	-6
		17.0	14	-63.5			20	-3
			8.5	-81		17.0	12.5	-81.5
							7	-93
0.037 to 0.088 mm	2/5/66		68	0	2/5/66		128	+1
			24	0			58	+1.5
			21	-2.5			23	-7
		17.5	13	-75			19.5	-5
			8	-80		17.5	13	-96.5
							9	-90.5
≤ 0.037 mm	2/5/66		68	+2	2/5/66		128	+1
			26.5	-0.5			59	0
			22	-6.5			29	0
		18.5	13.5	-77.5			22	-1
			8.5	-83		18.5	11.5	-92
							7	-92
≤ 1µ	2/3/66		68	-2	2/3/66		128	-1.5
			33	-1			59	-2
			25	-7.5			29	-1
		23.0	18.5	-80.5			24	-0.5
			14	-86		23.0	15.5	-94
							12	-91.5
VOLCANIC ASH NO. 1								
0.088 to 0.21 mm	2/7/66		68	0	2/7/66		128	0
			31	+0.5			58	-1
			26	-4.5			29.5	-2
		24.5	22	-77			27	+0.5
			15	-85.5		24.5	18	-101.5
							12	-92
≤ 1µ	2/8/66		68	+2.5	2/8/66		128	-3.5
			35	+1			58.5	-3
			28	-2.5			30	-3.5
		25.0	19	-83		25.0	25	-4
			11	-82			18	-95
			6.5	-82.5			9	-95

Table 11 (Continued)

VOLCANIC ASH NO. 4

Particle Size	Zero Degree Polarimeter				60 Degree Polarimeter			
	Date	Inversion Angle	Phase Angle	θ_r	Date	Inversion Angle	Phase Angle	θ_r
2.83 to 6.35 mm	1/31/66	21.0°	68°	+2°	1/31/66	21.0°	128°	-2°
			40	+2			110	-2.5
			24.5	-3			60	-2.5
			10	-86			40	-3.5
							30	-4
							25	-7.5
							13	-94
1.19 to 2.83 mm	1/31/66	21.5	68	+1.5	1/31/66	21.5	128	-1
			40	+2			61	-0.5
			30	+0.5			40	0
			25	-3			30	-2
			13	-84.5			25	-1
							14	-90
0.50 to 1.19 mm	1/31/66	23.0	68	+1.5	2/1/66	23.0	128	+1
			40	+1.5			61	-0.5
			30	-1			39	+0.5
			25	-6.5			30	+1.5
			13	-86.5			26	+1.5
							13	-90
	1/31/66	23.0	68	-1.5				
			26	-1				
			20.5	-66				
			18	-86.5				
			15	-85.5				
0.21 to 0.50 mm	2/1/66	23.5	68	+2	2/1/66	23.5	128	-2
			24.5	-5			58	-1.5
			23	-19.5			23	-0.5
			21	-76.5			22.5	-3
			15.5	-87.5			19.5	-94.5
							14	-92.5
0.088 to 0.21 mm	2/2/66	22.5	68	+1.5	2/1/66	22.5	128	+1
			24	-2.5			58	-0.5
			22	-8.5			26.5	+1
			19.5	-78			22	-0.5
			12.5	-87.5			19.5	-88.5
							13	-93
0.037 to 0.088	2/2/66	22.5	68	-1	2/1/66	22.5	128	-2
			25	-0.5			55	-1
			22	-8.5			25	-1.5
			19	-66.5			23.5	+4.5
			14	-85			18	-87
							9	-89.5
≤ 0.037mm	2/2/66	20.5	68	+1	2/2/66	20.5	128	+0.5
			28	-1.5			61	+0.5
			22	-7.5			24.5	+1.5
			18.5	-75.5			20.5	0
			12.5	-83			18.5	-90
							15	-90
≤ 1μ	2/4/66	24.0	68	+0.5	2/4/66	24.0	128	-2.5
			29	-4			55	-3
			24	-4			31	-3.5
			16	-82			24	-8
			8.5	-86			17	-95
							11.5	-93.5

CORAL NO. 1

Particle Size	Date	Inversion Angle	Phase Angle	θ_r	Date	Inversion Angle	Phase Angle	θ_r
0.088 to 0.21 mm	2/9/66	29.0	68	0	2/9/66	29.0	128	-1
			36	-0.5			57.5	+1.5
			30	-6			33	0
			26	-7			8.5	-96
			10	-77.5				
			7	-71				
≤ 1μ	2/10/66	27.5	68	+4	2/9/66	27.5	128	0
			42	-2			59.5	+2
			30	+1			32	0
							27	+2.5
							7	+1

Table 11 (Continued)

COPPER OXIDE

Particle Size	Zero Degree Polarimeter				60 Degree Polarimeter			
	Date	Inversion Angle	Phase Angle	θ_r	Date	Inversion Angle	Phase Angle	θ_r
0.088 to 0.21 mm	2/11/66		68°	+2.5	2/11/66		128°	-0.5
			39	+1.5			55	+0.5
			33	+0.5			35.5	-1.5
			27	-0.5			28	-3.5
		17.5°	19	-16.5		17.5°	20	-0.5
			12	-77.5			13	-89.5
			5.5	-78.5			6	-90
≤ 1μ	2/10/66		68	+1.5	2/10/66		128	-1.5
			23	-1.5			57	-4
		14.5	18	-5			27	-4
			10	-69.5			20.5	-5.5
			6	-70.5		14.5	5	-90.5

SILVER CHLORIDE

Particle Size	Zero Degree Polarimeter				60 Degree Polarimeter			
	Date	Inversion Angle	Phase Angle	θ_r	Date	Inversion Angle	Phase Angle	θ_r
0.088 to 0.210 mm	2/2/66		68	+1.5	2/12/66		128	0
			38	0			56	-0.5
		15.0	19	-4.5			32	-3
			10	-50.5		15.0	20	-2
			5	-78.5			12.5	-87
							5	-93.5
3-8μ	2/12/66		68	+3	2/12/66		128	-2.5
			35	0			57	-2.5
		17.0	20	-6.5			25	-3.5
			15	-12.5		17.0	18	-4.5
			8	-70.5			10	-88
							5	-92
≤ 1μ	2/14/66		68	+1	2/14/66		128	+1
			28	-9.5			55	-1
		26.5	23.5	-14			36.5	-1
			18.5	-72			30	-2.5
			13	-82.5		26.5	16	-98.5
							5	-95.5

4. On observations at phase angles below the inversion, there is an apparent wandering of the position of the plane of polarization from 90°; this is fundamentally the result of the low signal to noise ratio because of the small amount of polarization (negative) below inversion.

The lunar data of Gehrels et al. (Ref. 4) and the laboratory sample data of Coffeen (Ref. 16) do not clearly show a trend in the position of the plane of polarization with phase angle. We cannot definitely determine whether the plane of polarization continuously changes from 0° to 90° as the inversion angle is passed, as seen by the Russian observers (see Ref. 1). Their observations appear to be the result of an instrumental effect, and from our data, this effect cannot be determined.

Lunar Implications

On the basis of data obtained for the percent polarization of the various samples as a function of phase angle (summarized in Table 10) we may infer the appropriateness of particular samples as possessing properties characteristic of the lunar surface. At the bottom of Table 10 are summarized the properties of Mare Crisium and Clavius as well as the Lyot average curve. In addition, the Mare Crisium and Clavius curves are presented as comparison data in Figs. 40 through 63.

For Furnace Slag No. 4 (Fig. 51) the Mare Crisium curve is fitted best for particle sizes below 37 microns, Clavius for particle sizes below 1 micron. This assumes that one particle size alone exists in these areas, which is probably far from true. But the general trend does indicate that smaller particles fit the highland curves best.

Volcanic Ash No. 4 (Fig. 44) shows the same trend, but the particle sizes are larger, possibly the result of the lower density of the volcanic ash as compared to the furnace slag. Mare Crisium is best fit by particles between 37 and 88 microns, and Clavius by particles between about 37 microns and 1 micron.

Volcanic Ash No. 1 (Fig. 59) appears to require particles greater than the 0.088 to 0.21 mm range to match Mare Crisium, possibly because of the lighter color of our sample as compared to the material in the maria; a match to Clavius appears to necessitate particles less than 1 micron in size.

Copper oxide (Fig. 57), coral (Fig. 55) and silver chloride (Fig. 56) alone are unsatisfactory because of maximum polarization well out of the range required to simulate the lunar surface.

The Vesuvius Cinders (Fig. 61) match the Mare Crisium lowlands curve fairly closely, which is a rather interesting analogy considering the origin of the cinders.

The sponge-like slag (Fig. 63) obtained at NASA/MSC appears to offer some possibility as a lunar simulator, because it would only require a moderate modification of the polarization characteristics with a surface coating to match Mare Crisium; the maximum polarization would have to be diminished, the corresponding phase angle reduced to about 102 degrees, and the inversion shifted to about 23.7 degrees. This might be approximated by coating it with Furnace Slag No. 4 particles less than 1 micron. This, as well as color implications, will be investigated more completely in Phase III.

The Vesuvius Cinders appear to show greater promise if the polarization peak could be shifted to a smaller angle by combining the cinders with a nonpolarizing material of varying albedo. This too will be investigated in Phase III.

The effect of proton bombardment could alter the results observed on the powders (Refs. 15 and 18). It could conceivably change the results observed on the bulk samples of Vesuvius Cinder and Furnace Slag.

Our observed results on Volcanic Ashes are in agreement with those shown by Coffeen (Ref. 16) for a Fairy-Castle structure of Volcanic Ash. Thus, the G_u polarization observed by Coffeen increases from 6 to 11 percent as the average particle size is decreased from 3 to 1 mm. In Fig. 43 it is observed that as the particle size goes from the 2.83 to 6.35mm range to 0.5 to 1.19mm range, the polarization increases from 16.6 to 18.1 percent.

The albedo-polarization data summarized in Fig. 65 for Furnace Slag No. 4 and Volcanic Ash Nos. 1 and 4 yield additional information; the two straight lines show the appropriate trends for the Furnace Slag and the Volcanic Ashes. The difference in the two curves might be the result of the higher real density of the Furnace Slag above the Volcanic Ashes. Two lunar points from Gehrels et al. (Ref. 4) used in the present data analysis are shown; the Mare Crisium point lies on the Volcanic Ash curve, while the Clavius point is above both curves.

A comparison is made to the proton bombardment data of Wehner et al. (Ref. 18). The Wehner data for 74 to 300μ tholeiitic basalt and 44 to 74μ granodiorite are shown. These lie on the upper extreme of the Wehner data, with smaller particles lying below the curves; this is also true for 74 to 300μ tektite and 74 to 300μ greenstone. Wehner had used the Russian lunar data to compare with the laboratory polarization-albedo data. It is felt that the Russian lunar data is inaccurate and Gehrels' data more accurate (see Ref. 1). Thus, one would infer that bombarded particles of these materials having a size of about 74 to 300 microns would fit the lunar data best. This is larger than the range of sizes obtained from the present study.

The data on silver chloride, copper oxide, and coral were not plotted on the graph because it was felt that they were not representative of typical lunar surface data.

Conclusions

As a result of Phase II, we have delimited the range of particle sizes that would have to exist on the lunar surface, either as a contiguous volume or as a simple, thin layer of the order of up to 1 mm thickness. This model is consistent with the Luna 9 observations, and also with the thermophysical and photometric models analyzed at Grumman (Refs. 6-8 and 21- 23) It must also be remembered that the present observations are made under terrestrial conditions, and the high vacuum conditions on the moon plus the effect of solar wind proton bombardment could possibly alter the results.

Even though closely defined ranges of particle sizes were used in this investigation, one would not assume that these specific ranges exist on the lunar surface to give the observed polarization. The particle ranges observed in this work serve as guides in correlating photometric, polarization, and thermophysical data.

The nonuniqueness of a surface contrived to give an observed polarization must still be emphasized, although guides to a proper configuration evolve from a consideration of all available data.

It appears that the polarization - albedo - porosity relationship for the particles below 0.5 mm in size may be used to advantage in elucidating the mechanical properties as well as the thermal properties of a lunar surface model (Ref. 23).

The work of Phase III yields additional surface information based on color effects in polarization.

Fig. 37 Polarization Curves of the Moon

Phase Angle α, degrees

Percent Polarization

Crisium (Maria) (Gehrels)
Albedo = 0.137

Mean Lyot
Albedo = 0.11

Clavius (Crater Floor) (Gehrels)
Albedo = 0.268
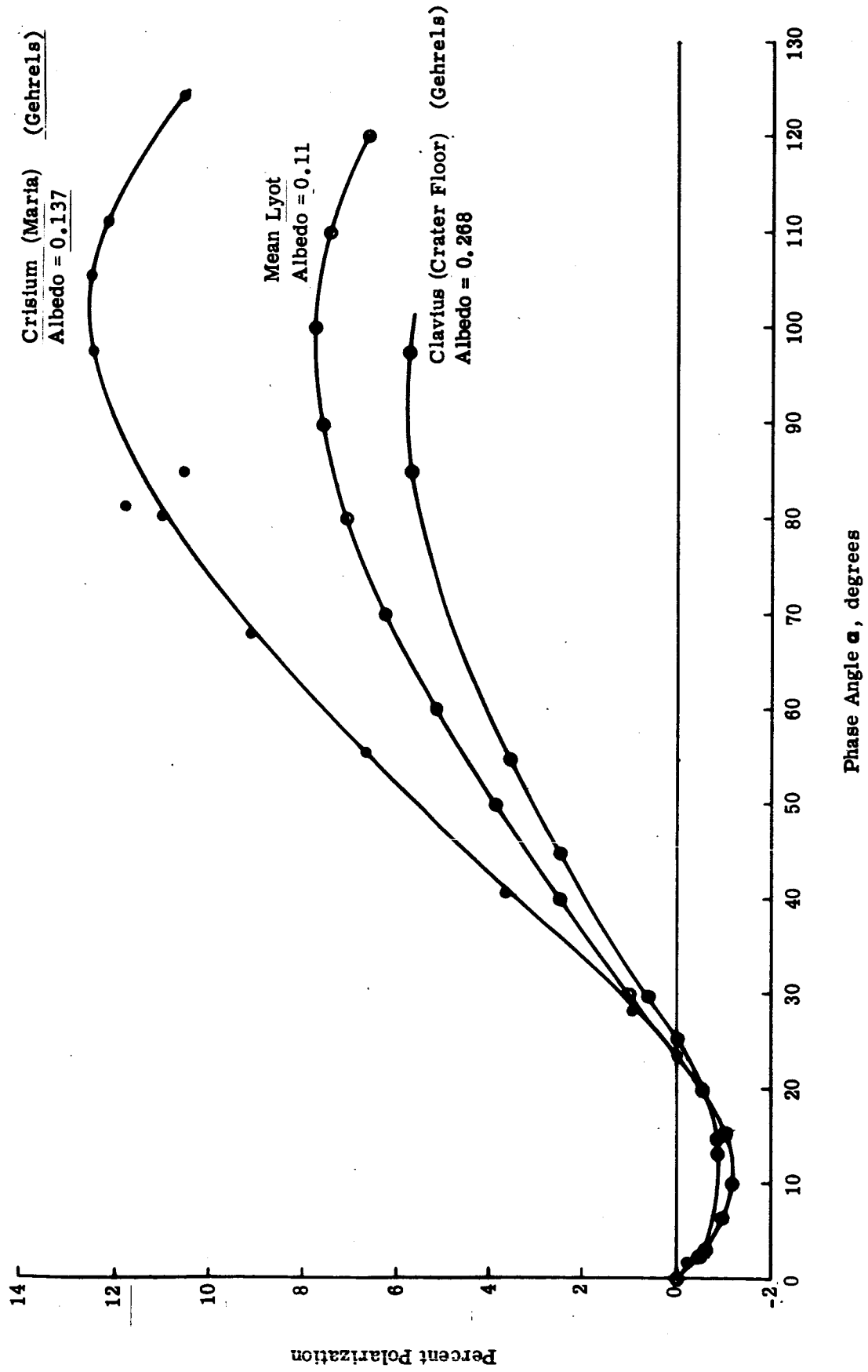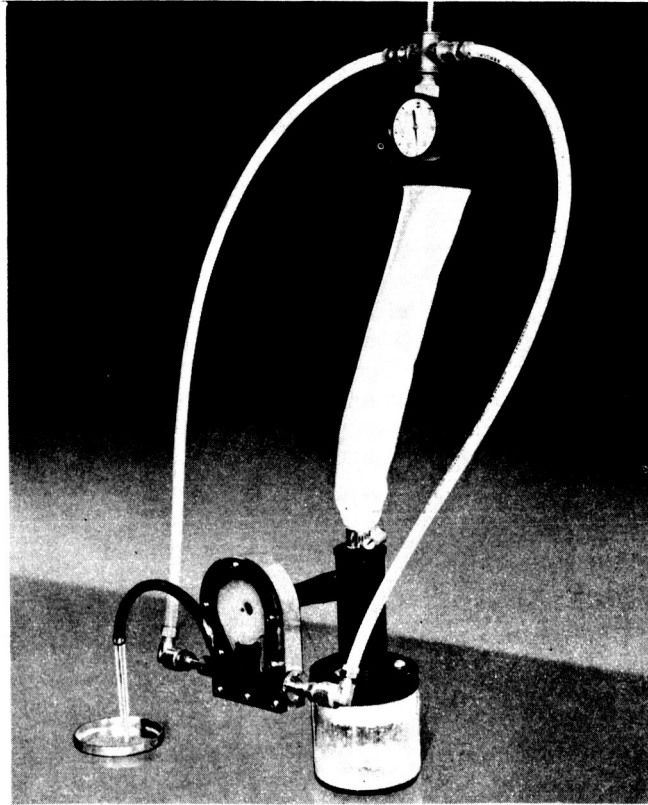
Fig. 38   Helme Fluid Energy Mill Assembly
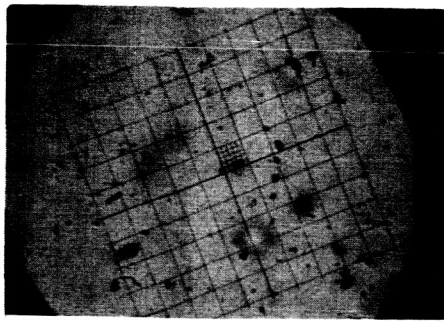
a) Volcanic Ash #4
   25μ/div ≤ 1μ (1-17-66)
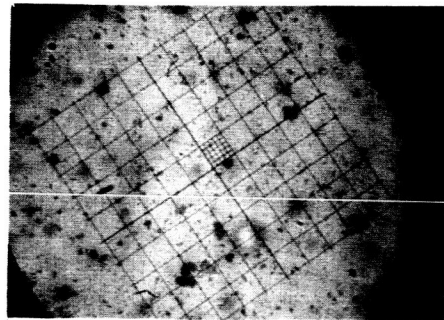
b) Furnace Slag #4
   25μ/div ≤ 1μ (1-18-66)
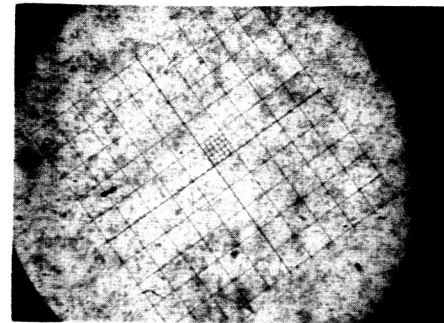
c) Volcanic Ash #1
   25μ/div ≤ 1μ (1-18-66)
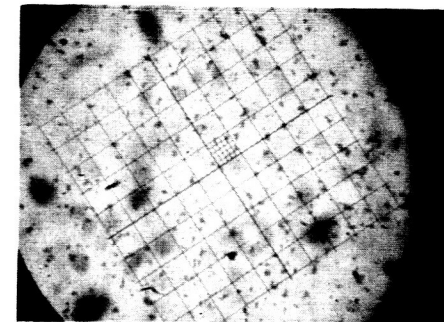
d) Copper Oxide
   25μ/div ≤ 1μ (1-18-66)
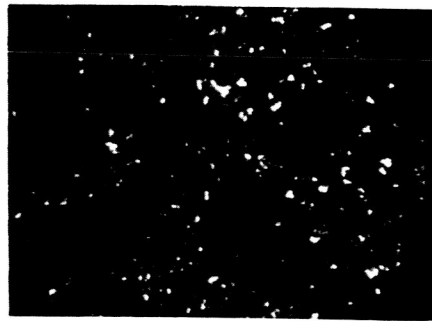
e) Silver Chloride
   Precipitate
   25μ/div < 1μ (2-10-66)
   (Dark Field Illumination)
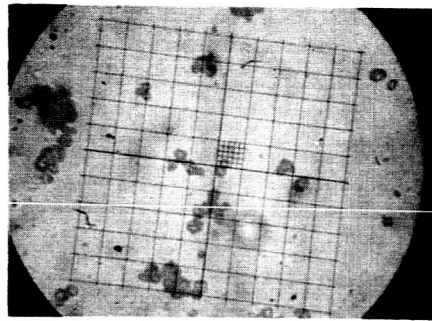
f) Silver Chloride
   Fluid Energy Mill Grind
   12.5μ/div 3-8μ (2-10-66)
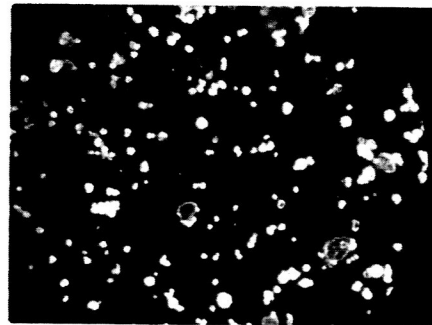
g) Silver Chloride
   Fluid Energy Mill
   25μ/div 3-8μ (2-10-66)
   (Dark Field Illumination)
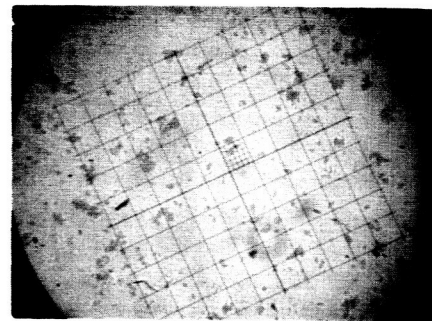
h) Coral #1
   12.5μ/div ≤ 1μ (1-14-66)

Fig. 39 Microscopic Photographs of Submicron Specimens
Used in Polarimetric Investigation

81
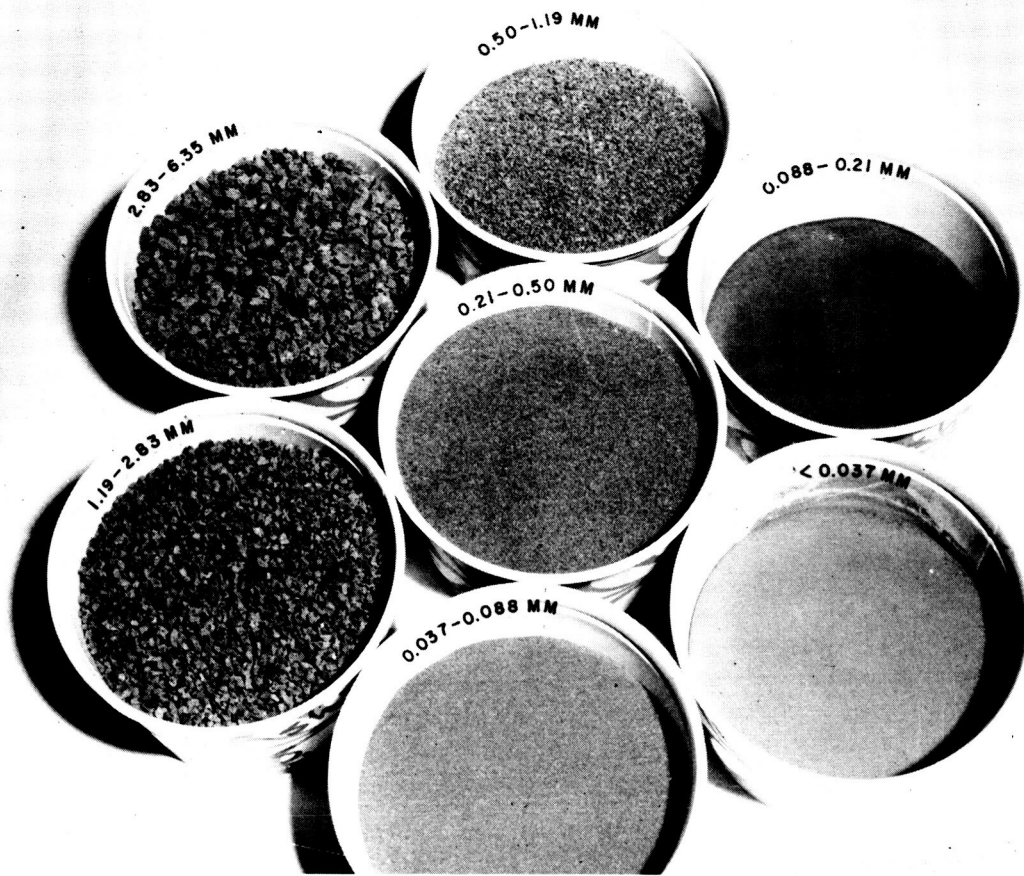
Ash No. 4, Ground and Sorted
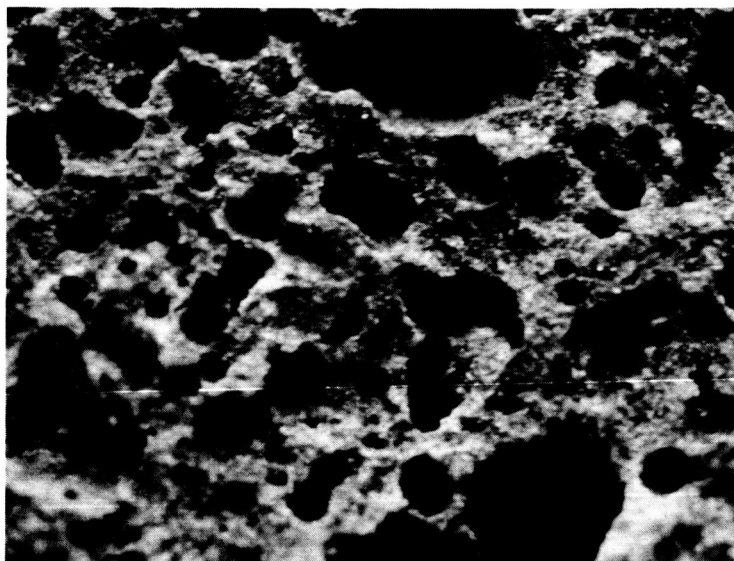
(a)   2.83-6.35 mm

Fig. 40   Volcanic Ash No. 4
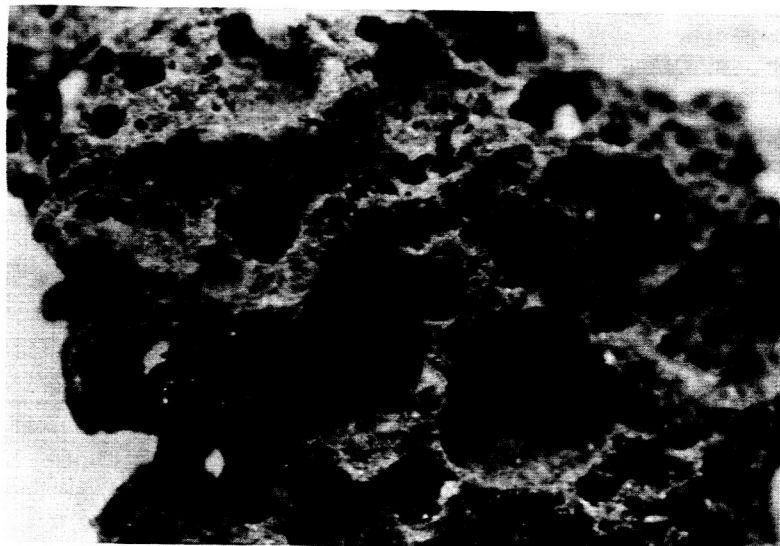
(b)   1.19-2.83 mm

(c)   0.50-1.19 mm

Fig. 40 (Cont.) Volcanic Ash No. 4
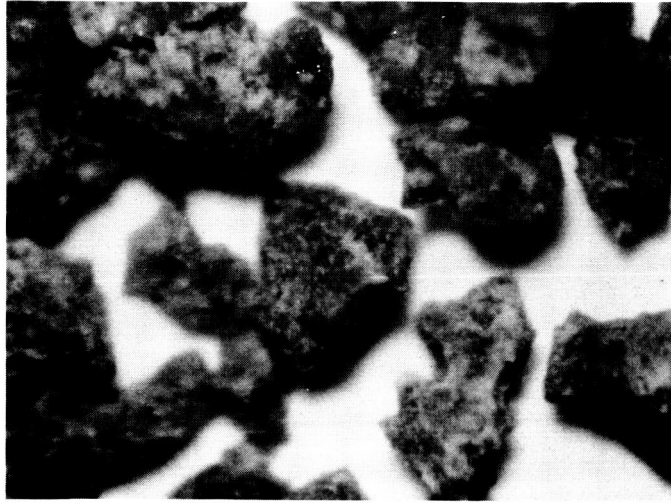
(d)   0.21-0.50 mm

(e)   0.088-0.21 mm

Fig. 40 (Cont.) Volcanic Ash No. 4

(f)   0.037-0.088 mm

(g) ≤ .037μ
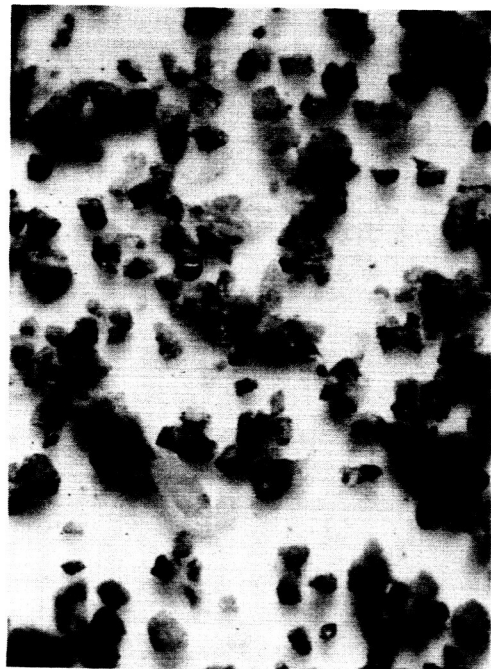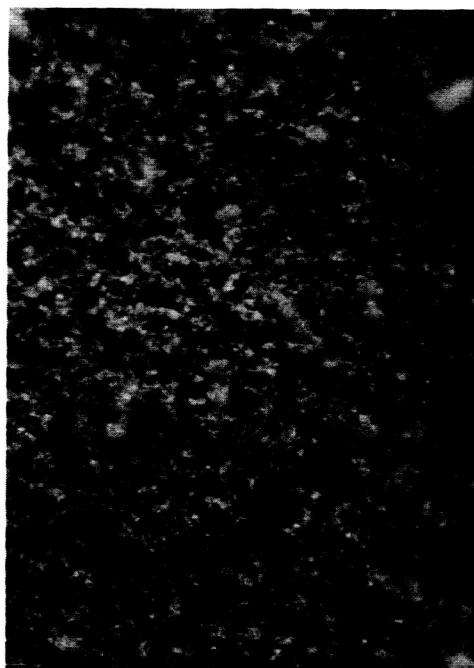
Fig. 40 (Cont.) Volcanic Ash No. 4

Fig. 41 Volcanic Ash No. 4: Percent Polarization as a Function of Particle Size for Largest Particles (Uncorrected for Instrumental Effect) - 0° Polarimeter

86
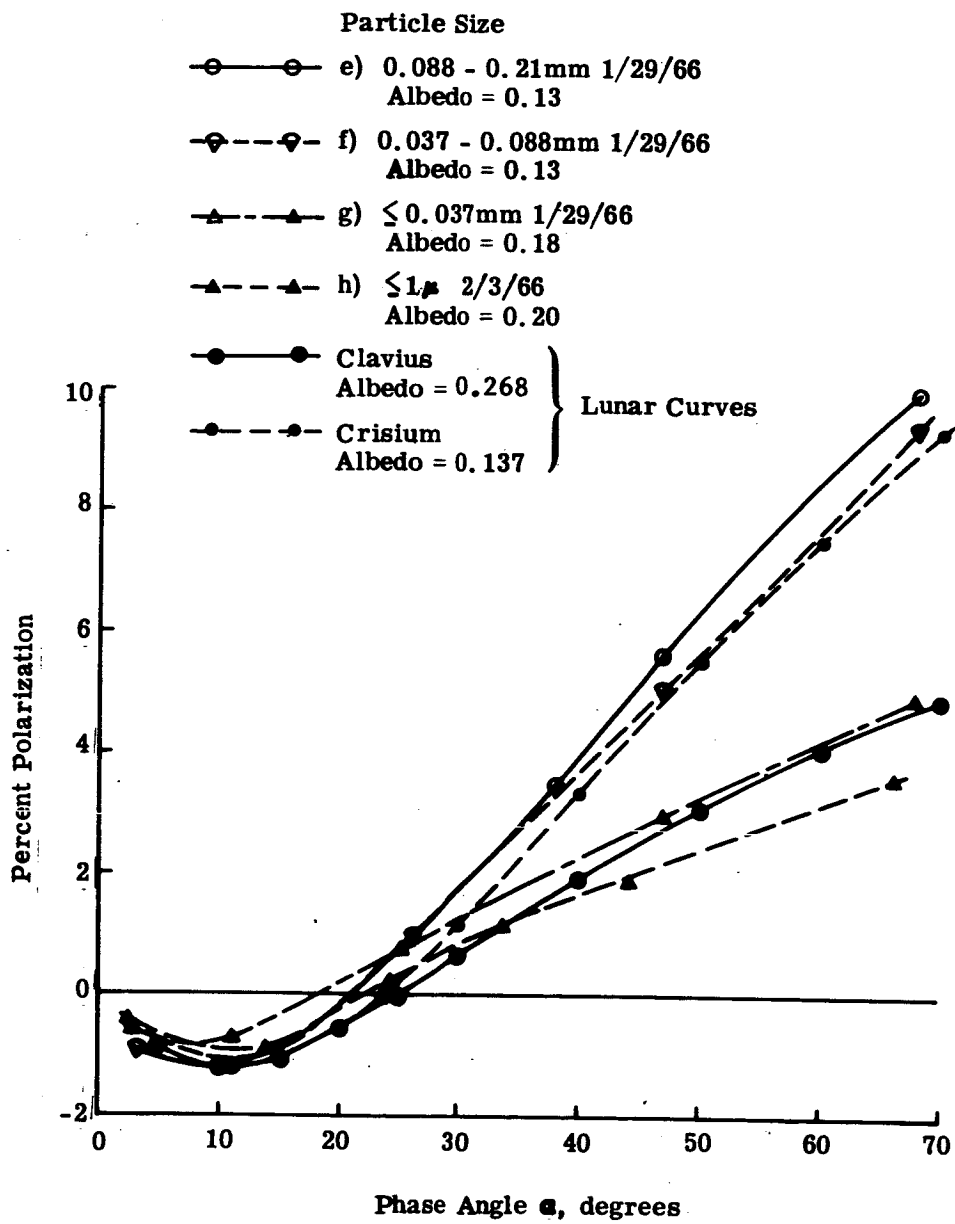
Fig. 42   Volcanic Ash No. 4: Percent Polarization as a Function of
Particle Size for Smallest Particles (Uncorrected for
Instrumental Effect)   0° Polarimeter
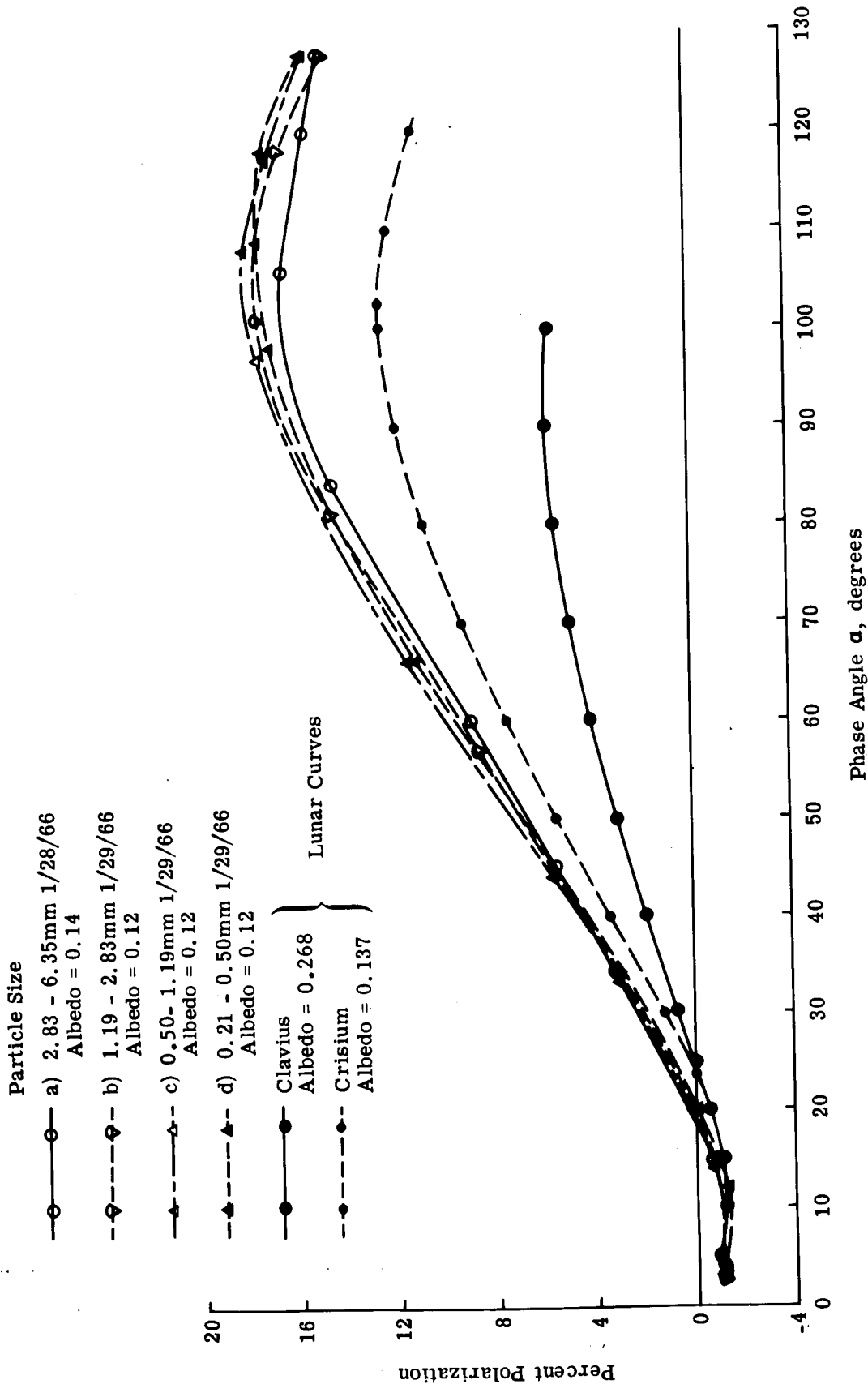
Fig. 43 Volcanic Ash No. 4: Percent Polarization as a Function of Particle Size for Largest Particles (Uncorrected for Instrumental Effect) 60° Polarimter

Fig. 44 Volcanic Ash No. 4: Percent Polarization as a Function of
Particle Size for Smallest Particles (Uncorrected for
Instrumental Effect) 60° Polarimeter
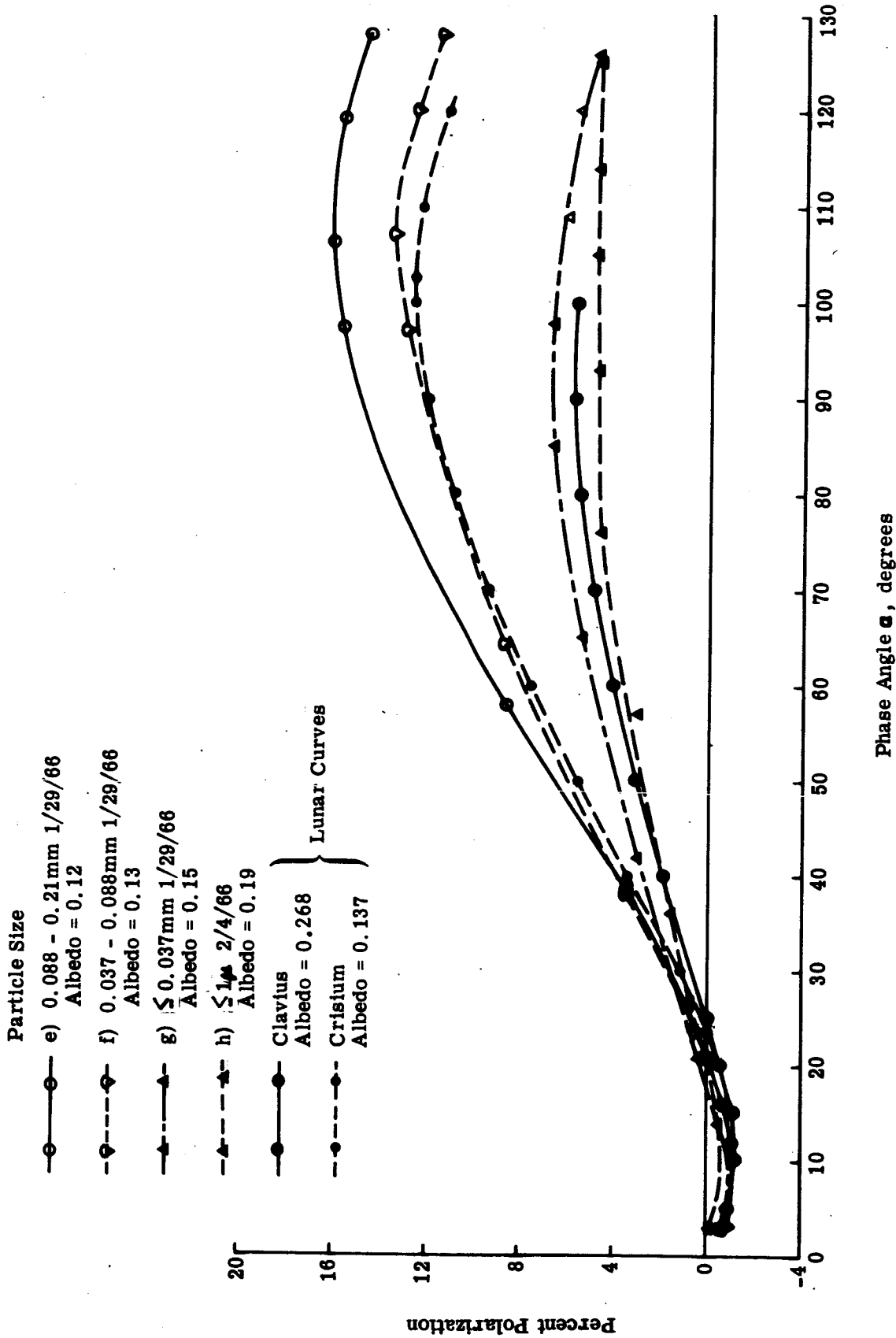
Particle Size

e) 0.088 - 0.21mm 1/29/66
   Albedo = 0.12

f) 0.037 - 0.088mm 1/29/66
   Albedo = 0.13

g) ≤ 0.037mm 1/29/66
   Albedo = 0.15

h) ≤ 1μ 2/4/66
   Albedo = 0.19

Clavius
Albedo = 0.268

Crisium
Albedo = 0.137

} Lunar Curves

Phase Angle α, degrees

Percent Polarization

89
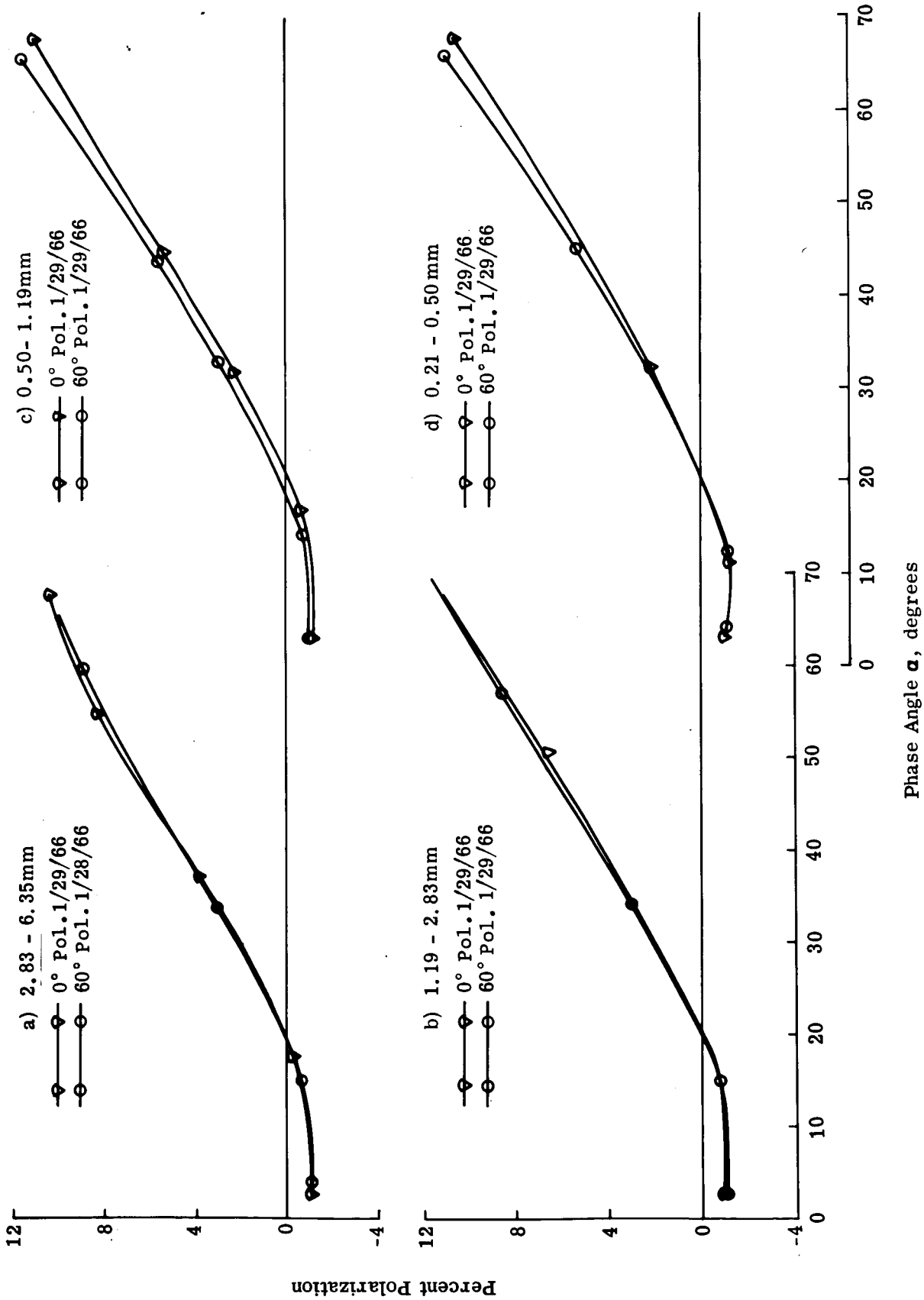
Fig. 45 Volcanic Ash No. 4: Simulated Lunar Longitude Effect on
Percent Polarization for Largest Particles (Uncorrected
for Instrumental Effect)

90

Fig. 46 Volcanic Ash No. 4: Simulated Lunar Longitude Effect on Percent Polarization for Smallest Particles (Uncorrected for Instrumental Effects)

e) 0.088 - 0.21mm
—◐— 0° Pol.1/29/66
—○— 60° Pol.1/29/66

f) 0.037 - 0.088mm
—◐— 0° Pol.1/29/66
—○— 60° Pol.1/29/66

g) ≤ 0.037 mm
—◐— 0° Pol.1/29/66
—○— 60° Pol.1/29/66

h) ≤ 1 μ
—◐— 0° Pol.2/3/66
—○— 60° Pol.2/4/66

Phase Angle α, degrees

Percent Polarization

16
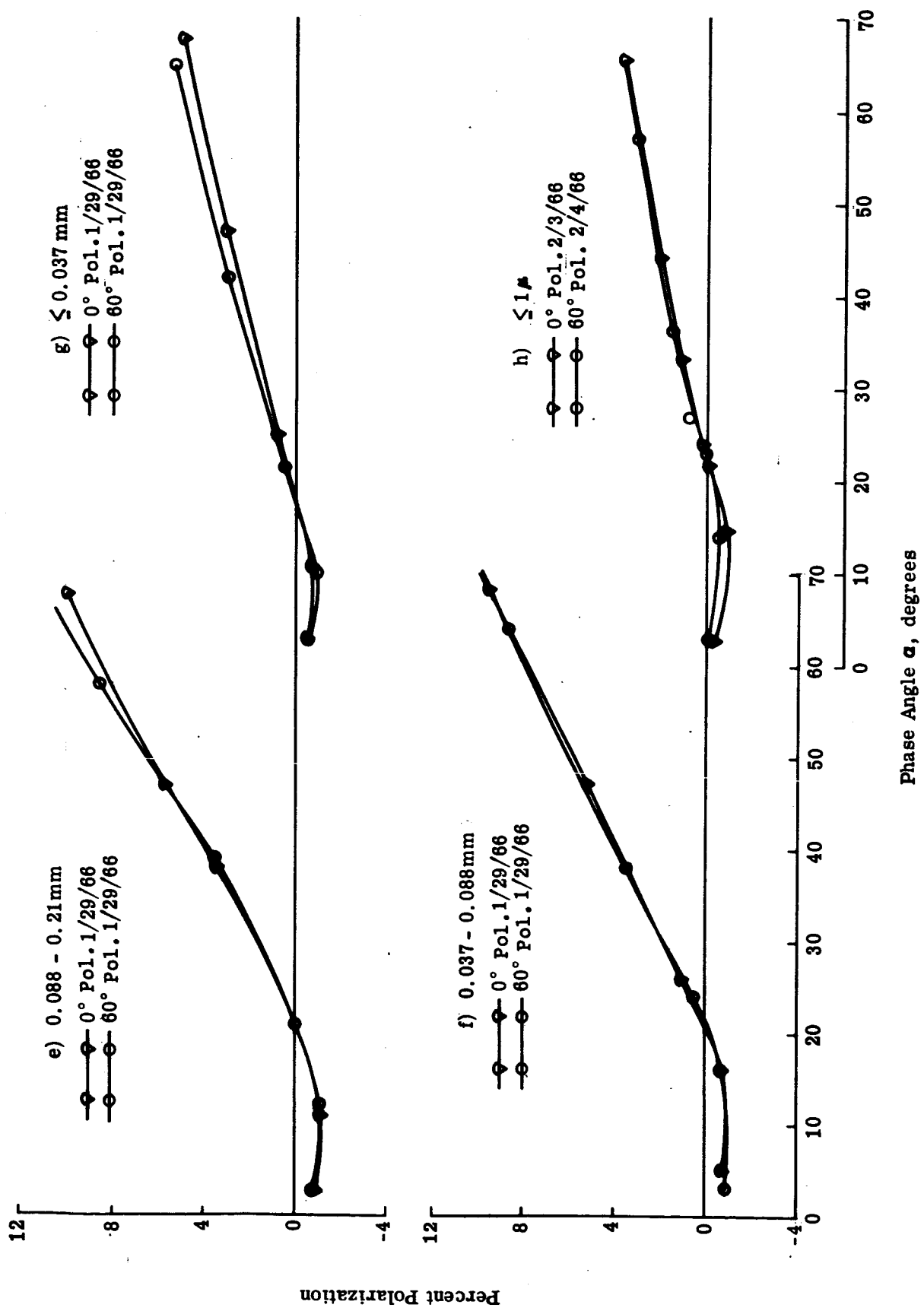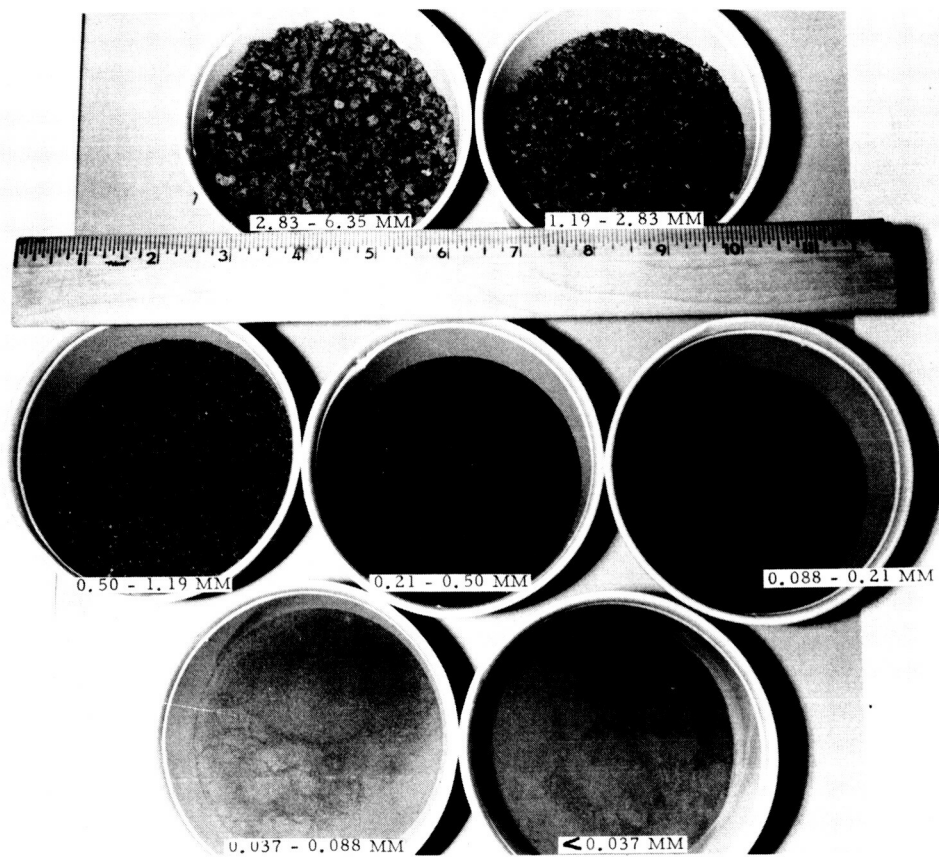
Fig. 47   Furnace Slag No. 4

Fig. 48   Furnace Slag No. 4: Percent Polarization as a Function of
          Particle Size for Largest Particles (Uncorrected for
          Instrumental Effects)   0° Polarimter

93

Particle Size

e) 0.088 - 0.21mm 1/28/66
Albedo = 0.07

f) 0.037 - 0.088mm 1/28/66
Albedo = 0.10

g) ≤ 0.037mm 1/28/66
Albedo = 0.11

h) ≤ 1µ 2/3/66
Albedo = 0.14

Clavius
Albedo = 0.268

Crisium
Albedo = 0.137

Lunar Curves

Phase Angle α, degrees
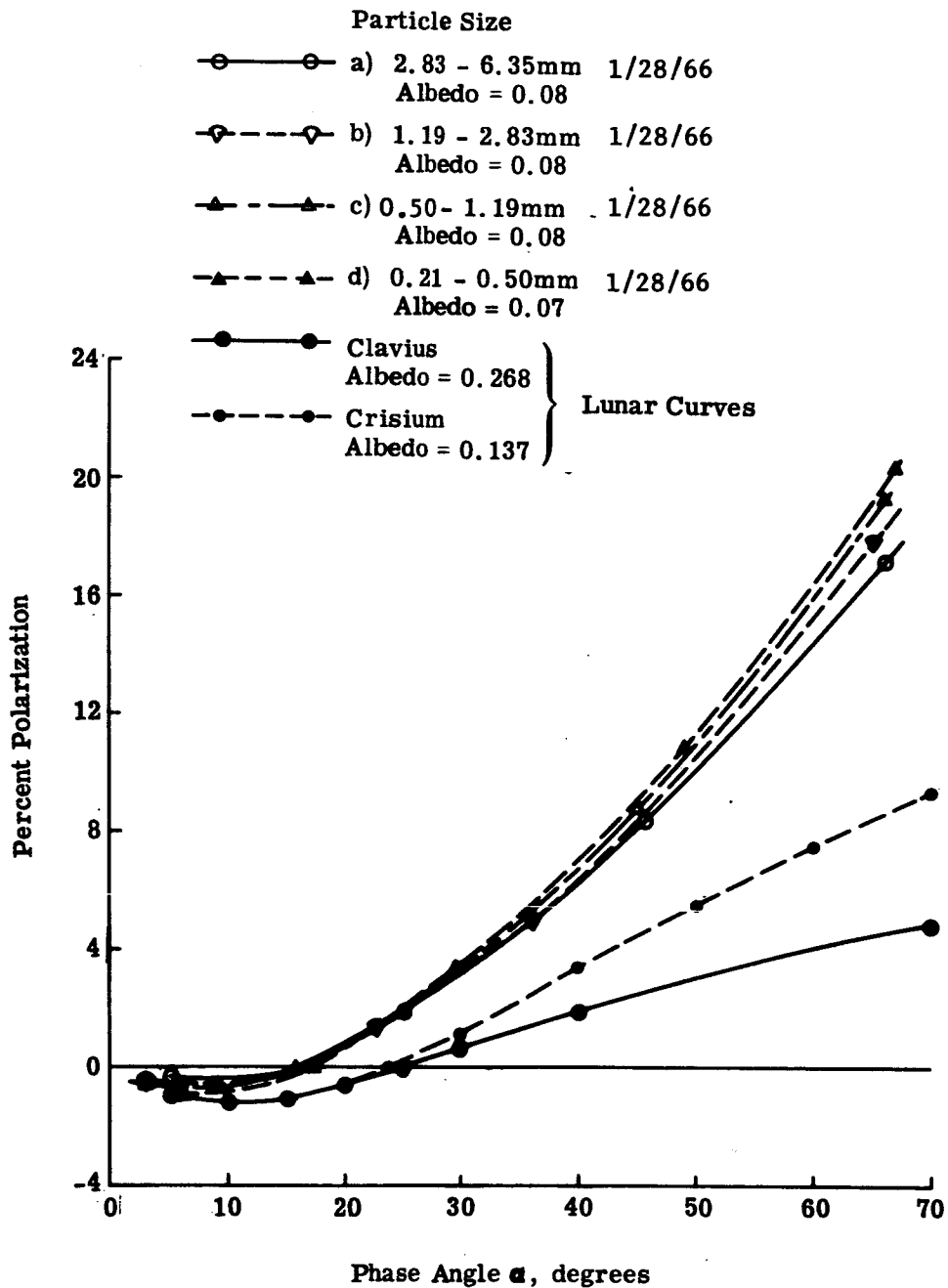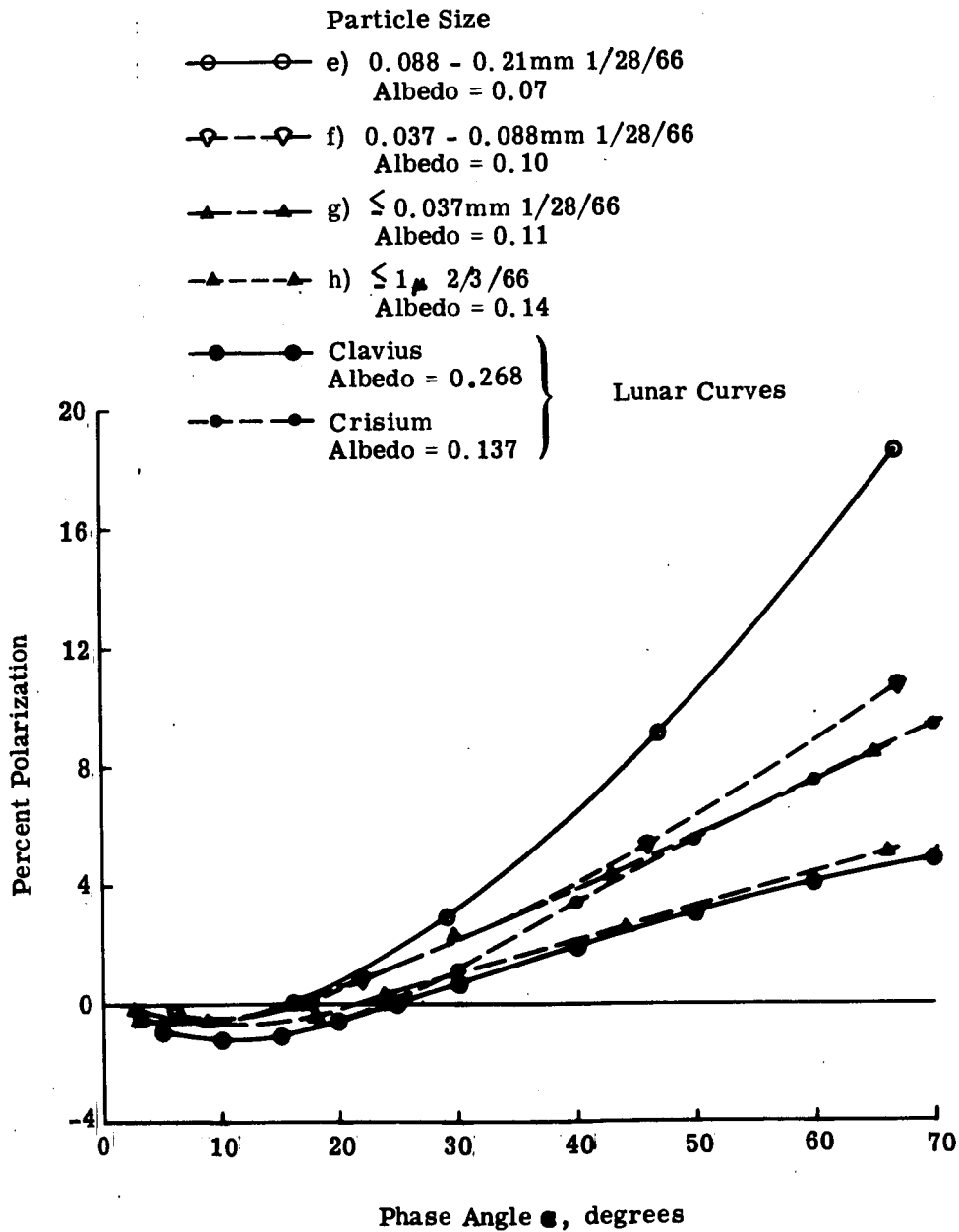
Fig. 49 Furnace Slag No. 4: Percent Polarization as a Function of
Particle Size for Smallest Particles (Uncorrected for
Instrumental Effects) 0° Polarimter Polarimeter

94
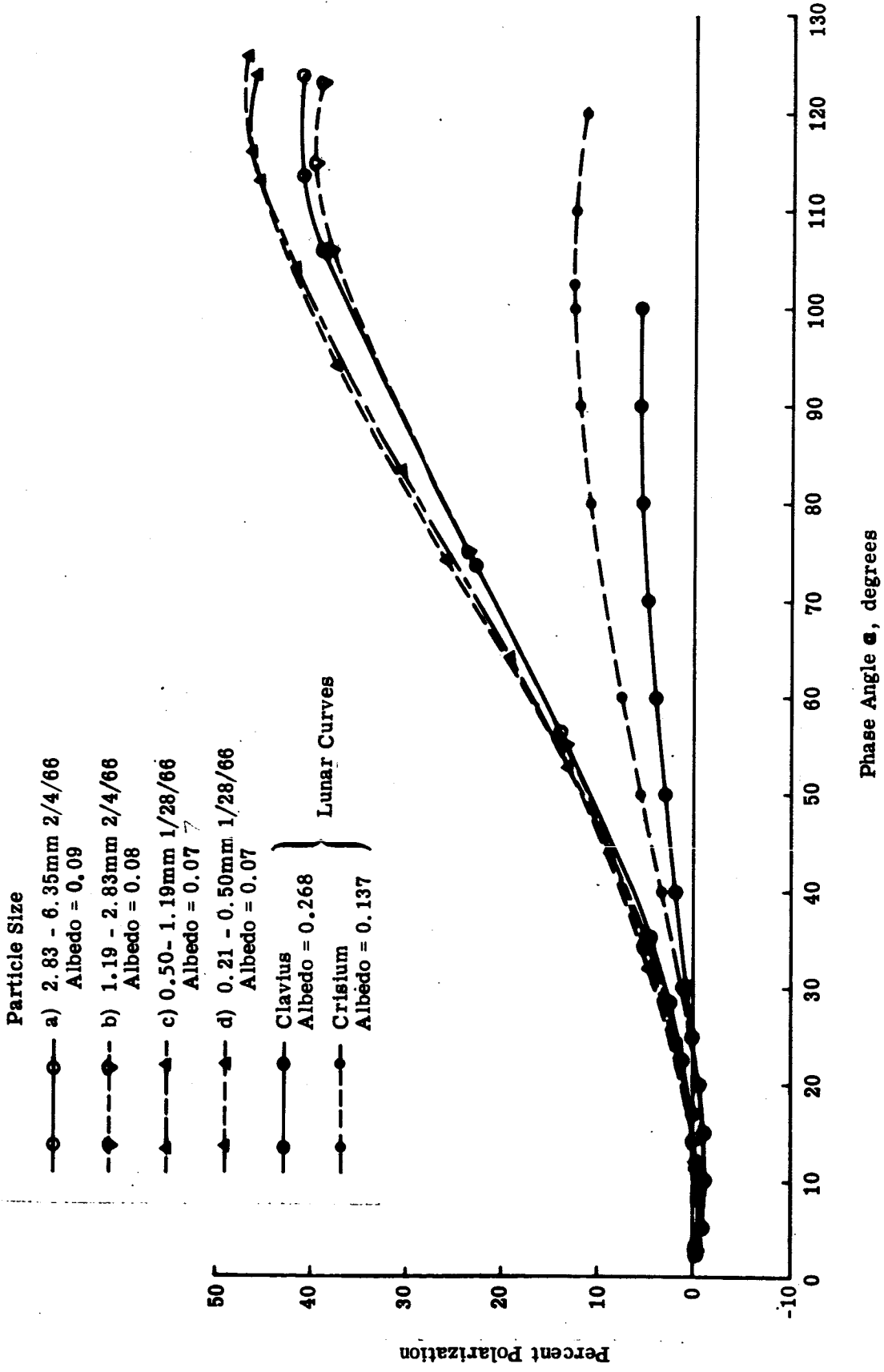
Fig. 50 Furnace Slag No. 4: Percent Polarization as a Function of
Particle Size for Largest Particles (Uncorrected for
Instrumental Effects) 60° Polarimeter

Fig. 51 Furnace Slag No. 4: Percent Polarization as a Function of Particle Size for Smallest Particles (Uncorrected for Instrumental Effects) 60° Polarimeter

Particle Size

○——○ e) 0.088 - 0.21mm 1/28/66
Albedo = 0.07

●——● f) 0.037 - 0.088mm 1/28/66
Albedo = 0.09

▲——▲ g) ≤ 0.037mm 1/28/66
Albedo = 0.10

▲——▲ h) ≤ 1μ 2/3/66
Albedo = 0.14

●——● Clavius
Albedo = 0.268

●——● Crisium
Albedo = 0.137

} Lunar Curves

Phase Angle α, degrees
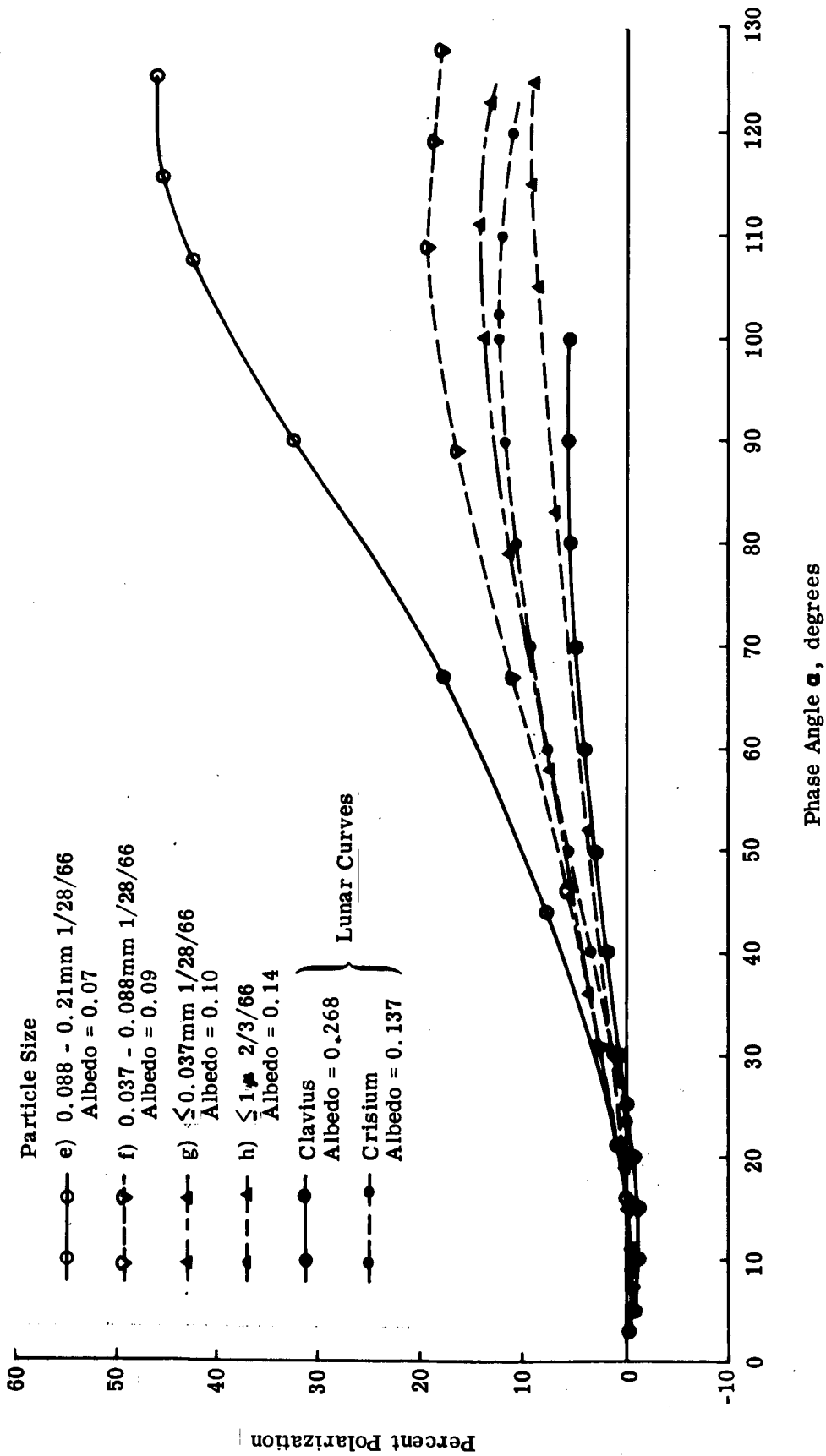
Percent Polarization
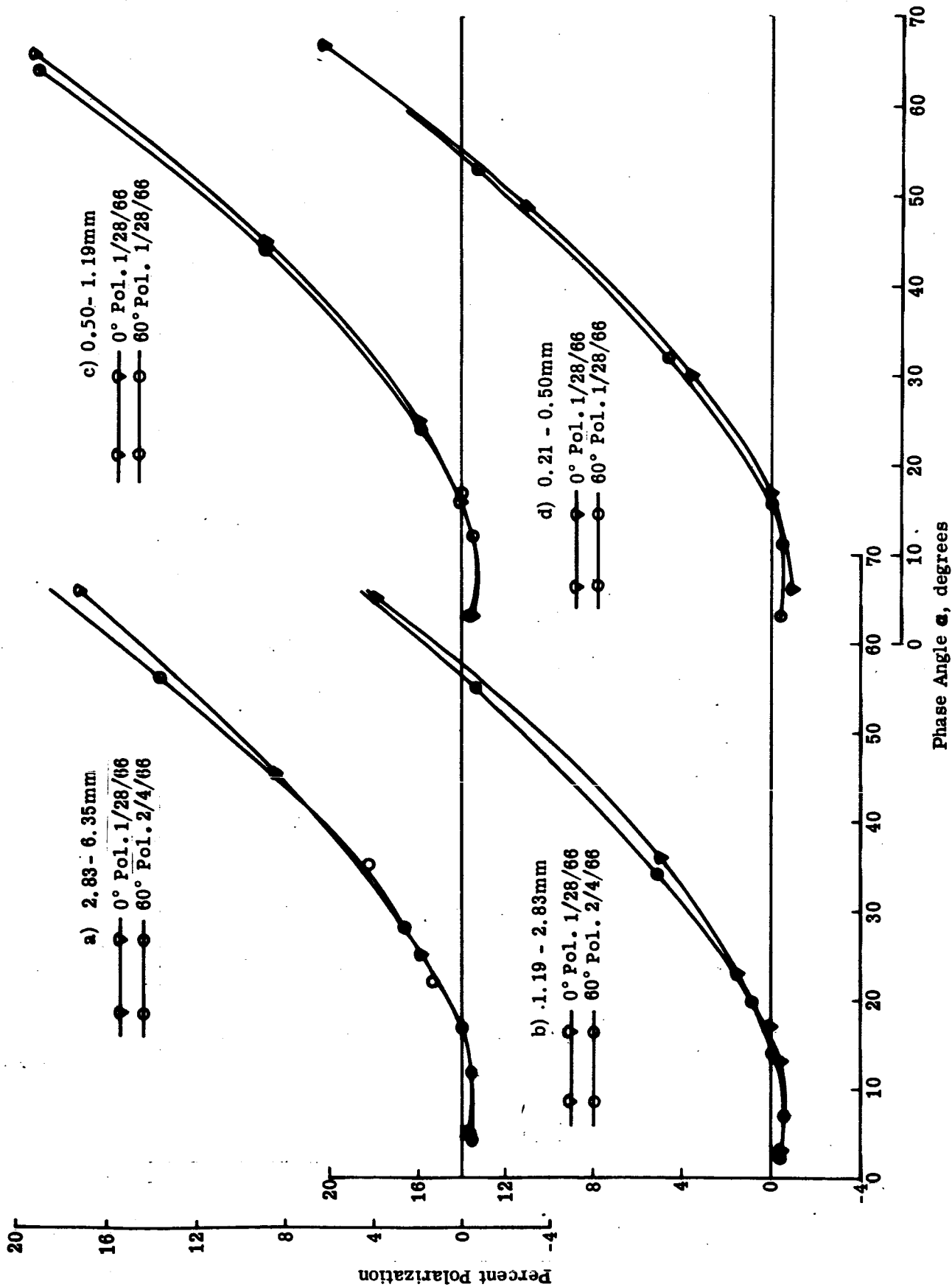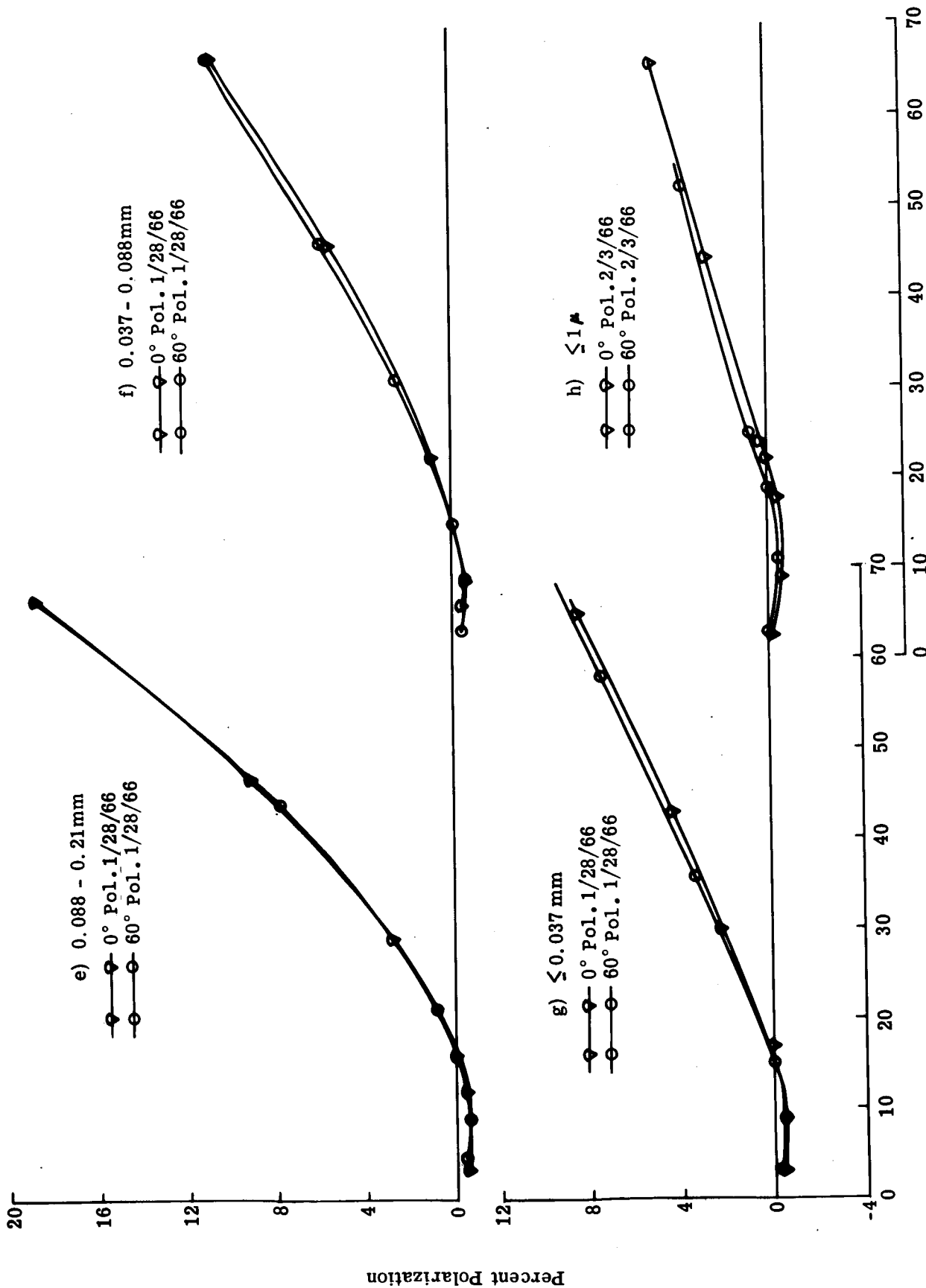
Fig. 52 Furnace Slag No. 4: Simulated Lunar Longitude Effects on Percent Polarization for Largest Particles (Uncorrected for Instrumental Effects)

Fig. 53 Furnace Slag No. 4: Simulated Lunar Longitude Effects on Percent Polarization for Smallest Particles (Uncorrected for Instrumental Effects)
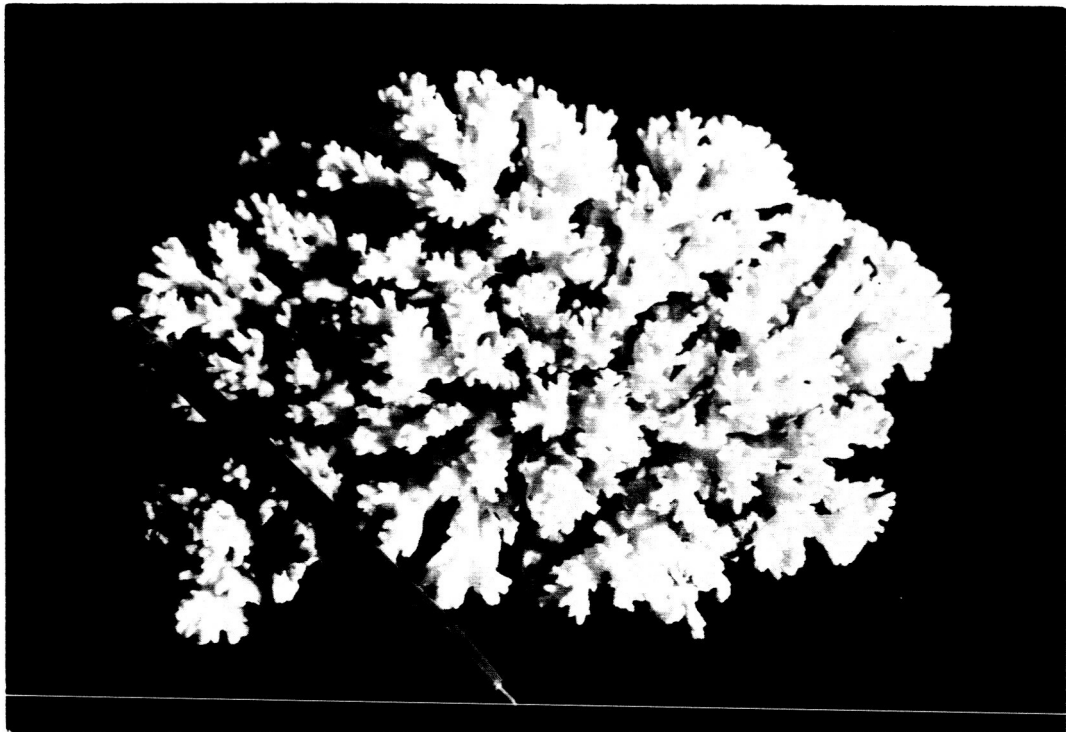
Fig. 54   Coral No. 1 (Unpulverized)
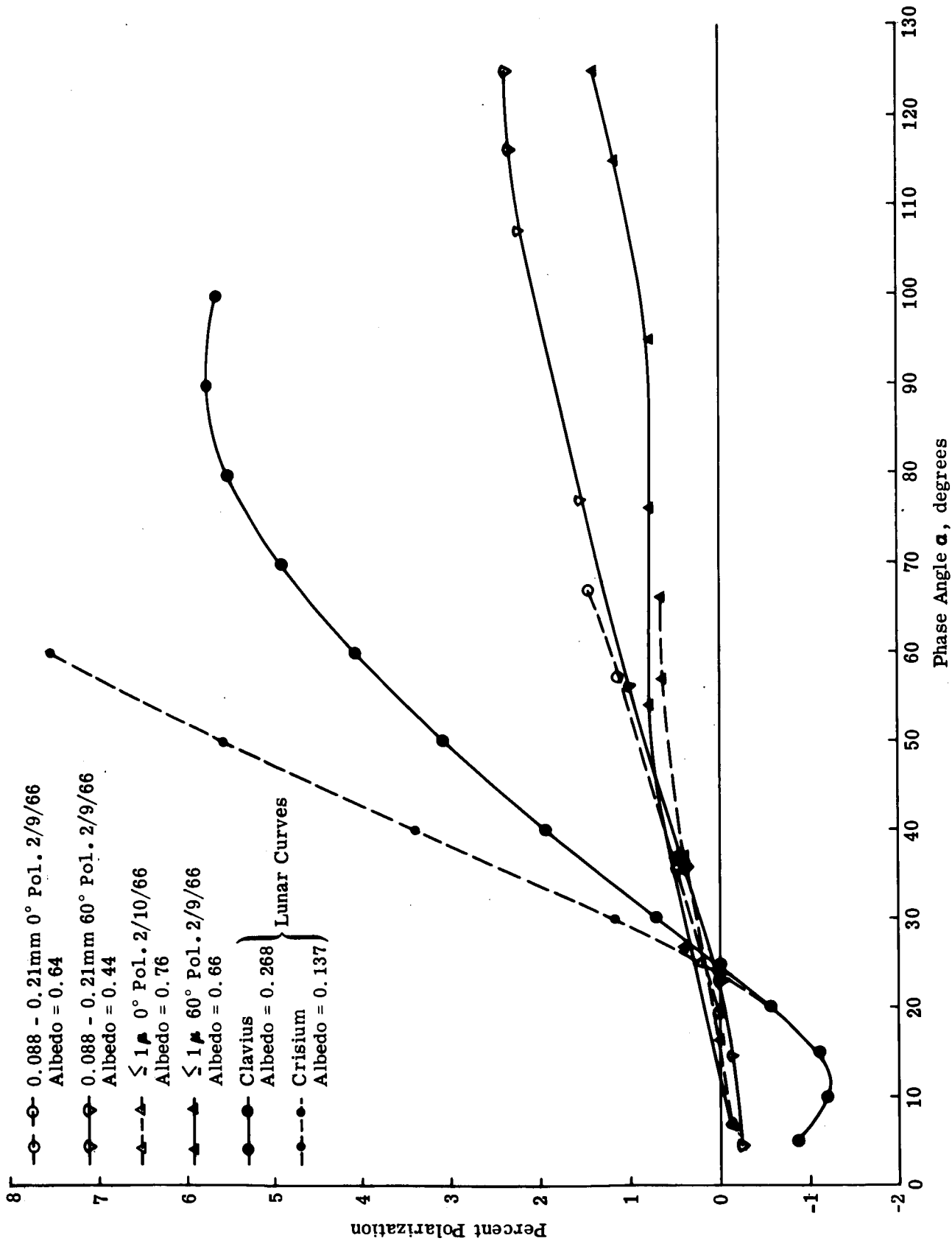
Fig. 55 Coral No. 1: Percent Polarization as a Function of Particle Size (Uncorrected for Instrumental Effects) 0° and 60° Polarimeters

Legend:

- 0.088 - 0.21mm 0° Pol. 2/9/66 Albedo = 0.64
- 0.088 - 0.21mm 60° Pol. 2/9/66 Albedo = 0.44
- ≤ 1μ 0° Pol. 2/10/66 Albedo = 0.76
- ≤ 1μ 60° Pol. 2/9/66 Albedo = 0.66
- Clavius Albedo = 0.268 } Lunar Curves
- Crisium Albedo = 0.137

X-axis: Phase Angle α, degrees

Y-axis: Percent Polarization
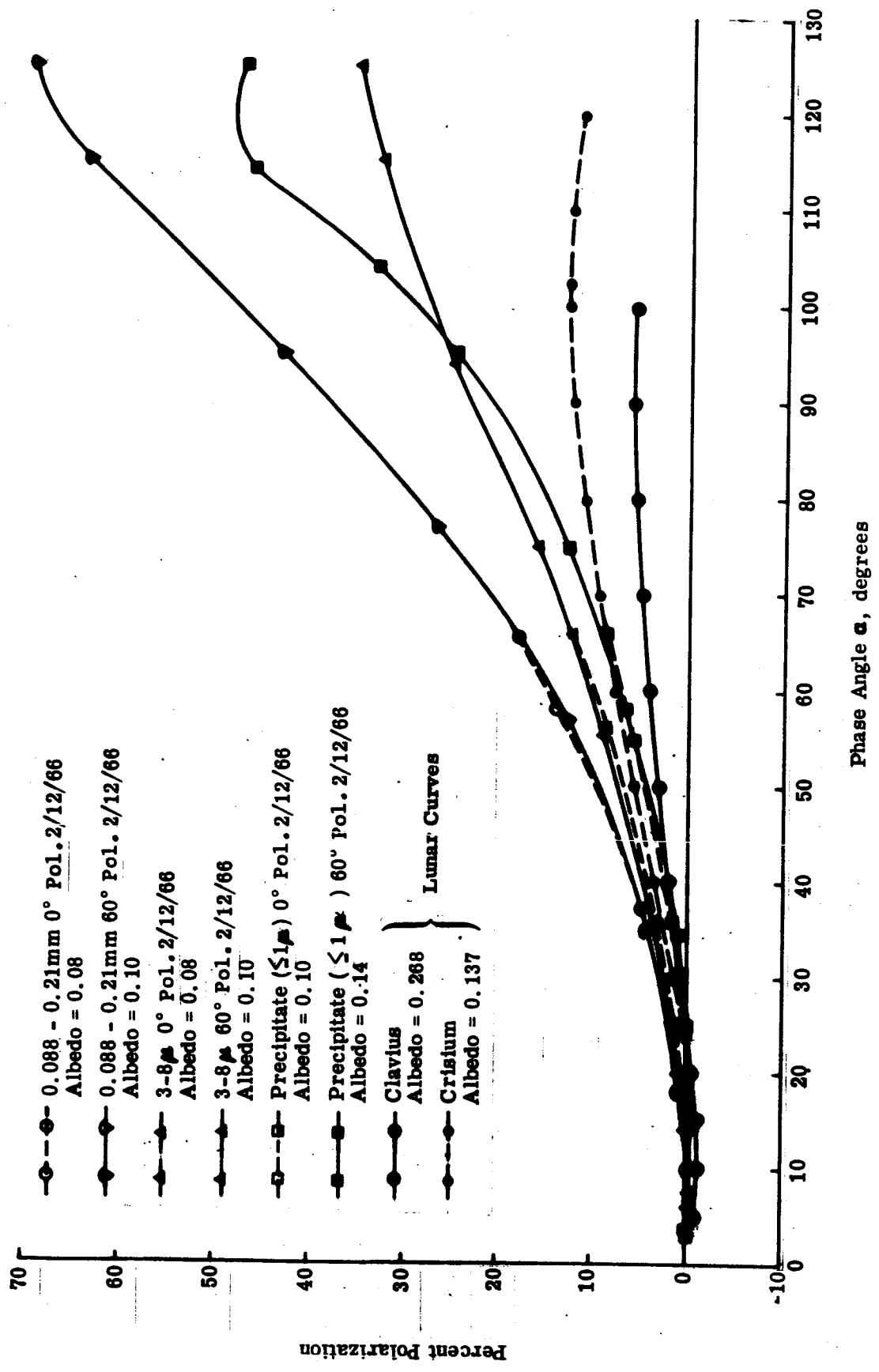
Fig. 56 Silver Chloride (Exposed to Light for Darkening): Percent Polarization as a Function of Particle Size (Uncorrected for Instrumental Effects) 0° and 60° Polarimeters

Phase Angle α, degrees
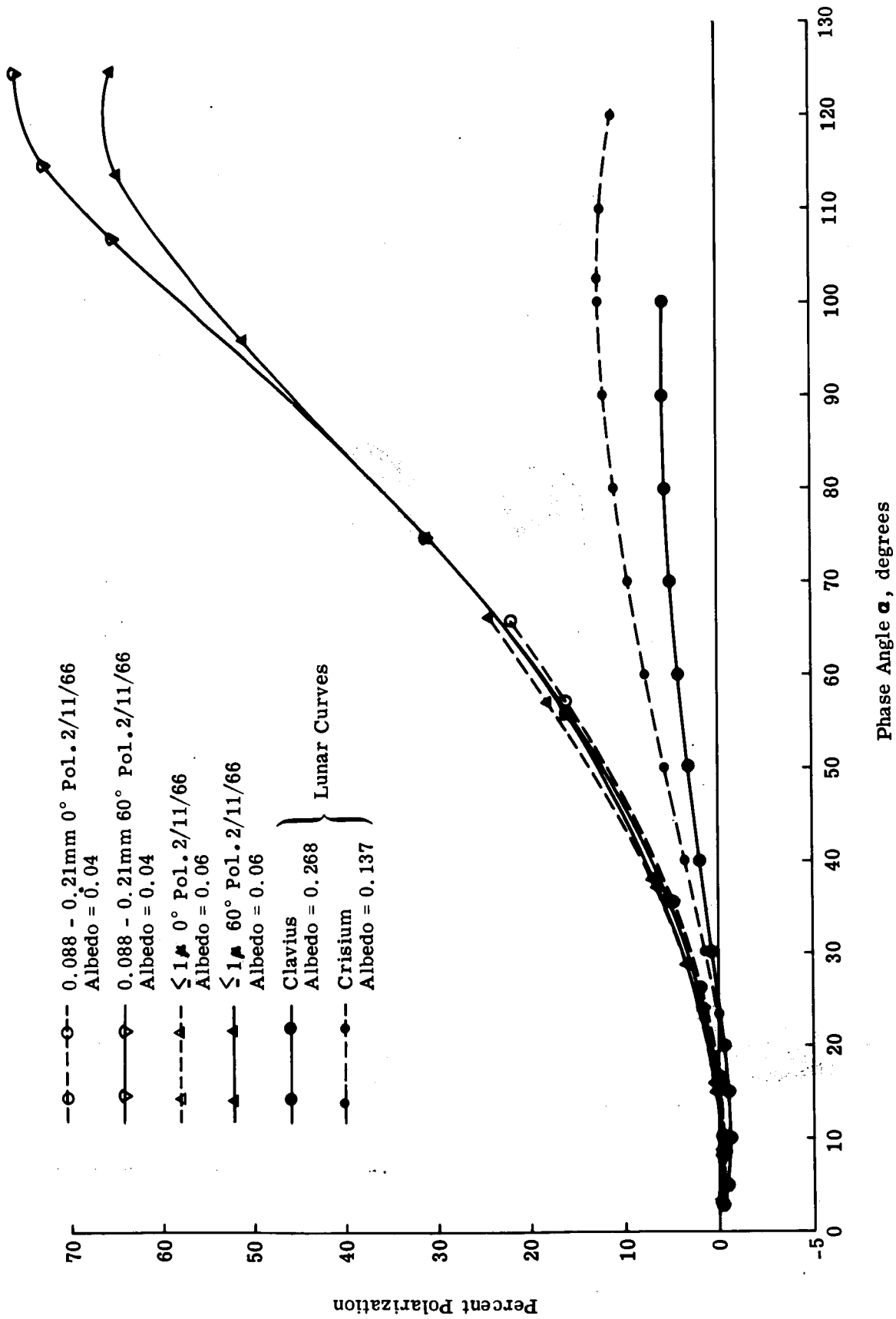
Fig. 57 Copper Oxide: Percent Polarization as a Function of Particle
Size (Uncorrected for Instrumental Effects) 0° and 60°
Polarimeters

Percent Polarization
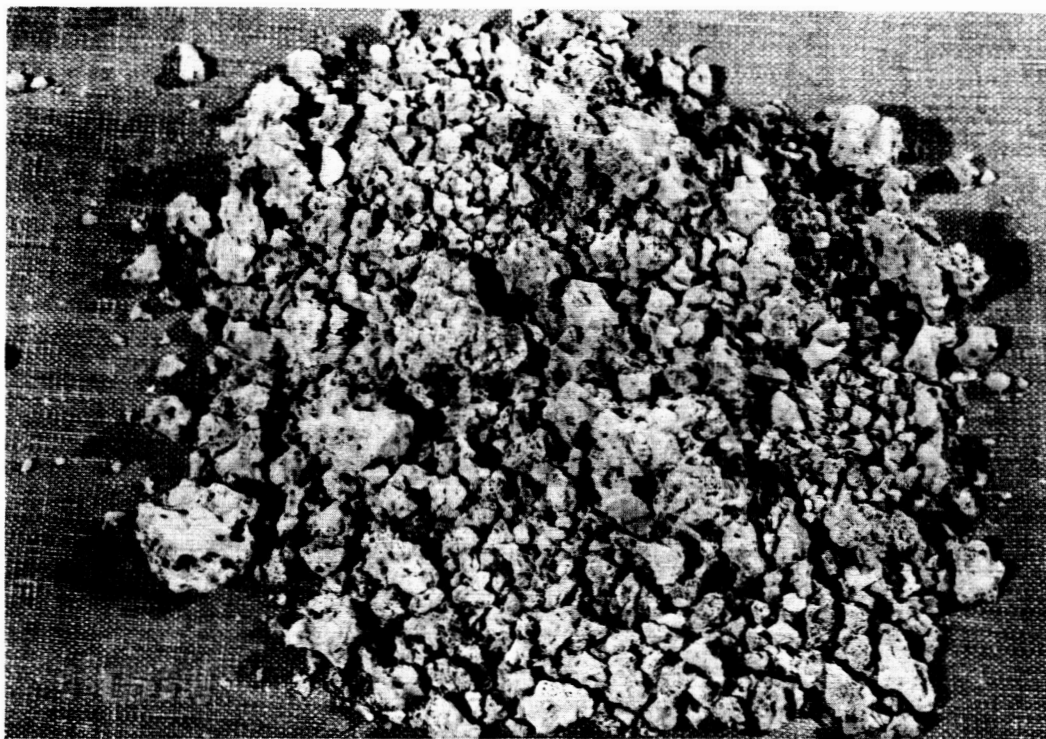
Fig. 58   Volcanic Ash No. 1 (Unpulverized)

Percent Polarization

Phase Angle **α**, degrees

0.088 - 0.21 mm 0° Pol. 2/7/66
Albedo = 0.16

0.088 - 0.21 mm 60° Pol. 2/7/66
Albedo = 0.14

≤1 μ 0° Pol.2/8/66
Albedo = 0.19

≤1 μ 60° Pol. 2/8/66
Albedo = 0.16

Clavius
Albedo = 0.268

Crisium
Albedo = 0.137
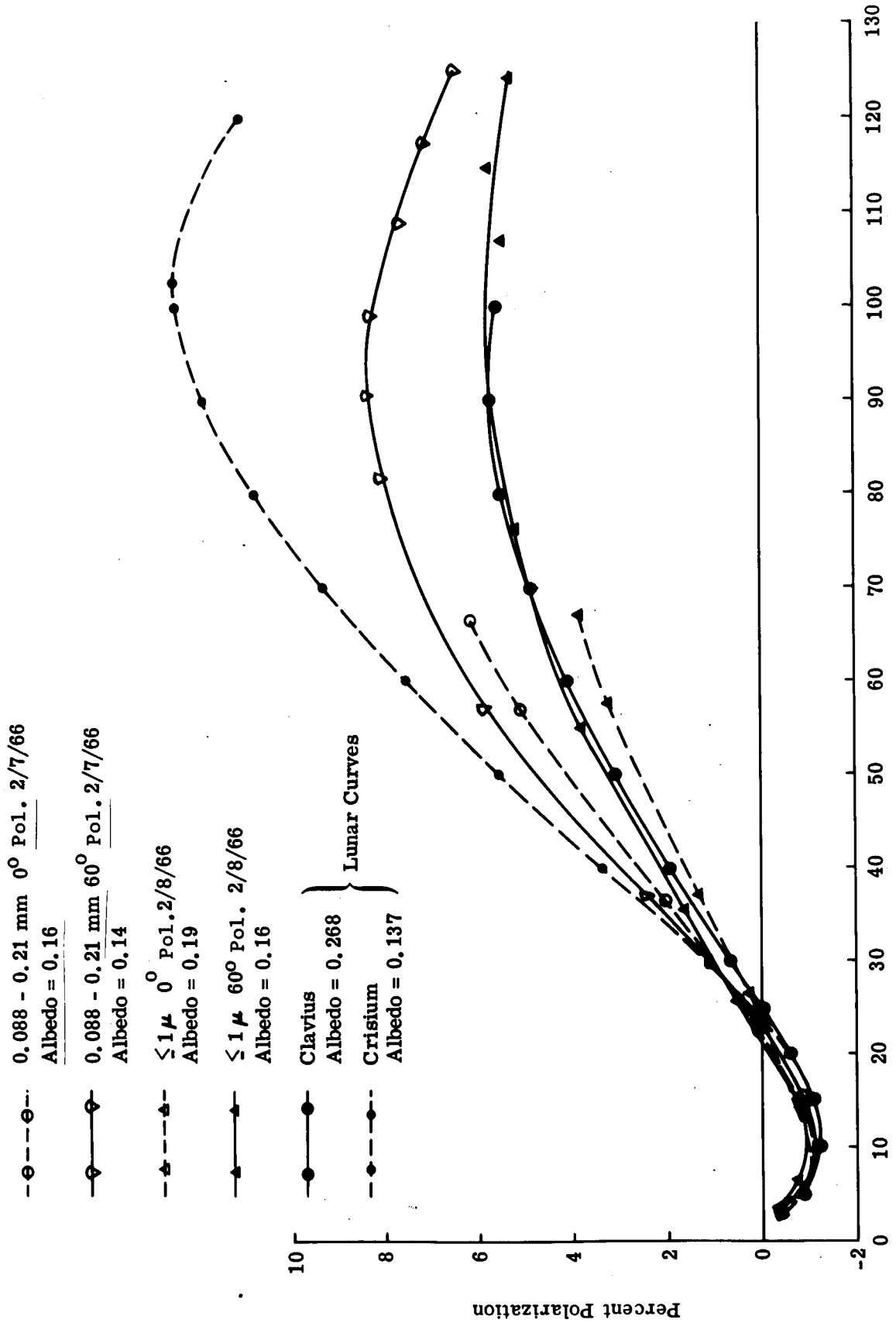
Lunar Curves

Fig. 59 Volcanic Ash No. 1: Percent Polarization as a Function of
Particle Size (Uncorrected for Instrumental Effects)
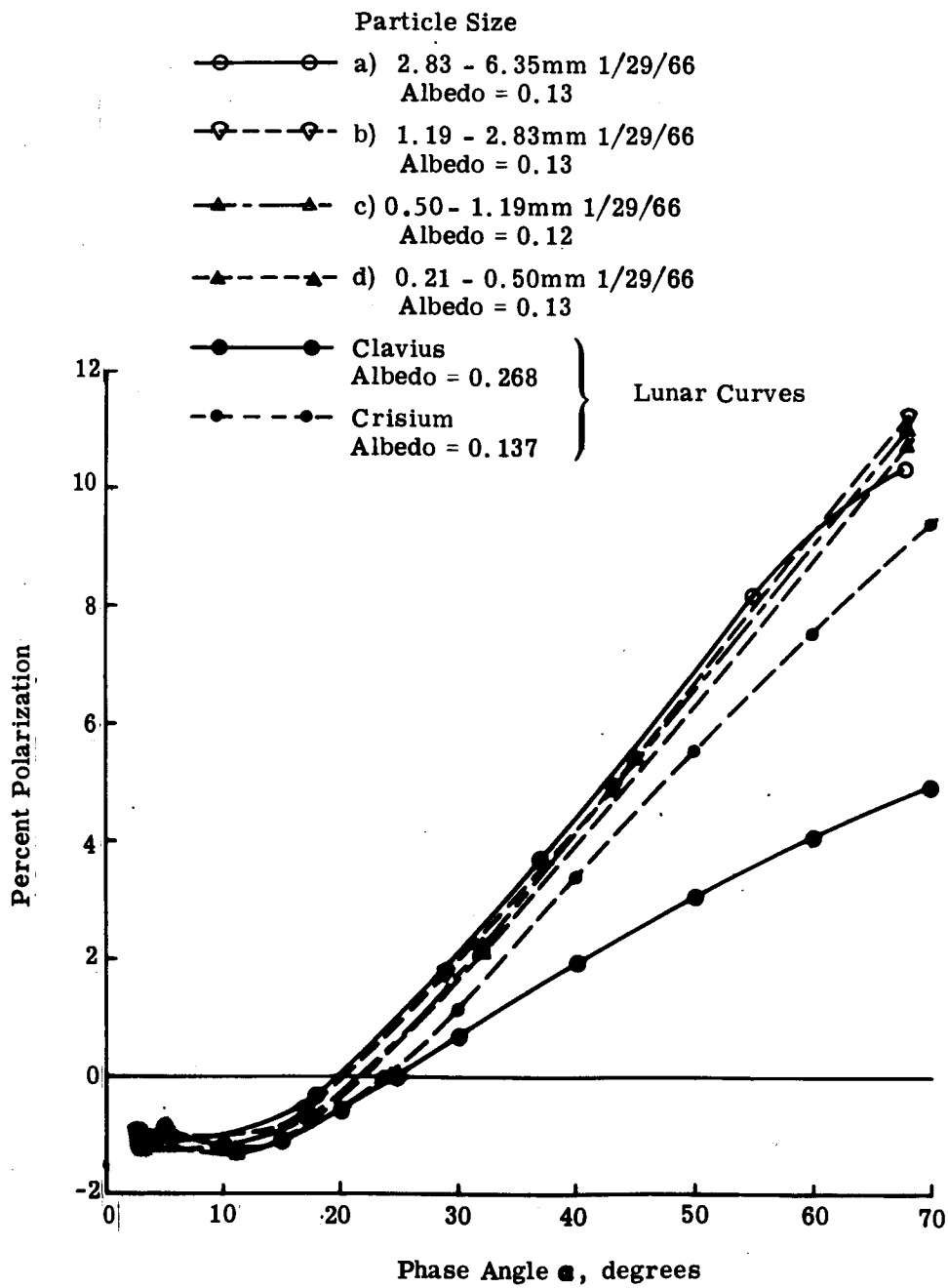0° and 60° Polarimeters

104
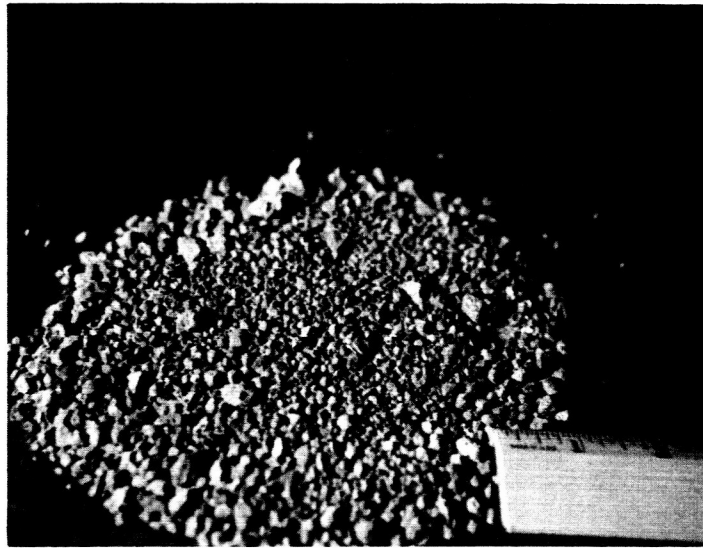
Fig. 60 Vesuvius Cinders (6/1/65)
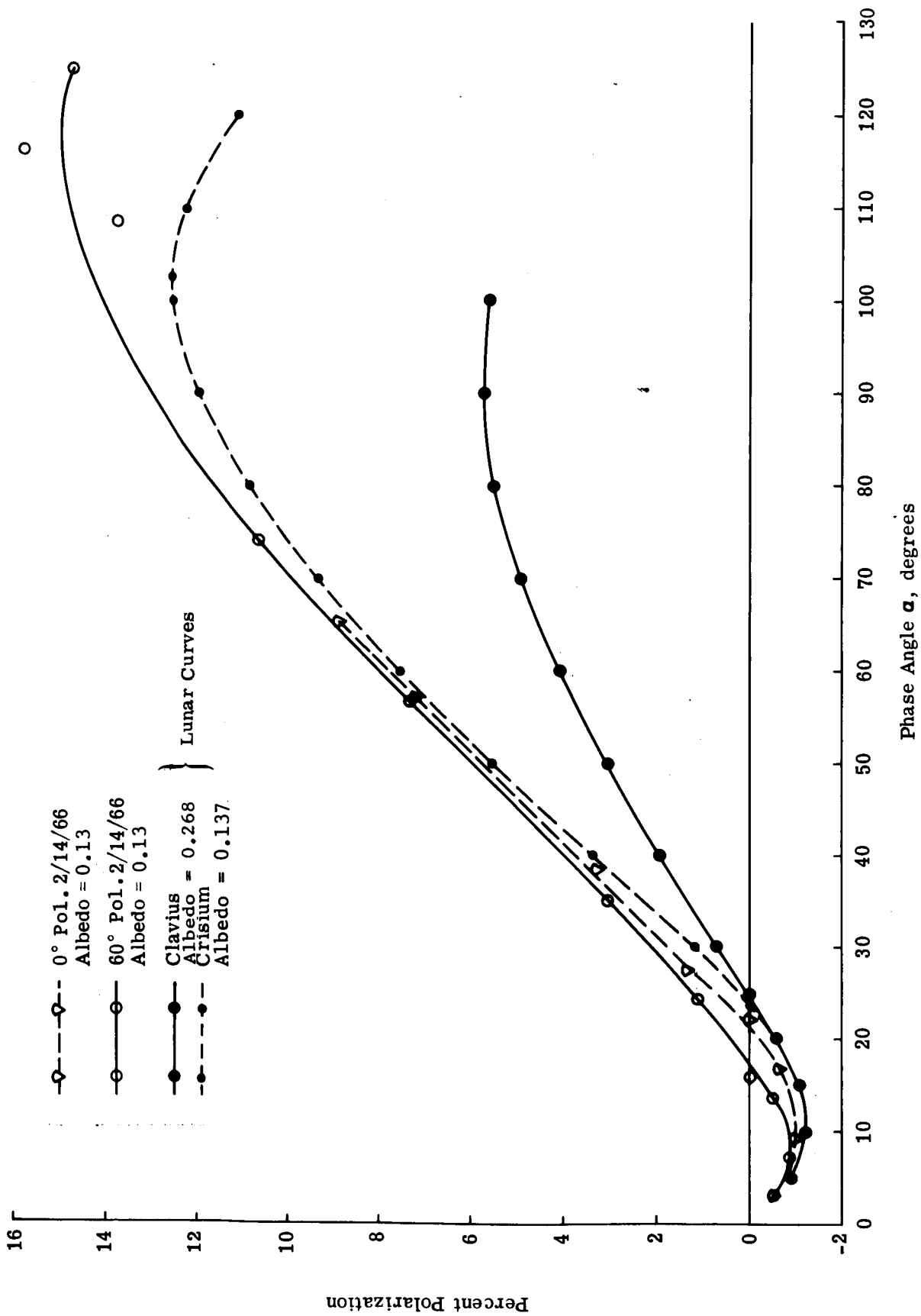
Fig. 61 Vesuvius Cinders (6/1/65): Percent Polarization - 60°
Polarimeter
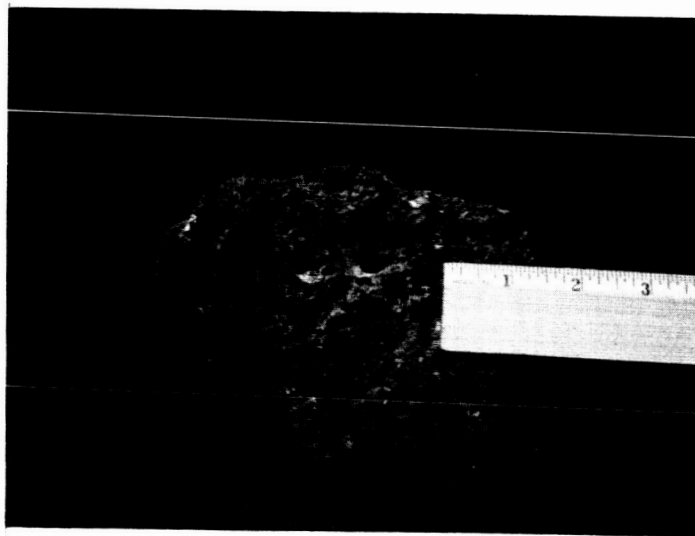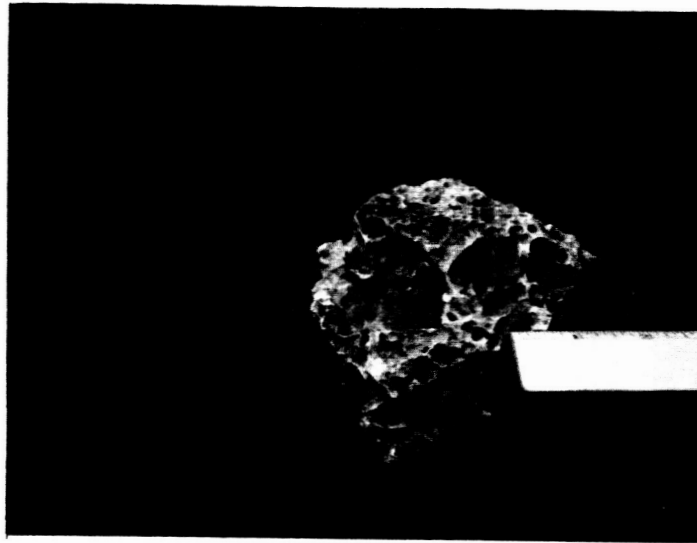
Fig. 62 Furnace Slags (Obtained at NASA/MSC 3/16/65)
Upper - Sponge-like; Lower - Rusty

107
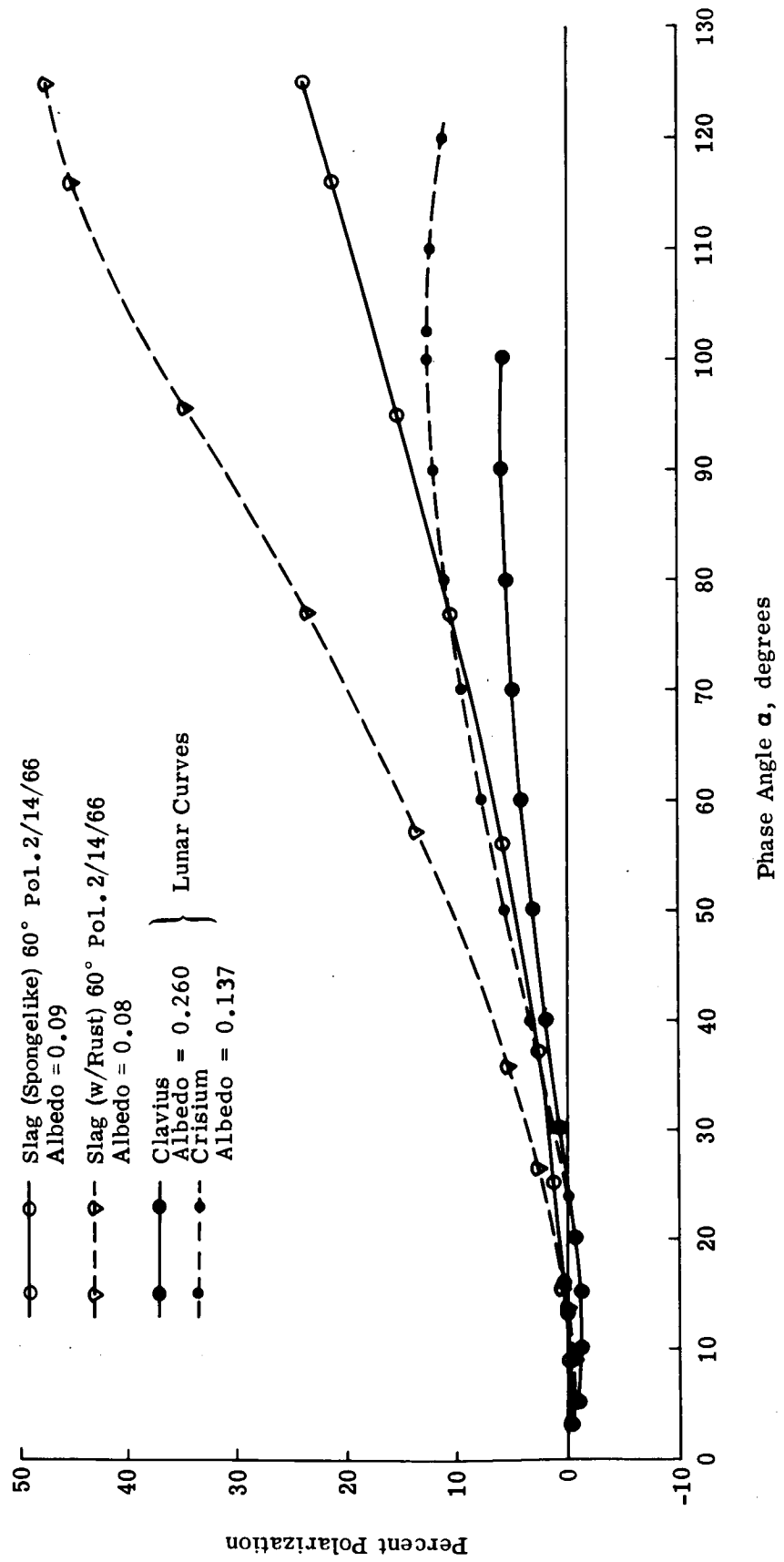
Fig. 63 Furnace Slags (Obtained at NASA/MSC 3/16/65): Percent Polarization - 60° Polarimeter
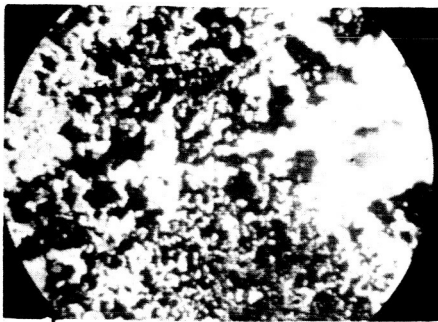
a) and b) Ashes of Vesuvius April 14, 1908
Lyot Configuration - Thesis p. 120
Curve E; Albedo = 0.166
(Sample Courtesy A. Dollfus)
25μ/div   (2-10-66)   63μ/div   (2-10-66)
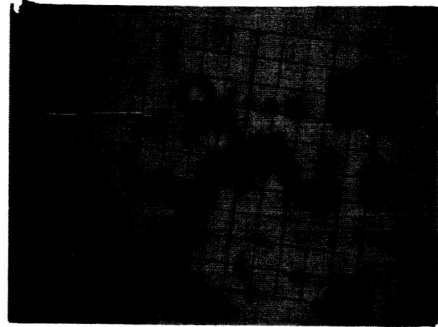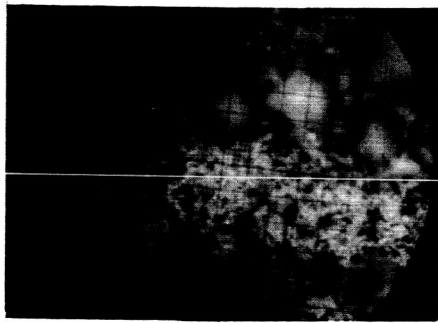
c) and d) Copper Oxide (Various Sizes)
25μ/div   (2-10-66)   25μ/div   (2-10-66)
(Bright Field Illumination)

e) Coral #1   ≤ 88μ   (2-10-66)
25μ/div
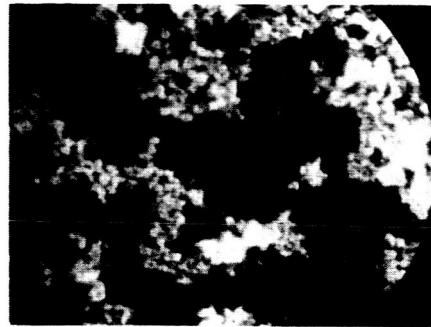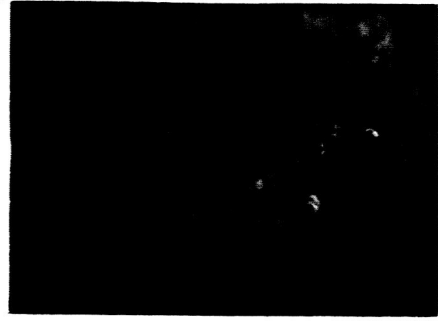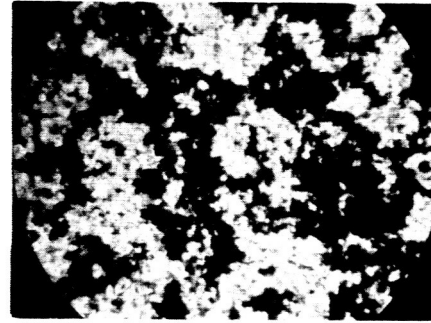
f) Volcanic Ash #1   (2-10-66)
25μ/div < 88μ

Fig. 64   Microscopic Photographs of Miscellaneous Specimens -
Lyot Volcanic Ash, Copper Oxide, Coral

109
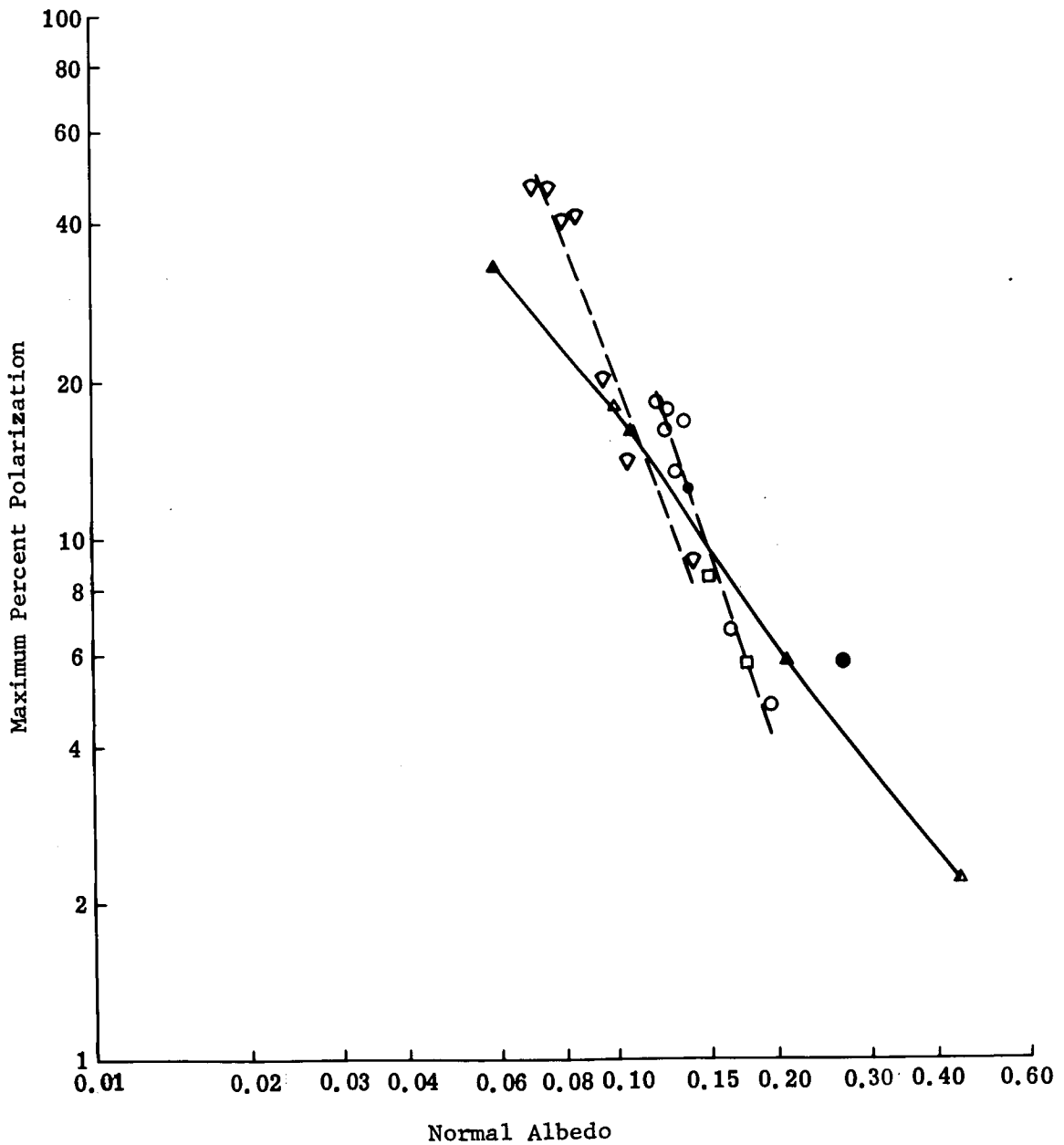
Fig. 65   Maximum Polarizations and Albedos of Various Samples
and Lunar Features

PHASE III — CONTRIVED MODELS

Purpose

Because certain of the models of Phase II duplicated the polarimetric properties of the lunar surface closely and others did not, an attempt was made to combine the photometrically and polarimetrically promising models of Phase I with the appropriate powders from Phase II sprinkled on in order to closely duplicate the polarimetric properties of a representative lunar maria, a lunar highland, and intermediate areas. This procedure was followed in order to gain an insight into the physical properties and geometries of the lunar surface.

Standard Polarimetric Curves and Data Presentation

As in Phase II, the analysis of data was made in terms of lunar observational information covering a range of values of percent polarization that served to differentiate lunar maria from highlands. As mentioned, the best detailed regional lunar polarization data appear to be that of Gehrels, Coffeen, and Owings (Ref. 4), the Russian observations appearing to be inaccurate.

Figures 66, 67, and 68 are plots of U (0.36μ), G (0.54μ), and I (0.94μ) data from Gehrels et al., for all lunar features observed. Since there were no B (0.44μ) data obtained by Gehrels et al., the U data may be compared with the B data in this report.

Referring to Fig. 66 the extreme polarization curves in U are those of Mare Imbrium and Clavius. For comparison purposes, the lowland curve for Mare Crisium is more complete than that of Mare Imbrium, since a maximum appears. Therefore, the Crisium curve was chosen as a comparison lowland curve to determine the relation of the experimentally observed maxima of Phase III to the lunar data. This reasoning applies similarly in Figs. 67 and 68 for G and I.

However, for the highland limiting curve, it appears that either Nicolai or Clavius would be appropriate. Since the Clavius curve is almost as complete as Nicolai, and appears to have less scatter for the Gehrels observed points, it was chosen. Incidentally, it can be seen that the location of the maximum on the Clavius curve moves to smaller angles as one goes from U to I or, synonomously, higher to lower polarization. This effect is not as clearly apparent for Crisium.

111

Thus, the limiting curves are those of Clavius and Mare Crisium for representative lunar highland and maria areas. In the curves to follow, a set of lunar comparison curves are presented on each of the Phase III experimental curves. For the section on Sample Preparation, the Gehrels limiting G curves are presented because they are closest to the Grumman polarimeter system in integrated visual light.

For subsequent Phase III experimental curves in B, G, and I light, the lunar G and I curves are presented for comparison on each plot. The elimination of U as a graphical comparison was done because it does not correspond to the B observations of this report, and the graphs would be unnecessarily cluttered if it were included. For a comparison to the U , one can easily refer to the curve given in Fig. 66.

The albedos given are averages of those obtained in 1956/59 and 1963/64 by Gehrels et al. This is not strictly accurate because the lunar observational data on polarization have inherently an effect due to lunar luminescence, an effect that apparently varies with variations in solar activity (Ref. 4).

Test Specimens and Sample Preparation

The specimens chosen for investigation were those polarimetrically and photometrically promising from Phase I (Ref. 19) plus an additional specimen, the Furnace Slag obtained at NASA by one of the authors (W. G. Egan) in March 1965 (Ref. 24) The samples were chosen on the basis of observations made in integrated visual light with the 60° polarimeter. The 60° polarimeter was used in the model selection as it yields the most complete polarimetric curve from negative minimum and inversion, to positive maximum in one complete run. Comparison was made to the G (0.54μ) data of Gehrels et al., on Crisium and Clavius.

In order to prepare a sample, a choice was made for the base material, and then a second choice was made for the powder overcoat. Thus, for Contrived Model No. 1 (the extra sample), the Furnace Slag obtained at NASA was chosen. It can be seen graphically (Fig. 69) that the polarization of the Furnace Slag is too high; therefore a considerably lower maximum polarization material with a suitable inversion angle was chosen (0.088 to 0.21 mm particles of Volcanic Ash No. 1, having maximum polarization 8.4 percent at 93.5° phase angle and inversion at 24.5°, (table 10) and lightly dusted over the Furnace Slag to obtain a coating. The coating was dusted onto the furnace slag as an almost particulate cloud so that it settled lightly. Modifications of the over-all model were obtained by dusting more onto it or carefully dusting some off. The resulting composite curve closely matches that of Crisium (Fig.69).

112

A similar procedure was followed for the remaining five required samples. A total of 17 variations of all samples was made before choosing the final versions.

The second sample, Contrived Model No. 2, was the original Coral No. 1 of Phase I, lightly dusted with Furnace Slag No. 4 particles < 0.037 mm which had a maximum polarization of 14 percent at 111° phase angle, and an inversion at 18.5° (Phase II). After a few tries, the resulting curve of Fig. 70 was obtained, with a close match to Clavius.

The third sample, which was not used, was pieces of Volcanic Ash No. 4 on a 0.088 to .21 mm particulate Coral No. 1 background. The resulting curve was too poor to be considered.

The fourth sample was Volcanic Ash No. 4 (maximum polarization 17 percent at 113° phase angle, (Phase I). In order to reduce the maximum, it was lightly dusted with coral particles $< 1\mu$ [maximum of > 1.4 percent at $> 125°$ with an inversion at 27.5°, (Phase II)]. The coral was found to be a powerful depolarizer, and very little was required to produce the desired result shown in Fig. 71. The resulting polarization is intermediate between Clavius and Crisium being somewhat nearer to Clavius.

Contrived Model No. 5 consisted of large pieces of Volcanic Ash No. 4 (maximum polarization 17 percent at 113° phase angle (Phase I)], which was dusted with $< 1\mu$ particles of itself. The attempt was to simulate a process that might occur on the lunar surface as a result of micrometeorite bombardment producing a thin fine dust layer. The $< 1\mu$ particles had a polarization of maximum of 4.8 percent at 105° phase angle, and an inversion at 24° (Phase II). The result of the proper combination can be seen in Fig. 72 to be near to that of Crisium.

Contrived Model No. 6 uses the other volcanic ash No. 1, with a dusting of $< 1\mu$ of itself. Volcanic Ash No. 1 has a maximum polarization of 20 percent at 115° (Phase I), whereas the $< 1\mu$ particles have a maximum of 5.8 percent at 99° phase angle, and an inversion at 25° (Phase II). The appropriate combination closely matches the polarization curve of Crisium (see Fig. 73).

With contrived Model No. 7, an attempt was made with the Furnace Slag No. 4 sample to produce a match to the lunar curves; the result was an intermediate curve shown in Fig. 74. Furnace Slag No. 4 has a maximum polarization of 39 percent at 130°

phase angle, while the $\leq 1\mu$ particles have a maximum of 9 percent at 115° and an inversion angle of 23° (Phase II). The combination produces an intermediate curve (Fig. 74).

Experiments

Percent Polarization

The percent polarization as a function of phase angle with color as a parameter for the five required and one additional sample is presented graphically in Figs. 75 through 92, and Table 12.

The data can be analyzed conveniently in terms of:

1. Wavelength and Phase Dependence of Percent Polarization

2. Effect of Color on Maximum Percent Polarization

3. Effect of Color on Normal Albedo

4. Effect of Color on Inversion Angle

5. Relationship between Normal Albedo and Maximum Percent Polarization

6. Relationship of Maximum Percent Polarization and the Corresponding Phase Angle

7. Incremental Color Changes on Percent Polarization as a Function of Sample

The correlation of the salient features on the percent polarization curves as a function of wavelength presented in Figs. 75 through 92 and Table 12 is shown graphically in Figs. 93 through 97. On all curves and in Table 12 a comparison is made to Crisium and Clavius as measured by Gehrels, et al. (Ref. 4).

Discussion of Test Results

Wavelength and Phase Dependence of Percent Polarization

Contrived Model No. 1 — Slag (sponge-like) topped with 0.088 to 0.21 mm particles of Volcanic Ash No. 1: Figures 75 (a) and 75 (b) are photographs of Contrived Model No. 1 taken

Table 12
DATA ANALYSIS

Sample	Albedo 0°	Albedo 60°	Maximum %	Maximum Angle	Corrected Minimum %**	Corrected Minimum Angle	Corrected Inversion Angle**
No. 1 Slag (Sponge-like) topped with 0.088 to 0.21 mm particles of Volcanic Ash No. 1							
B (0.48μ)	.12	.09	13.2	99°	-1.8	12°	25.0°
Visual (0.54μ)	.17	.13	11.5	114	-1.4	12	25.5
G (0.54μ)	.14	.09	10.7	106	-1.7	11	24.5
I (1.0μ)	.31	.28	4.6	100	- .9	10	25.5
No. 2 Coral No. 1 topped with Furnace Slag No. 4 particles ≤ 0.037 mm							
B	.11	.17	5.4	85	<-1.0	<-3.5	19.5
Visual	.12	.18	5.8	81	<-1.2	<-2.5	17.5
G	.14	.18	5.2	82	- .8	5	18.5
I	.13	.19	3.5	77	- .8	7.5	22.0
No. 4 Volcanic Ash No. 4 (Chunks) topped with particles of Coral ≤ 1μ							
B	.17	.19	10.2	118	-1.4	8	22.0
Visual	.19	.21	10.6	121	-1.2	9.5	22.5
G	.18	.20	9.9	123	<-1.2	<3	23.0
I	.27	.30	6.9	118	-1.0	6	25.5
No. 5 Volcanic Ash No. 4 topped with particles of itself ≤ 1μ							
B	.13	.18	13.9	95	-1.7	9	23.0
Visual	.16	.14	10.1	94	-1.4	9	23.0
G	.15	.13	12.1	94	-1.6	8.5	22.5
I	.27	.27	6.3	97	- .9	8	24.5
No. 6 Volcanic Ash No. 1 topped with particles of itself ≤ 1μ							
B	.11	.10	18.0	99	-2.1	9.5	24
Visual	.14	.14	13.2	99	-1.9	9	24
G	.12	.12	15.0	103	-1.9	10	23.5
I	.25	.25	8.0	105	<-1.0	<3	26.5
No. 7 Furnace Slag No. 4 topped with particles of itself ≤ 1μ							
B	.12	.10	12.9	121	-1.1	9.5	22.5
Visual	.12	.12	10.3	118	- .9	8.5	23.5
G	.13	.11	12.8	119	-1.1	11	24
I	.12	.12	10.2	117	- .9	11	27
Crisium U (0.36μ)	.087		22.0	100	-1.2	10	20.7
G (0.54μ)	.137*		12.5	102	-1.2	11	23.7
I (0.94μ)	.206		8.3	98	-1.2	12.5	24.3
Clavius U (0.36μ)	.175		~9.5	>98	-1.0	10	22.1
G (0.54μ)	.268*		5.8	91	-0.9	11	25.0
I (0.94μ)	.401		4.4	82	-1.1	8	22.2

*Average albedos determined in V (0.55μ) from Gehrels et al.

**Minimum Percent Polarization and Inversion Angle are corrected for +1/4 percent Residual Polarization of Polarimeters

at $0°$ and $65°$ illumination angles at $10°$ viewing angle with the same exposure to show shadowing effects. In order that the camera not block the incident illumination, it was displaced out of the plane of incidence by $10°$ to the average normal of the sample. The Furnace Slag was obtained, as mentioned previously, by one of the authors (W. G. Egan) from the astronaut training pit at NASA/MSC. The sample was selected in March 1965 as representative of the lunar surface, as well as could be determined, from a visual inspection. The necessary shadowing features for good photometry were evident, and it appeared dark enough in order to produce sufficient polarization. As modified with 0.088 to 0.21 mm particles of Volcanic Ash No. 1 used in this program, it generally matches Mare Crisium (Fig. 76. and Table 12. The integrated visual light curve V (0.54μ) shown (used for matching, see Fig. 69) is within about 1 percent of the Crisium standard G (0.54μ) curve at the upper portion, and much closer at the lower portion; however, the upper portion of the contrived model curve deviates from the general trend of Crisium. The use of the Gehrels et al. G curve to compare to the contrived model measured in integrated visual light (0.54μ) appears legitimate in terms of the effective wavelengths; however, this does not take into account the shape of the response of the system, as it washes out in the determination of the effective wavelength. Thus, it is seen that the contrived model G curve (0.54μ) closely follows the curve shape of the standard G (0.54μ) curve at larger phase angle, since perhaps the effect of the red end of the spectrum is minimized. The contrived model can be seen to produce a decrease in polarization of 6.1 percent between G and I, and hence the contribution of the I to the Visual response can be significant. At phase angles below inversion, the polarization produced by the contrived model in I (1.0μ) is greater than the standard I (0.94μ), with a higher corrected inversion angle (see Table 12). Also, at angles above inversion, the observed polarization is less than that for the lunar standard. A portion of this effect is possibly the result of the I measurements for Phase III being made at 1.0μ as contrasted to the standard at 0.94μ.

The trend of higher maximum polarization with lower albedo found in Phase II is followed in Phase III, where the albedo changes as a function of color instead of as a function of particle size as in Phase II. However, there are variations between the $0°$ and $60°$ albedos. The $0°$ albedos are consistently higher than the $60°$ albedos, and this is attributed to the method of deposition of the Volcanic Ash and the configuration of the Furnace Slag. The Volcanic Ash No. 1 did

not adhere as well to the vertical surfaces of the Furnace Slag as it did to the horizontal surfaces. Since the albedo of the Volcanic Ash No. 1 in the size range 0.088 to 0.21 mm is 0.15, compared to 0.11 for the sponge-like Slag (see Table 10), the volcanic ash increased the 0° albedo above the 60° albedo. Referring to Fig. 77 where the effect of polarimeter viewing angle is presented, it can be seen that, above the inversion angle, the 60° polarimeter measures a higher polarization than the 0° polarimeter which is consistent with the lower albedo at 60° viewing angle. The effect on the minimum and inversion angle is more complicated. However, photometrically, we have an unusual sample with a composite albedo. This will be elaborated upon subsequently in the section on Lunar Implications.

Contrived Model No. 2 — Coral No. 1 topped with Furnace Slag No. 4 particles $\leq$ 0.037 mm: Figures 78(a) and 78(b) are photographs of Contrived Model No. 2 taken at 0° and 65° illumination angles to show again the effect of shadowing. The coral was also subject to the limitations mentioned for Contrived Model No. 1, in that the particles of Furnace Slag No. 4 dusted upon it adhered to the areas where the coral was rough. Certain vertical areas where the coral was broken did not pick up much furnace slag, and, in general, vertical surfaces picked up less than horizontal surfaces.

The curves shown in Fig. 79 indicate a match (within 1.5 percent) to Clavius which is fair at phase angles below the maximum (compare Visual 0.54μ with Clavius G 0.54μ), but very poor above the maximum. The general shapes of the B, G and I curves for the sample are similar, with a displacement of the maximum toward higher polarizations from I through G to B. The Visual curve is higher than either the B, G, or I curve, contrary to the effect on Contrived Model No. 1, where the Visual is lower than the B above the inversion angle (Fig. 76). Thus, it appears that the combination of percent polarizations is not a simple additive one for color.

The trend toward higher maximum percent polarization for decreased albedo can be discerned above the experimental error (see Table 12). The effect of non-uniform distribution of the Furnace Slag No. 4 particles on the Coral No. 1 can be seen in the consistently higher albedos for the viewing angle of 60° (see Table 12). The vertical surfaces are whiter, producing a higher albedo at 60°. However, an exception occurs in that

117

the higher albedo does not clearly produce a lower polarization
at higher phase angles, (see Fig. 80). Because of the compli-
cated shadowing nature of the coral, the trend of lower polari-
zation for higher albedo is not followed.

Contrived Model No. 4 — Volcanic Ash No. 4 (chunks) topped
with particles of Coral $\leq 1\mu$: This sample is shown in Figures
81 (a) and (b). The effect of the white coral on the increase
in albedo is readily apparent.

The polarimetric results can be seen in Fig. 82 and are
intermediate between Clavius and Crisium, but nearer the former,
to which it is compared. The general curve shape is good except
that the maximum occurs at too large an angle to be comparable
to the lunar surface. The high maximum polarization of Volcanic
Ash No. 4 of 17 percent at 113° phase angle (see
Table 9), has been altered by the coral in effect reducing
the maximum to 10.6 percent and increasing the location of
the maximum to 121° in Visual light. The peculiar effect of
the coral in giving in a Visual percent polarization above the
B, G, and I curves was also noted for Contrived Model No. 2.
There is not much difference between the maximum percent polari-
zation in the B, G, or Visual curves for Model No. 4; also
the differences are small in regard to the negative minimum for
B and G. The higher minimum value for the I may possibly be
the cause of the increase in the V minimum (see Fig. 82).
For phase angles between 26 and 67 degrees, the contrived
model in I lies fairly close to the standard I curve for
Clavius, but it differs greatly above 67°.

The trend of higher maximum polarization for lower albedo
is followed, with the slight trend to higher albedos for the
60° viewing angle. This small difference in albedo is the re-
sult of the mode of sample preparation where the vertical surfaces
pick up more coral than the horizontal surfaces, resulting in a
slightly higher albedo at 60° viewing angle. Referring to
Fig. 83 it can be seen that usual albedo-polarization trend is
observed, the higher albedo produces lower polarization at
large phase angles. This shows that the coral is dominated by
the effect of the base material.

Contrived Model No. 5 — Volcanic Ash No. 4 (chunks) topped
with particles of itself $\leq 1\mu$: This sample is shown in Fig.
84 (a) and (b) at 0° and 65° illumination angles. It is to

be remarked that all photographs have been taken at the same exposure in order to permit a relative appraisal of the photometric properties from the photographs.

The polarimetric curves shown in Fig. 85, and summarized in Table 12 reveal a trend following closely the lunar data for Crisium. Contrary to the curves involving coral (either coral on a base material [Model No. 4] or another material on coral [Model No. 2]), the Visual curve lies below the G curve, as expected, possibly being the result of the lower polarization contribution of the red end of the system response. The B and G curves, following closely the shape of the standard, differ mainly in the magnitude of the maximum, B being at 13.9 percent and G at 12.1 percent, which is to be expected as the albedos are 0.13 and 0.15 respectively. The corrected inversion angles are low by about 1°. The minimum percent polarization for I is greater than Crisium by 0.3 percent. (The B and G negative polarizations are slightly low).

The albedos at 0° and 60° do not show any clear trend resulting from sample preparation. Possibly the Visual zero degree albedo is higher because the $\leq 1\mu$ powder has an albedo of 0.195 Table 10, and the chunks have an albedo of 0.14 Table 9), with the effect previously noted that the horizontal surfaces predominately viewed at 0° would have the higher albedo. An exception occurs for the B albedo measurement where the 60° reading is higher, possibly the result of a surface color of the underlying chunks of Volcanic Ash.

The highest albedo (0.27) occurs at I, and this curve has the lowest maximum percent polarization, even lower than Crisium (albedo 0.206). It is probable that, as remarked before, the observations of I in Phase III at 1.0μ, compared to the lunar standard observation at 0.94μ, would produce a lower polarization because of the higher albedos toward the infrared (Ref. 25).

Over - all, this sample is a fair match to Mare Crisium.

There appears to be an effect due to viewing angle (Fig. 86), the 60° curves being higher than the 0° curves. This is most probably the effect of the higher maximum polarization of the base material (17 percent; Table 9) as

119

compared to the topping material (4.8 percent;
Table 10). The base material would be seen more at the higher
viewing angle because the powder would not adhere to the vertical
surfaces.

Contrived Model No. 6 — Volcanic Ash No. 1 (chunks) topped
with particles of itself $\leq$ 1μ: Photographs of this sample are
shown in Figures 87 (a) and (b). This sample appears to be the
best lunar model, on the basis of these photographs alone, Fig.
87 (b) bearing a close resemblance to the photographs obtained
by the Luna 9 vehicle (Ref. 22).

Referring to Fig. 88, it is seen that the curves for B,
G and I are close matches of the shapes obtained from lunar
observations. It is rather significant that the I curve
obtained is slightly higher than the lunar I curve in the
region of negative polarization below the inversion angle. Even
though a good match in the visual region is obtained, this does
not mean that a good match would be observed in the infrared.
Since our observations are slightly redder than Gehrels et al.,
the observed effect could be indicative of what is to be expected
when the selected terrestrial samples are examined in longer
wavelength infrared. Additional evidence is obtained by referring
back to Contrived Model No. 5; the same diminished polarization
minimum is observed. This phenomena is elaborated upon in the
subsequent section on Conclusions.

The general over-all curve trend is excellent, with the
maximum percent polarization for the B being above the G,
and G being above the Visual. The I curve is the lowest,
and the trend is borne out by the relationship between the respec-
tive albedos. The Visual curve lies below the G curve since
it has a higher albedo resulting from the higher albedo toward
the red. The volcanic ash has a brownish appearance, indicating
material with a higher reflectivity in the red.

There is a slight effect of viewing angle (Fig. 89) also -
most probably the result of the higher maximum percent polari-
zation base material (20 percent; Table 9)
compared with the topping powder (5.8 percent;
Table 10). The effect is small, indicating a fairly good distri-
bution of the $\leq$ 1μ powder on the base material.

Over-all, this is the sample which gives the best match to
the lunar surface based on polarization-wavelength measurements,
remembering the infrared anomaly mentioned.

120

Contrived Model No. 7 — Furnace Slag No. 4 (2.83 to 6.35 mm) topped with ≤ 1 μ of itself: This sample is shown in Figures 90 (a) and (b).

The polarimetric results are depicted in Figure 91. The model lies between Clavius and Crisium being relatively closer to Crisium. It is unusual that the polarization in G is considerably larger than in Visual light. It is not a very good match, since the maxima for B, G, I, and Visual occur at around 120°, compared to about 100° for Crisium. There is a peculiarity in that the peak of the Visual curve lies very close to the I curve. As the albedos are the same, within experimental error, for B, G, and I, the substance appears gray.

The minima are greater than the -1.2 percent required for a match to Crisium, and the I inversion angle is too high by about 2 1/2°.

The viewing angle dependence, shown in Fig. 92, indicates that the polarization is higher for a zero degree viewing angle, above a phase angle of about 43°. This may possibly be attributed, as previously, to the viewing of the base material at the 60° viewing angle, because the base material has a higher maximum polarization (41 percent; Table 9) than the topping powder (9 percent; Table 10).

Effect of Color on Maximum Percent Polarization

In Fig. 93, a comparison of maximum percent polarization as a function of reciprocal wavelength in (microns)$^{-1}$ is presented, together with comparison curves from Gehrels et al., for Crisium and Clavius. For a perfect match, the curve for the contrived model should lie upon one of the lunar curves. Thus, Contrived Model No. 5 (Volcanic Ash No. 4 topped with ≤ 1μ particles of itself) is seen to be a good fit with No. 6 (Volcanic Ash No. 1 topped with ≤ 1μ particles of itself) being the next best fit. Contrived Model No. 2 (Coral No. 1 topped with Furnace Slag No. 4 particles ≤ 0.037 mm) appears to be a good fit to Clavius, based on this criterion alone. Contrived Models No. 1 (Slag topped with 0.088 to 0.21 mm particles of Volcanic Ash No. 1), No. 4 (Volcanic Ash No. 4 topped with particles of Coral ≤ 1μ) and No. 7 (Furnace Slag No. 4 topped with particles of itself ≤ 1μ) are poor fits to the lunar data.

It must be remembered that the maximum polarization wave-
length dependence is only one of the criteria for lunar comparison.
What is involved here is the relative maximum polarization, and
this is only one feature of the entire polarization — phase
angle curve.

Effect of Color on Albedo

The effect of color on the observed normal albedo is plotted
in Fig. 94. It is seen that Contrived Models Nos. 5 and 6 are
fair matches to Crisium, as they were in terms of maximum polari-
zation mentioned in the previous section. Contrived Models No.
2 and 7 are poor matches, even though Model No. 2 was a good
match in terms of maximum polarization. Model No. 1 is a ques-
tionable match, having a higher curve slope than Crisium. Model
No. 4 is parallel to Crisium and therefore a good color fit.

The physical property involved here is color of the sample.
If the sample is reddish or brownish, it would have a higher
albedo in the red, as does the lunar surface.

Effect of Color on Inversion Angle

It is seen in Fig. 95 that for the six samples a comparison
of the effect of color on the inversion angle shows an increase
in the inversion angle as the wavelength increases from G to
I (1/λ decreasing from 1.85 to 1.0μ-1). No such trend can
be discerned between B and G (1/λ decreasing from 2.08 to
1.85μ-1). Clavius shows an opposite trend between G and I,
with decreasing inversion angle with increasing wavelength.
However, the inversion angle increases with increasing wavelength
between U and G. For Crisium the inversion angle remains
fairly constant with increasing wavelength between G and I,
while it increases between U and G.

None of the contrived model curves from Phase III have the
same inversion angle-color dependence as the lunar standards.
Therefore this criterion cannot be used effectively to differ-
entiate between adequate simulated lunar surface models.

Essentially, the inversion angle appears to be an effect
tied up in the overall details of surface polarization.

Relationship between Albedo and Maximum Percent Polarization

In Fig. 96 is plotted a comparison of the maximum polarization and normal albedo for the six samples together with the standard curves of Clavius and Crisium. It is seen that Contrived Models No. 2 and 7 (the Coral No. 1 topped with Furnace Slag No. 4 and Furnace Slag No. 4 topped with itself) are not appropriate matches to the lunar surface. Samples 1, 4, 5 and 6 have approximately the same slope as Clavius and Crisium, while differing slightly in their zero points.

An empirical relationship has been mentioned between polarization and normal albedo by Clarke (Ref. 26), and the general trend of decreasing albedo with increasing maximum percent polarization is observed for all models which we consider to be good matches.

Relationship of Maximum Percent Polarization and the Corresponding Phase Angle

Figure 97 depicts the relationship between maximum percent polarization and the corresponding phase angle for the six Contrived Models and the lunar standards. Models No. 1, 2, 4 and 7 as well as Clavius seem to show a decrease of the position of the maximum polarization as the maximum value decreases. Models No. 5 and 6 seem to show the opposite effect while Crisium apparently shows no dependence.

It is not yet clear if the phase angle of maximum polarization is a basic parameter of the polarization curve. Possibly some additional experiments could clarify this effect.

Incremental Color Changes of Percent Polarization as a Function of Sample

A rough evaluation of the amount of polarization change for each sample as a function of color change yielded no significant results. The increment in polarization going from I to G depended upon the sample, as well as the increment going from G to B. This sample dependence on incremental color changes should be extended to allow one to determine the characteristics of a possible lunar landing area using polarization techniques.

Lunar Implications

Thus far, the emphasis has been on the polarimetric properties of the contrived models investigated. Although not required for the contract, photometric observations were made, under a Grumman supported program, in order to augment the integrated multi-disciplined approach to the definition of the lunar surface. These curves are presented in Figs. 98 through 103. A good photometric match is obtained from Contrived Model No 1, the Furnace Slag (from NASA) topped with 0.088 to 0.21 mm particles of Volcanic Ash No. 1 (see Fig. 99 [a] and [b]). A 60° viewing angle photometric run was made in order to observe not only the low phase angle opposition effect, but to observe the effect of the sample at high phase angles. Because the normal albedo was lower as a result of the composite albedo effect, a zero degree viewing angle curve was run (Fig. 98 b). The match is good on one side, but not on the other because of non-uniformities in the sample.

An equally good match was Contrived Model No. 6 (Fig. 102) which was the best polarimetric match. In descending order of match are Contrived Models 7 and 5 (Figs. 103 and 101 , but the deviations are small.

The samples utilizing coral in any form (Contrived Models No. 4 and 2) were unsatisfactory photometrically (see Figs. 100 and 99).. As a check on Contrived Model No. 2, (Coral No. 1 topped with Furnace Slag No. 4 particles), a zero degree photometric curve was run. It is seen that the zero degree viewing angle photometer produces a poor match (Fig. 99 b). The normal albedo for Contrived Model No. 2 was found to be lower because of the non-adherence of the slag to the vertical surfaces. This produced a darker sample when viewed in the normal direction relative to being viewed at 60°, thus constituting a composite albedo.

It is of interest to consider the opposition effect, relative to the normalization at 4°. A good opposition effect at 60° viewing angle is observed for Contrived Models No. 1, 6, 7, 5, 4, 2 in order of which is the same order of decreasing photometric match.

The following criteria were used to evaluate the relative merits of the six contrived models:

(1) Percent Polarization Curves, Integrated Visual
     Light

(2) Percent Polarization Curves, B, G, and I
     Light

(3) Albedo-Color Relationship (Fig. 94)

(4) Albedos at Zero and 60° Viewing Angles

(5) Albedo-Maximum Percent Polarization (Fig. 96)

(6) Maximum-Percent Polarization — Color
     Relationship (Fig. 93)

(7) Photometry

(8) Uniformity of Polarization — Zero and 60°
     Polarimeter

     Thus, using the lunar data of Gehrels et al., Models 5 and
6 are the closest matches to Mare Crisium, with Model 6 being
the overall best match. Model 1 is a fair match to Crisium.
Models 2, 4, and 7 are poor matches with Model 2 coming closest
to Clavius.

     It has been observed that the highest polarization occurs
on all samples in the B (0.48μ) where the albedo is the lowest;
the increased albedo in the infrared I (1.0μ) lowers the
polarization, similar to the lunar observations. The dependence
of the location of the polarization maximum in relation to the
maximum percent polarization cannot be determined from our data
(see Fig. 97). The inversion angle tends to higher phase angles
for decreased maximum polarization. No clear trend is seen for
the negative minimum percent polarization (see Table 12).

Conclusions

In essence, it has been shown in Phase III that a satisfactory photometric and polarimetric model may be constructed by using a large scale photometric model that produces the shadowing necessary for good photometry (Ref. 7-8) with a powder that produces the scattering and refraction properties necessary for good polarization (Ref. 24). The results obtained here are consistent with present knowledge of the lunar surface (Refs. 1, 4, 5, and 22).

The results obtained remain to be reconciled with thermal, mechanical and radar observations of the lunar surface. It appears possible that a thin dust layer of the order of 1 mm thick on top of the underlying material could explain some of the observed lunar thermal observations (Ref. 21 and J. Reichman - Private communication).

The fundamental conclusion of Phase III is that the polarization properties of the lunar surface can be produced by a suitable particulate coating of the underlying material. This particulate coating could be the result of the deterioration of the underlying material into a dust by micrometeorite bombardment, and the resulting powder adhering to the lunar surface possibly by high vacuum bonding. Thus the surface properties could yield information on the underlying matter and ultimately give information as to the choice of good landing areas for the Apollo mission.
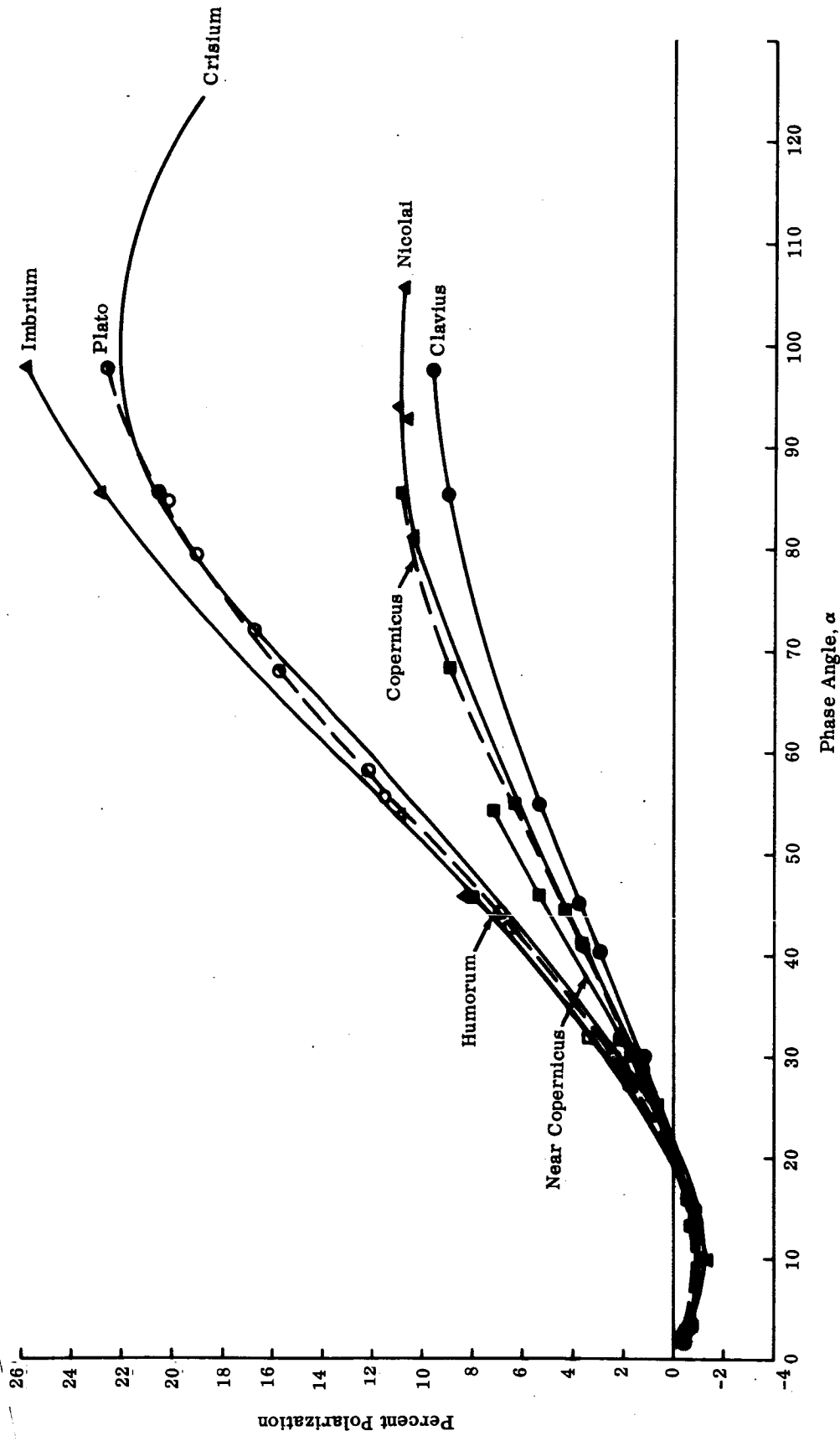
Fig. 66 Polarization Curves of the Moon -- Ultraviolet
Range, 0.36μ (Gehrels et al.)

127
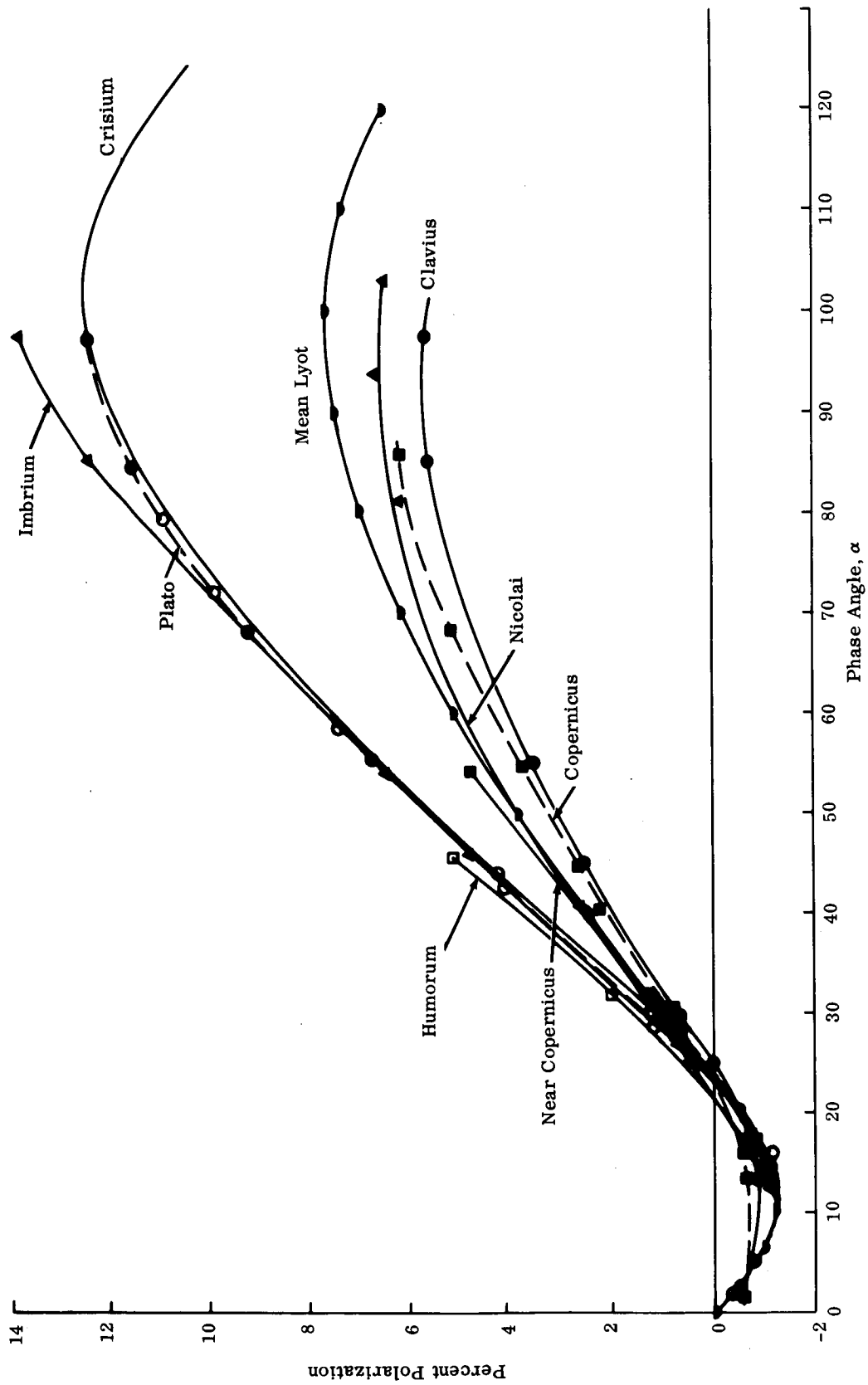
Fig. 67 Polarization Curves of the Moon -- Green Range, 0.54μ (Gehrels et al.)

128
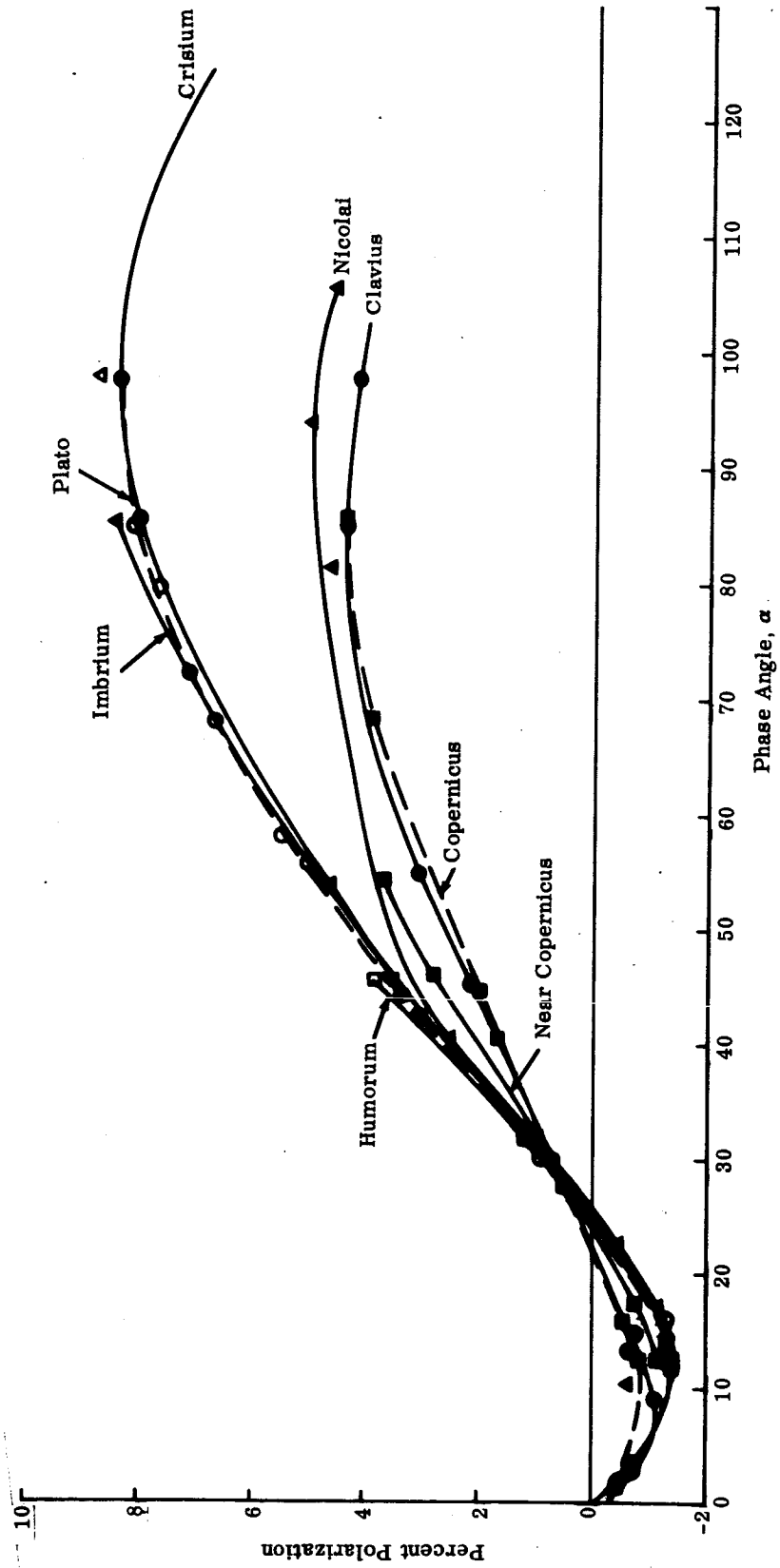
Fig. 68 Polarization Curves of the Moon -- Infrared
Range, 0.94μ (Gehrels et al.)
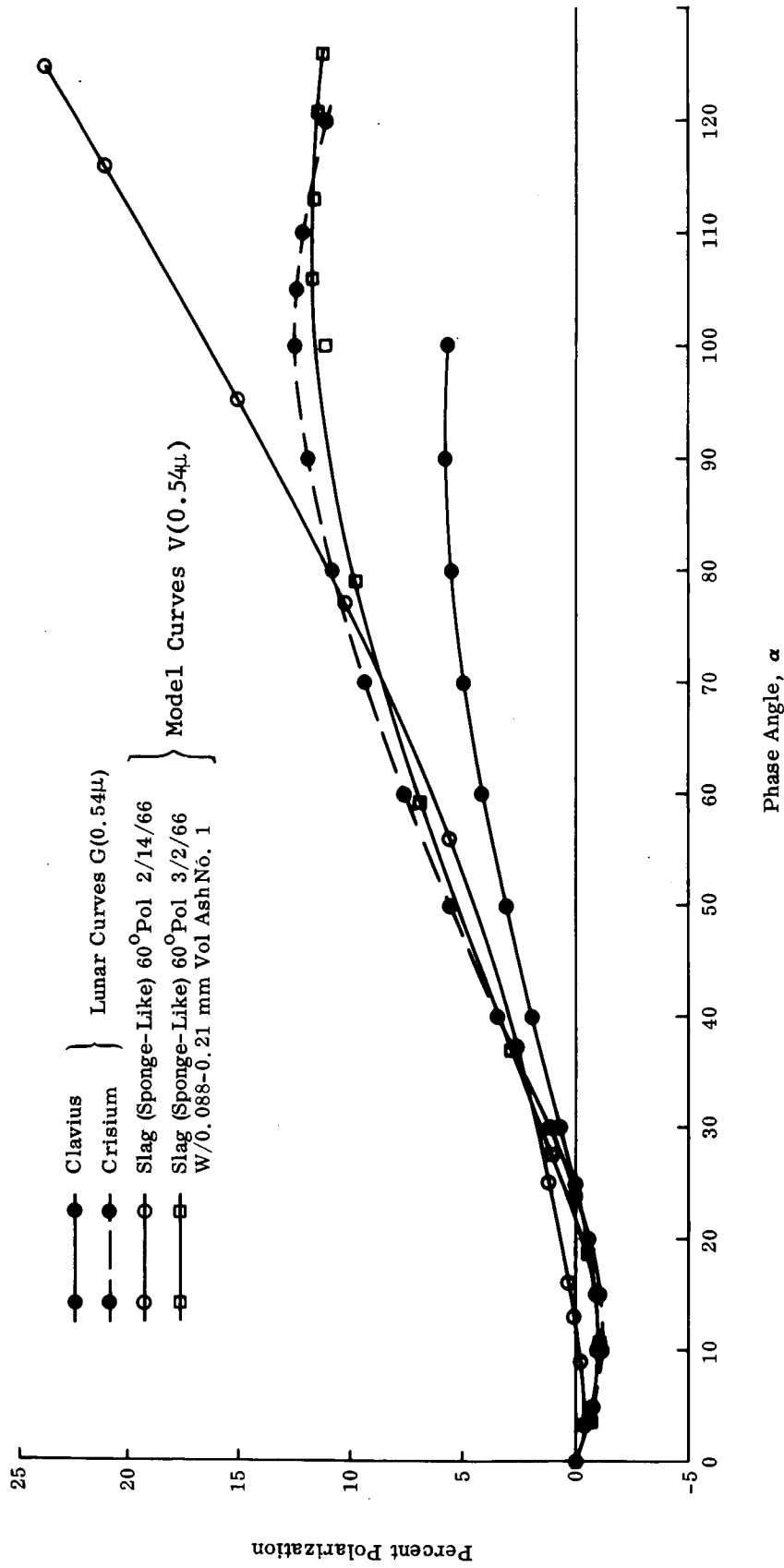
Fig. 69 Contrived Model No. 1 — Preparation of Composite Model

Percent Polarization

14
12
10
8
6
4
2
0
-2

Clavius } Lunar Curves G(0.54μ)
Crisium }
Coral No. 1 60°Pol 10/27/65
Coral No. 1 W/≤ 0.037 mm Furn Slag No. 4
60°Pol 3/3/66
} Model Curves V(0.54μ)

0 10 20 30 40 50 60 70 80 90 100 110 120

Phase Angle, α
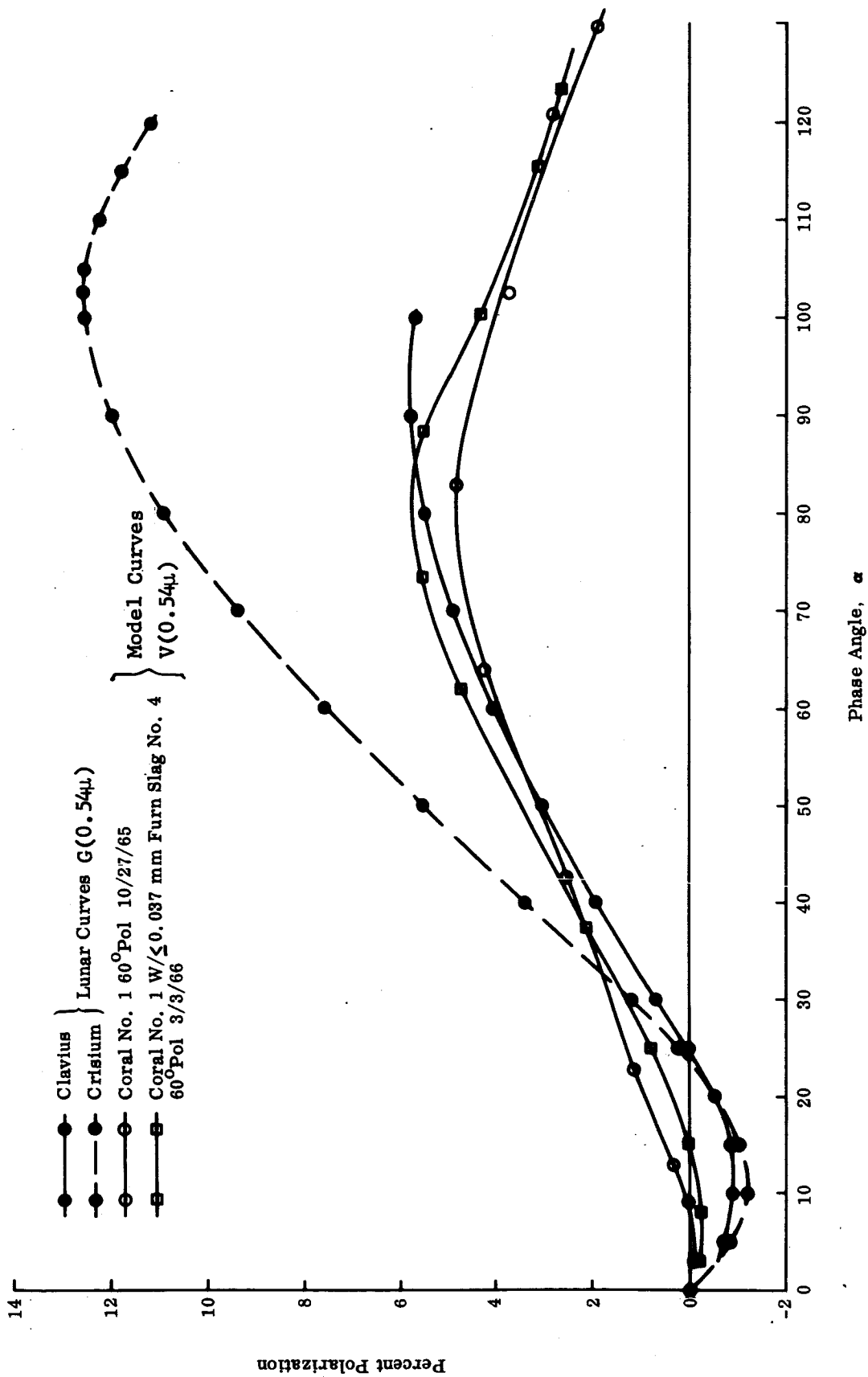
Fig. 70 Contrived Model No. 2 — Preparation of Composite Model
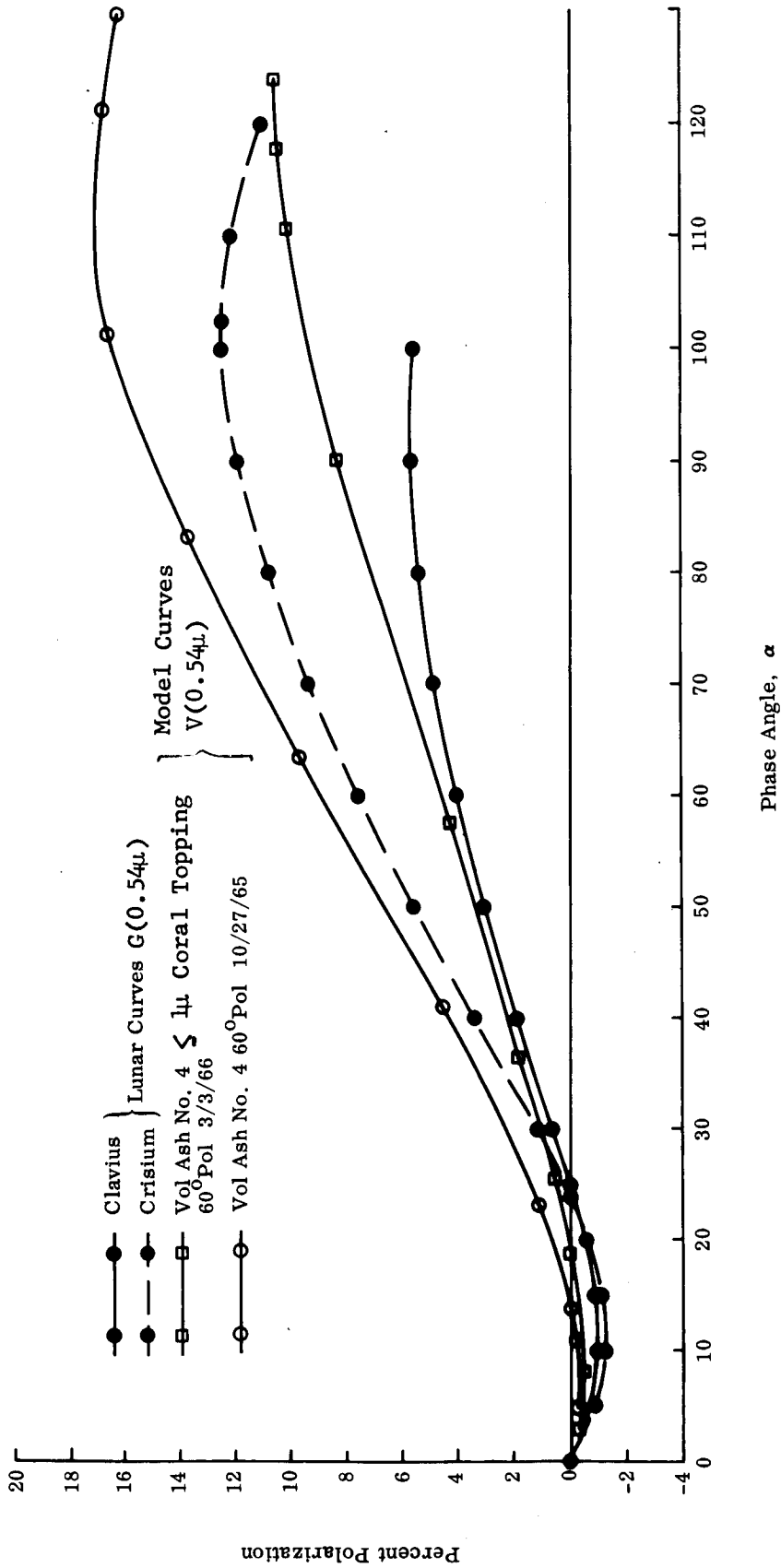
Fig. 71 Contrived Model No. 4 — Preparation of Composite Model
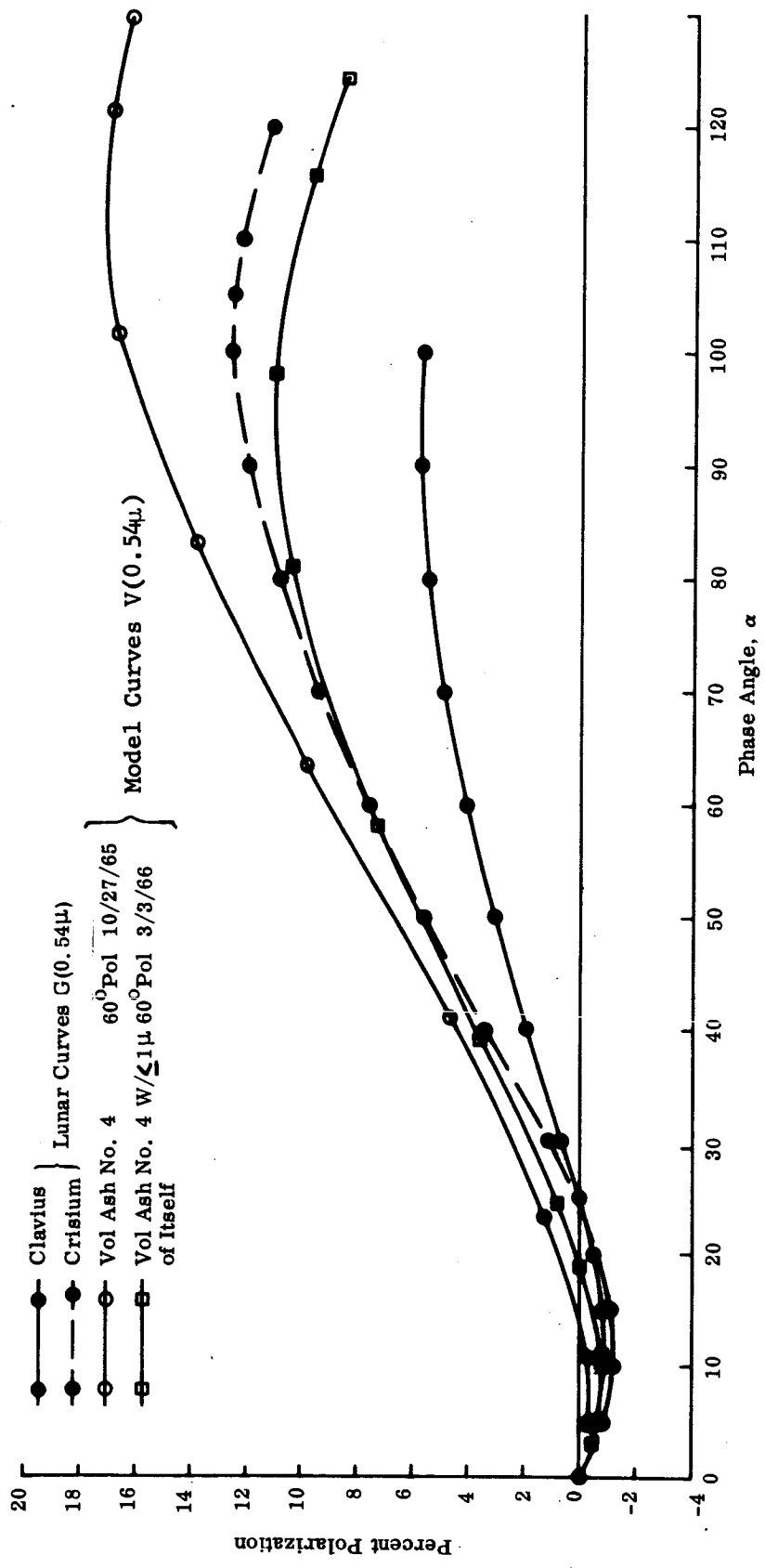
Fig. 72 Contrived Model No. 5 — Preparation of Composite Model

133
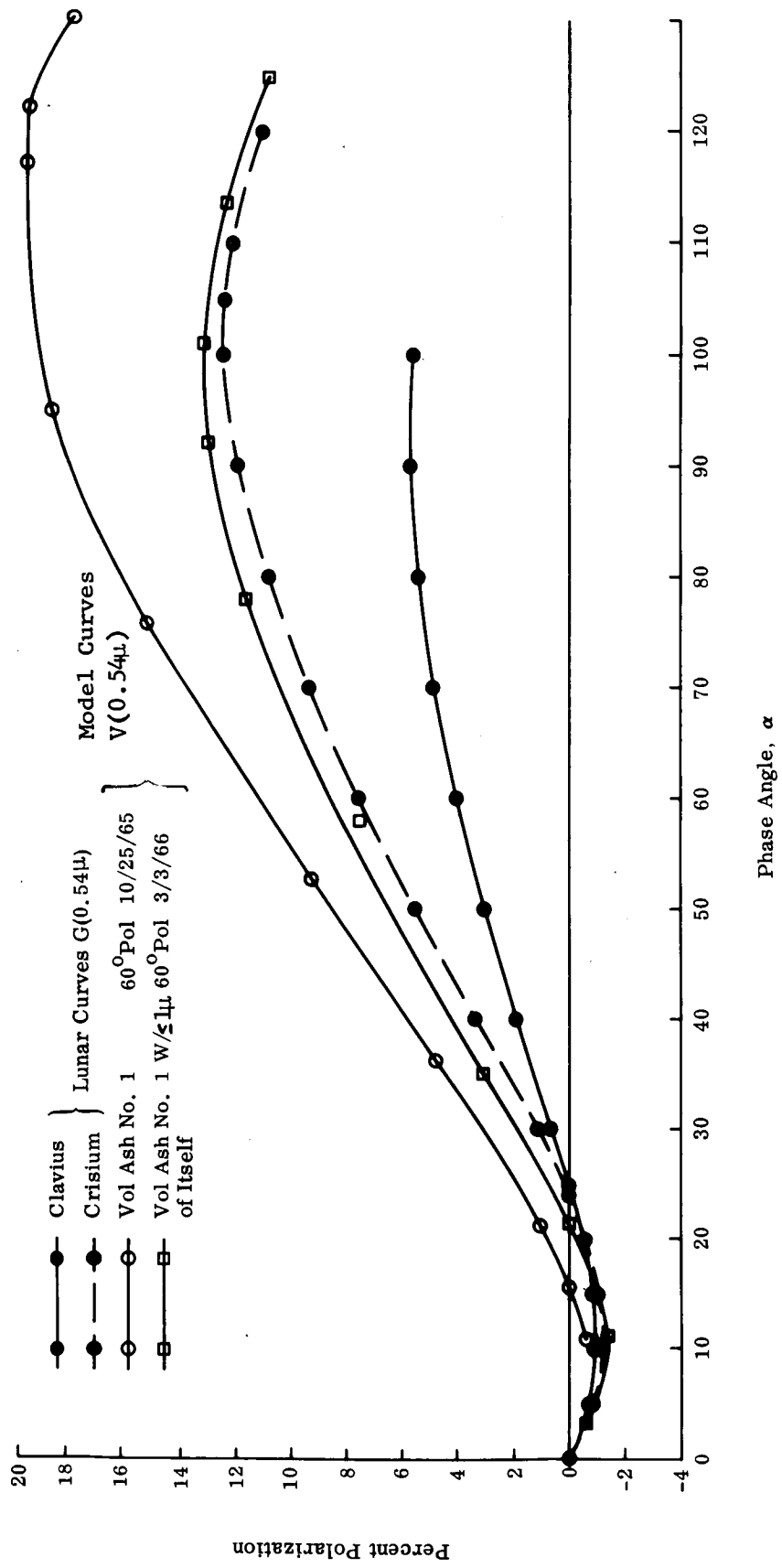
Fig. 73 Contrived Model No. 6 — Preparation of Composite Model

134
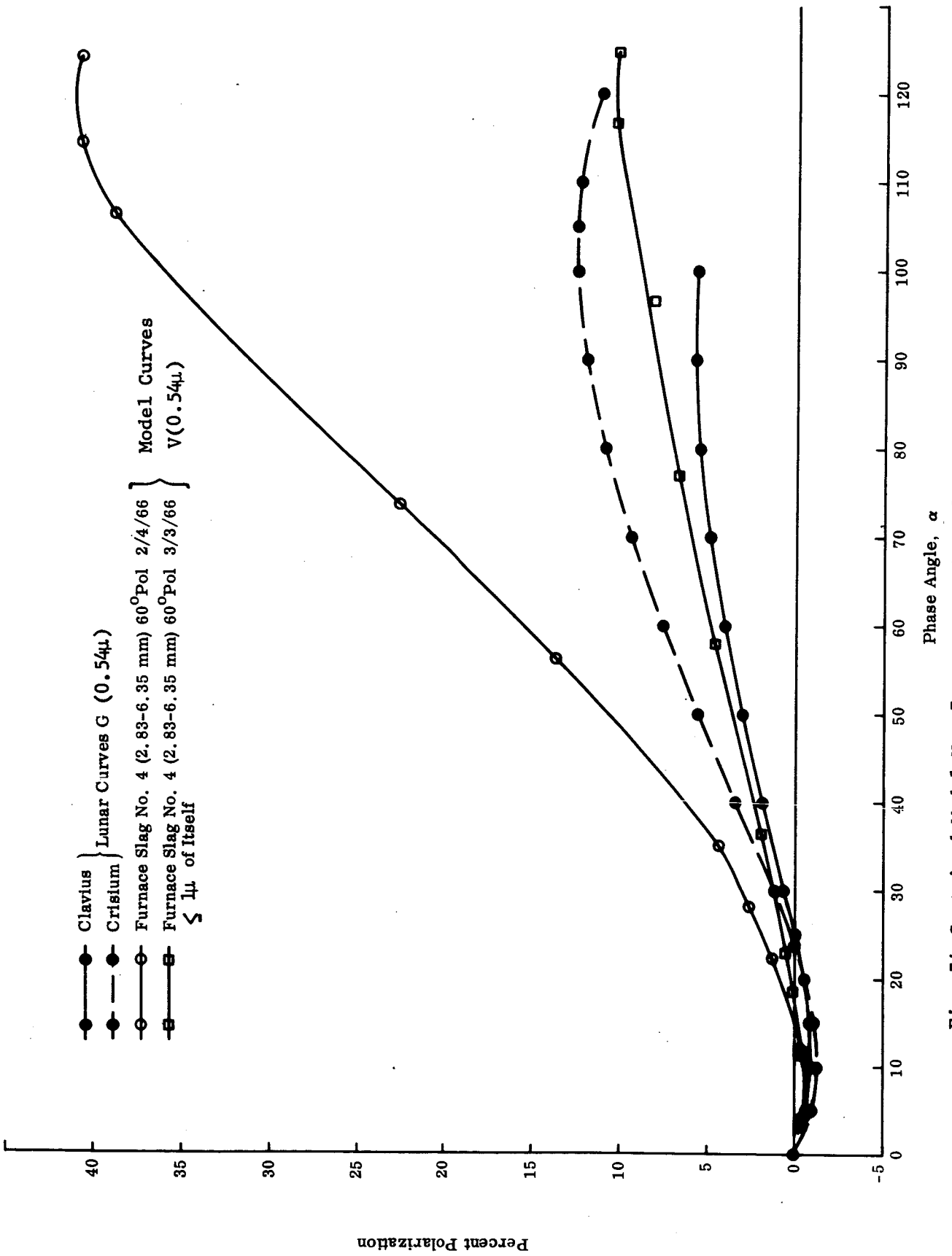
Fig. 74 Contrived Model No. 7 — Preparation of Composite Model

a) Normal Incident Illumination

b) 65° Incident Illumination

Fig. 75 Contrived Model No. 1: Furnace Slag
         (Sponge Like-NASA) Topped with 0.088
         to 0.21 mm Particles of Volcanic Ash No. 1

136
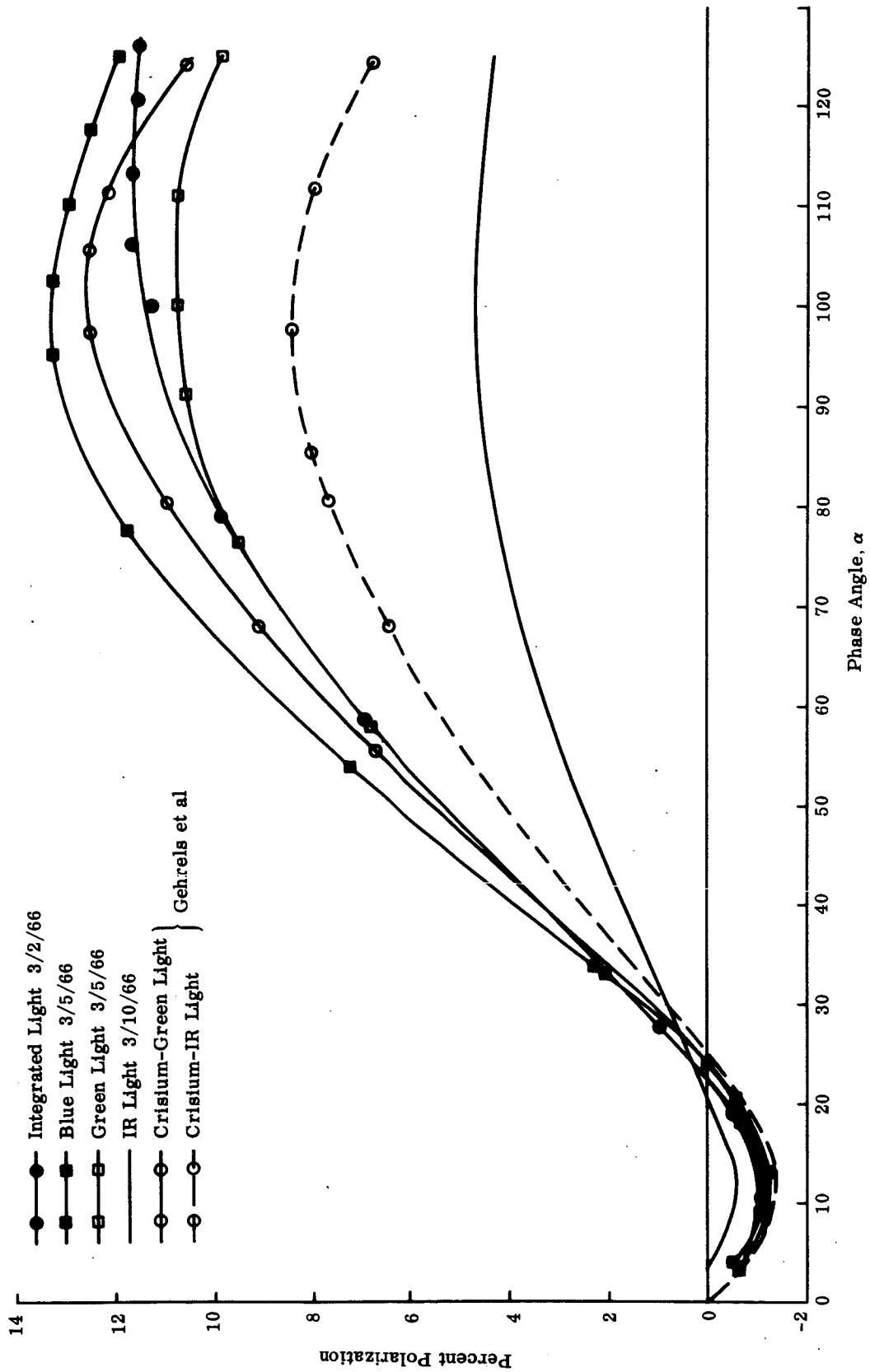
Fig. 76 Contrived Model No. 1: Percent Polarization
as a Function of Color -- 60° Polarimeter

Phase Angle, α

Percent Polarization

Integrated Light 3/2/66
Blue Light 3/5/66
Green Light 3/5/66
IR Light 3/10/66
Crisium-Green Light ⎫
Crisium-IR Light ⎬ Gehrels et al

137
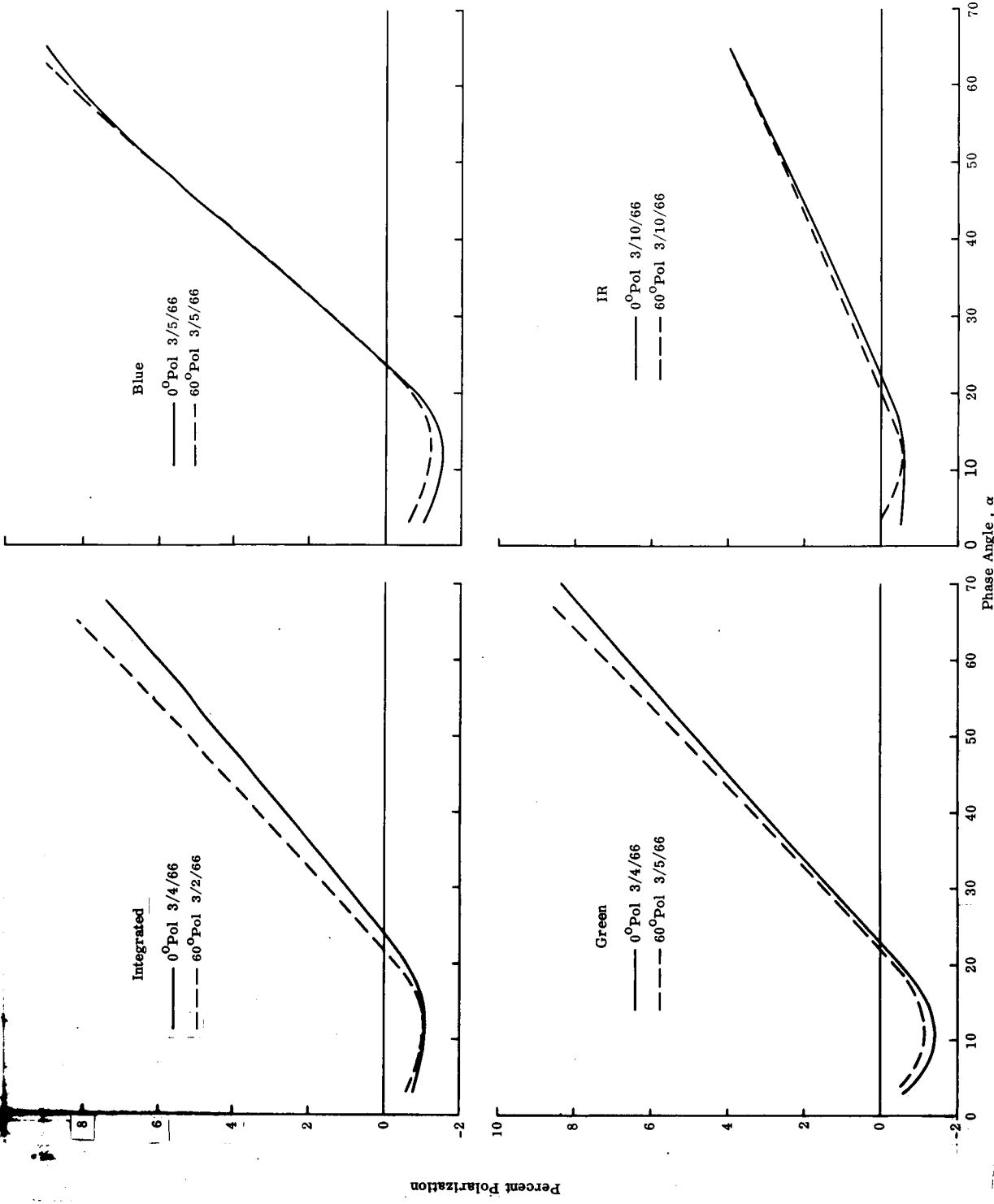
Fig. 77 Contrived Model No. 1: Simulated Lunar Longitude Effect on Percent Polarization
as a Function of Color
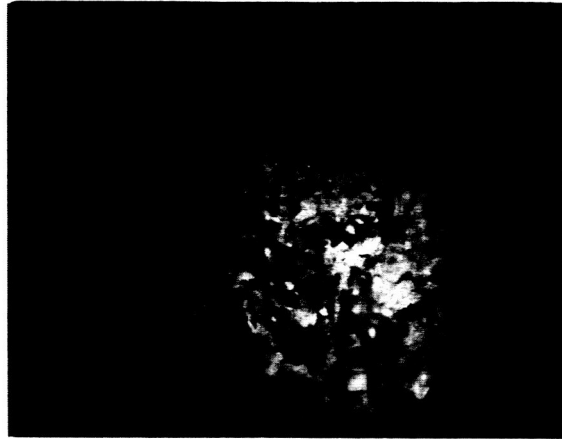
a) Normal Incident Illumination
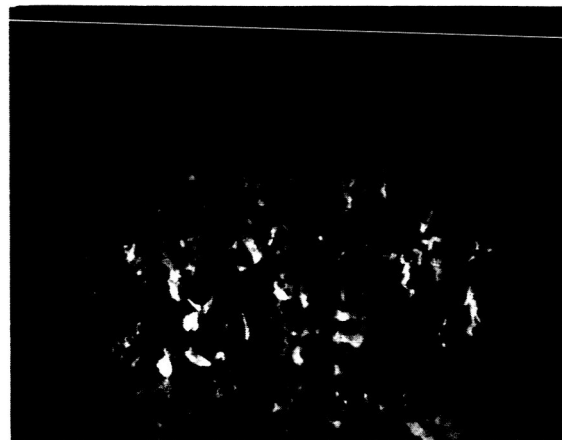
b) 65° Incident Illumination

Fig. 78 Contrived Model No. 2: Coral No. 1 Topped with
Particles of Furnace Slag No. 4 $\leq$ 0.037 mm
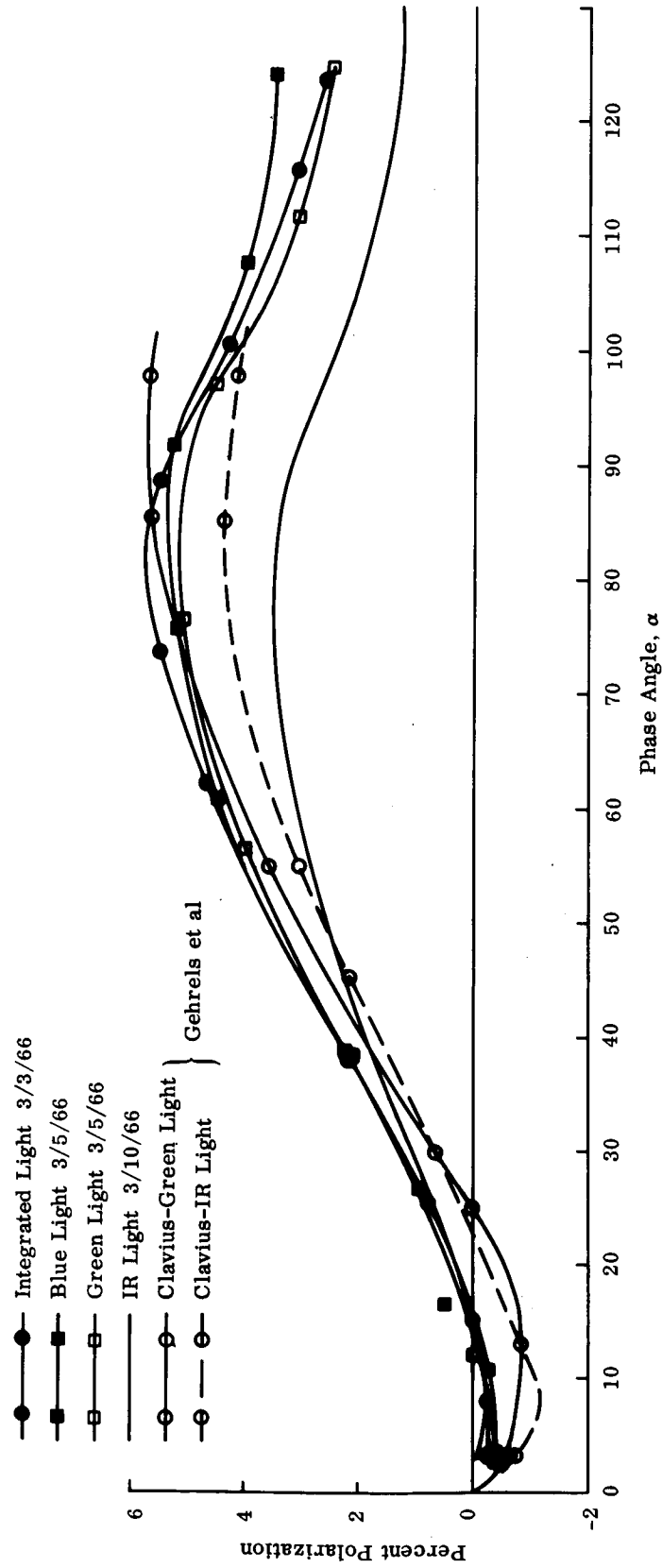
Fig. 79 Contrived Model No. 2: Percent Polarization as a Function of Color -- 60° Polarimeter

140
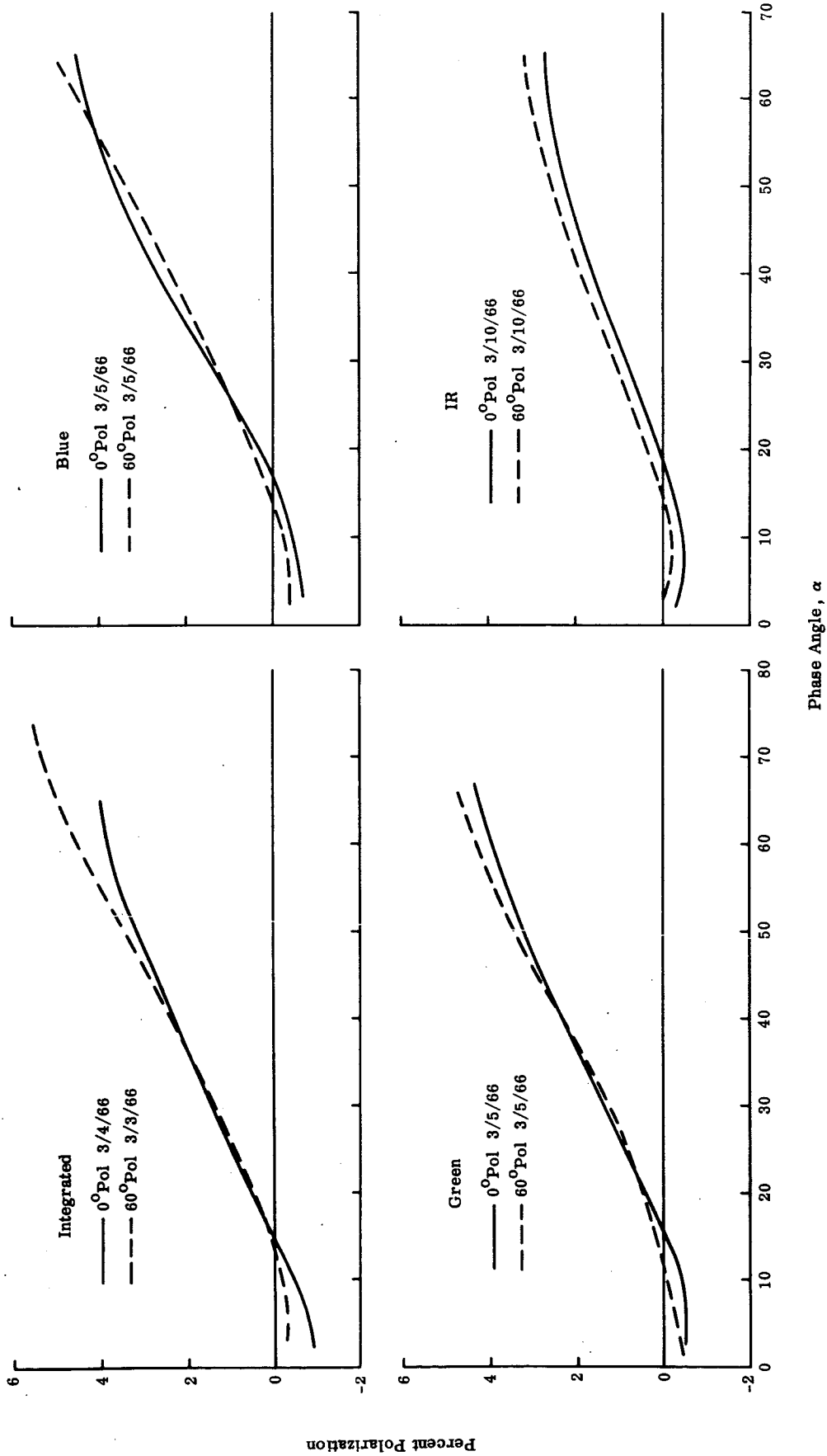
Fig. 80 Contrived Model No. 2: Simulated Lunar Longitude Effect on Percent Polarization as a Function of Color

141
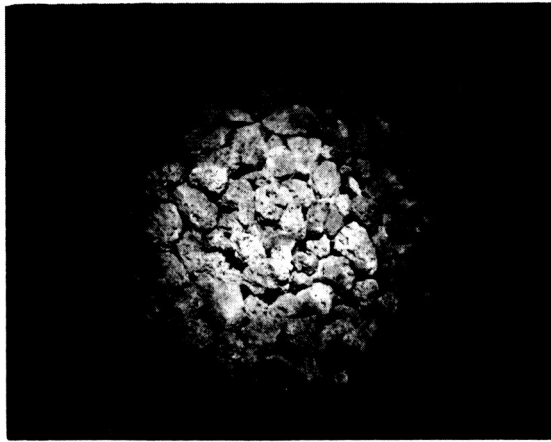
a) Normal Incident Illumination
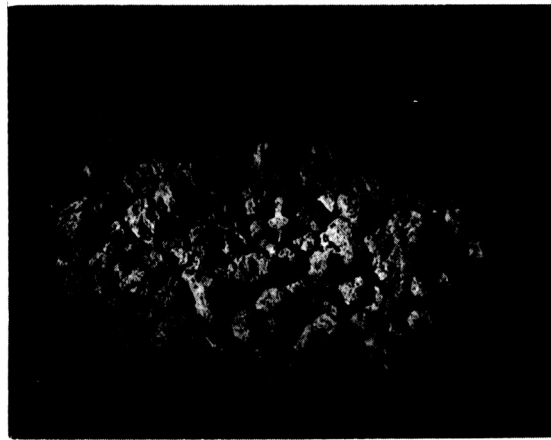
b) 65° Incident Illumination

Fig. 81 Contrived Model No. 4: Volcanic Ash No. 4 (chunks)
Topped with Particles of Coral $\leq$ 4μ

142
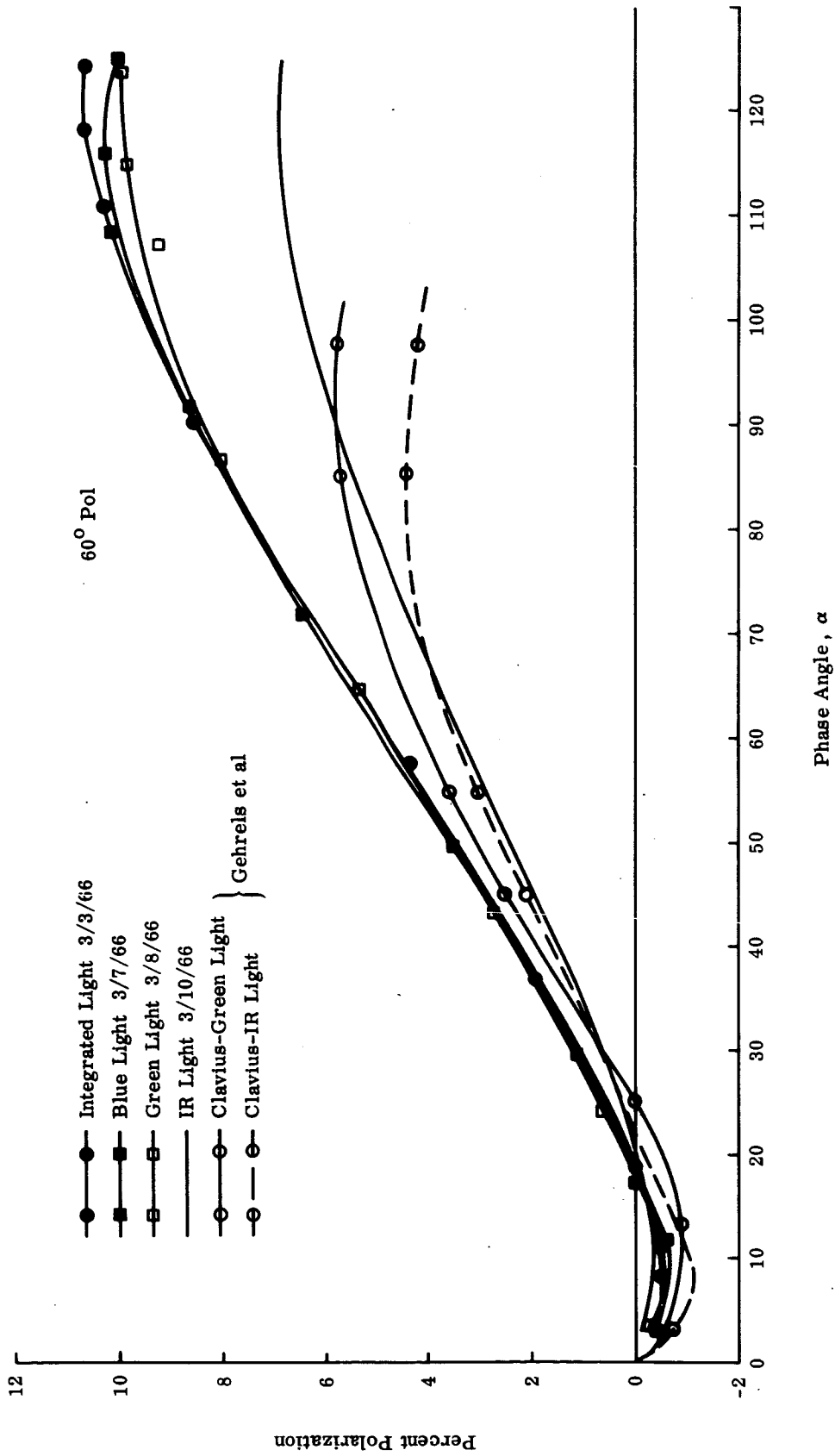
Fig. 82 Contrived Model No. 4: Percent Polarization
as a Function of Color -- 60° Polarimeter

143

Phase Angle, α
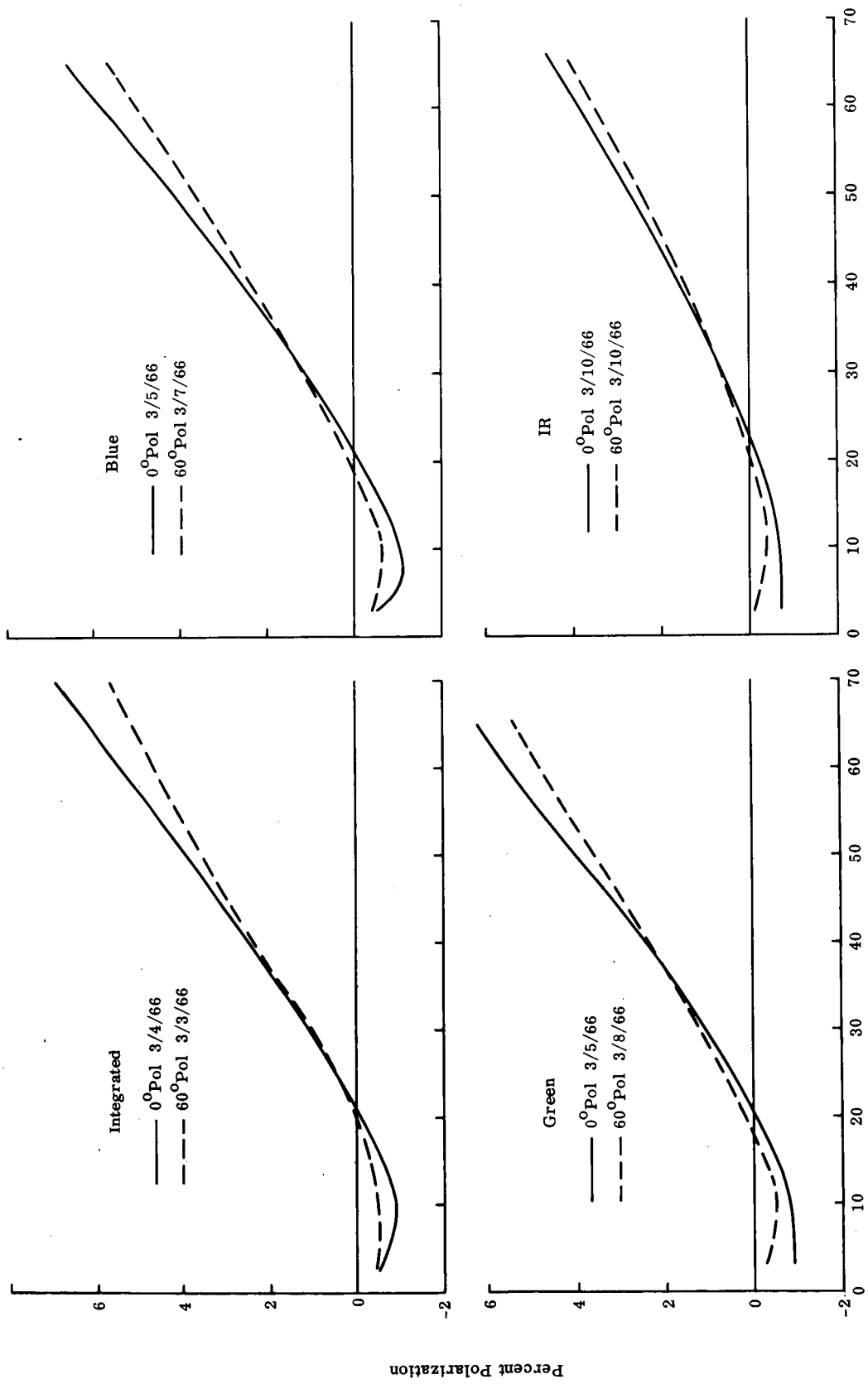
Percent Polarization

Fig. 83 Contrived Model No. 4: Simulated Lunar Longitude Effect on Percent Polarization
as a Function of Color

144

a) Normal Incident Illumination

b) 65° Incident Illumination

Fig. 84 Contrived Model No. 5: Volcanic Ash No. 4 Topped
with Particles of Itself $\leq$ 1µ
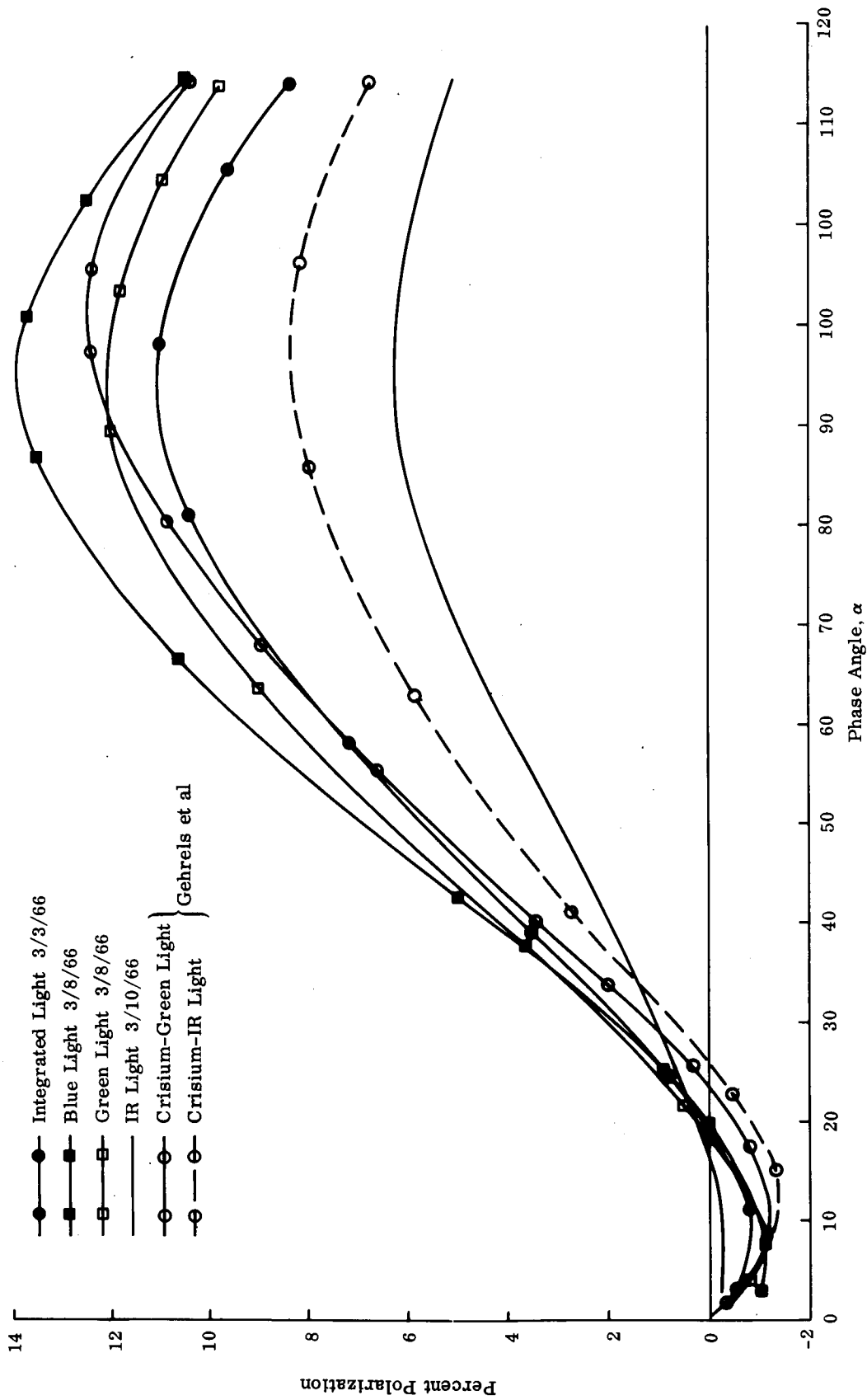
Fig. 85 Contrived Model No. 5: Percent Polarization
as a Function of Color -- 60° Polarimeter

Percent Polarization

Phase Angle, α

Integrated Light 3/3/66
Blue Light 3/8/66
Green Light 3/8/66
IR Light 3/10/66
Crisium-Green Light } Gehrels et al
Crisium-IR Light

146
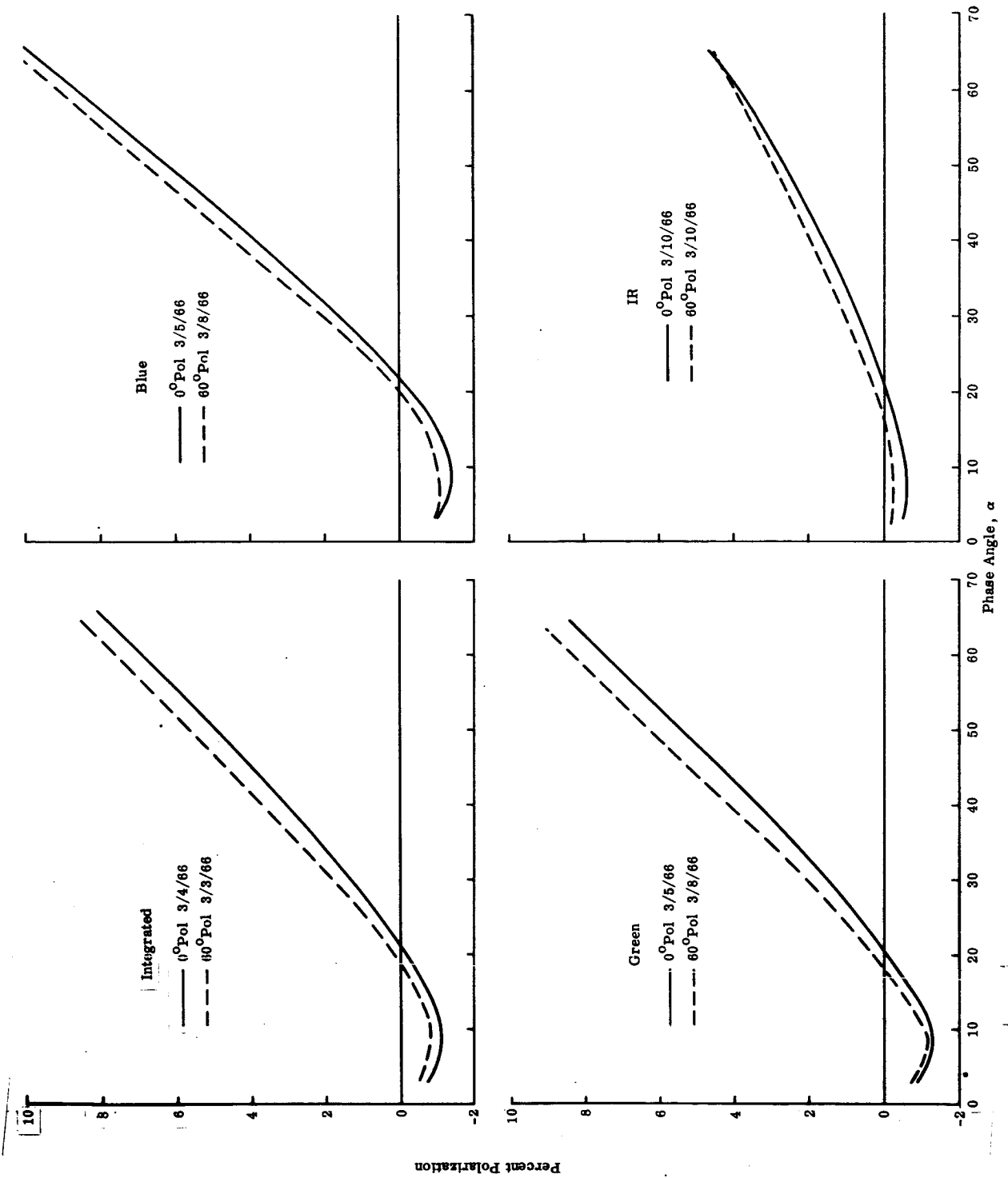
Fig. 86 Contrived Model No. 5: Simulated Lunar Longitude Effect on Percent Polarization as a Function of Color

147
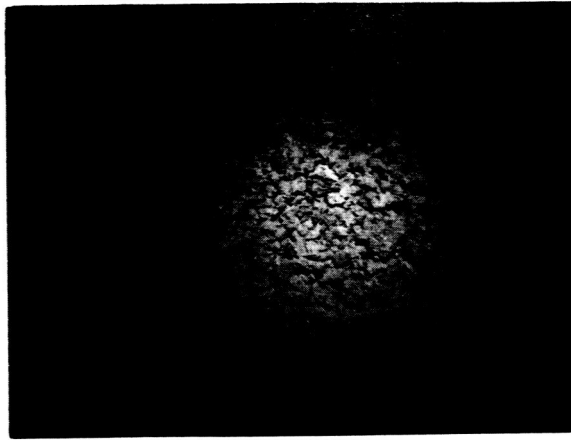
a) Normal Incident Illumination

b) 65° Incident Illumination

Fig. 87 Contrived Model No. 6: Volcanic Ash No. 1 Topped
with Particles of Itself $\leq$ 4μ

148
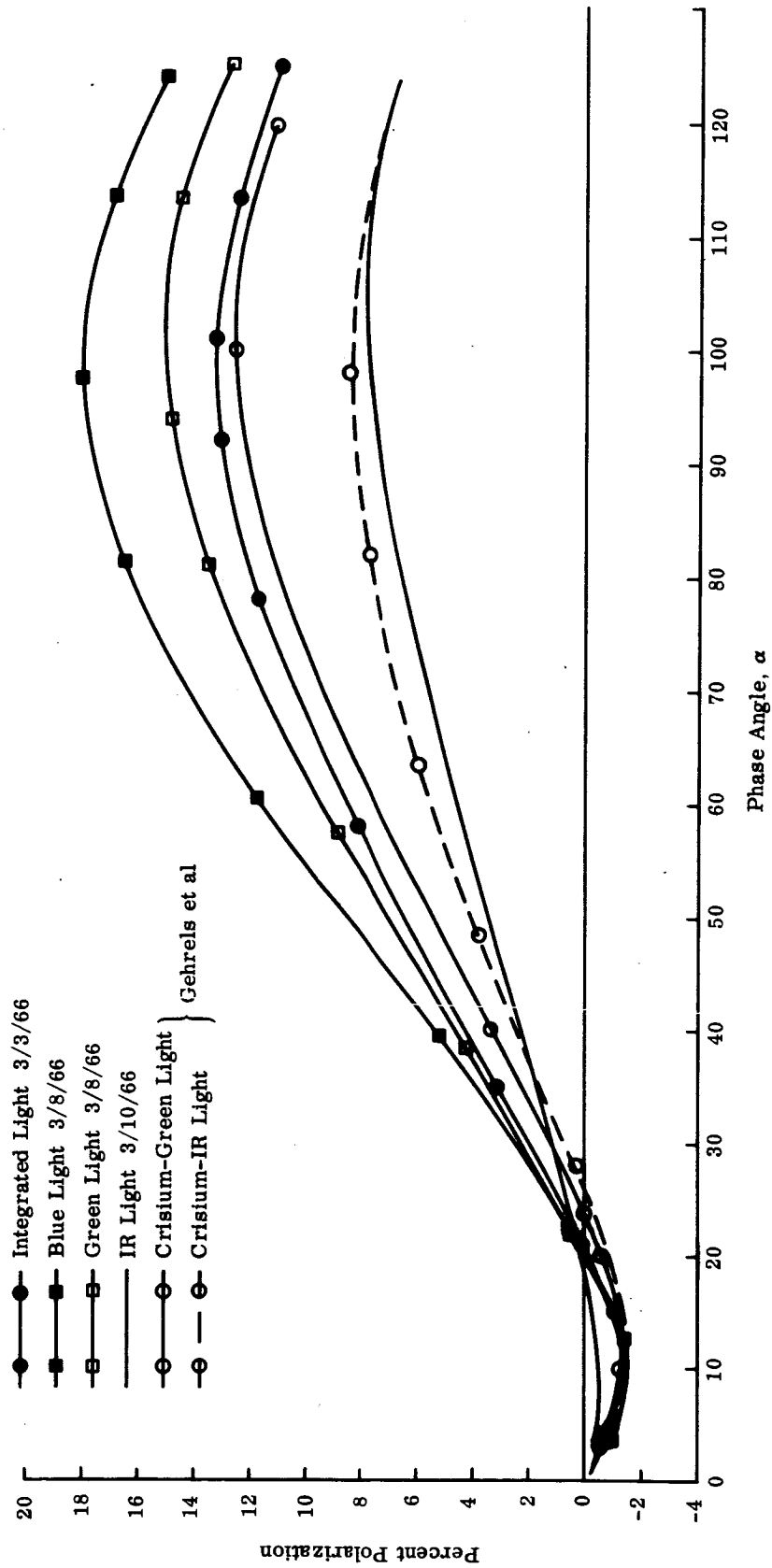
Fig. 88 Contrived Model No. 6: Percent Polarization
as a Function of Color -- 60° Polarimeter

149
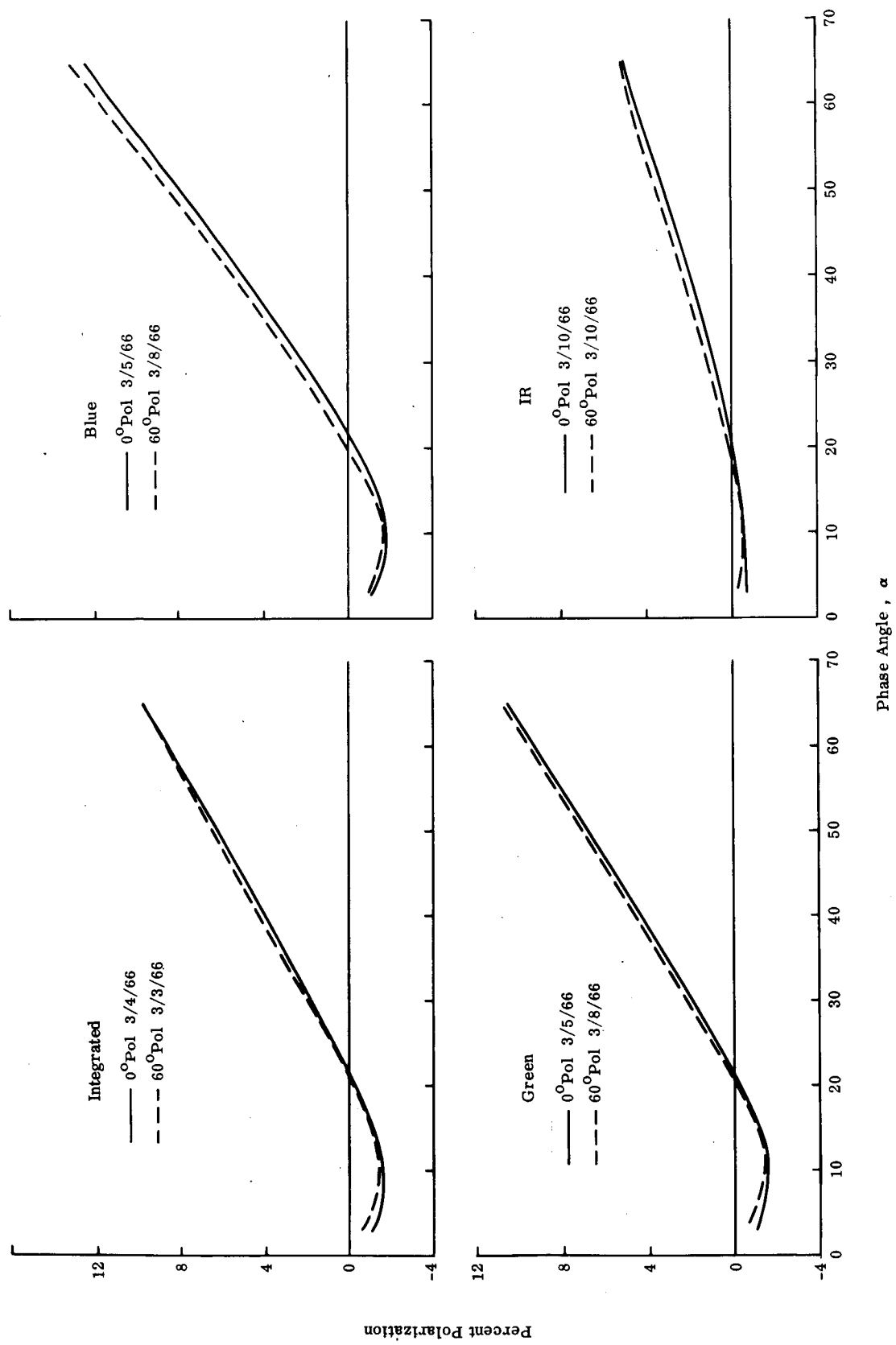
Fig. 89 Contrived Model No. 6: Simulated Lunar Longitude Effect on Percent Polarization as a Function of Color

150
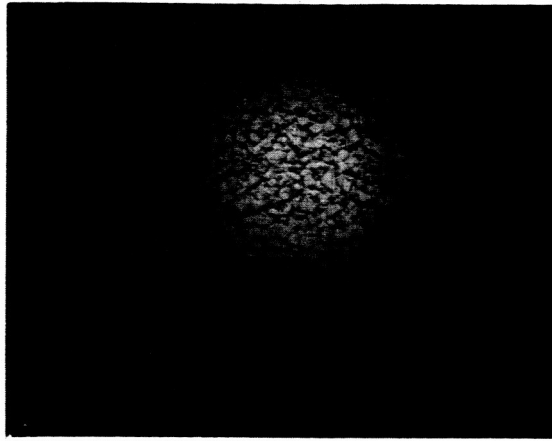
a)   Normal Incident Illumination

b)   65° Incident Illumination

Fig. 90   Contrived Model No. 7:   Furnace Slag No. 4 Topped
with Particles of Itself $\leq$ 1μ
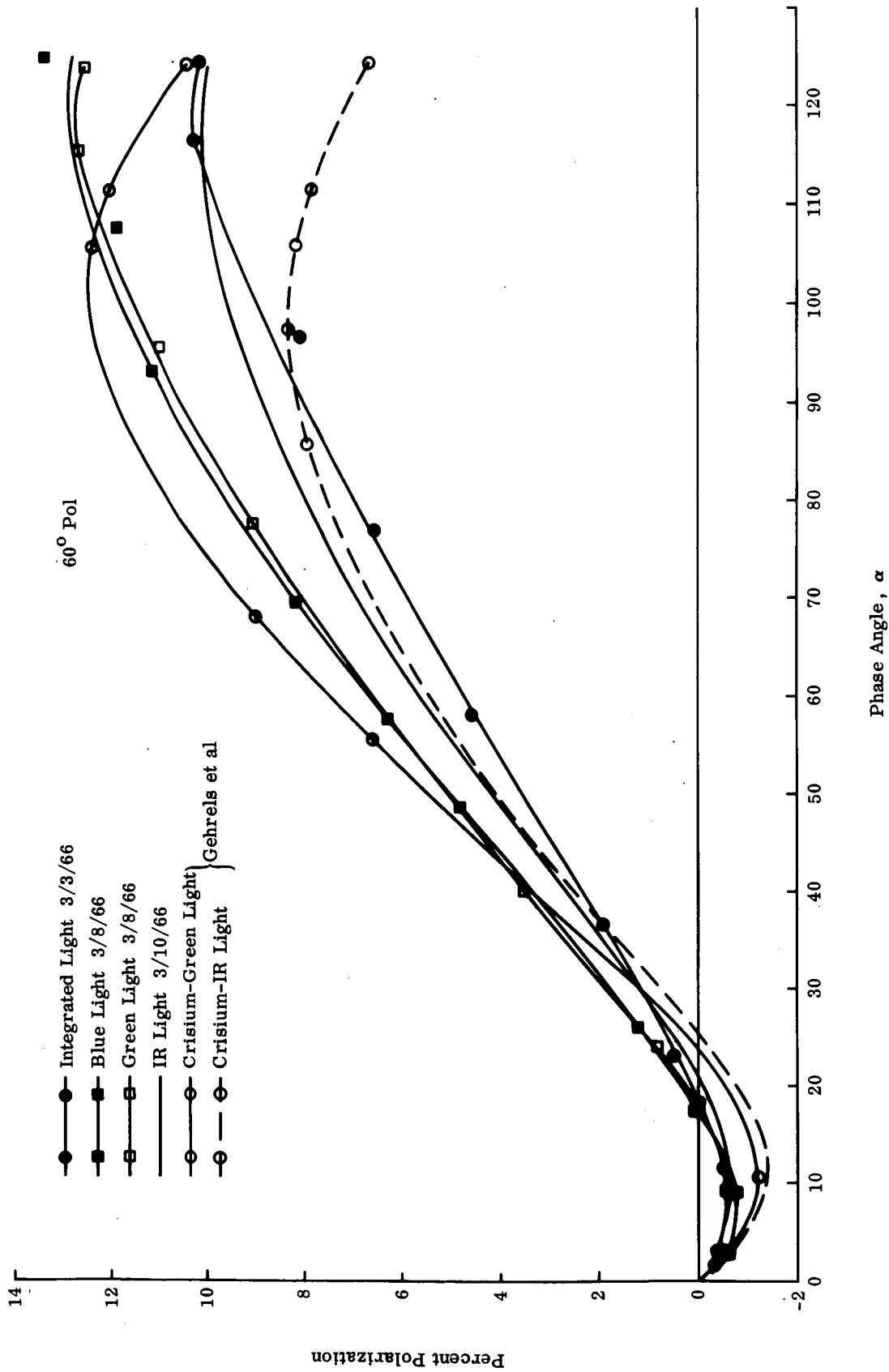
Fig. 91 Contrived Model No. 7: Percent Polarization
as a Function of Color -- 60° Polarimeter
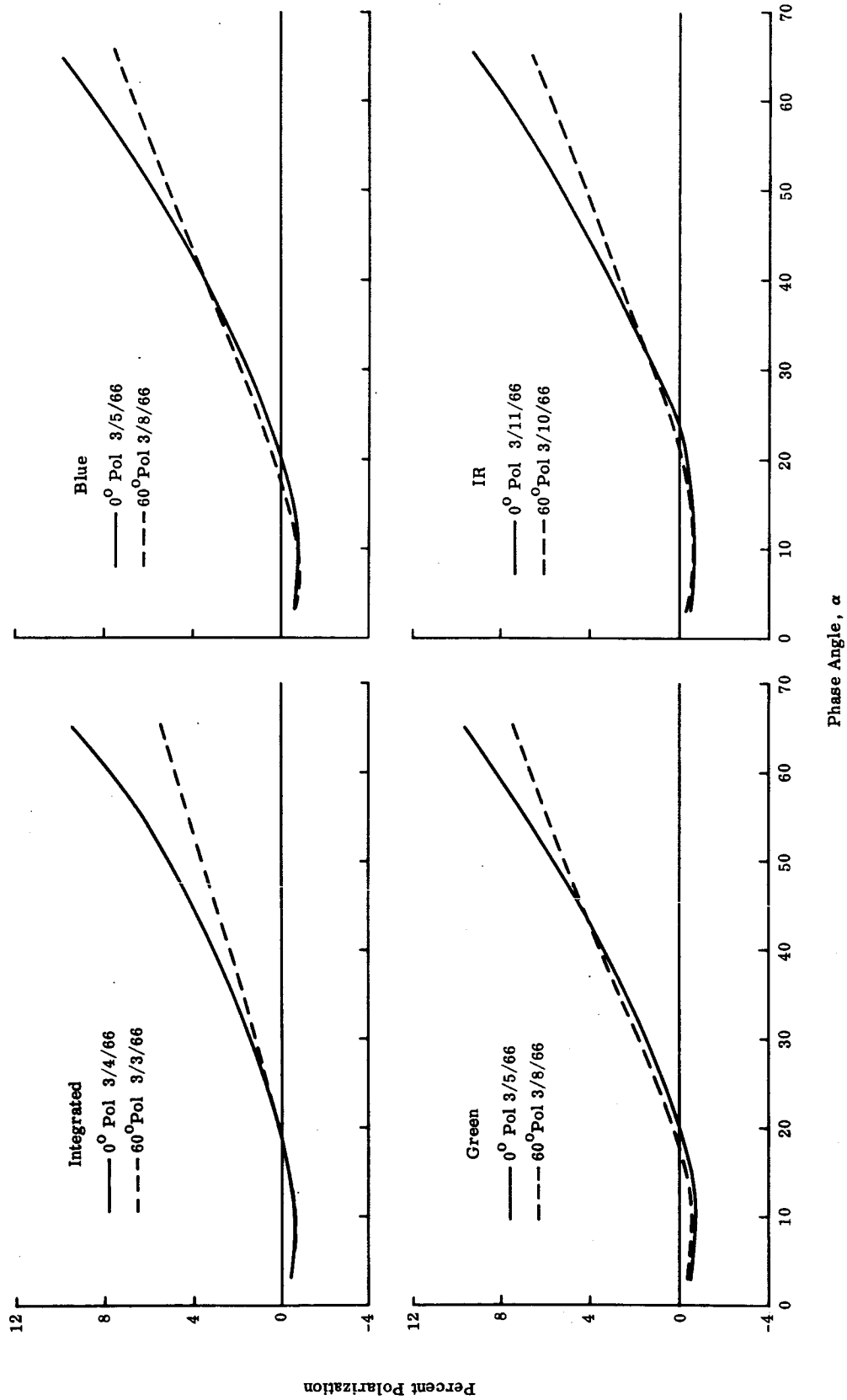
Fig. 92 Comtrived Model No. 7: Simulated Lunar Longitude Effect on Percent Polarization
as a Function of Color

153
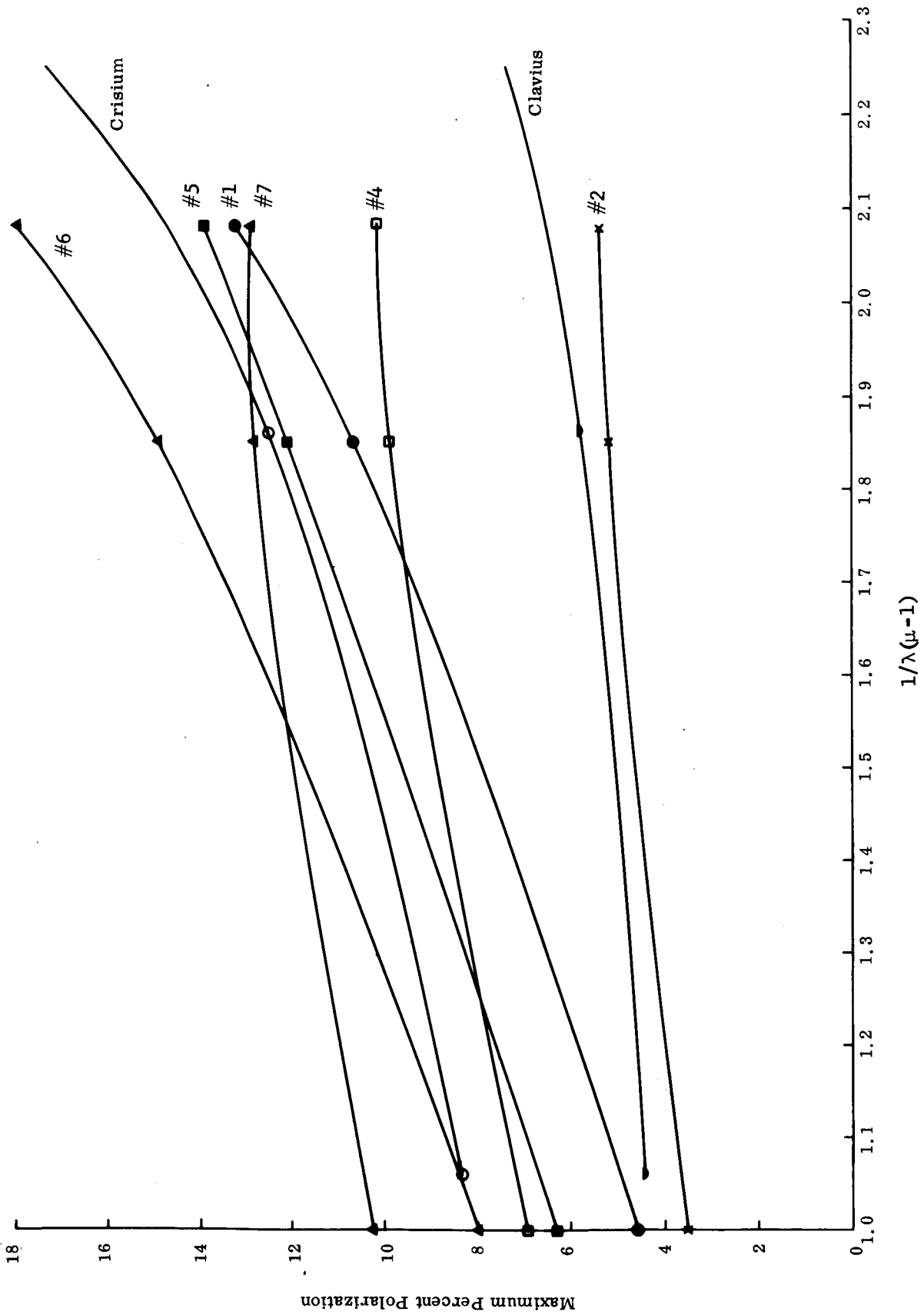
Fig. 93 Comparison of Maximum Percent Polarization as a Function of $1/\lambda$

154
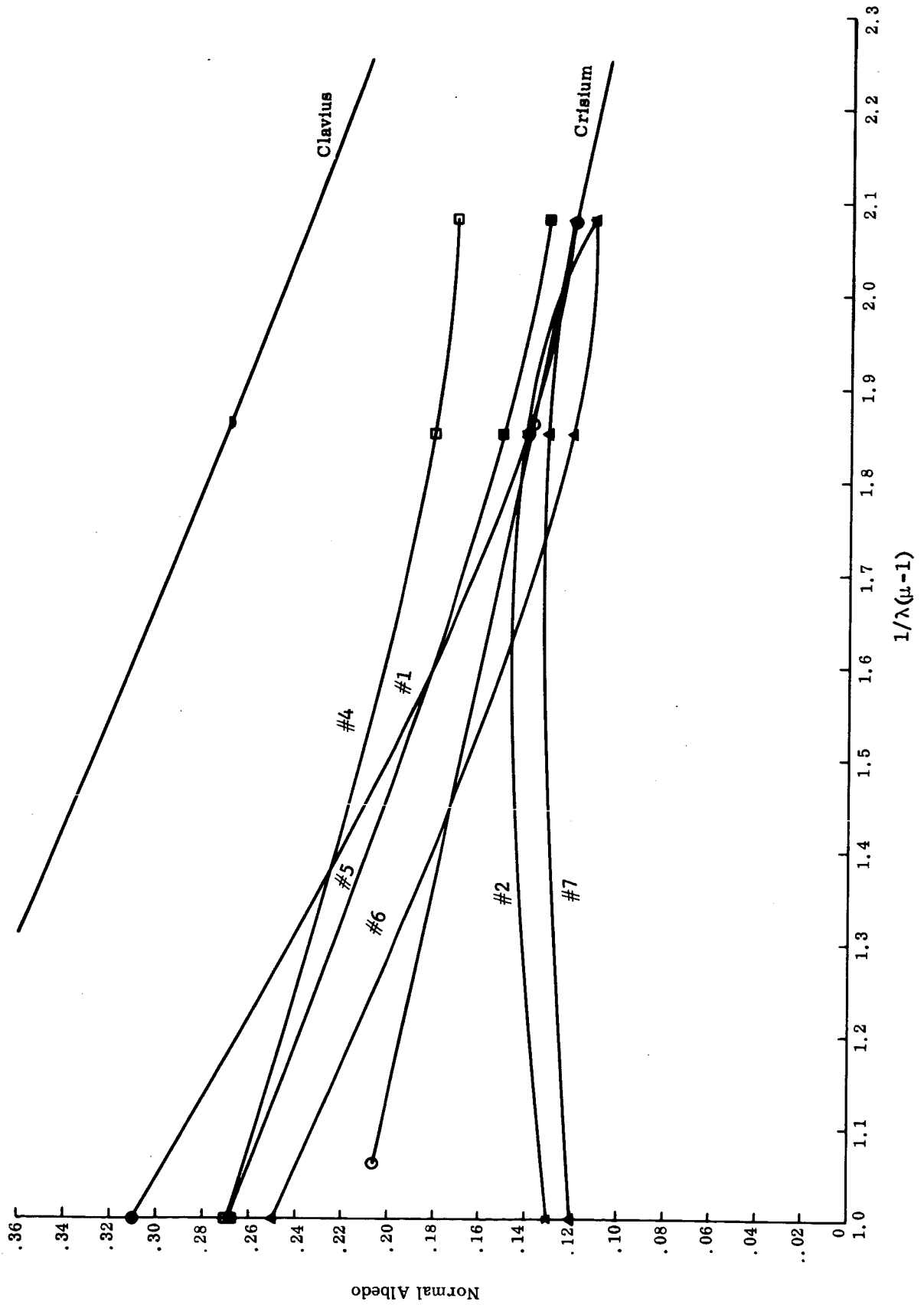
Fig. 94 Comparison of Normal Albedos as a Function of $1/\lambda$

155
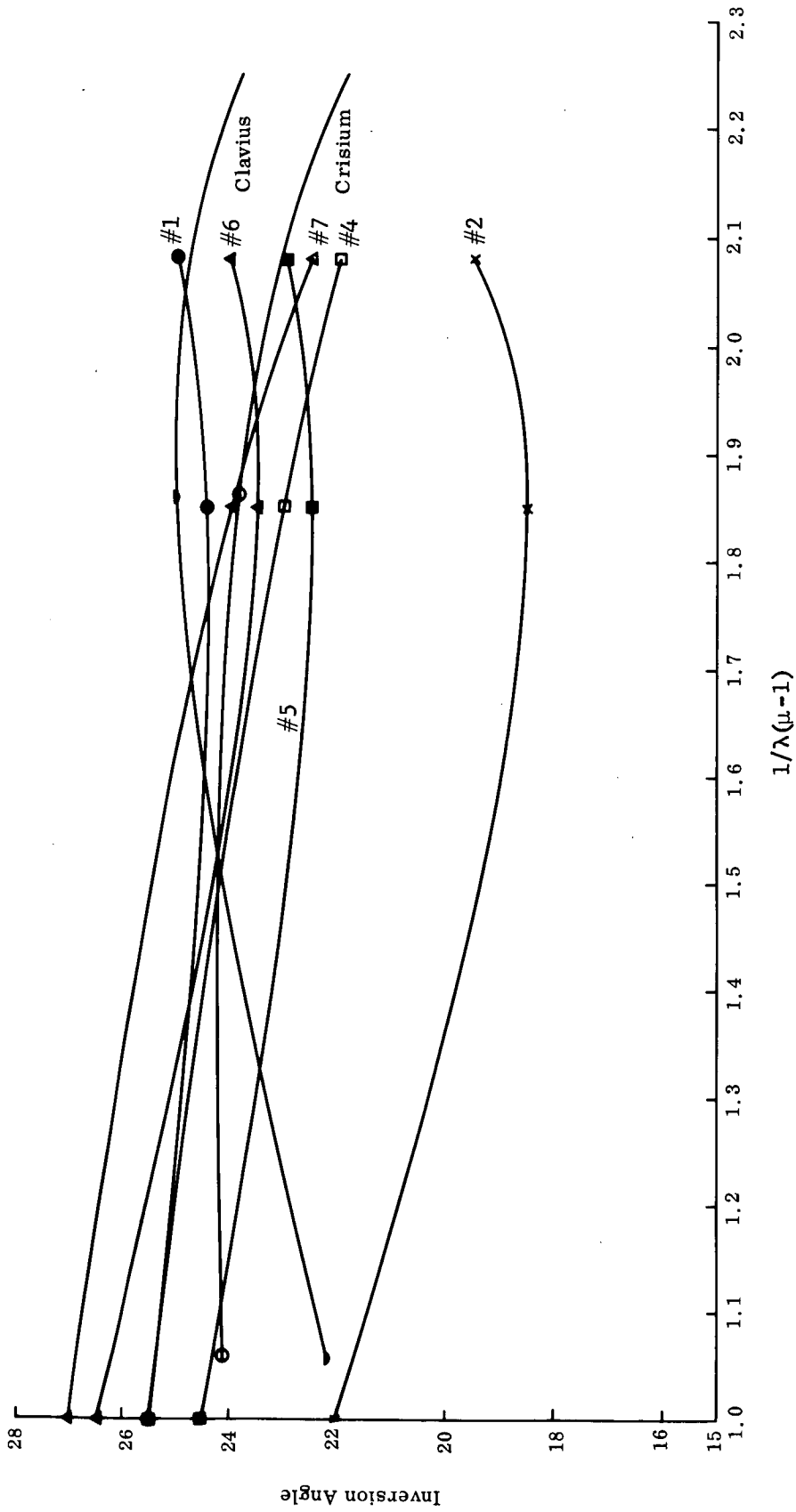
Fig. 95 Comparison of Inversion Angles as a Function of $1/\lambda$
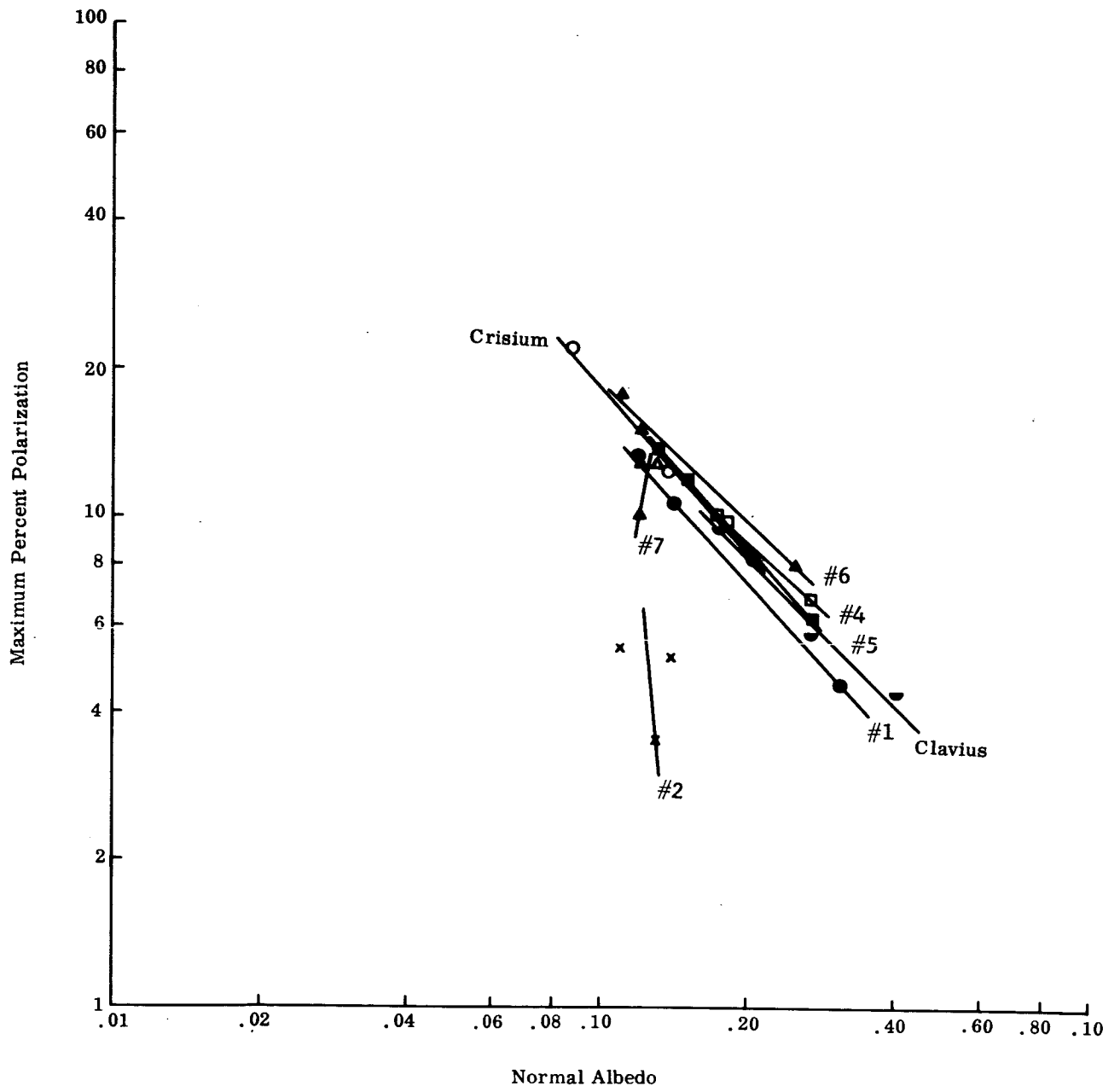
Fig. 96   Comparison of Maximum Percent Polarization
as a Function of Normal Albedo
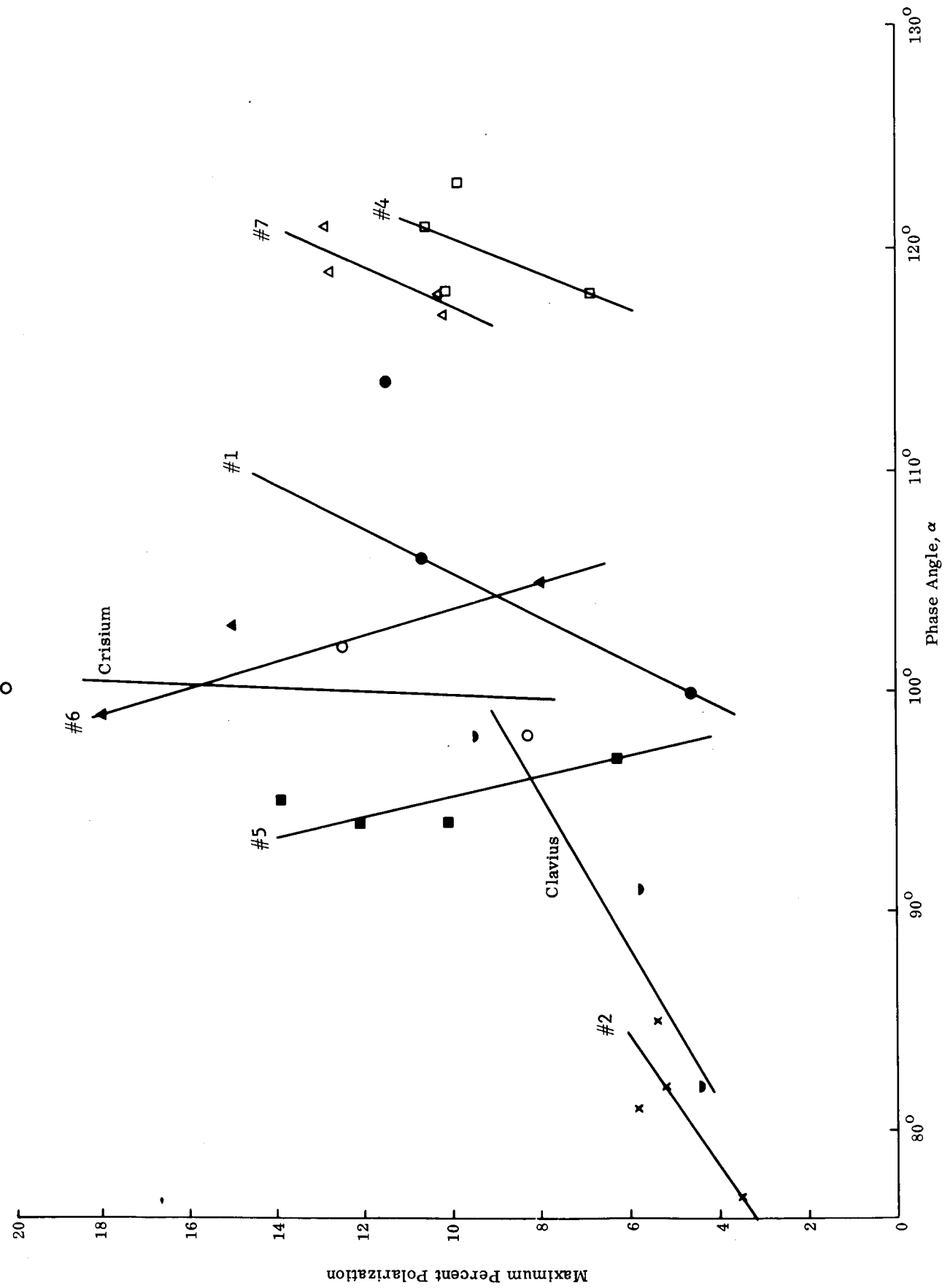
Fig. 97 Comparison of Maximum Percent Polarization and Corresponding Phase Angle
as a Function of Color
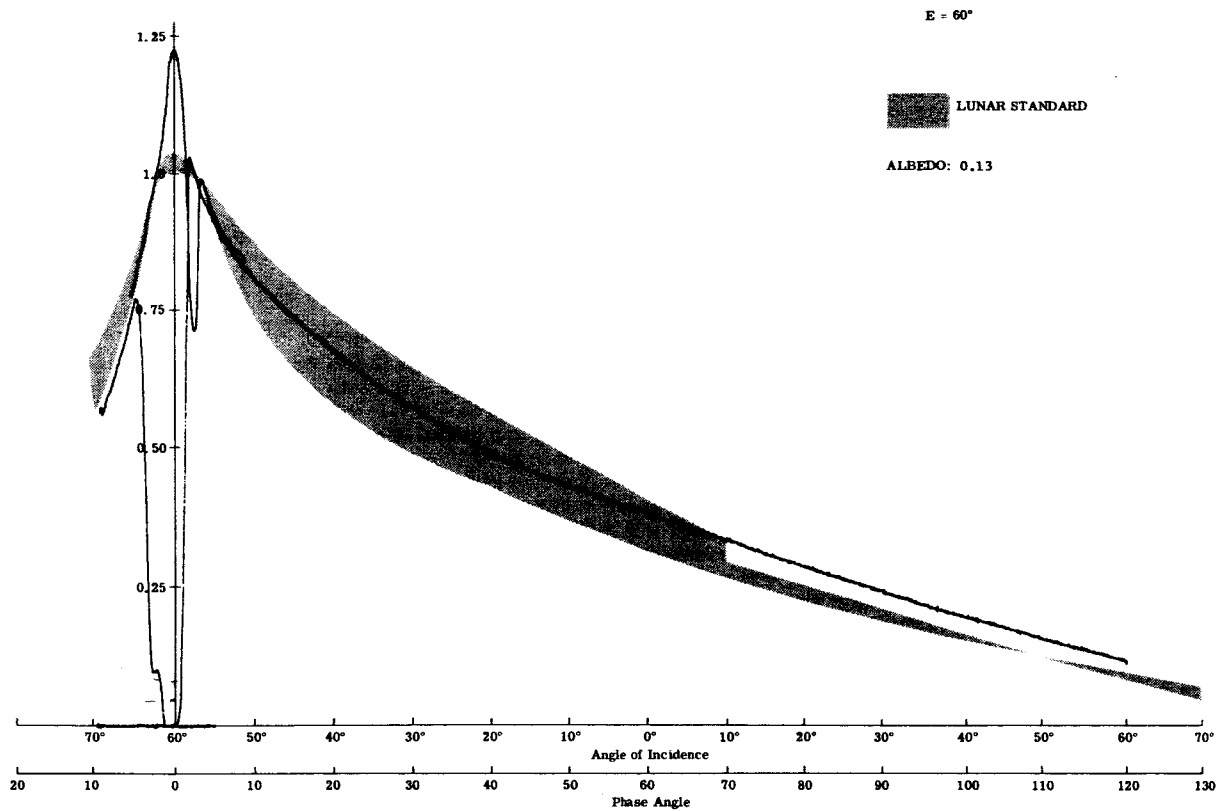
a)   60° Photometer-Visual Light
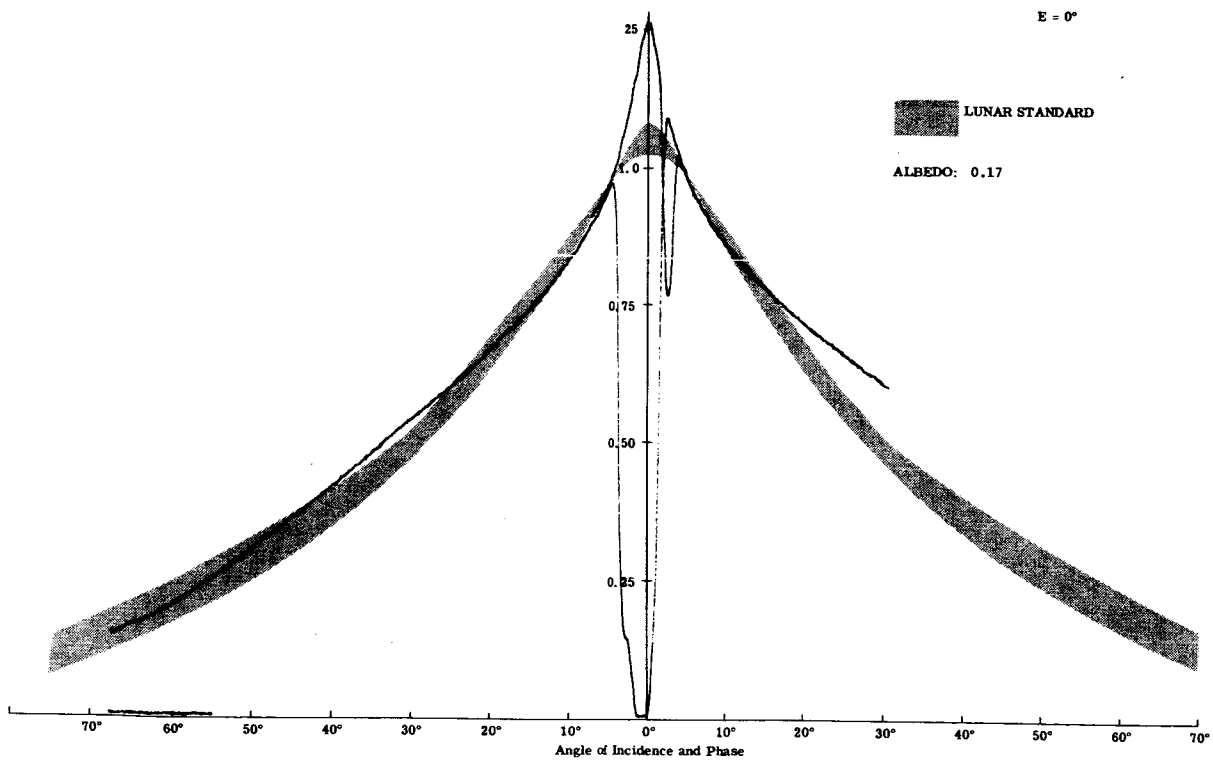
b)   0° Photometer-Visual Light

Fig. 98   Photometry of Contrived Model No. 1:   Furnace
           Slag (Spongelike-NASA) Topped with 0.088 to
           0.21 mm Particles of Volcanic Ash No. 1
           (Brightness (Arbitrary Units) versus Phase Angle)

159
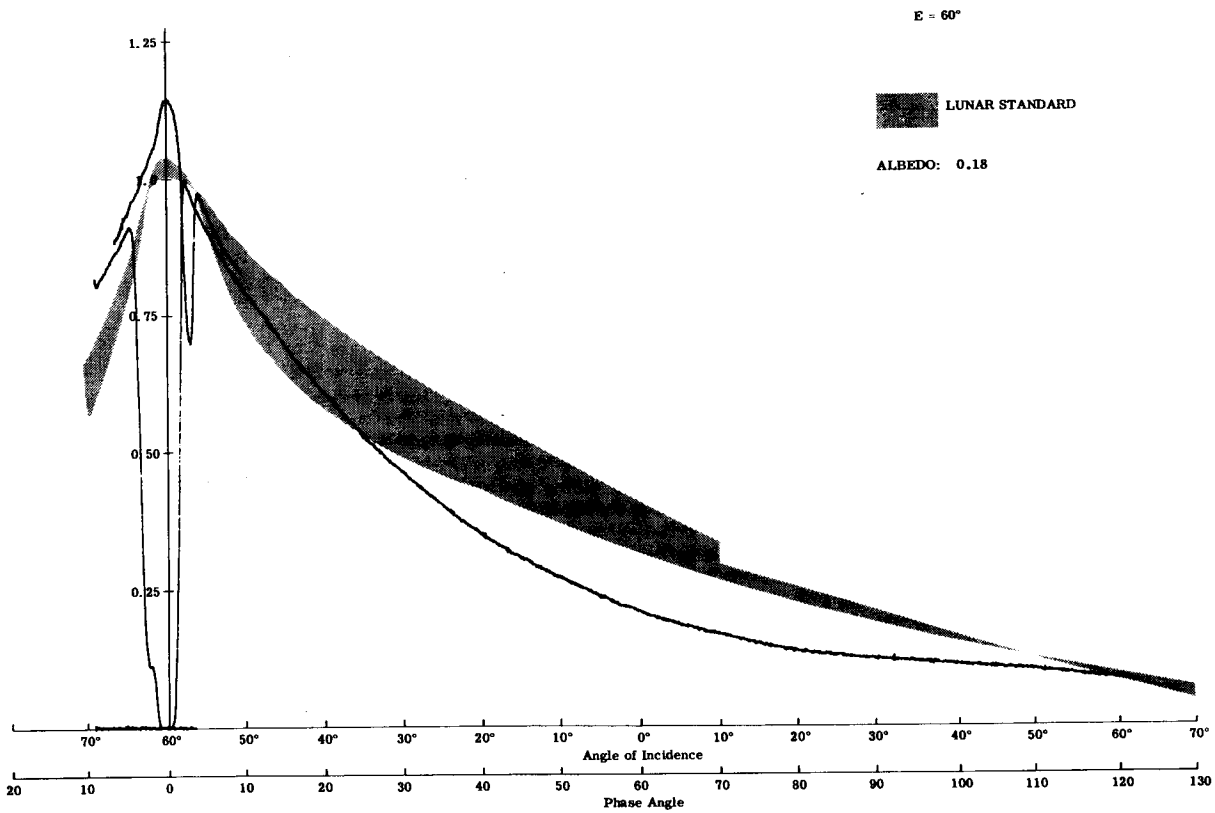
a) 60° Photometer-Visual Light
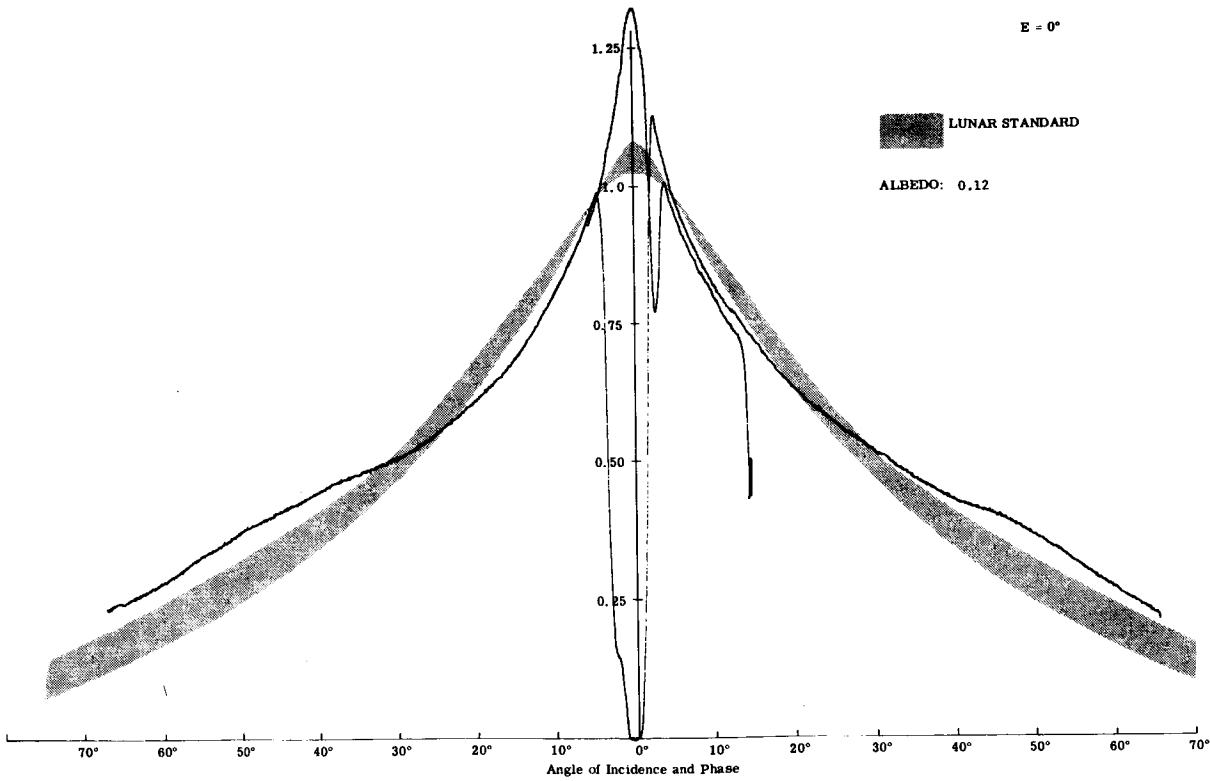
b) 0° Photometer-Visual Light

Fig. 99 Photometry of Contrived Model No. 2: Coral
No. 1 Topped with Particles of Furnace Slag
No. 4 ≤ 0.037 mm (Brightness (Arbitrary Units)
versus Phase Angle)

160
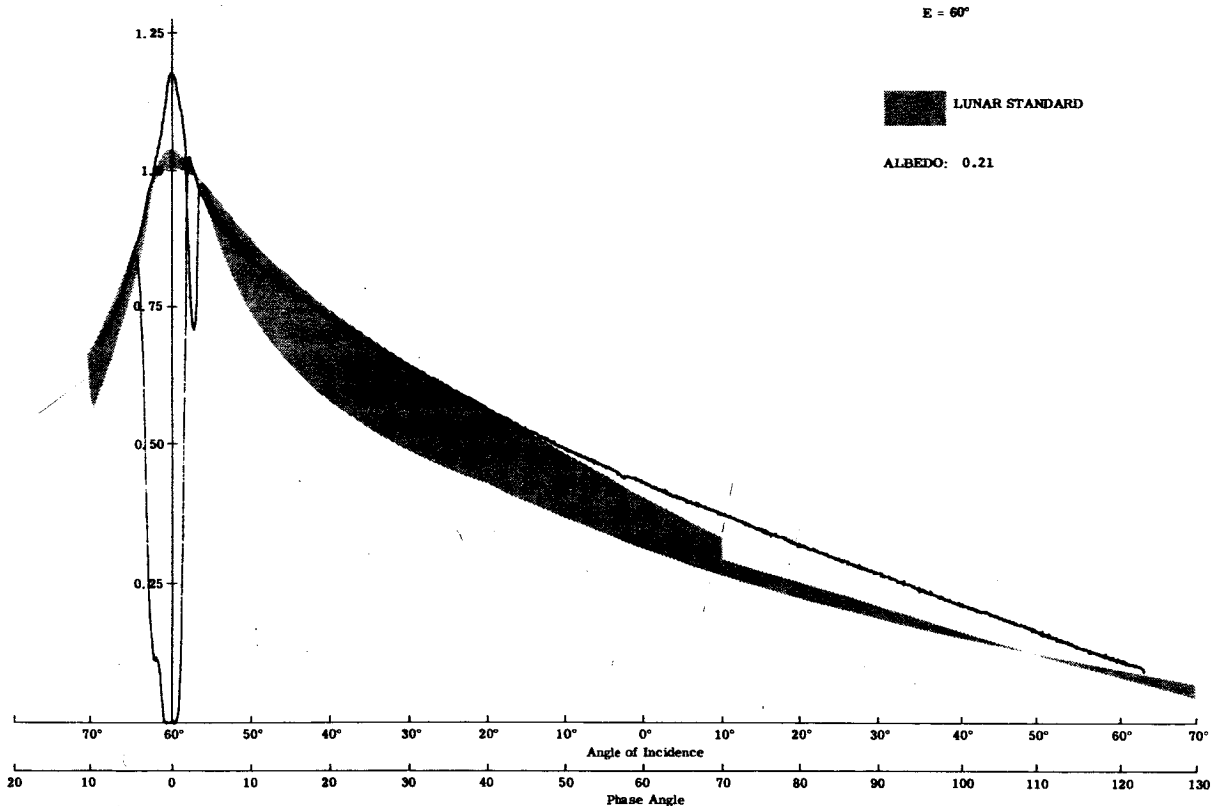
Fig. 100   Photometry of Contrived Model No. 4:   Volcanic
            Ash No. 4 (Chunks) Topped with Particles of
            Coral $\leq$ 1μ -- 60° Photometer-Visual Light
            (Brightness (Arbitrary Units) versus Phase Angle)
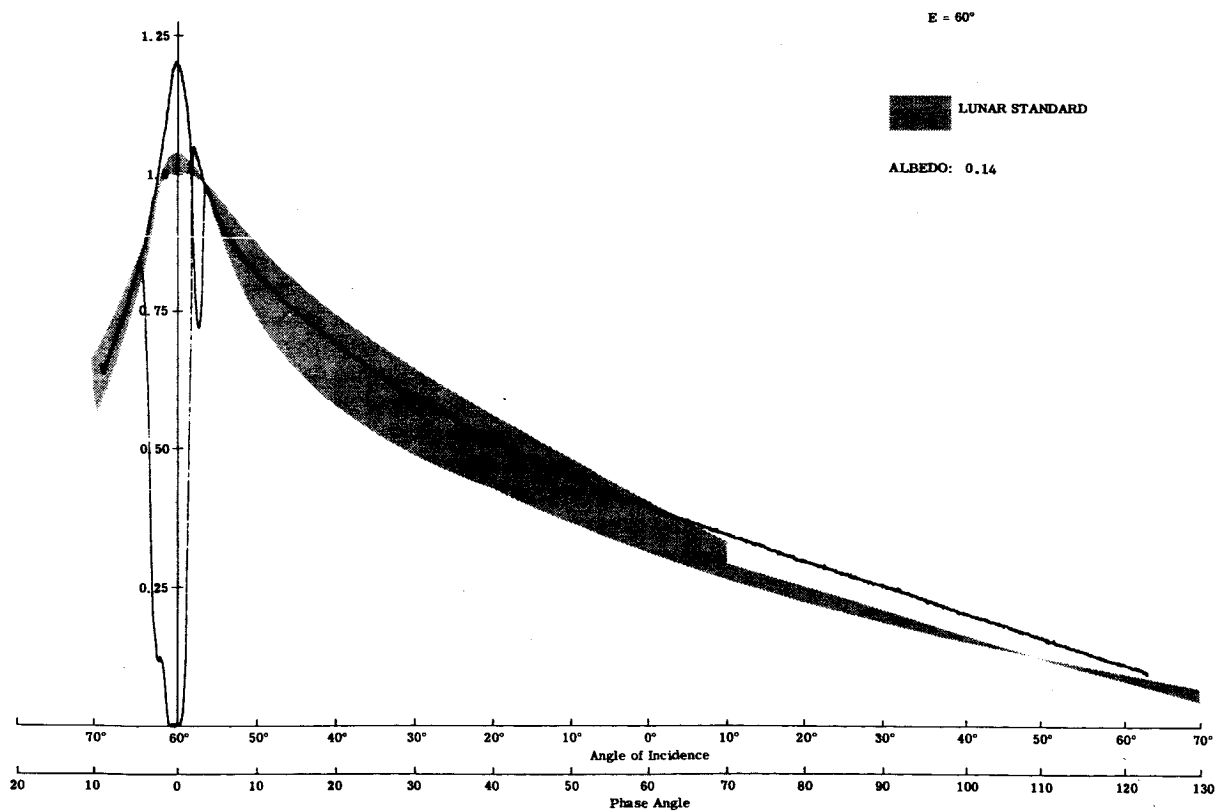
Fig. 101   Photometry of Contrived Model No. 5:   Volcanic
            Ash No. 4 Topped with Particles of Itself $\leq$ 1μ
            (Brightness (Arbitrary Units) versus Phase Angle)

161

E = 60°

LUNAR STANDARD

ALBEDO: 0.14

(Chart with axes "Angle of Incidence" ranging from 70° to 70° and "Phase Angle" from 20 to 130, brightness axis from 0.25 to 1.25)
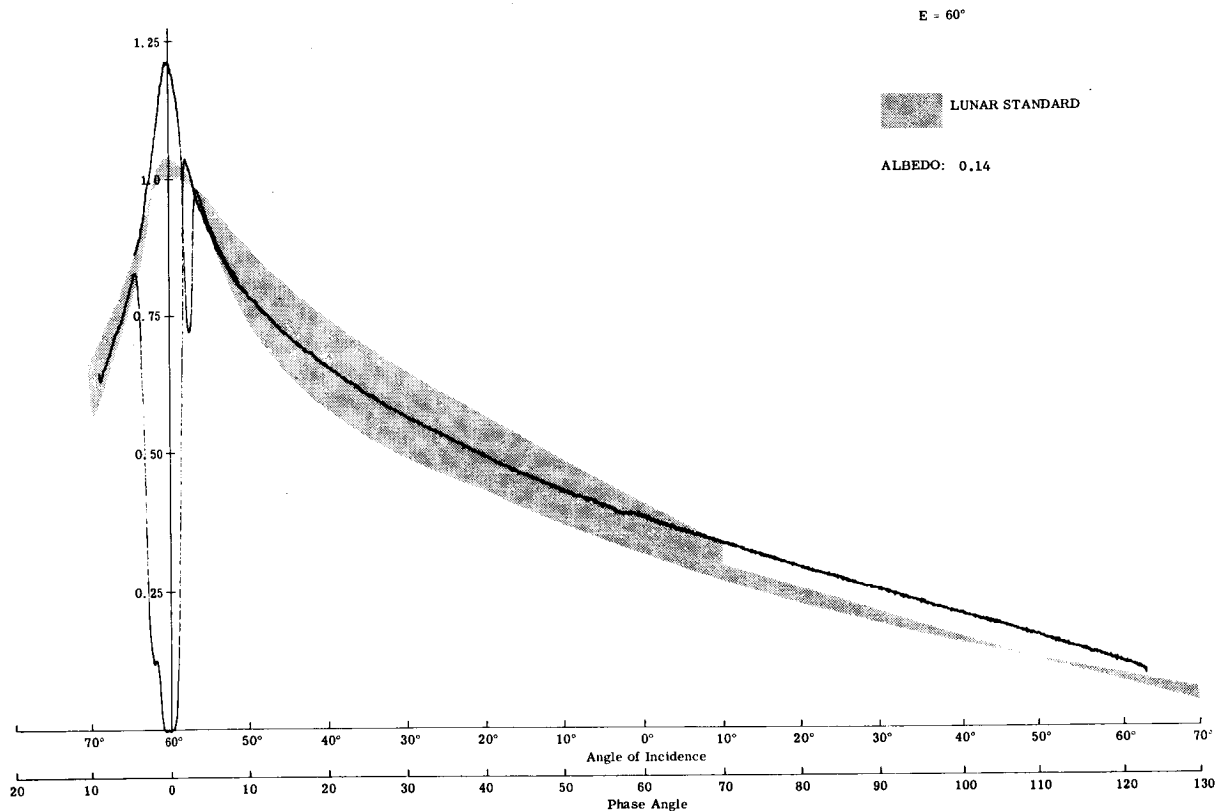
Fig. 102 Photometry of Contrived Model No. 6: Volcanic
Ash No. 1 Topped with Particles of Itself $\leq$ 1μ
(Brightness (Arbitrary Units) versus Phase Angle)

E = 60°

LUNAR STANDARD

ALBEDO: 0.12

(Chart with axes "Angle of Incidence" ranging from 70° to 70° and "Phase Angle" from 20 to 130, brightness axis from 0.25 to 1.25)
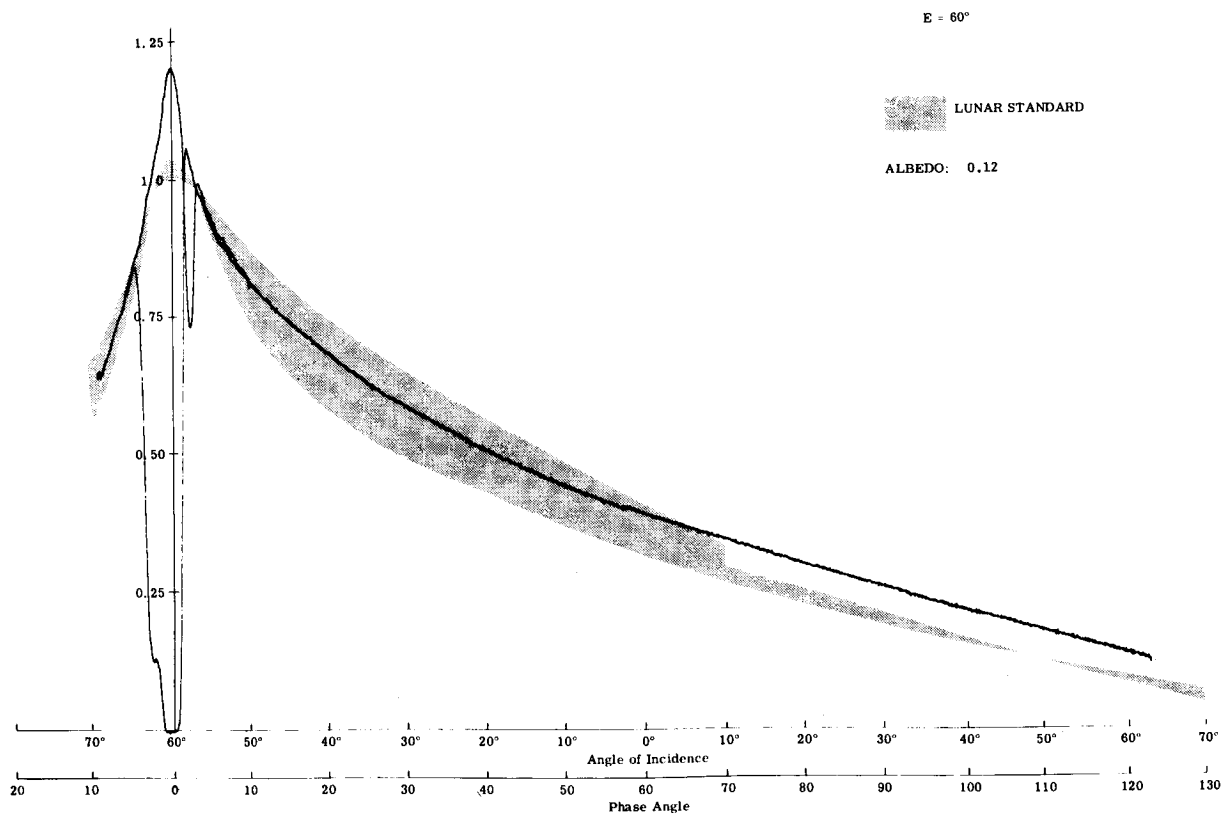
Fig. 103 Photometry of Contrived Model No. 7: Furnace
Slag No. 4 Topped with Particles of Itself $\leq$ 1μ
(Brightness (Arbitrary Units) versus Phase Angle)

162

PHASE IV — ANALYSIS OF LUNAR AND LABORATORY DATA

Purpose

Information about the lunar surface can be obtained by observing the polarization of various promising terrestrial specimens, and interpreting these and the lunar observations in terms of a theoretical electromagnetic model. A direct approach to the problem of interpreting the optical scattering properties of any surface would require the ability to calculate the properties of the surface (geometry, dielectric constant, and conductivity) from a knowledge of the characteristics of the incident and scattered beams. At the present time, this inverse scattering problem cannot be solved except under certain, limited assumptions. Thus, an indirect approach, through models, must be adopted. Using whatever information is available, one constructs theoretical models that may be reasonable approximations to the physical surface under study. The calculated optical signatures of these models are then compared to the experimental signature of the physical surface so as to explain the origin of some of the features of the latter.

Approaches

To set the various theoretical models of the lunar surface in the proper perspective, to relate them to the observed lunar and laboratory data, and to determine vector transformation characteristics, the program is divided into five sections:

1) The problem of interpreting the lunar polarimetric signature in terms of the signature of laboratory models
2) Examination of the Mie theory (Gehrels' model)
3) Contrived polarimetric models
    a) single layer plane facet model
    b) double layer plane parallel slab
    c) double layer plane facet model
4) Investigation of the Stokes vector as a tool for interpreting the lunar signature
5) Correlation of polarization factors and comparison of models to lunar and laboratory data

Results

The Problem of Interpreting the Lunar Polarimetric Signature in Terms of the Signatures of Laboratory Samples

Laboratory measurements in Phases I, II, III, and elsewhere have provided us with polarimetric signatures of various materials. If we wish to utilize this information in interpreting the lunar polarization signature, we must realistically assume that in any observed region of the moon there may be more than one type of

component material present. It is important to examine briefly the consequences of this.

Let us assume that there are two types of material, A and B, in the region under observation, and that on a scale smaller than the resolution limits, but at least as large as that of our laboratory samples, the region is divided into sub-regions, each of which consists exclusively of type A or B. With these assumptions, the intensity signature of the composite is obtained by addition of the individual signatures, weighted by the total area of each component. For simplicity we assume unit total area and the area of component A is x, and that of component B is (1 - x).

The signatures, normalized to unit area, of each component are

$$I_\perp^i \quad , \quad I_\parallel^i \quad ,$$

where $I_{\perp(\parallel)}^i$ is the intensity as a function of phase angle, α , of light scattered from component i that is polarized perpendicular (parallel) to the plane of vision. We define the polarization as

$$q^i = \frac{I_\perp^i}{I_\parallel^i} \quad ,$$

the percent polarization as

$$P^i = \frac{I_\perp^i - I_\parallel^i}{I_\perp^i + I_\parallel^i} \quad ,$$

and the brightness as

$$B^i = (I_\perp^i + I_\parallel^i) \ (\cos E)^{-1} \quad ,$$

where E is the angle between the macro-normal to the surface and the direction of viewing.

The significant features of the lunar and laboratory signatures are:

α_{inv}^i = the inversion angle (where $P^i = 0$)

α_{max}^i = the angle of maximum percent polarization

P_{max}^i = the value of maximum percent polarization

α_{min}^i = the angle of minimum percent polarization

P^i_{min} = the value of minimum percent polarization

A^i = the albedo, which is directly proportional to the brightness at zero phase angle, i.e.,

$$A^i = k \, B^i \, (\alpha = 0) \ .$$

Note that, in general, $I^i_{\perp(\parallel)}$ is a function of α, E, and the intensity of the incident beam, I_o ; A^i is a function only of E. Unless otherwise stated we will assume constant E and I_o.

To formulate the problem in terms simple enough to hope for some conclusions, we assume that all components have brightness functions with the same functional dependence on the phase angle,

$$B^i \, (\alpha, \ E) = \frac{A^i(E)}{k} \, b \, (\alpha, \ E) \quad ,$$

where $b \, (0, \ E) = 1$.

Then, the brightness of the composite will be

$$B \, (\alpha, \ E) = x \, B^A \, (\alpha, \ E) \ + \ (1-x) \, B^B \, (\alpha, \ E)$$

$$= \frac{b \, (\alpha, \ E)}{k} \left\{ x \, A^A(E) + (1-x) \, A^B(E) \right\} \ ,$$

and its albedo is given by

$$A(E) = k \, B \, (0, \ E)$$

$$= x \, A^A \, (E) \ + \ (1-x) \, A^B \, (E).$$

Thus, the albedo of the composite is a weighted average of the albedoes of each component. The percent polarization of the composite is:

$$P = \frac{x(I^A_\perp - I^A_\parallel) \ + \ (1-x) \, (I^B_\perp - I^B_\parallel)}{x(I^A_\perp + I^A_\parallel) \ + \ (1-x) \, (I^B_\perp + I^B_\parallel)}$$

165

$$P = \frac{x\,(I_{\perp}^A - I_{\parallel}^A) + (1-x)\,(I_{\perp}^B - I_{\parallel}^B)}{[x\,B^A + (1-x)\,B^B]\,\cos E}$$

$$= \frac{x\,(I_{\perp}^A - I_{\parallel}^A) + (1-x)\,(I_{\perp}^B - I_{\parallel}^B)}{[x\,A^A + (1-x)\,A^B]\,b\,(\alpha, E)} \quad \frac{k}{\cos E} \quad .$$

It can be seen that

$$I_{\parallel}^i = \frac{B^i \cos E}{q^i + 1} \quad ; \quad I_{\perp}^i = \frac{q^i\,B^i \cos E}{q^i + 1}$$

$$I_{\parallel}^i = \frac{A^i\,b\,(\alpha, E)\,\cos E}{k\,(q^i + 1)} \quad ; \quad I_{\perp}^i = \frac{q^i\,A^i\,b\,(\alpha, e)\,\cos E}{k\,(q^i + 1)}$$

$$P = \frac{x\left\{\dfrac{q^A\,A^A - A^A}{q^A + 1}\right\} + (1-x)\left\{\dfrac{q^B\,A^B - A^B}{q^B + 1}\right\}}{x\,A^A + (1-x)\,A^B}$$

$$P = \frac{x\,A^A}{A} \quad \frac{q^A - 1}{q^A + 1} + \frac{(1-x)\,A^B}{A} \quad \frac{q^B - 1}{q^B + 1} \quad ,$$

but $$\frac{q^i - 1}{q^i + 1} = P^i$$

so that

$$P = \frac{x\,A^A}{A}\,P^A + \frac{(1-x)\,A^B}{A}\,P^B. \tag{1}$$

Thus, the percent polarization of the total is an average of the components weighted by both the area and albedo. It is clear that we may expect to reproduce the principle features of the lunar signature with many different combinations of components.

If we differentiate P with respect to α and set it equal to zero, we find as a condition for both maximum and minimum

$$\frac{\partial\ P^A}{\partial\ \alpha} = -\ \frac{(1-x)\ A^B}{x\ A^A}\ \frac{\partial\ P^B}{\partial\ \alpha}\qquad \alpha = \alpha_{max}\ (min)\ .$$

This indicates that at the extrema, $\partial\ P^A/\partial\ \alpha$ and $\partial\ P^B/\partial\ \alpha$ must have opposite signs, so that α_{max} lies between α^A_{max} and α^B_{max} with similar conditions for the minima. It is clear from Eq. (1) that the same relation, i.e., α_{inv} lies between α^A_{inv} and α^B_{inv}, holds also for the inversion angles.

Because of the very low peak polarization observed on the moon, it is sometimes suggested that there may be polarizing and nonpolarizing regions contributing to the overall signature. If $P^B = 0$ for all α, Eq. (1) indicates that the magnitude of P^A will be reduced by a constant factor at all phase angles, and that the angles $\alpha_{max} = \alpha^A_{max}$, $\alpha_{min} = \alpha^A_{min}$, and $\alpha_{inv} = \alpha^A_{inv}$. With a slight modification in the interpretation of x, these comments [see, especially Eq. (1)] will be seen as explaining the remarks made in the Phase II report (Ref. 24) concerning the effects of a luminescent component on the over-all polarization signature.

Examination of Mie Theory (Gehrels' Model)

The Mie theory was investigated inttially to find out if it could be used to explain the observed lunar polarization. The theory entails the solution of the boundary value problem of an electromagnetic wave scattered by an isolated sphere of radius $\underline{a}$ and refractive index, $\underline{m}$ which may be complex. Van de Hulst (Ref. 29) has given a very complete analysis of the problem and there are many published data on polarization by spheres, characterized by the two parameters $\underline{x} = 2\pi a/\lambda$ and $\underline{m}$.

The polarization curves for the particular case of $m = 1.25$ (dielectric sphere) and $\underline{x} = 1.8$ to 2.4 in increments of 0.1 shown in Fig. 104 is from Remy-Battiau (Ref. 30). In the limit $\underline{x} = 0$ (very small particles), the Mie theory reduces to the familiar case of Rayleigh scattering. As $\underline{x}$ increases from 0 (particle size increasing with respect to λ) the phase angle of maximum polarization (α_{max}) shifts from $90°$ towards smaller angles, while P_{max} remains near 100 percent. Only positive polarization is present here, as in the Rayleigh case. Somewhere between

$\underline{x}$ = 2.0 and 2.1, P_{max} starts to decrease, shifts towards larger angles, and the curves go very slightly negative. As $\underline{x}$ increases beyond 2.1, P_{max} becomes less positive, while P_{min} goes more negative, and both move towards larger angles. When $\underline{x}$ increases beyond about 3.0 (not shown in Fig. 104), multiple values of P_{max} and P_{min} occur, and in general the curves get very complicated. The same general trend is followed for other real values of $\underline{m}$, whereas $\underline{m}$ increases, P first goes negative at smaller values of $\underline{x}$. This is shown in Fig. 105, where the curves m = 1.25 are from Remy-Battiau (Ref. 30) and m = 1.33, 1.44, and 1.55 are from Lowan (Ref. 31).

For very small particles, most of the scattered light is reflected from the surface of the particle and tends to be positively polarized. As the particle size increases, more light penetrates the particle, and upon emergence tends to be negatively polarized. Hence, the curves of Fig. 104 can be explained, at least qualitatively, by saying that as the particle size increases, negative polarization from the interior is added to positive polarization from the surface in varying amounts.

The same reasoning applies when an imaginary component is added to real $\underline{m}$. The increase of absorption within the particle tends to suppress the contribution of the negative polarization and generally shifts the polarization curve toward more positive values. This is shown quite clearly in Fig. 10 of Deirmendjian, Clasen, and Viezee (Ref. 32), and reproduced here in Fig. 106.

The polarization from several lunar areas observed by Gehrels et al, as well as the curves of the contrived laboratory samples presented in Phases I, II, and III of this report, are all very similar in shape. The polarization never goes more negative than -2.0 percent from zero to about 25° phase angle, and then smoothly rises to a maximum value around an angle of 100°. However, the shape of the polarization curves computed from the Mie theory very critically depend on the choice of $\underline{x}$, $Re(\underline{m})$, and $Im(\underline{m})$. It is difficult to explain how all the laboratory samples, from chunks with pores up to 1 centimeter in size down to powders less than 1 micron in size, plus the lunar data, all seem to fit the Mie theory with $\underline{x}$ approximately equal to 2 for $\underline{m} \approx 1.33$ ($\underline{a}$ = 0.2 microns for G light [0.54μ]). This seems to indicate quite clearly the inapplicability of the theory to explain the observed polarization.

It might be argued that by suitably combining several Mie curves of differing x and $\underline{m}$, a smooth polarization curve might result that would fit the lunar data (i.e., the large positive values decreasing and the large negative values averaging out). But this would be a non-unique solution to the problem and would be very hard to realize in practice.

Hapke (Ref. 20) has criticized a model of the lunar surface proposed by Gehrels et al (Ref. 4), which is based in part on the Mie theory. Briefly, his criticism as it applies to the use of the theory is:

1) Crystals in particles of lunar rock composed of rough and planar surfaces would be expected to give different scattering diagrams than spherical Mie particles of similar size.

2) Deirmendiian et al (Ref. 32) show that there is a strong scattering of light in the forward direction. This is contrary to the back-scatter of light and opposition effect observed by Gehrels et al for the lunar features.

3) It is doubtful whether the range of x and m on the lunar surface could be as small as would be necessary to explain the negative polarization by Mie theory (see previous discussion).

4) Figure 6 of Gehrels et al (see Ref. 1) shows that the scattering efficiency Q (ratio of scattering cross section to geometric cross section) of a 0.8μ Mie particle should decrease with increasing λ for $\lambda \geq 1\mu$. However, recent observations (Watt on and Danielson, Ref. 33) indicate that the reflectivity of the moon continues to rise in the infrared.

It is pointed out here that Gehrels et al determine the particle size ($\underline{a} = 0.8 \pm 0.1\mu$) by fitting Q to the albedo of Crisium (see their Fig. 6 in Ref. 1). If Clavius is used, which is brighter by a factor of two, a size of 0.4μ is derived. Thus, the particle size cannot be uniquely determined for the lunar surface.

For the Mie theory to be applicable at all, it is necessary for the particles to be far enough apart (i.e., three times their radius, Ref. 29) so that there is no interaction between them, i.e., no multiple scattering takes place. The theory of Gehrels et al proposes that the particles are separated by electrostatic suspension above the lunar surface. However, according to Hapke's calculations, the electrostatic forces acting on the lunar surface are insufficient by eight orders of magnitude to maintain the particles against the force of gravity. Also, it might be pointed out that a suspension of such a cloud would be a violation of Earnshaw's theorem which states that a body cannot remain in stable equilibrium between electrostatic or electromagnetic forces and gravity (Epstein, Ref. 34). The Mie theory is usually applied to spherical particles in noninteracting form (air molecules, colloidal suspensions in liquids, interstellar grains in space, etc.). The application to a surface such as the moon with unknown boundary values, due to its unknown properties, seems unjustified.

Contrived Polarimetric Models

The indirect approach to the interpretation of scattering signatures through the construction of models has two principal limitations. The first is that there is no proof of uniqueness, that is, even if one were to find a model that reproduced exactly all the features of the observed signature, he could not state that the model and the physical surface were identical. The second limitation has to do with the level of sophistication permitted in the model. The range of models for which Maxwell's equations can be exactly solved is very limited. Further, since the intention is to explore changes in the signature as the model is varied, the form of the solution should be fairly simple. There exist, for example, numerical techniques for approximating the signatures of many shapes, that cannot be solved exactly, but they are probably too unwieldly to permit extensive exploration of the effects of model changes. Thus, the models chosen must have an order of complexity considerably lower than the physical surface.

With these limitations in mind, let us consider some of the properties of the lunar surface and its optical signature. The lunar surface has a very low conductivity and is probably very rough on the order of millimeters. This roughness was indicated by photometric studies and has been verified by the Luna 9 photographs. The principal features of the polarization curve are a

negative minimum at low phase angles, an inversion in the vicinity of 20° phase angle, and a positive maximum of the order of 10 percent polarization in the vicinity of 100° phase angle (Ref. 4). There is also an inverse relationship between the albedo and the magnitude of the maximum peak of the polarization curve.

The photometric properties of the lunar surface have been fairly well explained in terms of shadowing effects (Refs. 2, 7, 35, and 36). The polarization properties should then be explained within the context of these photometric models. All the photometric models are scalar models, in which the signature is the result of postulated brightness functions for various macroscopic elements and the shadowing caused by the geometry of the elements. In fact, however, the light scattering functions of the elements will not be scalar but vector in nature, and the complete optical signature should be obtained by computing separately the brightness functions for the parallel and perpendicular polarization modes.

In Refs. 2 and 7 the elements were considered to have diffusely scattering surfaces. Hapke assumed small irregularly shaped objects and Halajian and Spagnolo assumed plane strips. The logical starting point for constructing polarimetric models is a study of the polarization properties of these diffusely scattering elements of the photometric models.

To do this, it is necessary to make assumptions about the detailed structure of the surface of these diffusely scattering elements. It is at this point that we run into considerable limitations in the ability to obtain calculated solutions for the reflection properties. Since these surfaces scatter diffusely, they must be rough and the theoretical polarization properties of rough surfaces are not well known. The few attempts that have been made to study this problem are limited to perfectly conducting surfaces (Refs. 37 and 38).

The discussion in this phase of the report will be limited to materials that are perfect dielectrics, since this and the other extreme case of perfect conductors are the simplest to handle. This definitely represents a departure from the conditions to be expected on the moon. It is also superficially inconsistent with the photometric models mentioned above, since they specify opaque elements. However, both of these deficiencies could be rectified by including the effects of a small absorption coeffi ient in the medium. This, in fact, may be a reasonable way to estimate the thickness required for the strip elements in the Grumman contrived photometric models (Ref. 7). However, there is no point in

complicating the present discussion by including absorption until such time as the polarimetric properties are better uncerstood.

Other effects that are neglected in this report are multiple scattering, diffraction, and shadowing. It appears that the most serious of these is probably shadowing, and the possible effects of neglecting it will be discussed under each of the models below. Neglecting multiple scattering and diffraction is reasonable if the reflectivity of model facets and the ratio of wavelength to facet dimensions are small. Recently, however, Hopfield (Ref. 39) has suggested a mechanism for explaining the negative polarization at small phase angles that depends on diffraction effects in the shadow region of the edge of an opaque half plane. Since the photometric models and the polariztion models discussed below all contain such edges, this explanation seems to be promising and should certainly be explored further.

The polarimetric models in this report will be seen to fit the structure of the Grumman photometric models better than they fit Hapke's model, the reason being that we chose simple models and the Grumman model has a simpler geometry than Hapke's. The polarimetric models describe the scattering properties of the ne r surface region of the macroscopic elements, and it should be fairly simple to modify them to fit macroscopic elements that have closed surfaces rather than plane surfaces.

An unsuccessful attempt was made to determine directly the polarization properties of Hapke's model by means of the Born approximation that expresses the far field scattered by a closed surface dielectric, of index of refraction close to unity, in the form of an infinite series. If the approximation is to be useful, successive terms in the series must represent corrections of decreasing magnitude. Regardless of the shape of the scatterer, the first Born approximation gives a percent polarization

$$P = \frac{1 - \cos^2\alpha}{1 + \cos^2\alpha}$$

for a homogeneous scatterer, where α is the phase angle.

This expression is derived from Eq. 14 of Ref. 40, which for our purposes can be written

$$\vec{E}_1 = (\hat{e}_o - \hat{k}_j \hat{k}_j \cdot \hat{e}_o)\, f\, (\vec{k})\ ,$$

where $\vec{E}_1$ is the far scattered field in the first Born approximation, $\hat{e}_o$ is a unit vector in the direction of polarization of the incident wave, $\vec{k} = \vec{k}_j - \vec{k}_o$, $\vec{k}_o$ is the wave vector of the incident wave, and $\vec{k}_j$ is the wave vector of the scattered wave, and f is a scalar function whose form is not of interest here. The intensity components of the scattered field parallel and perpendicular to the plane of vision are

$$I_\perp = |\ \hat{e}_\perp \cdot \vec{E}_{sc}\ |^2$$

$$I_{\shortparallel} = |\ \hat{e}_{\shortparallel} \cdot \vec{E}_{sc}\ |^2$$

where a common factor has been omitted and $\hat{e}_\perp$ and $\hat{e}_{\shortparallel} = \hat{e}_\perp \times \hat{k}_j$ represent unit vectors respectively perpendicular and parallel to the plane of vision. In the first Born approximation $\vec{E}_{sc} = \vec{E}_1$.

For incident light polarized perpendicular to the plane of vision:

$$\hat{e}_o = \hat{e}_\perp$$

$$\hat{e}_\perp \cdot \vec{E}_{sc} = f\, (\vec{k})\ ; \quad \hat{e}_{\shortparallel} \cdot \vec{E}_{sc} = 0$$

$$I_\perp^{(\perp)} = |\ f\, (\vec{k})\ |^2\ ; \quad I_{\shortparallel}^{(\perp)} = 0\ ,$$

with the superscripts on I indicating the polarization of the incident wave. For incident light polarized parallel to the plane of vision:

$$\hat{e}_o = \hat{e}_\perp \times \hat{k}_o$$

$$\vec{E}_1 = \left\{\ \hat{e}_\perp \times \hat{k}_o - \hat{k}_j \sin \alpha \right\} f\, (\vec{k})\ .$$

Since

$$\hat{k}_j \cdot \hat{e}_\perp \times \hat{k}_o = \sin \alpha,$$

then

$$\hat{e}_\perp \cdot \vec{E}_{sc} = 0$$

$$\hat{e}_\parallel \cdot \vec{E}_{sc} = \left\{ (\hat{e}_\perp \times \hat{k}_j) \cdot (\hat{e}_\perp \times \hat{k}_o) \right\} f(\vec{k})$$

$$= \hat{k}_j \cdot \hat{k}_o \; f(\vec{k})$$

$$I_\perp^{(\parallel)} = 0 \; ; \quad I_\parallel^{(\parallel)} = \cos^2 \alpha \; | \, f(\vec{k}) |^2$$

For unpolarized light incident we obtain the expression for P above. This result is what one expects from Rayleigh scattering, since this is equivalent to the first Born approximation. Thus, the first Born approximation alone is not suitable, and computational difficulties prevented us from determining the second Born approximation. Indeed in cases where this method has been applied to electromagnetic scattering problems, the second Born approximation has only been computed for zero phase angle (Refs. 40, 41).

Single Layer, Plane Facet Model

The simplest surface is a plane interface between two semi-infinite dielectric media with indices of refraction n_1 and n_2. This, however, is a specular reflector. To obtain diffuse reflection, consider an interface composed of small, plane facets whose micro-normals are oriented randomly with respect to the macro-normals. In two dimensions, which is the only case necessary for this model, it would appear as in Sketch 1 with the micro-normals all in the plane of the paper.
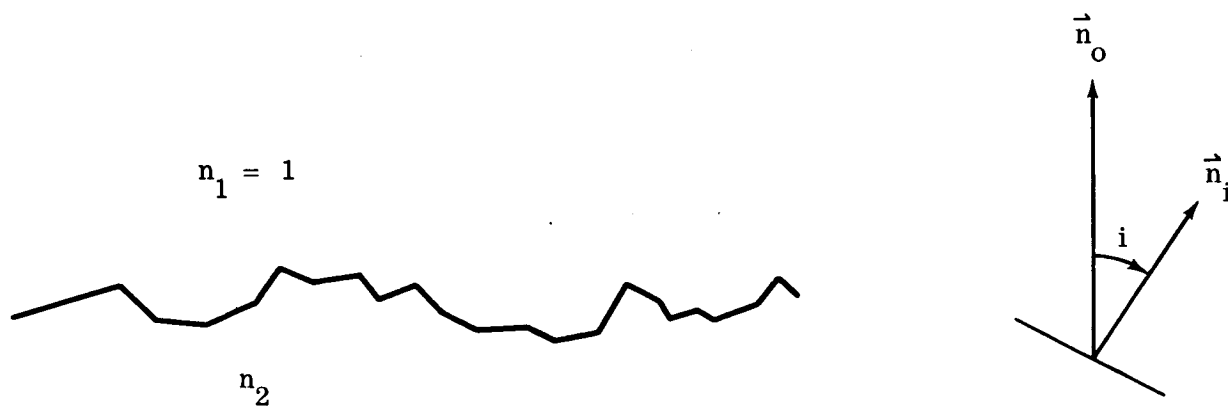
Sketch 1

The surface is described by the distribution of micronormals, $f(i)$, which specifies the total surface area $d\sigma_i$ of all facets whose micro-normals $\vec{n}_i$, lie within the angle increment, di, at an angle i from the macronormal, $\vec{n}_o$. (Refs. 42, 43)

$$d\sigma_i = \sigma_o \, f(i) \, di \, .$$

The projected area on the plane perpendicular to $\vec{n}_o$ is obtained by integrating

$$d\sigma_p = \sigma_o \, f(i) \, \cos i \, di$$

to obtain

$$\sigma_p = \sigma_o \int_{-\pi}^{\pi} f(i) \, \cos i \, di \, ,$$

which is the total area of the particular surface element of the photometric model under consideration. In most of this work it will be assumed that the surface is symmetrical about $\vec{n}_o$, that is, $f(i) = f(-i)$, and that it is not double valued, that is $f(i) = 0$ for $|i| > \frac{\pi}{2}$. For two dimensional models it will also be assumed that the model has unit depth, so that $d\sigma_i$ represents both the area and the linear dimension of the facet.

Consider the flux and polarization of light reflected from one facet, with local normal $\vec{n}_i$ (see Sketch 2 below) assuming unpolarized (natural) light incident.
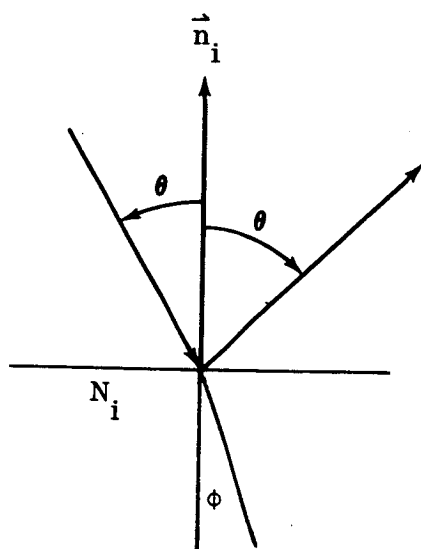
Sketch 2

If the area of the facet is N_i, the flux polarized perpendicular to the plane of vision, which for these simple plane facets is always the plane of incidence, is

$$I_{(i)\perp} = F_\perp^2(\theta)\, N_i \cos\theta\, I_{o\perp} ,$$

and the flux polarized parallel to the plane of vision is

$$I_{(i)\parallel} = F_\parallel^2(\theta)\, N_i \cos\theta\, I_{o\parallel} ,$$

where $F_\perp$ and $F_\parallel$ are the Fresnel reflection coefficients,

$$F_\perp(\theta) = - \frac{\sin(\theta-\phi)}{\sin(\theta+\phi)}$$

$$F_\parallel(\theta) = \frac{\tan(\theta-\phi)}{\tan(\theta+\phi)}$$

$$n_1 \sin\theta = n_2 \sin\phi ,$$

and for later use the Fresnel transmission coefficients are

$$T_\perp(\theta) = \frac{2\sin\phi\cos\theta}{\sin(\theta+\phi)}$$

$$T_\parallel(\theta) = \frac{2\sin\phi\cos\theta}{\sin(\theta+\phi)\cos(\theta-\phi)} .$$

$I_{o\perp}$ and $I_{o\parallel}$ are the perpendicular and parallel intensity components of the incident beam. They are equal for natural light and will be assumed to be unity.

If the surface element (composed of a distribution of facets) is viewed by a detector whose viewing axis makes an angle ε with the macro-normal $\vec{n}_o$ and the incident beam makes an angle ψ with $\vec{n}_o$ (see Sketch 3), then the only facet
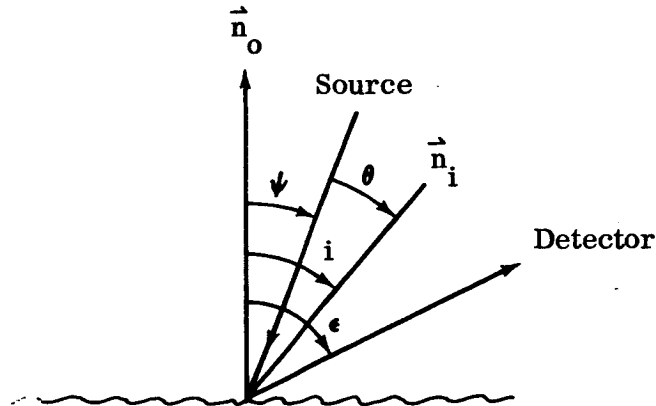
Sketch 3

which contributes is that for which $i = \frac{1}{2}(\epsilon + \psi)$,
so that $\theta = i - \psi = \frac{1}{2}(\epsilon - \psi)$.

For a continuous distribution of facets, N_i should be replaced by $d\sigma_i$ and

$$I_{(i)\perp} = \sigma_0 \int f\left(\frac{\epsilon+\psi}{2}\right) F_\perp^2 \left(\frac{\epsilon-\psi}{2}\right) \cos\left(\frac{\epsilon-\psi}{2}\right) di ,$$

where the integration is carried out over all facets that contribute to the detector for this value of ψ. If the fixed detector acceptance angle $d\epsilon_0$ is small, the integral can be approximated by

$$I_{(\epsilon,\psi)\perp} = \sigma_0 \, f\left(\frac{\epsilon+\psi}{2}\right) F_\perp^2 \left(\frac{\epsilon-\psi}{2}\right) \cos\left(\frac{\epsilon-\psi}{2}\right) \frac{d\epsilon_0}{2} ,$$

and

$$I_{(\epsilon,\psi)\parallel} = \sigma_0 \, f\left(\frac{\epsilon+\psi}{2}\right) F_\parallel^2 \left(\frac{\epsilon-\psi}{2}\right) \cos\left(\frac{\epsilon-\psi}{2}\right) \frac{d\epsilon_0}{2} .$$

The brightness function for this element of the photometric model is

$$B = \frac{I_\perp + I_\parallel}{\sigma_p \cos \epsilon}$$

177

$$B = \frac{\sigma_o}{\sigma_p} \; f \; (\frac{\varepsilon + \psi}{2}) \; \left\{ \; F_\perp^2 \; (\frac{\alpha}{2}) + F_{||}^2 \; (\frac{\alpha}{2}) \right\} \; \frac{\cos \frac{\alpha}{2}}{\cos \varepsilon} \; \frac{d\varepsilon_o}{2} \; ,$$

where $\alpha = \varepsilon - \psi$ is the phase angle, and the percent polarization is

$$P = \frac{I_\perp - I_{||}}{I_\perp + I_{||}}$$

$$P = \frac{F_\perp^2 \; (\frac{\alpha}{2}) - F_{||}^2 \; (\frac{\alpha}{2})}{F_\perp^2 \; (\frac{\alpha}{2}) + F_{||}^2 \; (\frac{\alpha}{2})} \; . \qquad (2)$$

The polarization properties of this model are unsatisfactory for the purpose of simulating the lunar surface. Since Eq. 2 involves only the Fresnel coeffiecients, and since $F_{||}$ (θ) is zero when θ equals the Brewster angle for the interface, this model predicts 100 percent polarization at a phase angle equal to twice the Brewster angle. Further, since the percent polarization is a function only of the phase angle and not of ψ or ε, the shadowing caused by facets within an element or by elements of the macroscopic model will have no effect on the polarization properties.

The behavior of the brightness function for this model has been examined for a uniform distribution of facet normals, i.e., $f \; (\frac{\varepsilon + \psi}{2})$ = constant, and for $\varepsilon = 0$, $n_2 = 1.5$. For phase angles less than 80° the function is roughly comparable to $\cos \frac{\alpha}{2}$, being only slightly greater. Beyond this point, the curve changes drastically, and at $\alpha = 160°$ the value is an order of magnitude larger than $\cos \frac{\alpha}{2}$ and twice the value of B at $\alpha = 80°$. From that point on, it decreases rapidly to zero at $\alpha = 180°$. This strange behavior is attributed to the fact that the derivation of the expression for B has ignored shadowing effects that, though small at small phase angles, are expected to be considerable at large phase angles. Therefore, any attempt to derive the brightness function from a consideration of the micro-structure should include the effects of shadowing.

Double Layer, Plane Parallel Slabs

The previous model failed to explain the polarimetric properties of the moon because no light is reflected in the parallel polarization mode when the phase angle equals twice the Brewster angle, so that the peak of the polarization curve is always 100 percent. To remedy this defect, it is necessary that some of the parallel polarized light transmitted into the medium be scattered back out again. This is also a closer fit to the real physical situation, since it is reasonable to suppose that the surface layers of the moon are not completely homogeneous. Therefore, any light which penetrates into these layers will be scattered by inhomogeneities, and some will be transmitted back through the surface to contribute to the observed intensity.

The simplest model which accomplishes this, is a two layer model with plane parallel interfaces and a semi-infinite second layer as in Sketch 4. Since we are assuming perfect dielectrics and broadband noncoherent light, the thickness of the first layer (n_2) is not important. The model is, of course, a specular scatterer. For a diffuse scatterer the model would consist of slabs of material n_2 cemented to the facets of a single layer model of material n_3 constructed as in the previous example. However, from the previous model, it is clear that the polarization properties are caused by the facet that is a specular reflector for any given source-detector configuration, and do not depend in any way on cooperative effects between facets. Therefore, it is desirable to explore the properties of one slab, without encumbering the discussion with details of a distribution function and viewing angles.

Sketch 4 shows the rays that arise from a single incident ray. The f's are reflection or transmission coefficients. Since the top layer is assumed thick enough so that no interference effects are introduced, the total intensity of perpendicular polarized light received by the detector for a phase angle α is

$$I_\perp = \left\{ f_1^2 + f_2^2 f_4^2 \left[f_3^2 + f_3^4 f_5^2 + f_3^6 f_5^4 \cdots \right] \right\} .$$

Since the series in brackets is a geometric progression, this becomes

$$I_\perp = f_1^2 + \frac{f_2^2 f_3^2 f_4^2}{1 - f_3^2 f_5^2} .$$
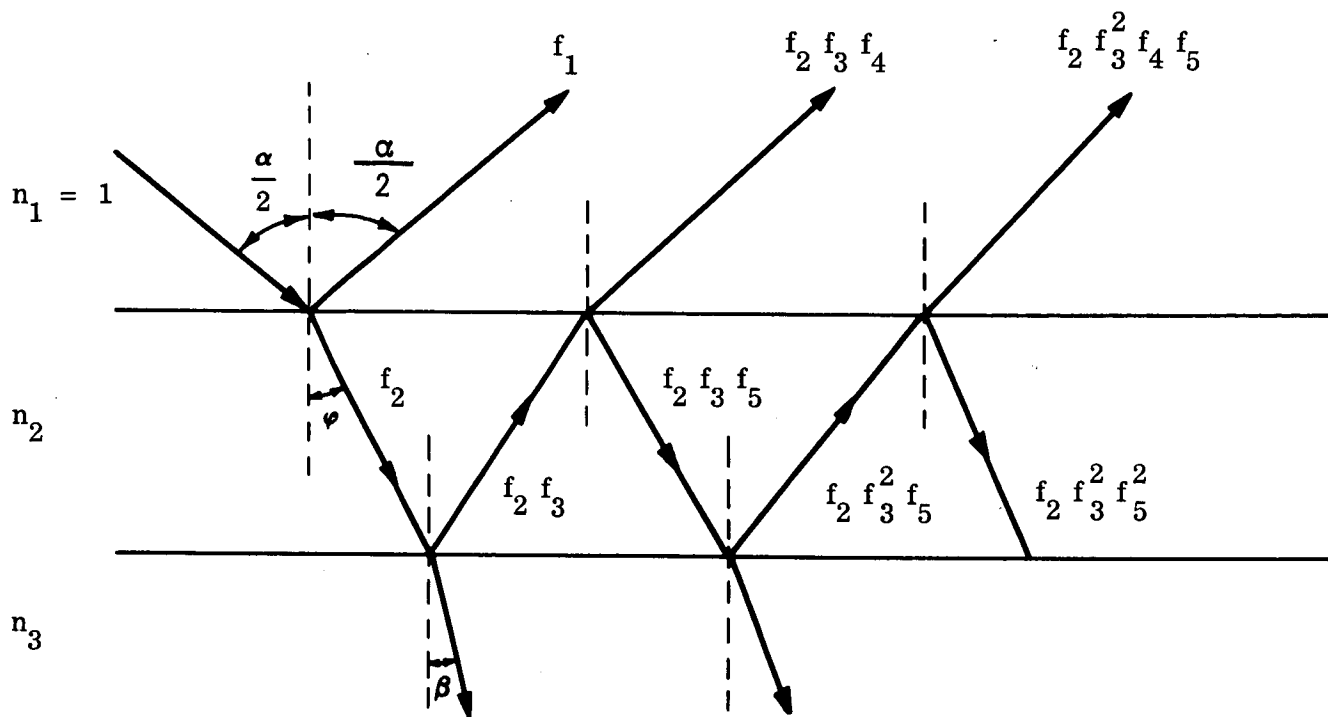
Sketch 4

The f's are the Fresnel coefficients. By using Snells' law

$$\sin \frac{\alpha}{2} = n_2 \sin \varphi = n_3 \sin \beta$$

they can be reduced to

$$f_1^2 = \frac{\sin^2\left(\frac{\alpha}{2} - \varphi\right)}{\sin^2\left(\frac{\alpha}{2} + \varphi\right)} \quad \xrightarrow{\alpha \to 0} \quad \frac{(n_2 - n_1)^2}{(n_2 + n_1)^2}$$

$$f_3^2 = \frac{\sin^2(\varphi - \beta)}{\sin^2(\varphi + \beta)} \quad \xrightarrow{\alpha \to 0} \quad \frac{(n_3 - n_2)^2}{(n_3 + n_2)^2}$$

$$f_5^2 = f_1^2$$

$$f_2^2 f_4^2 = \left(1 - f_1^2\right)^2$$

$$I_\perp = \frac{f_1^2 - 2f_1^2 f_3^2 + f_3^2}{1 - f_1^2 f_3^2} \, . \tag{3}$$

In a similar fashion, the intensity of parallel polarized light
received by the detector is

$$I_\parallel = \frac{\bar{f}_1^2 - 2\bar{f}_1^2 \bar{f}_3^2 + \bar{f}_3^2}{1 - \bar{f}_1^2 \bar{f}_3^2} \, , \tag{4}$$

where

$$\bar{f}_1^2 = \frac{\tan^2\left(\frac{\alpha}{2} - \varphi\right)}{\tan^2\left(\frac{\alpha}{2} + \varphi\right)} \quad \xrightarrow{\alpha \to 0} \quad \frac{(n_2 - n_1)^2}{(n_2 + n_1)^2}$$

$$\bar{f}_3^2 = \frac{\tan^2(\varphi - \beta)}{\tan^2(\varphi + \beta)} \quad \xrightarrow{\alpha \to 0} \quad \frac{(n_3 - n_2)^2}{(n_3 + n_2)^2} \, .$$

181

These relations are valid for $n_2 > 1$, $n_3 > 1$. If either n_3 or n_2 is less than one, the possibility of total internal reflection arises, and the formulae would have to be examined for applicability. However, this does not represent a physical situation in which we are interested.

The percent polarization is

$$P = \left\{ \left(f_1^2 - 2f_1^2 f_3^2 + f_3^2 \right) \left(1 - \bar{f}_1^2 \bar{f}_3^2 \right) \right.$$

$$\left. - \left(\bar{f}_1^2 - 2\bar{f}_1^2 \bar{f}_3^2 + \bar{f}_3^2 \right) \left(1 - f_1^2 f_3^2 \right) \right\} \times$$

$$\times \left\{ \left(f_1^2 - 2f_1^2 f_3^2 + f_3^2 \right) \left(1 - \bar{f}_1^2 \bar{f}_3^2 \right) \right.$$

$$\left. + \left(\bar{f}_1^2 - 2\bar{f}_1^2 \bar{f}_3^2 + \bar{f}_3^2 \right) \left(1 - f_1^2 f_3^2 \right) \right\}^{-1} .$$

It has not been possible to prove that this expression is always positive. However, the value of P for every $\alpha = 2\theta$ (θ integral, and $0° \leq \theta \leq 89°$) has been computed for slightly more than 200 cases (i.e., set of values of n_2 and n_3), and in no case have negative values been obtained. This model, therefore, also fails to predict the negative polarization observed on the moon.

However, this model does provide qualitative agreement with some other features of the lunar signature, specifically the behavior of the position and magnitude of peak polarization and the albedo. Let us consider the albedo first. Since this is a specular surface, let us define the albedo simply as the reflectivity for zero phase. This avoids the apparent inconsistency of albedoes greater than one which would occur if it were defined in reference to a diffuse reflector. With this definition, then, the albedo is

$$A = \frac{1}{2} \left[I_\perp + I_{\parallel} \right] \quad \text{at} \quad \alpha = 0 ,$$

the factor $\frac{1}{2}$ arising from the assumption that $I_{o_{\parallel}} = I_{o_\perp} = 1$. Then, using Eqs. (3) and (4),

$$A = \frac{n_3(n_2 - n_1)^2 + n_1(n_3 - n_2)^2}{(n_1 + n_3)(n_2^2 + n_1 n_3)} \, ,$$

which shows the symmetry between n_1 and n_3. Substituting $n_1 = 1$ and rewriting, this can be put into a better form for calculation

$$A = 1 - \frac{4 n_2 n_3}{(1 + n_3)(n_2^2 + n_3)} \, .$$

Let us examine the behavior of the albedo as either n_2 or n_3 is held constant:

n_2 = constant: $\qquad \dfrac{\partial A}{\partial n_3} = - \dfrac{4 n_2 (n_2^2 - n_3^2)}{(1 + n_3)^2 (n_2^2 + n_3)^2}$

$$\frac{\partial^2 A}{\partial n_3^2} = \frac{4 n_2}{(1 + n_3)^3 (n_2^2 + n_3)^3} \left\{ 2 n_2^4 + 2 n_2^2 + 6 n_2^2 n_3 - 2 n_3^3 \right\}$$

$\dfrac{\partial A}{\partial n_3} = 0 \qquad$ at $\qquad n_3 = n_2 \quad$ and $\quad n_3 \rightarrow \infty$

and

$\dfrac{\partial^2 A}{\partial n_3^2} > 0 \qquad$ at $\qquad n_3 = n_2$

$\dfrac{\partial^2 A}{\partial n_3^2} < 0 \qquad$ as $\qquad n_3 \rightarrow \infty$

$$A = \frac{(n_2 - 1)^2}{n_2^2 + 1} \qquad \text{at} \qquad n_3 = 1 \quad \text{or} \quad n_3 = n_2^2$$

$$A = \frac{(n_2 - 1)^2}{(n_2 + 1)^2} \qquad \text{at} \qquad n_3 = n_2$$

$$A \to 1 \qquad \text{as} \qquad n_3 \to \infty$$

The behavior of A as a function of n_3 for n_2 constant is shown in Sketch 5.

n_3 = constant:
$$\frac{\partial A}{\partial n_2} = - \frac{4n_3(n_3 - n_2^2)}{(1 + n_3)(n_2^2 + n_3)^2}$$

$$\frac{\partial^2 A}{\partial n_2^2} = \frac{4n_3}{(1 + n_3)} \frac{(6n_2 n_3 - 2n_2^3)}{(n_2^2 + n_3)^3}$$

$$\frac{\partial A}{\partial n_2} = 0 \qquad \text{at} \qquad n_2 = \sqrt{n_3} \quad \text{and} \quad n_2 \to \infty$$

and

$$\frac{\partial^2 A}{\partial n_2^2} > 0 \qquad \text{at} \qquad n_2 = \sqrt{n_3}$$

$$\frac{\partial^2 A}{\partial n_2^2} < 0 \qquad \text{as} \qquad n_2 \to \infty$$

$$A = \frac{(n_3 - 1)^2}{(n_3 + 1)^2} \qquad \text{at} \quad n_2 = 1 \quad \text{or} \quad n_2 = n_3$$

$$A = \frac{(1 - \sqrt{n_3})^2}{1 + n_3} \qquad \text{at} \quad n_2 = \sqrt{n_3}$$

$$A \to 1 \qquad \text{as} \quad n_2 \to \infty$$

The behavior of A as a function of n_2 for n_3 constant is shown in Sketch 6.

For a change in both n_2 and n_3,

$$dA = - \frac{4n_3(n_3 - n_2^2)}{(1 + n_3)(n_2^2 + n_3)^2} \, dn_2 - \frac{4n_2(n_2^2 - n_3^2)}{(1 + n_3)^2(n_2^2 + n_3)^2} \, dn_3$$

so that the requirement for an _increase_ in albedo is

$$- n_3(1 + n_3)(n_3 - n_2^2) \, dn_2 - n_2(n_2^2 - n_3^2) \, dn_3 > 0$$

or

$$- (1 + n_3)(n_3 - n_2^2) \frac{dn_2}{n_2} - (n_2^2 - n_3^2) \frac{dn_3}{n_3} > 0 \; .$$

Unfortunately, the expression for the polarization cannot be written in a simple manner as a function only of the phase angle. Therefore, the only practical way for determining the position and magnitude of the polarization peak is by computer calculation. A program has been written that computes, for any n_2 and n_3, the intensities $I_\perp$ and $I_{\parallel}$, and the percent polarization for every
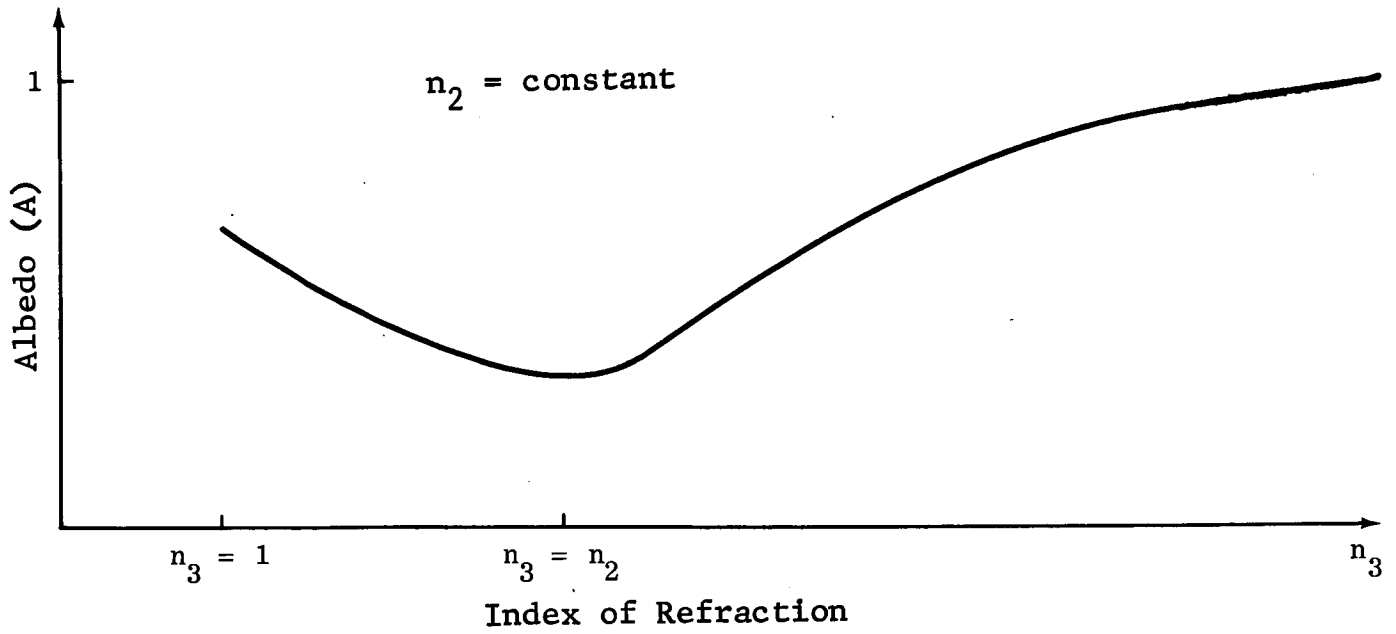
Sketch 5
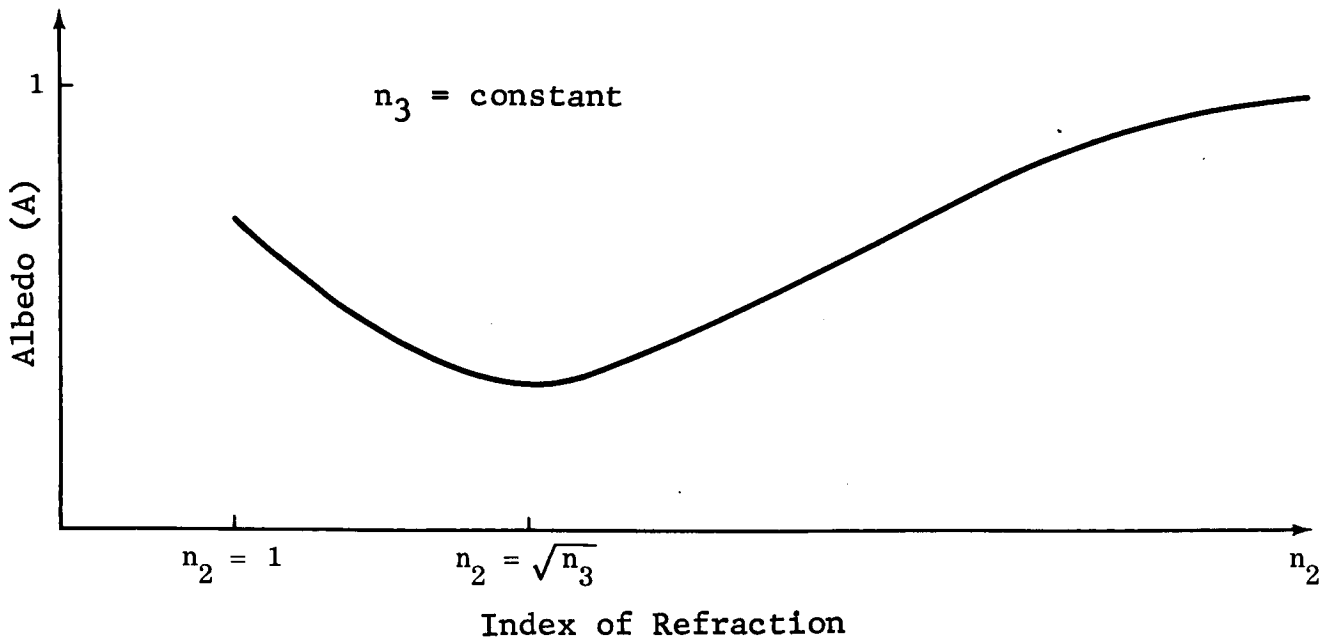
Sketch 6

186

even degree phase angle. Table 13 contains a compilation of the data relevant to a discussion of the peak polarization. The phase angles given in this table were estimated from the computer print-out only which explains the few apparent irregularities in the trend of α_{max}.

The full polarization-phase angle curves have been plotted in Figs. 107, 108, and 109 for $n_2 = 1.09$, 2.6, 6.76, and $n_3 = 1.2$, 3.0, 10.0, where all the curves on a single figure correspond to a fixed value of n_2. These curves all have the same general shape. The differences among them can be adequately discussed in terms of the position and magnitude of the maxima. In Fig. 107 the maxima move down and to the right as n_3 increases, in Fig. 109 they move up and to the left, and in Fig. 108 they move up and to the left at first, and then down and to the right. This behavior, which is fully supported by the data in Table 13, can be explained in terms of the relative magnitude of n_2 and n_3.

When $n_3 = 1$, the equations describing this model simplify to:

$$\beta = \frac{\alpha}{2}$$

$$f_1^2 = f_3^2 \quad ; \quad \bar{f}_1^2 = \bar{f}_3^2$$

$$P = \frac{f_1^2 - \bar{f}_1^2}{f_1^2 + \bar{f}_1^2 + 2f_1^2\bar{f}_1^2} .$$

This expression for P is a maximum (equal to unity) when $\bar{f}_1^2 = 0$, which occurs when $\alpha = \alpha_B$, where α_B is the phase angle equal to twice the Brewster angle for medium n_2. Also, when $n_3 = n_2$, the model reduces to a single layer model, and P is again equal to unity at $\alpha = \alpha_B$. This point ($\alpha = \alpha_B$, $P = 1$) is indicated by a cross (+) on the figures. Further, as n_3 (or n_2) increases without limit, $P \to 0$ at all phase angles. The behavior of P_{max} now can be described. At $n_3 = 1$ it is at point (+) ($P = 1$, $\alpha = \alpha_B$). As n_3 increases, it moves to smaller P values, but returns to (+) again when n_3 reaches the value n_2. With further increase in n_3, it moves to smaller P values and approaches zero.

187

Table 13

Parametric Behavior of the Locus of Maxima for the Two Layer Parallel Plane Slab Model

m_2 / m_3		1.00	1.09	1.40	1.42	1.44	1.46	1.48	1.50	1.52	1.54	1.60	1.73	2.00	2.24	2.45	2.60	3.16	5.48	6.76
5.00	A	.444	.412	.329	.326	.322	.318	.312	.316	.307	.344	.295	.279	.254	.254	.258	.263	.297	.478	.554
	ρ_{max}	1	.580	.368	.368	.369	.371	.373	.374	.379	.383	.347	.437	.538	.629	.762	.748	.877	.995	.954
	α_{max}	157	148	134	134	139	139	140	140	140	140	140	140	141	141	142	142	146	159	163
		↓	I		↓	↓				A			II	↓	↓	↓		↓	↓	II
6.00	A	.516	.480	.347	.343	.388	.384	.380	.377	.324	.342	.351	.346	.315	.303	.301	.301	.323	.424	.552
	ρ_{max}	1	.509	.368	.367	.367	.368	.309	.316	.313	.315	.322	.365	.435	.519	.588	.634	.728	.895	.991
	α_{max}	141	150	142	142	142	143	142	142	143	143	143	143	144	144	144	145	148	159	163
		↓	I		↓	↓			A				II		↓	↓	B	B		III
6.76	A	.551	.523	.441	.436	.432	.428	.424	.420	.416	.413	.402	.382	.352	.337	.331	.336	.342	.481	.551
	ρ_{max}	1	.465	.273	.272	.272	.272	.273	.274	.275	.277	.285	.316	.383	.455	.519	.563	.707	.906	1
	α_{max}	163	151	143	143	143	144	144	144	144	144	145	145	146	146	146	147	149	160	163
		↓	I	I	↓	↓		↓		A			II		↓	↓	↓	B		III
10.0	A	.649	.646	.574	.570	.566	.563	.559	.556	.550	.548	.537	.512	.481	.458	.443	.436	.425	.503	.558
	ρ_{max}	1	.340	.185	.184	.183	.182	.181	.181	.182	.182	.185	.185	.241	.289	.334	.366	.484	.829	.923
	α_{max}	168	154	147	148	148	148	148	149	149	149	150	151	153	153	152	152	152	160	163
		↓		I	↓	↓		I	↓	A		A	II		II	II	↓	↓	B	↓
3.00	A	.875	.866	.830	.829	.826	.835	.823	.820	.817	.815	.816	.788	.772	.752	.737	.726	.695	.645	.655
	ρ_{max}	.620	.620	.628	.626	.606	.648	.656	.684	.629	.574	.567	.577	.672	.798	.924	.102	.241	.313	.401
	α_{max}	176	161	156	157	157	157	157	158	158	151	161	164	168	168	168	168	166	164	165
		↓			↓			I				A	II	A		II		↓	B	B

Table 13 (cont.)

Parametric Behavior of the Locus of Maxima for the Two Layer Parallel Plane Slab Model

m_3		1.00	1.09	1.40	1.42	1.44	1.46	1.48	1.50	1.52	1.54	1.60	1.73	3.00	2.24	2.45	2.60	3.16	5.48	6.76
1.20	A	.00826	.00416	.0534	.0368	.0403	.0430	.0474	.0514	.0554	.0594	.0714	.0948	.141	.214	.258	.288	.354	.417	.484
	ρ_{max}	1	.984	.469	.988	.987	.926	.985	.923	.981	.981	.973	.970	.957	.933	.911	.906	.844	.656	.542
	σ_{max}	100	160	111	111	113	113	114	115	115	117	119	123	131	136	140	143	149	162	165
		I	III	III							III								
1.50	A	.0400	.0268	.0289	.0308	.0329	.0352	.0375	.0400	.0426	.0454	.0542	.0746	.127	.175	.216	.244	.344	.513	.656
	ρ_{max}	1	.964	.994	.996	.998	.990	.990	1	1.06	1.00	.994	.984	.959	.933	.909	.891	.825	.597	.510
	σ_{max}	113	114	109	110	111	112	112	113	113	114	116	121	129	134	138	140	148	141	165
		I		II				III			III								
1.94	A	.105	.0829	.0541	.0542	.0544	.0550	.0556	.0563	.0573	.0584	.0623	.0748	.111	.150	.185	.216	.300	.546	.635
	ρ_{max}	1	.910	.962	.873	.883	.894	.904	.913	.923	.931	.954	.955	.990	.988	.971	.957	.897	.665	.572
	σ_{max}	124	128	117	117	117	117	117	117	117	117	118	121	127	152	136	139	146	141	144
		I	I		B				II A	II	III				B	III		III		
2.56	A	.193	.163	.109	.107	.106	.105	.104	.105	.102	.162	.161	.104	.123	.150	.172	.142	.276	.514	.592
	ρ_{max}	1	.838	.691	.699	.707	.716	.724	.734	.747	.757	.789	.855	.948	.986	.944	.966	.975	.723	.675
	σ_{max}	137	136	126	126	126	125	125	125	125	125	125	126	129	133	136	138	145	140	143
		I	I					A	II A	II	II			B		III		III		
3.00	B	.250	.219	.153	.151	.149	.147	.144	.143	.141	.140	.137	.134	.143	.162	.164	.201	.276	.503	.584
	ρ_{max}	1	.783	.599	.644	.611	.618	.625	.633	.642	.651	.681	.747	.844	.935	.971	.986	.922	.843	.746
	σ_{max}	143	140	130	130	136	129	129	130	130	129	129	129	131	134	136	138	145		144
		I	I					A	A	II	II			B	B	B		III	III	
4.00	B	.360	.328	.248	.245	.242	.238	.235	.232	.229	.227	.220	.208	.200	.205	.246	.230	.277	.493	.565
	ρ_{max}	1	.470	.451	.450	.462	.465	.469	.474	.480	.484	.506	.559	.678	.723	.846	.878	.945	.680	.875
	σ_{max}	152	145	136	134	136	136	136	136	136	136	136	136	136	137	134	140	145	153	165
		I	I					A	A		II		I			B		III		III

189

Thus, the locus of maxima is composed of a closed loop that begins and ends at (+), and a tail that begins at (+) and decreases to zero. These loops have not been shown in the figures for constant n_2 since they are very small. In the figures for constant n_3 (see below) the loops have been drawn. The behavior with respect to α can be determined from Table 13. As n_3 increases from 1 to n_2, the loop is traversed in a clockwise sense, and as it increases beyond n_2 the tail moves down and to the right. Furthermore, for all curves for which n_2 is constant, all points on the loop lie to the right of point (+). The locus of P_{max} for constant n_2 can therefore be divided into three trends, if we define n' as the value of n_3 between $n_3 = 1$ and $n_3 = n_2$, for which P_{max} is a minimum. The trends are defined for n_3 increasing.

Region I: $1 \leq n_3 \leq n'$ P_{max} decreasing, α_{max} increasing and then decreasing

Region II: $n' \leq n_3 \leq n_2$ P_{max} increasing, α_{max} decreasing and then constant at α_B

Region III: $n_2 \leq n_3 \to \infty$ P_{max} decreasing, α_{max} increasing

The regions are defined in terms of the behavior of P_{max} only. The notes concerning α_{max} are observations of the behavior of α_{max} within the regions. The relative positions of the curves for $n_3 = 1.2$, 3.0, and 10.0 in Figs. 107, 108, and 109 can be understood in terms of these trends. In Fig. 107 all three are in Region III, in Fig. 108 $n_3 = 1.2$ is in Region I, $n_3 = 3.0$ and 10.0 are in Region III, and in Fig. 113 $n_3 = 1.2$ is in Region I, $n_3 = 3.0$ is in Region II, and $n_3 = 10.0$ is in Region III.

The behavior of P_{max} for n_3 held constant is more complicated. Nine polarization-phase angle curves have been drawn in Figs. 110, 111, and 112, this time holding n_3 constant for all curves in one figure, and the loci of P_{max} have been drawn in Figs. 113, 114, and 115. The behavior can

be studied by considering changes in P_{max} as n_2 increases from 1. When $n_2 = 1$ or $n_2 = n_3$, the model reduces to a single layer model with $P_{max} = 1$ at $\alpha = \alpha_B'$ where α_B' is the phase angle equal to twice the Brewster angle for medium n_3. Again, as n_2 varies from $n_2 = 1$ to $n_2 = n_3$, we have a closed loop beginning and ending at point (+) ($P_{max} = 1$, $\alpha = \alpha_B'$) and as n_2 increases beyond n_3, a tail beginning at (+) and approaching $P_{max} = 0$. The same trends can, therefore, be defined again and they have been indicated on Table 13 for n_3 constant. In all cases, the behavior of the tail is down and to the right for n_2 increasing. However, the behavior of the loop with respect to α_{max} changes.

For $n_3 = 1.2$ the loop is small and lies to the right of α_B'. The minimum value of P_{max} in the loop gets smaller as n_3 increases. The loop also rotates clockwise about (+) as n_3 increases (see Table 13). For $n_3 = 1.50$ and 1.96, the loop is partly to the right and partly to the left of α_B'. For values of n_3 equal to and greater than 2.56, the loop lies wholly to the left of α_B'. In Fig. 115 the loop crosses itself near the bottom. This is believed to be a valid property of the model, and not caused simply by inaccuracies in estimating α_{max} from the computer print-out. The same behavior can be seen in the data in Table 13 for $n_3 = 10$ and 30.

The behavior of P_{max} with respect to albedo is more interesting and can be seen on the same curves. When n_2 is constant, the albedo is a minimum for $n_3 = n_2$ (see Sketch 5). Then the albedo decreases monotonically as the loop is traversed clockwise starting at (+). As n_3 increases beyond n_2, the albedo increases monotonically along the tail. The complete behavior of the polarization maximum for n_2 constant is shown in Table 14.

When n_3 is constant, the albedo is a minimum for $n_2 = \sqrt{n_3}$ (see Sketch 6). Since the loop is defined between $n_2 = 1$ and $n_2 = n_3$, the minimum albedo occurs somewhere on the loop. Further, for all cases in Table 13, $n' \le \sqrt{n_3}$ so that the minimum albedo occurs within Region II. This is indicated in Table 13 where Region II has been further subdivided into IIA and IIB. Insufficient data for $n_3 = 1.2$ and 1.96 prevents a complete separation into IIA and IIB. The behavior of P_{max} for n_3 constant is shown in Table 15. There are no consistent trends for α_{max} in Regions I and IIA.

Tables 14 and 15 show that for certain ranges of n_2 and n_3, this model has the same behavior as has been observed on the moon and

Table 14

BEHAVIOR OF P_{max}

n_2 constant; n_3 increasing

Region		
I	$1 \leq n_3 \leq n'$; P_{max}	decreasing, A decreasing,
	α_{max}	increasing and then decreasing
II	$n' \leq n_3 \leq n_2$; P_{max}	increasing, A decreasing
	α_{max}	decreasing and then constant at α_B
III	$n_2 \leq n_3 \rightarrow \infty$; P_{max}	decreasing, A increasing
	α_{max}	increasing

Table 15

BEHAVIOR OF P_{max}

n_3 constant; n_2 increasing

| Region		
I	$1 \leq n_2 \leq n'$	P_{max} decreasing, A decreasing
IIA	$n' \leq n_2 \leq \sqrt{n_3}$	P_{max} increasing, A decreasing
IIB	$\sqrt{n_3} \leq n_2 \leq n_3$	P_{max} increasing, A increasing
		α_{max} constant or increasing
III	$n_3 \leq n_2 \rightarrow \infty$	P_{max} decreasing, A increasing
		α_{max} increasing

in laboratory samples, i.e., the inverse relationship between albedo and polarization maximum (Regions IIA, III). It should be recalled that the albedo in Table 13 is not the albedo of the macrosurface, but of the microfacets. The albedo of the macro-surface will be smaller than A by the ratio of the total area of the macrosurface projected onto the direction of viewing to the total area of microfacets that reflect light into the detector at zero phase angle. However, the polarization-phase angle curve is characteristic of the macrosurface as well as the microfacets and is not affected by shadowing. Therefore, in this model, the polarization-phase angle curve is a function of n_2 and n_3 only, and is not affected by the geometry of the surface (provided, of course, that the surface is rough enough to scatter diffusely).

Double Layer, Plane Facet Model

The previous model has reproduced the observed behavior of the lunar signature near the peak of the polarization curve for certain ranges of n_2 and n_3. However, it has not explained the negative polarization at low phase angles, and the values of P_{max} and α_{max} predicted by this model are higher than those observed on the lunar surface. Further, as noted above, the polarization properties of the model do not depend on the geometry of the macrosurface. To examine the dependence of the polarization on the geometry, it is necessary to construct a model in which the rays that are refracted within the upper layer pass out through a facet other than the one through which they entered the layer.

A simple model that will accomplish this is shown in Sketch 7. This is a two layer model, the upper surface being constructed as in the previous single layer model. The interface between the two layers is now plane and horizontal. A broad distribution of facet normals makes this a diffusely scattering model. Further, it is clear from the sketch that a ray which enters the top layer through a particular facet may, after reflection from the lower interface, leave the top layer through a different facet.

For a given position of source and detector, the flux reaching the detector is composed of light that is reflected from the top surface, and light that is transmitted through the top surface, reflected at the lower interface, and retransmitted through the top surface. The first component (reflected) arises from a limited number of facets that are so oriented that they reflect the image of the detector back along the source direction. The second component (refracted), however, may arise from any facet that is

Source

Detector

$n_1 = 1$

n_2

n_3
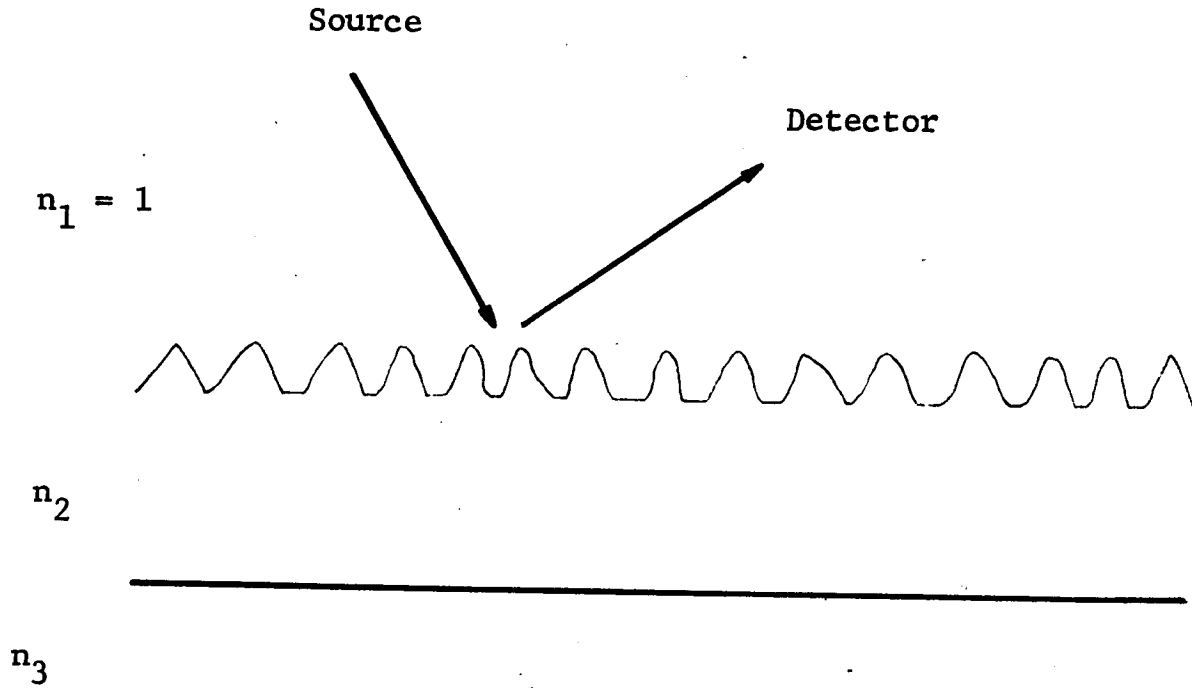
Sketch 7

illuminated by the incident beam. To calculate the refracted component, it is necessary to follow the incident beam as it enters each facet and trace its path through the model to determine whether or not it reaches the detector. A detailed formulation of the solution of this problem in the geometrical optics approximation has been obtained, and will be reported in Ref. 44.

This solution has been programmed for the computer so that the polarization properties of specific models, i.e., specific values of n_2 and n_3, can be obtained. At the time of this writing, the program is still being debugged and no results are available.

Investigation of the Stokes Vector as a Tool for
Interpreting the Lunar Signature

Another approach that did not meet with success was that of utilizing the properties of the stokes vector to interpret the lunar data. There is no more information in the Stokes vector than there is in the brightness and polarization curves coupled with a knowledge of albedo, plane of polarization and state of elliptical polarization. However, since the Stokes vector is formulated in a compact manner that relates it directly to the $\vec{E}$ and $\vec{H}$ field transformations, it was hoped that it could be used as a further tool for inferring the nature of the scattering surface.

Assume that the exact nature of the scatterer were known. Then the scattered field could, in principle, be determined from the incident field

$$\begin{pmatrix} E_\ell \\ E_r \end{pmatrix} = \begin{pmatrix} A_2 & A_3 \\ A_4 & A_1 \end{pmatrix} \begin{pmatrix} E_{o\ell} \\ E_{or} \end{pmatrix} \quad ;$$

where $E_{\ell(r)}$ is the component of the scattered field parallel (perpendicular) to the plane of vision and $E_{o\ell(r)}$ represents the same quantities for the incident field. The elements of the matrix (A) depend upon the detailed nature of the scatterer, as well as the propagation vectors of both the incident and the scattered fields. The analysis of a scattering problem consists essentially of determining the matrix (A). In the optical region, the features of the incident and scattered beams that are usually observed are the energy intensities in various polarization modes. The most complete description of such a beam is given by the four element Stokes vector that can be determined by experiment (Ref. 50).

The Stokes vectors of the incident and scattered beams are also related by a matrix transformation

$$\begin{pmatrix} I_\ell \\ I_r \\ U \\ V \end{pmatrix} = \begin{pmatrix} F_{11} & F_{12} & F_{13} & F_{14} \\ F_{21} & F_{22} & F_{23} & F_{24} \\ F_{31} & F_{32} & F_{33} & F_{34} \\ F_{41} & F_{42} & F_{43} & F_{44} \end{pmatrix} \begin{pmatrix} I_{o\ell} \\ I_{or} \\ U_o \\ V_o \end{pmatrix} \quad ,$$

where I_ℓ, I_r, U, and V provide information about the intensity of light polarized parallel to the plane of vision, the intensity of light polarized perpendicular to the plane of vision, the position of the plane of polarization, and the extent of circular polarization present. The elements of the matrix (F) can be expressed in terms of the elements of the matrix (A). (Ref. 29) Thus, given a knowledge of the scatterer, one can, in principle, determine the properties of the scattered beam, i.e., the Stokes vector.

However, in the problem of interpreting the lunar signature, we are given the Stokes vector and seek to determine the properties of the scatterer. This requires: 1) determining the elements of the matrix (F) from the observational data; 2) inverting the relationship between (A) and (F) so that the elements of (A) can be determined from the elements of (F); and 3) determining the properties of the scatterer from a knowledge of the matrix (A). The last of these is exactly the inverse scattering problem mentioned earlier and so, at the present time, there is no expectation that it can be accomplished. It might be argued that a determination of the matrix (A) might still provide more insight than is available from the Stokes vector alone. Before this can be done, the first of the requirements above must be completed, namely; the determination of the matrix (F).

The elements of (F) are functions of wavelength and the propagation vectors of the incident and scattered fields. It is clear that to determine (F) for one wavelength and at each phase angle, one must perform four experiments, each of which measures the Stokes vector of the scattered beam. The incident beam for the four experiments must be, repectively: 1) linearly polarized parallel to the plane of vision; 2) linearly polarized perpendicular to the plane of vision; 3) linearly polarized at some angle to the plane of vision other than 90° or 0°; and 4) circularly polarized. Since the data for the moon is generally limited to an unpolarized incident beam, the matrix (F) cannot be determined beyond a knowledge of the ratios of the elements in the first column to the corresponding elements in the second column. Therefore, no attempt was made to establish the functional dependence of the elements of (A) on the elements of (F) since this could not have been utilized to interpret the lunar signature.

Correlation of Polarization Factors and Comparison of Models to Lunar and Laboratory Data

Polarization of Composite Lunar Surfaces

In Phase III (Ref. 45) various composite laboratory samples were investigated. These samples were produced by sprinkling the powder from Phase II upon the specimens of Phase I. Except for coral, composite surfaces resulted, since the powders completely covered the horizontal or nearly horizontal portions of the Phase I specimens. The powders did not adhere very well to the inclined or vertical surfaces. For these samples, when observed at other than normal viewing, (i.e., $\epsilon = 60°$ in Phase III) the observed polarization is a combination of the characteristics of the powder and the underlying material. For such models, as well as for actual lunar areas where macroareas of different polarization characteristics exist, the theoretical analysis presented in Phase IV, Approach 1

of this report applies. However, for Model No. 4 of Phase III, for instance, so little of the coral powder $\leq 1\mu$ was sprinkled on volcanic ash No. 4 chunks, that the result appeared to be a dispersion of microareas (of the order of the particle sizes) on the base material (volcanic ash). For such a system, the individual particle scattering characteristics, combined with the background material, produces the observed polarization characteristics, and a macroarea combination could not be expected to apply.

Let us now consider the lunar surface. If it consisted of a meteoritic dust layer from interplanetary space and a uniform layer existed, the polarization would be the same all over the lunar surface. But the fact that the maria differ from the highlands, and that pits and irregularities were visible in the Ranger VII photographs (Ref. 46) attest the disruption of the lunar surface by some phenomena. If the lunar surface is, or was, disrupted by various size meteoritic impacts and/or volcanism, it would be expected that the undersurface material would be exposed in varying amounts. This would generally result in a composite surface on a macroscale. Earth based observations of the lunar surface cannot resolve areas less than about 1/2 mile across, and thus polarization characteristics of the moon will be restricted at best to that of 1/2 mile diameter areas.

For detailed investigation of the lunar surface and the delineation of suitable landing areas, better resolution of the lunar surface would be necessary, and the use of polarimetric analysis appears to hold promise in the analysis of the mineral constituents of the surface (Ref. 47).

The effect of luminescence could be a composite effect, if a general area is entirely composed of the luminescent material. If the luminescent material is particulate, and intermingled with other particulate matter, the analysis would be more complicated.

Polarization and Particle Sizes (Mie Theory)

To evaluate the application of the Mie theory to the lunar surface, let us consider a good, typical, simulated lunar model from Phase III, and elaborate upon the implications.

Models 5 and 6, which consisted of Haleakala volcanic ash sprinkled with a $\leq$ 1 μ powder of itself were good models for Mare Crisium. An analysis of the ash indicated these models to be of the Alkalitic Basalt group with the following probable chemical composition (Ref. 48) and of the corresponding real index of refraction (Ref. 49):

Material	Relative Amount (Ref. 48)	Index of Refraction (Ref. 49)
S_iO_2	43%	1.5
Al_2O_3	14%	1.7
Fe Oxides	15%	~3
MgO	6%	1.7
(Na_2O)*	4%	~1.5
(K_2O)*	1%	~1.5
T_iO_2	6%	2.5-2.7
CaO	11%	1.8

* These materials are not usually present as such; they are only reported as these compounds as a means for analysis and specification of the quantities of Na and K.

For this volcanic ash, being a predominantly silicate (S_iO_2) and aluminum oxide (Al_2O_3) surface, with a small amount of other contaminants, one could initially assume a real index of refraction (m) of 1.5. Then, referring to Phase IV, Approach 2, the Lowan curves for m = 1.55 (Fig. 105), show a large negative polarization for the indicated values of x. An x smaller than 1.8 could possibly yield a lower inversion angle, to correspond to that of the sample (and the lunar surface), and yield a particle size less than 1 micron (as used in the laboratory model). However, as was pointed out in the discussion of the Mie theory, a unique particle size cannot be determined. Further, from the results of Phase II, a unique particle size was not produced by the pulverization process used therein, and only a range of sizes $\leq$ 1μ resulted.

It thus appears that the Mie theory has little to offer in the polarimetric simulation of lunar surfaces. It is fruitless to proceed with an analysis utilizing the real and imaginary components, with the added complexity that would be involved in the use of this theory.

Albedo-Maximum Polarization

For the moon, as well as for the laboratory samples, the maximum polarization produced by a surface (as a function of phase angle) is found to be an involved inverse function of albedo (see Refs. 1, 17, 24, 45).

The single layer, plane facet model of Phase IV, Approach 3 was inadequate to explain the albedo-maximum polarization relationship, because the maximum polarization was always 100 percent and the maximum occurred at a phase angle of twice the Brewster angle.

However, the double layer, plane parallel slab model (discussed in Phase IV, 3) produced up to four definite correlation patterns between albedo and maximum polarization, which are defined by ranges of n_2 and n_3 (see Tables 14 and 15). Specifically, for this model, the albedo-polarization relationship for lunar and laboratory samples is obeyed in Regions II and III for constant n_2 and varying n_3; Region I violates the required condition. For the variation of n_2 with constant n_3 in Regions IIA and III, the albedo-polarization relation holds, whereas for Regions I and IIB it is violated.

Maximum Polarization and Corresponding Phase Angle

The shift of the location of the maximum polarization peak as a function of a particular material or lunar area is quite involved (see Figs. 116, 117, 118, and 119).

The data of Fig. 116 is a compilation of the Polarization of Solids given by Lyot (Ref. 13). Most materials have polarization maxima lying between about 120° and 150° phase angles, with the highest maxima appearing within this range. The mean phase angle is roughly 130°. From this limited data, one can infer that as the polarization maximum increases, it generally occurs at higher phase angles between 90 aand 130°. Above 130° (up to 170°) the general trend is for the maximum polarization to decrease as its location moves to higher phase angles.

Figure 117 is a compilation of the results of Phases I and II described previously. There is a general trend of increased maximum

polarization, located at higher phase angles between 81 and 124°, agreeing with the data of Lyot in this range. In Fig. 118 (except for Crisium, Models 5 and 6), taken from Phase III, the same general trend is followed. Crisium, Models 5 and 6 (which matched Crisium very well), have no dominant change of the location of the maximum polarization (+) as P_{max} varies. This group forms an average scatter of points located at about 98°.

The Wehner, Rosenberg, and KenKnight data summarized in Fig. 119 (Ref. 18) indicates a similar general upward trend of the magnitude of maximum polarization with the corresponding phase angle location. Two-thirds of the points are below 100° and one-third at or above 100°.

The results of the analysis of Phase IV, 3 (double layer, plane parallel slab model), presented in Tables 13 and 14 for variation of n_3 with n_2 constant, indicate that the initial portions of Regions I, II, and III would generally typify laboratory observations above approximately 120° or 130°, where P_{max} decreases as α_{max} increases (Fig. 116). Below about 120° or 130°, the second portion of Region I reproduces the general trend of most laboratory samples and Clavius (Figs. 116, 117, 118, and 119); notable exceptions (Fig. 116) are Crisium and the very good model Nos. 5 and 6. These latter three, having no apparent change in location of maximum with magnitude, lie within the second portion of Region II.

There is no clear trend shown for the effect of variations of n_2 with constant n_3 in Regions I and IIA (Table 15). The second portion of Region IIB (Table 15) depicts the lunar and laboratory trends below phase angles of 120° or 130°, whereas Region III depicts that above approximately 120° or 130°. The first portion of Region IIB again depicts the exceptions (Crisium and Model Nos. 5 and 6).

Conclusions

These models demonstrate that the analysis of polarimetric properties is inherently more difficult than the analysis of photometric properties, which was certainly to be expected because of the vector nature of the polarimetric problem as opposed to the scalar nature of the photometric problem. As a consequence, the level of sophistication initially possible in polarimetric models will be lower than in photometric models.

The single layer, plane facet model has not provided insight into the origin of the lunar polarimetric signature. It has, however, clearly emphasized one of the requirements for a meaningful

attempt at constructing a composite model designed to explain both photometric and polarimetric signatures. For such a model, it will not be sufficient to postulate a brightness function for the various model elements (Ref. 7) since the photometric and polarimetric properties must be mutually consistent. Therefore, both must be determined from an analysis of the microstructure (i.e., physical and geometrical properties) of the rough surface elements. The discussion of the single layer, plane facet model shows that the effects of shadowing within the microstructure must be considered.

The double layer, plane parallel slab model is a conceptually simple model, just one step removed from the plane interface. Despite this simplicity the model proved a few unanticipated results, the first of which is the difficulty of interpreting its polarization properties. It was not possible to determine by analytical methods, the values of P_{max} and α_{max} as functions of n_2 and n_3. The general behavior of these quantities as a function of n_2^2 (with n_3 held constant) or n_3 (with n_2 held constant) has been explored by numerical computations.

The second unexpected feature of this model is the complexity of the behavior of the $P_{max} - \alpha_{max}$ locus as n_2 or n_3 is varied. As discussed in the Correlation of Polarization Factors and Comparison of Models to Lunar and Laboratory Data subsection, this model reproduces, depending on the values of n_2 and n_3, the P_{max} - Albedo and $P_{max} - \alpha_{max}$ trends observed for the moon and many laboratory samples. This model produced up to four definite correlation patterns between albedo and maximum polarization (see Tables 14 and 15). The albedo-polarization relationships for lunar and laboratory samples is obeyed in certain ranges of values of the refractive indices n_2, n_3.

The relationship between maximum polarization and corresponding phase angle, observed on the moon and for most laboratory samples is reproduced by the model for certain ranges of values of the indices of refraction. When n_2 is constant and n_3 varies, laboratory observations whose peaks occur above about 120 or 130 degrees are matched by the initial portions of regions I, II, and III. The second portion of Region I reproduces the general trend of most laboratory samples and Clavius whose peaks occur below about 120 or 130 degrees.

For n_3 constant and varying n_2, the second portion of region IIB is similar to lunar and laboratory trends for samples whose peaks occur below approximately 120 or 130 degrees, whereas Region III is similar to those samples whose peaks occur above 120 or 130 degrees.

The two layer, plane facet model will be discussed when results are available.

Perhaps the principal limitation of these models is the fact that they are two dimensional. This eliminates all cross polarization effects and introduces an asymmetry that, in the two layer, plane facet model, may cause a nonzero percent polarization at zero phase. Further work on this problem should, therefore, be directed first at rectifying this limitation. Other work that should be considered includes:

1) Three layer, plane parallel slab

2) Inclusion of absorption effects

3) Inclusion of edge diffraction effects

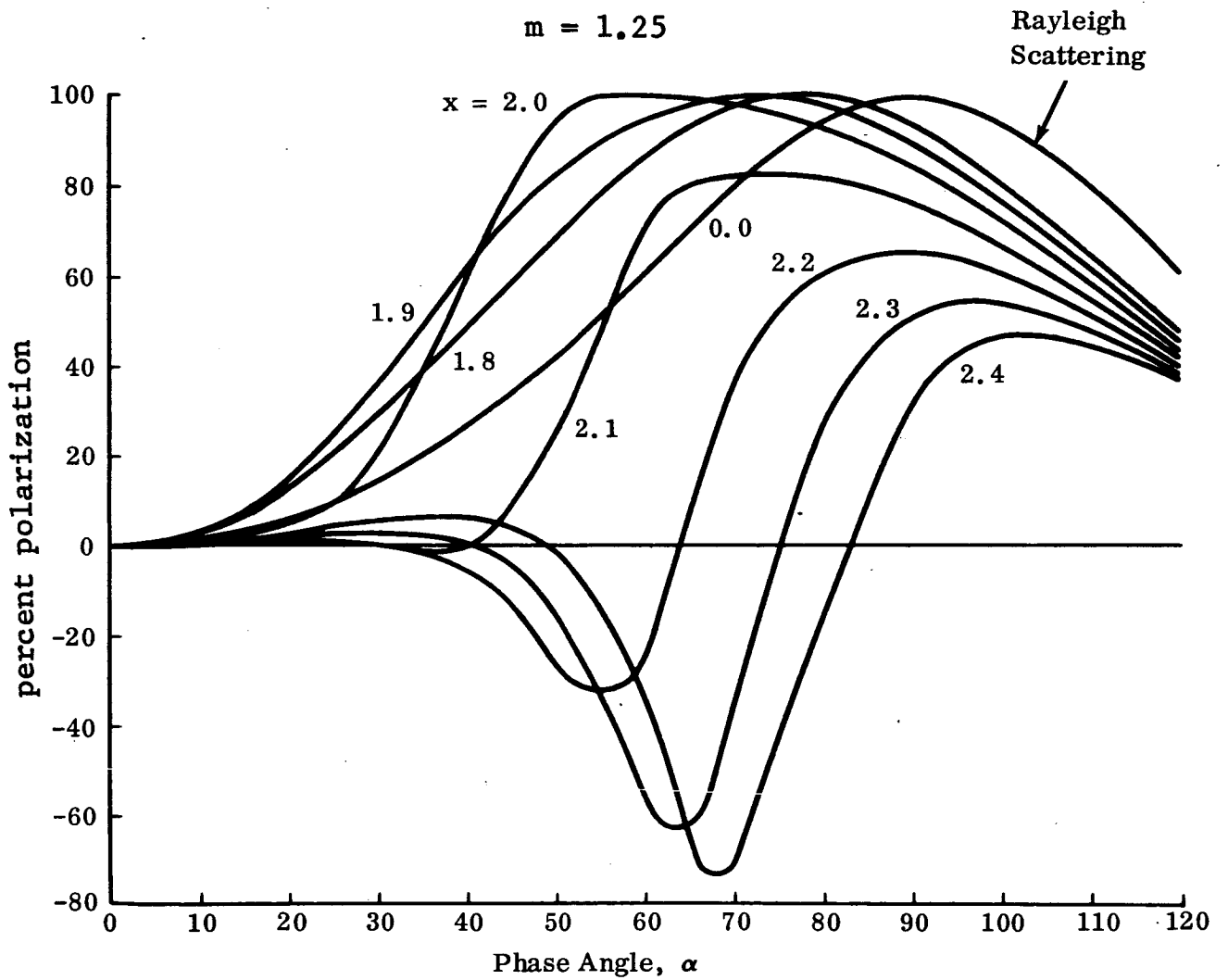4) Attempt to analyze both photometric and polarimetric properties of a composite model, including shadowing effects.

Fig. 104 Effect of Particle Size (x) on Polarization Curves
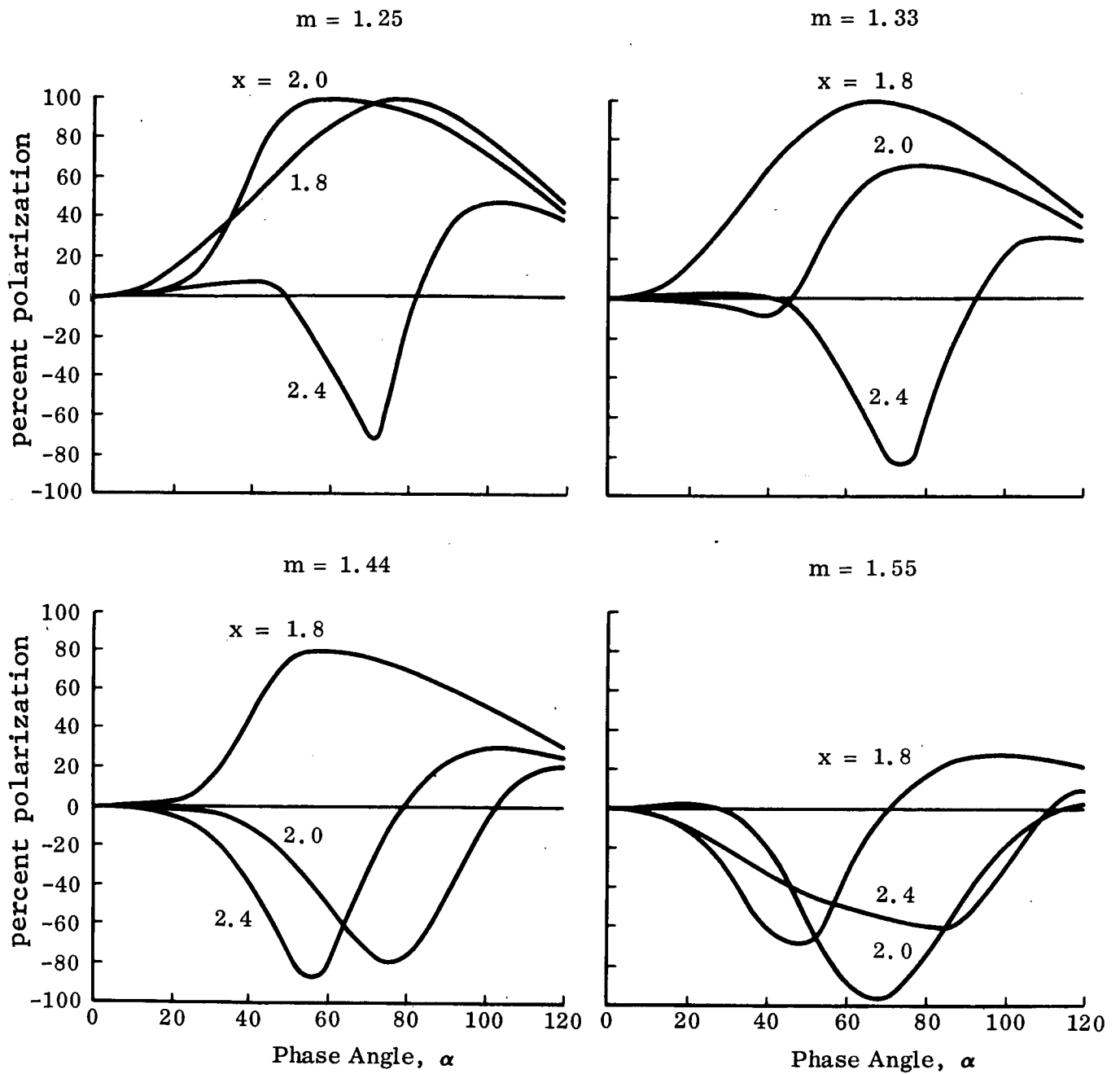Computed from Mie Theory for m = 1.25, and x = 1.8
to 2.4 in increments of 0.1

203

Fig. 105   Effect of Index of Refraction (m) on Polarization Curves
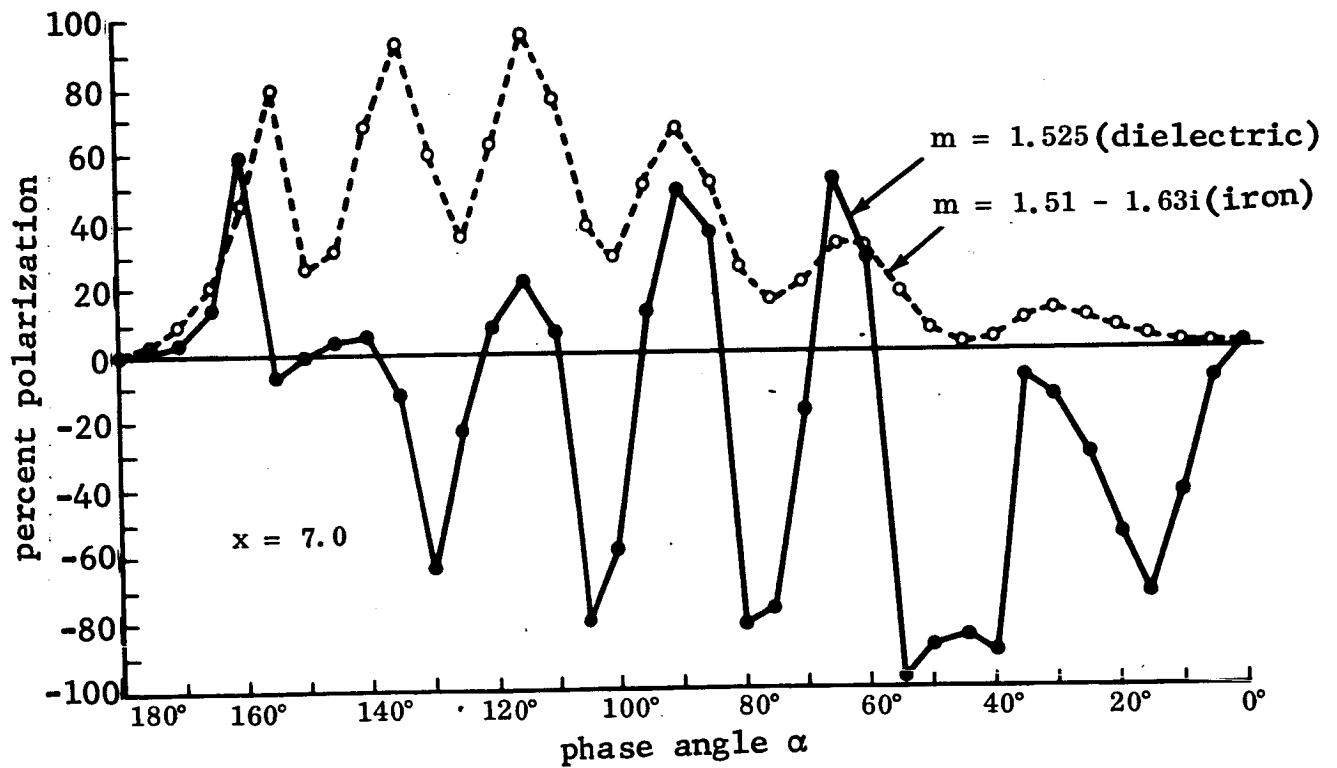from Mie Theory for x = 1.8, 2.0, 2.4 and m = 1.25,
1.33, 1.44 and 1.55

Fig. 106   Effect of Absorption on Polarization Curves Computed from
Mie Theory for x = 7 and m = 1.525 (dielectric) and
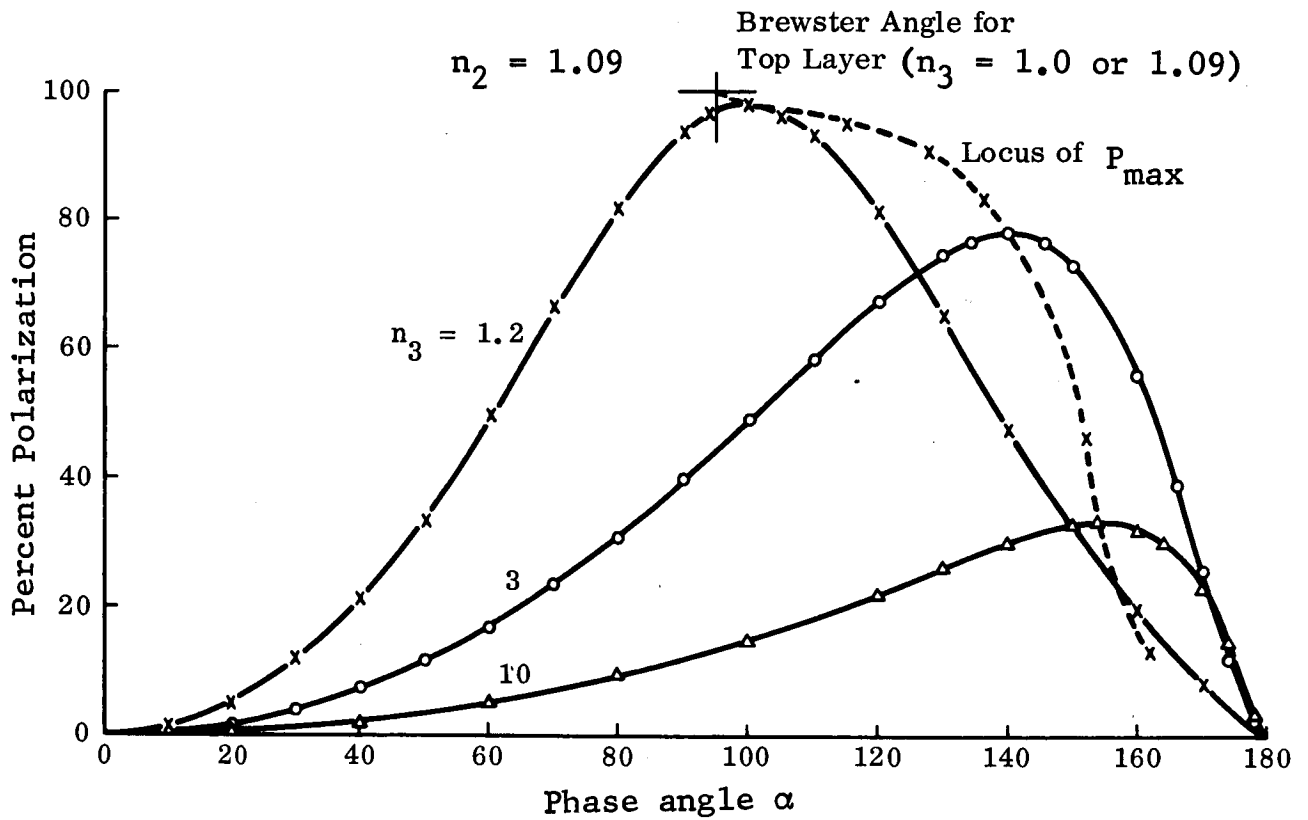m = 1.51-1.632 (iron)

205

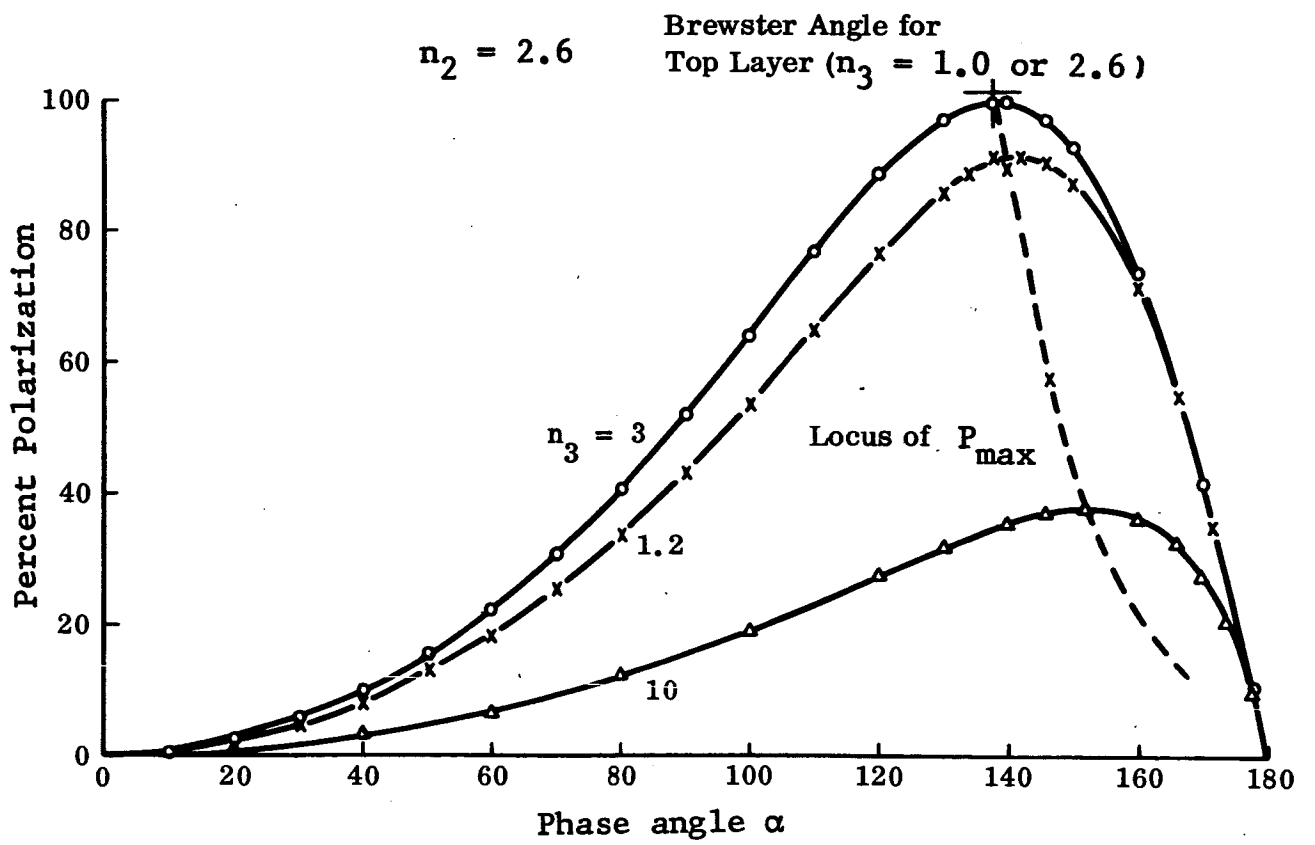Fig. 107   Double Layer, Plane Parallel Slab Model for $n_2 = 1.09$

Fig. 108   Double Layer, Plane Parallel Slab Model for n_2 = 2.6
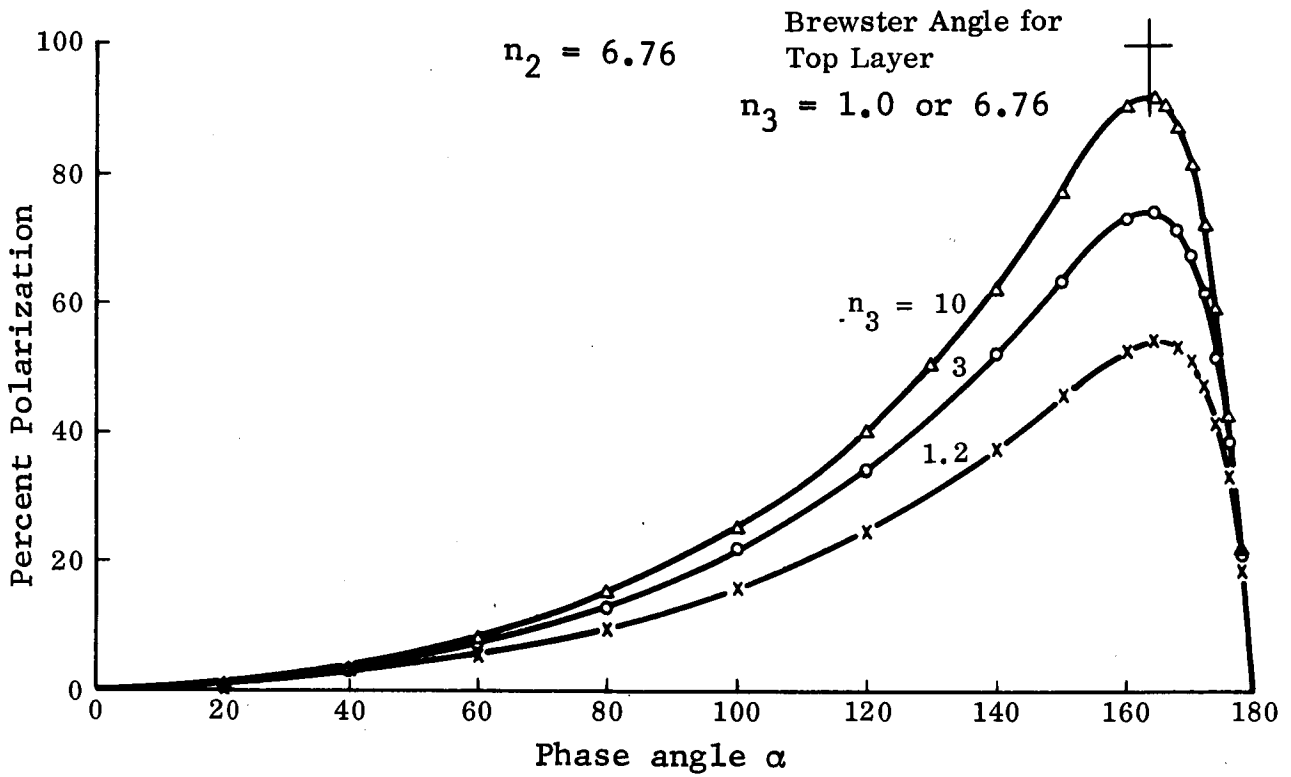
Fig. 109   Double Layer, Plane Parallel Slab Model for n_2 = 6.76
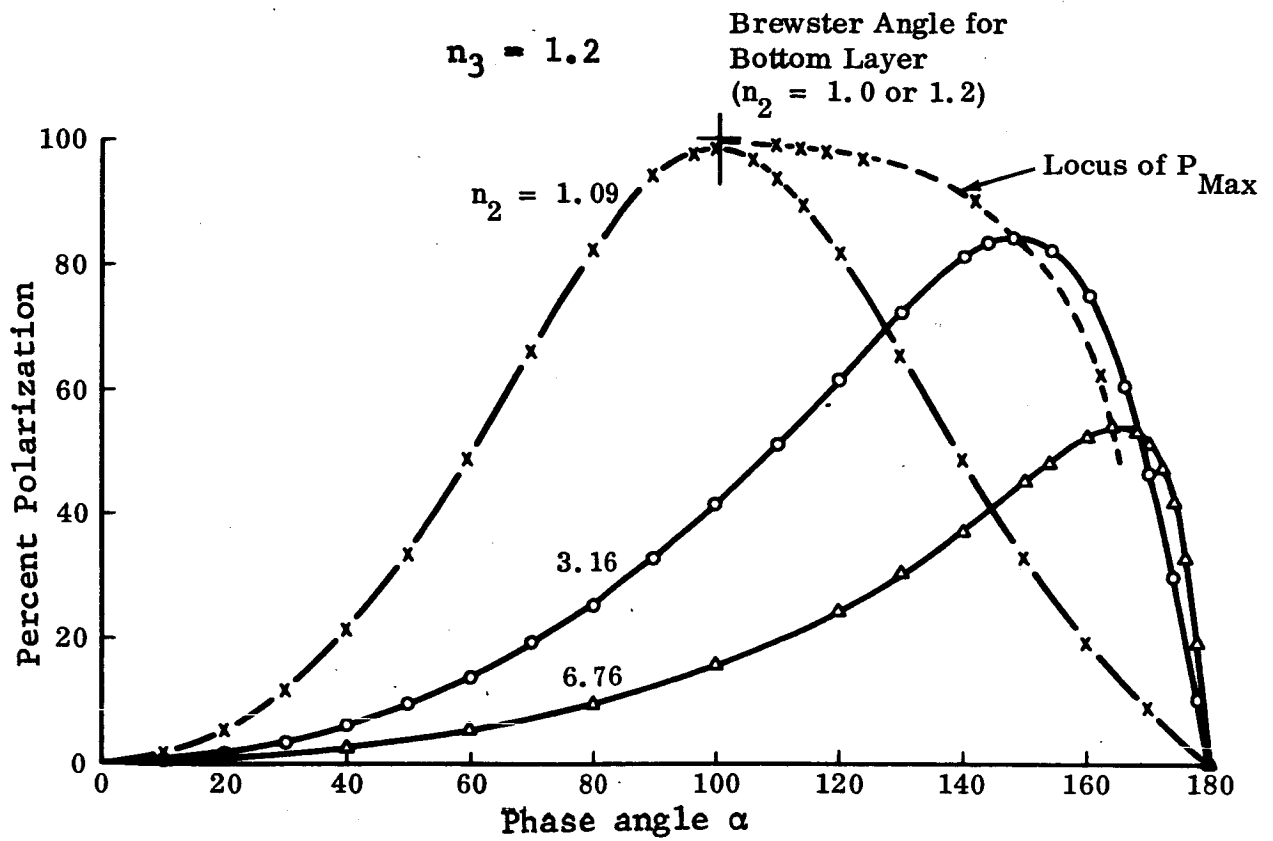
Fig. 110   Double Layer, Plane Parallel Slab Model for n_3 = 1.2
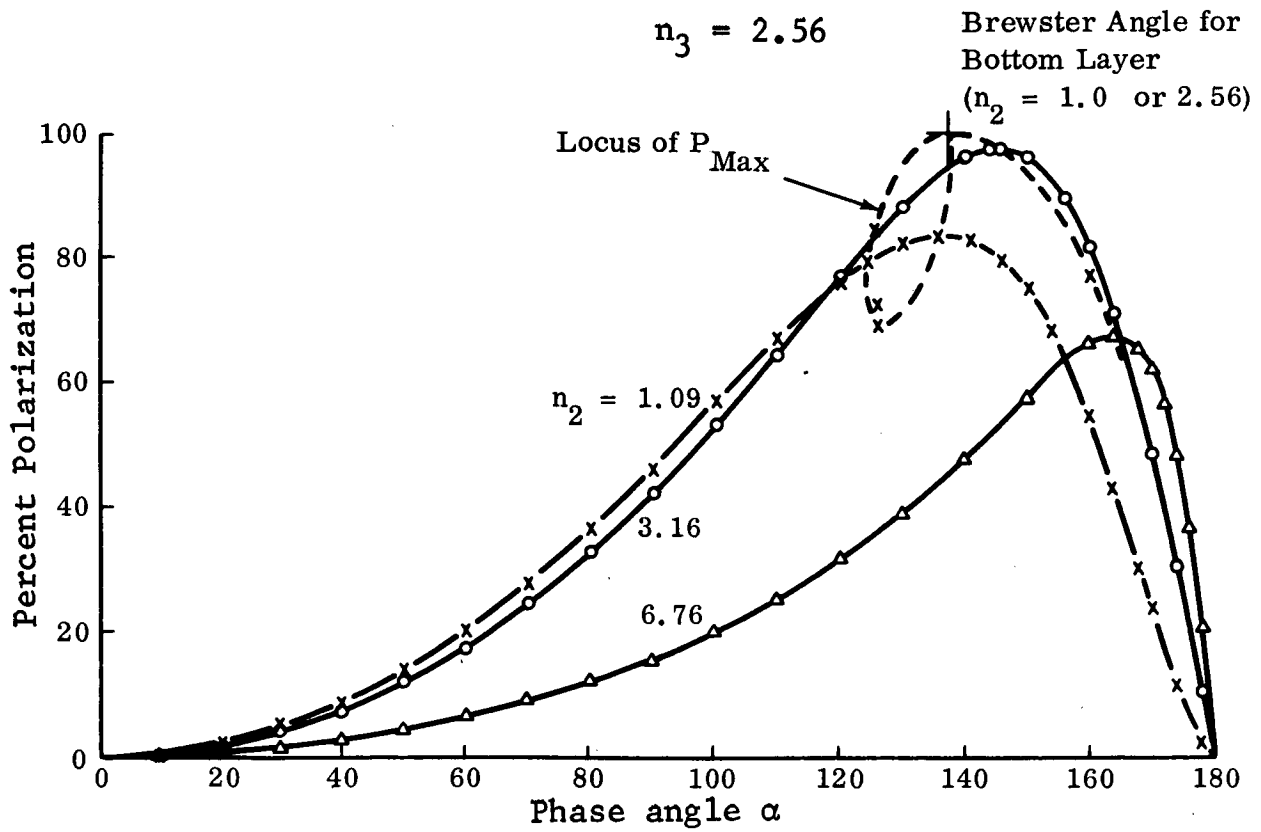
Fig. 111   Double Layer, Plane Parallel Slab Model for n_3 = 2.56

210
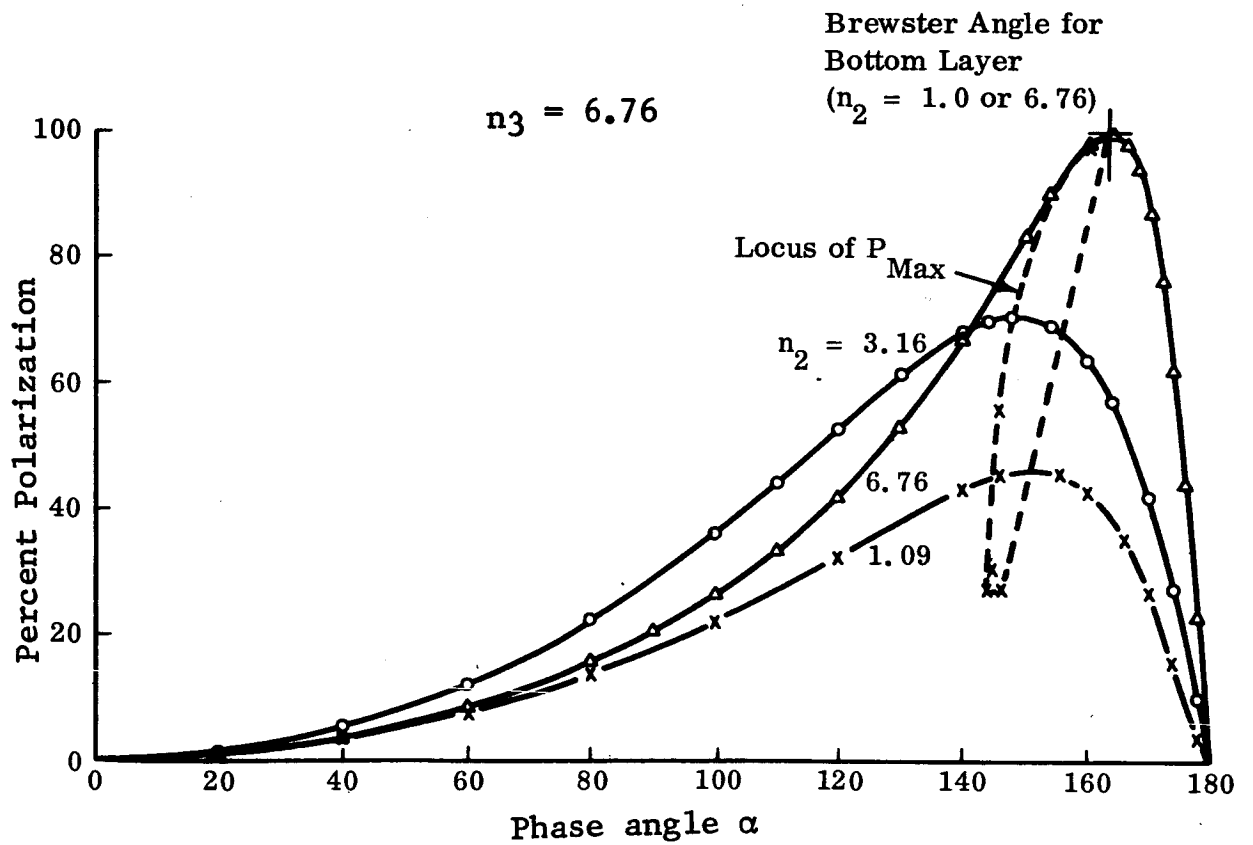
Fig. 112   Double Layer, Plane Parallel Slab Model for n_3 = 6.76
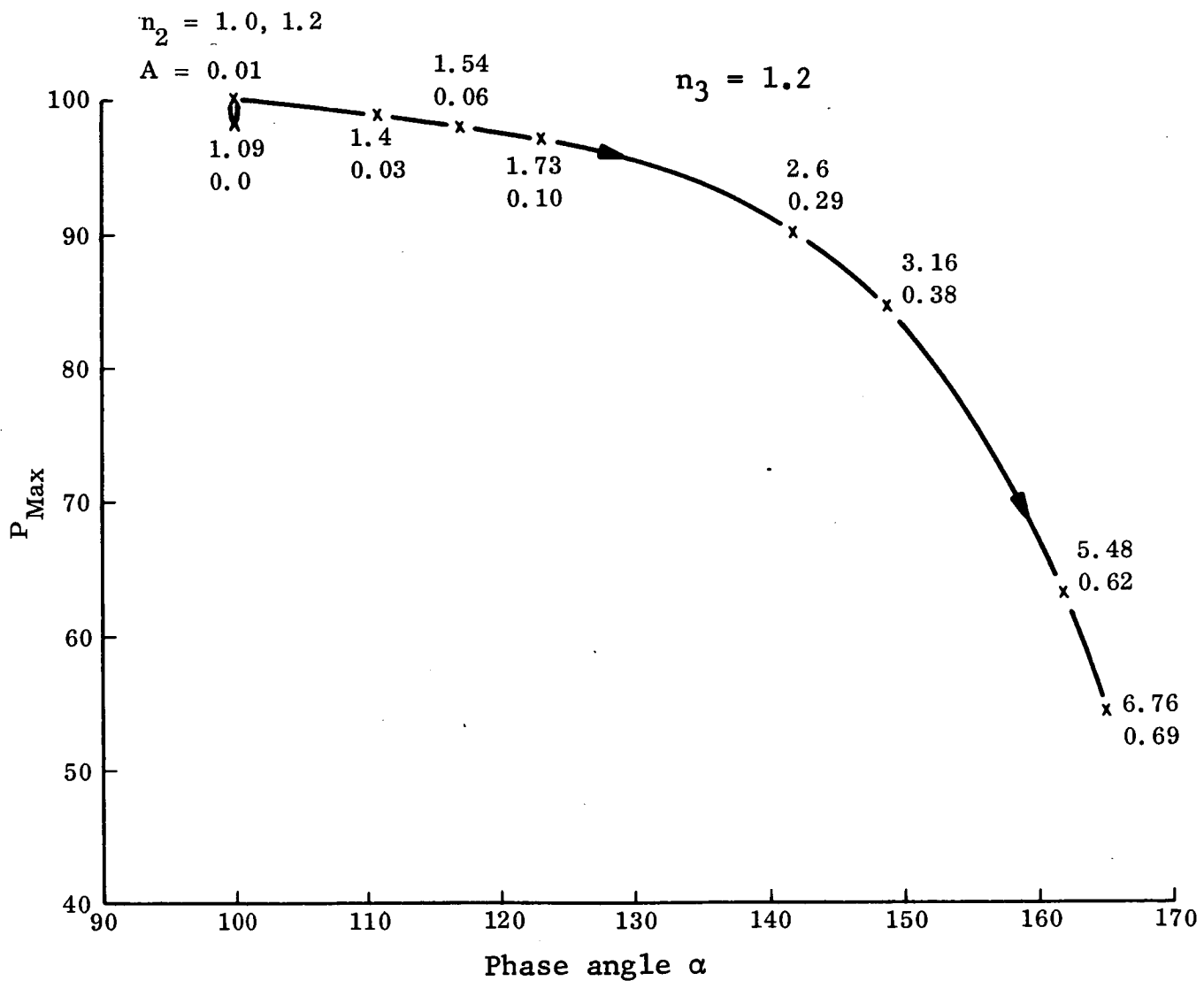
Fig. 113 Locus of P_{Max} for Double Layer, Plane Parallel
Slab Model for $n_3 = 1.2$

212
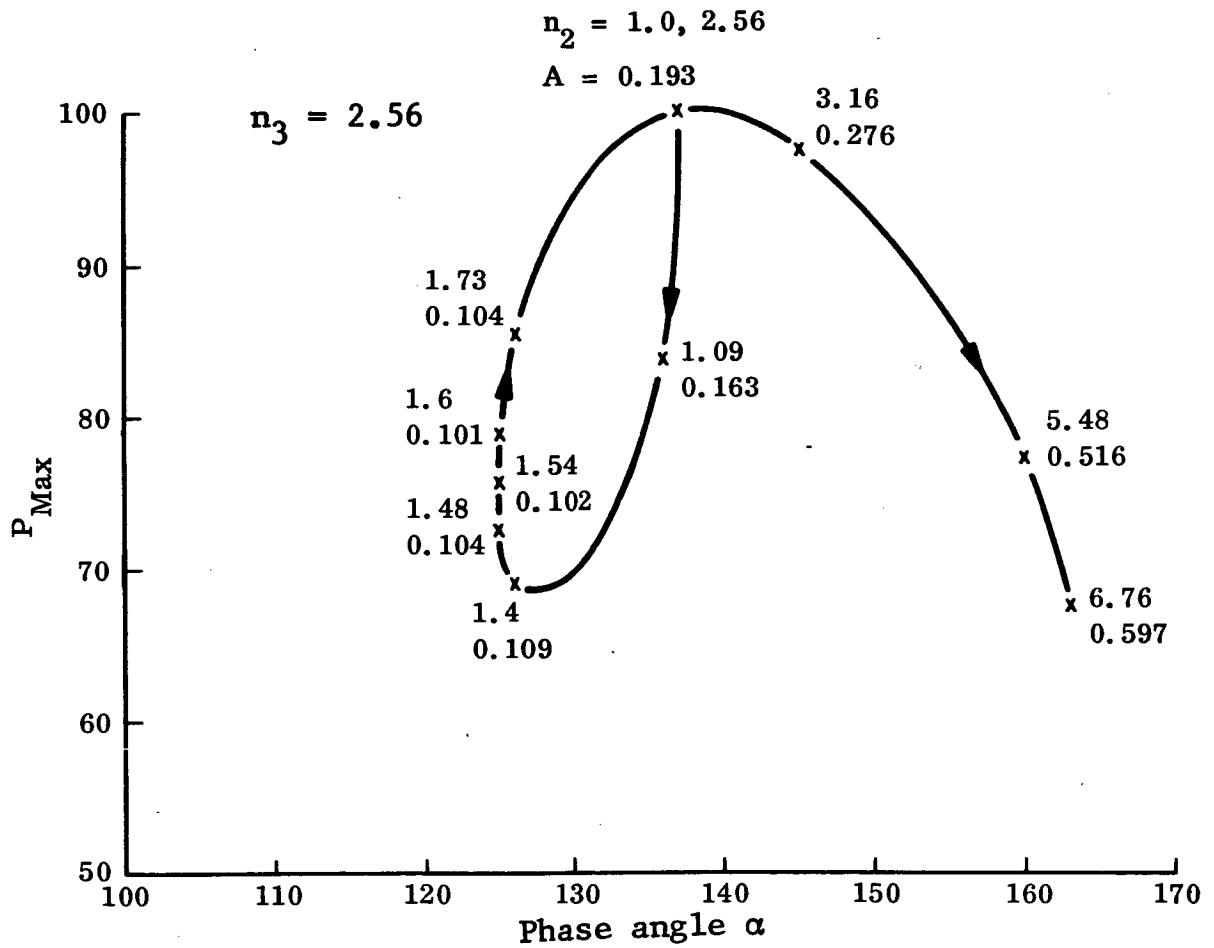
Fig. 114 Locus of P_{Max} for Double Layer, Plane Parallel
Slab Model for n_3 = 2.56
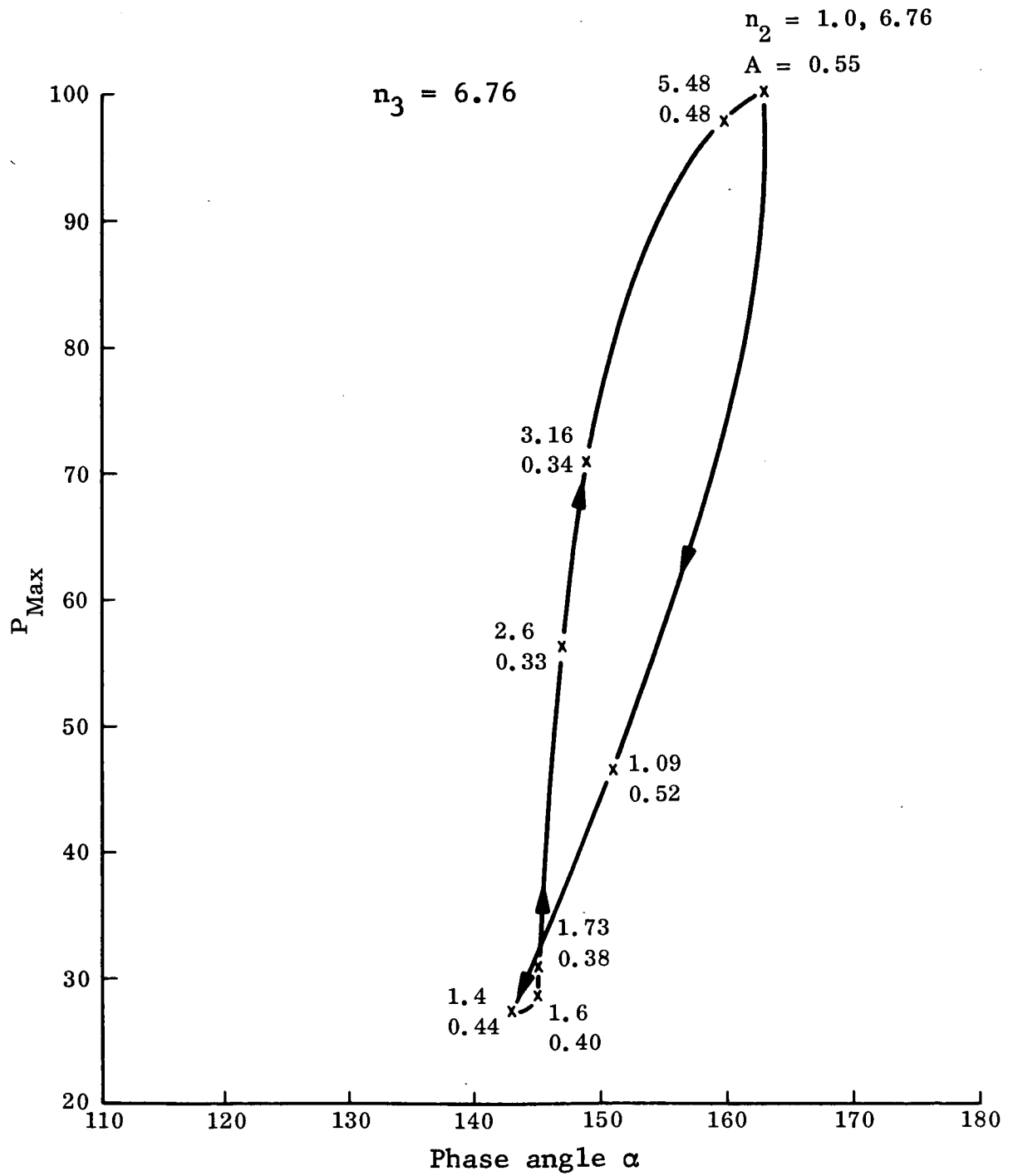
Fig. 115   Locus of P_{Max} for Double Layer, Plane Parallel
Slab Model for n_3 = 6.76
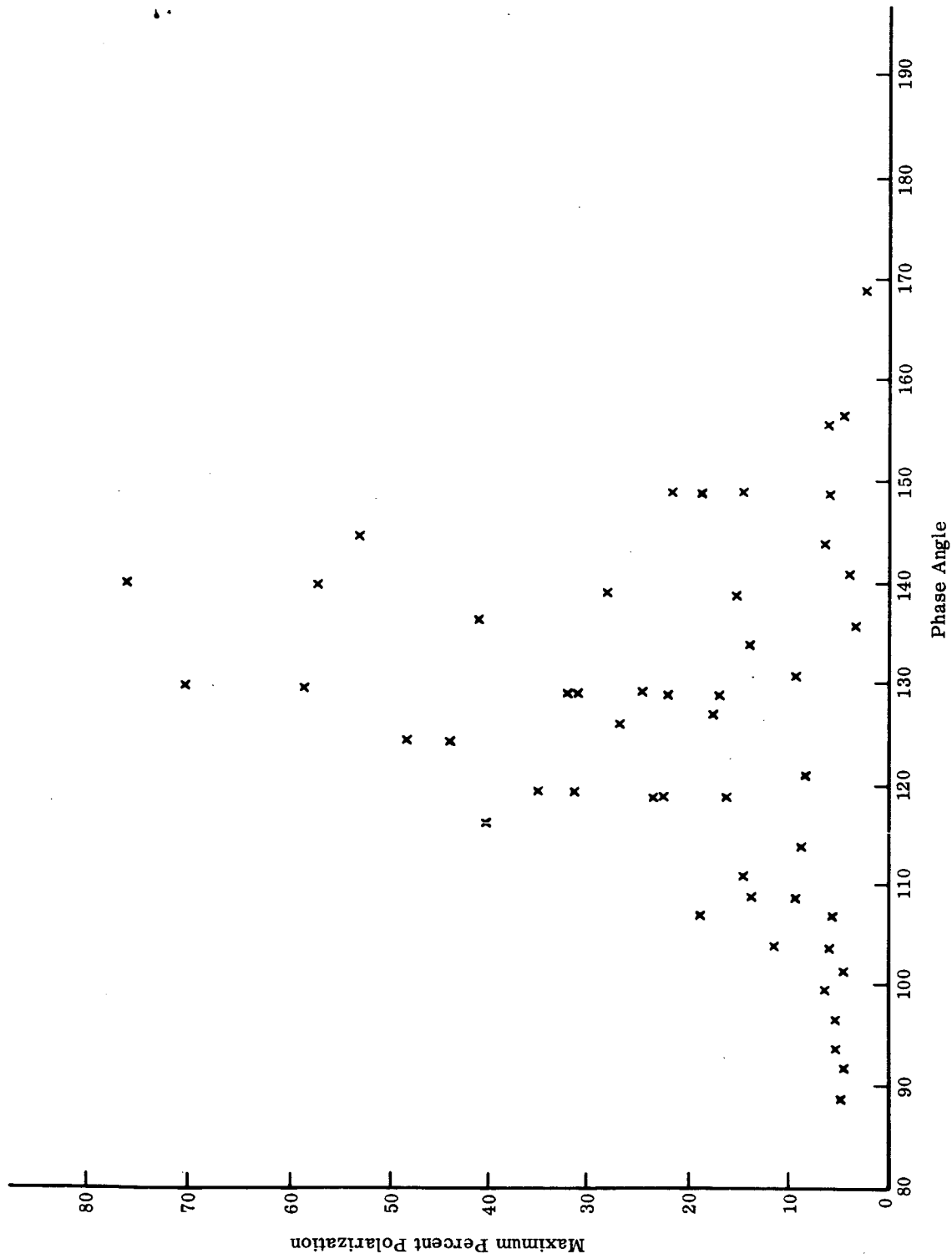
Fig. 116   Lyot (Ref. 13) — Polarization Maximum versus Phase Angle Location

Fig. 117 Egan and Smith (Phases I and II) – Polarization Maximum versus Phase Angle Location
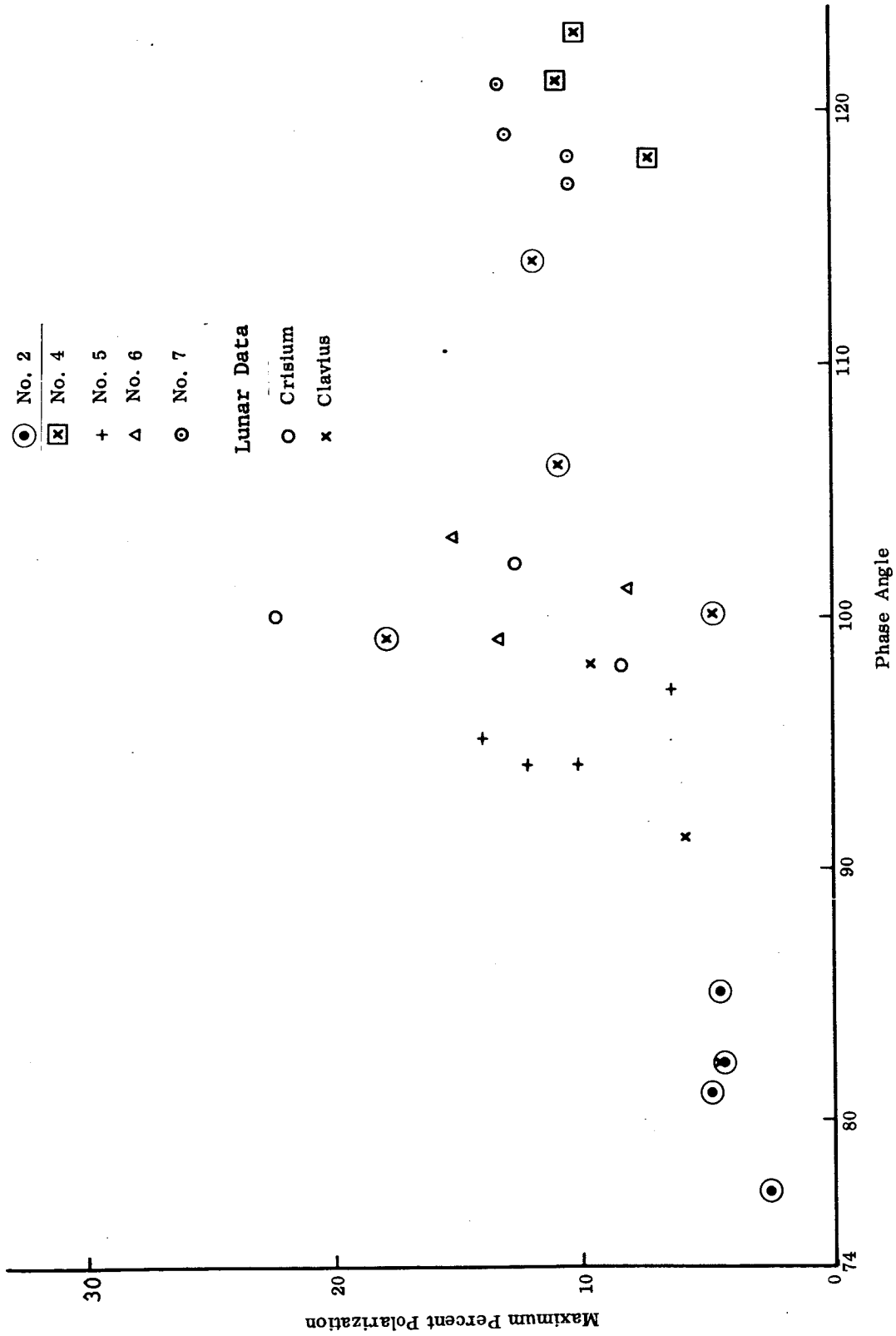
Fig. 118 Egan and Smith (Phase III) — Polarization Maximum versus Phase Angle Location
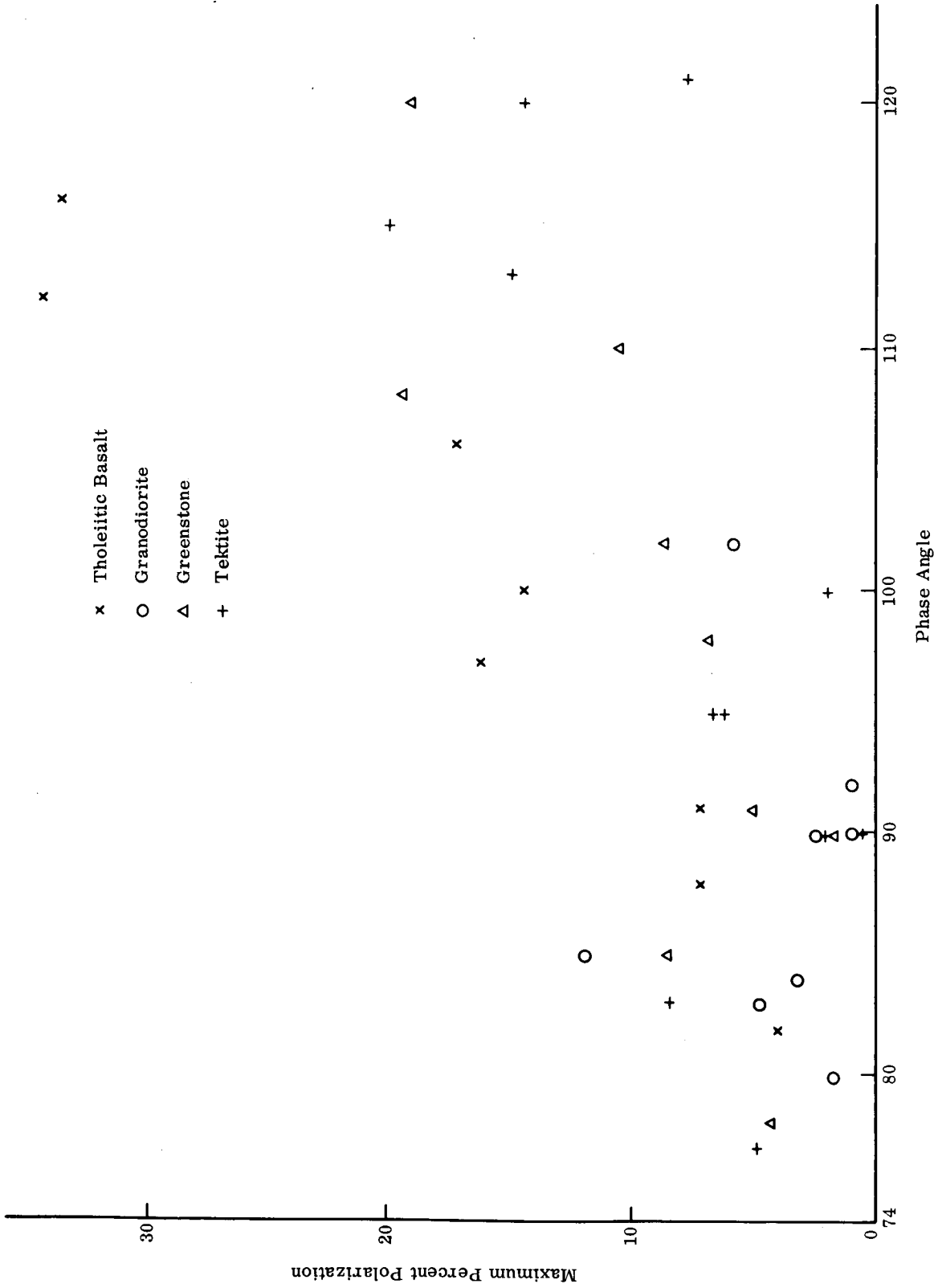
Fig. 119 Wehner et al. (Ref. 18) — Polarization Maximum versus Phase Angle Location

218

CONCLUSIONS TO OVER-ALL INVESTIGATION

Initially for this investigation, materials were chosen that were photometrically promising, in order to minimize the time and effort necessary to achieve a satisfactory polarimetric model utilizing them. As a result of this investigation of natural and pulverized specimens, it has been shown that a satisfactory photometric and polarimetric model may be constructed by combining a large scale model that produces the shadowing necessary for good photometry with a powder that produces the scattering and refraction properties necessary for good polarization.

The fundamental conclusion of the contrived model investigation is that the polarization properties of the lunar surface can be produced by a suitable particulate coating of the underlying material. This particulate coating could be the result of the deterioration of the underlying material into dust by micrometeorite bombardment, and the resulting powder possibly adheres to the lunar surface by high vacuum bonding. Thus the surface properties could yield information on the underlying matter and ultimately give information as to the choice of good landing areas for the Apollo mission, as well as the working properties of lunar materials for sample removal and core sampling.

A surface commonality exists on the basis of the initial investigation of natural and particulate specimens, which indicates that clearly defined limits cannot be set for lunar particle sizes, porosity, roughness, homogeneity, or complex index of refraction. In other words, previously reported models such as those of Lyot, Dollfus, Gehrels, Hapke, and Wehner are not unique.

From the investigation of particulate specimens, we have delimited the range of particle sizes that would have to exist on the lunar surface, either as a contiguous volume or as a simple, thin layer of the order of up to 1 mm thickness. Either model is consistent with the Luna 9 observations, and also with the thermophysical and photometric models analyzed at Grumman. High vacuum conditions on the moon plus the effect of solar wind proton bombardment could possibly alter the results. The particle ranges observed in this work serve as guides in correlating photometric, polarization, and thermophysical data.

The polarization - albedo - porosity relationship for the particles below 0.5 mm in size may be used to advantage in elucidating the mechanical properties as well as the thermal properties of a lunar surface model. This technique is presently under investigation at Grumman.

Theoretical approaches to the elucidation of the polarimetric properties of materials were pursued concurrently. Because the analysis of polarimetric properties is inherently more difficult than the analysis of photometric properties (due to the vector nature of the polarimetric problem as opposed to the scalar nature of the photometric problem), the level of sophistication initially possible in polarimetric models will be lower than in photometric models.

Investigation of a single layer plane facet model has clearly emphasized that, for a meaningful attempt at constructing a composite model designed to explain the photometric and polarimetric signatures, both signatures must be determined from an analysis of the microstructure of the rough surface elements, including shadowing effects. It will not be sufficient to postulate a brightness function for the various model elements, as in previous photometric investigations, since the photometric signature must be consistent with the polarimetric signature.

Our analysis of a double layer, plane parallel slab model has successfully explained the complexity of the behavior of the position (α_{max}) and magnitude (P_{max}) of the maximum polarization as the indices of refraction of the two media are varied. This model reproduces, depending on the values of the indices of refraction, the P_{max} - Albedo and P_{max} - α_{max} trends observed for the moon and many laboratory samples. The values of P_{max} and α_{max} are generally too high for a match to the moon, and this model does not produce negative values of percent polarization.

However the preliminary results of a parallel Grumman investigation of a more complex double layer model are now available and indicate that both negative polarization and magnitudes of P_{max} closer to the lunar data can be obtained with this more complex model.

RECOMMENDATIONS .

As a result of the work carried out in Phase III, as well as that pursued previously, additional recommendations that would appear fruitful are:

1. Additional investigations of material properties are required in order to define the scientific and engineering properties that yield the proper lunar polarimetric and photometric signatures. Typical investigations might be differential thermal analysis and X-ray diffraction.

2. Extension of infrared investigations to 1μ to 3μ and 8μ to 14μ for simulated lunar samples in terms of the over-all integrated interdisciplinary approach (see Ref. 25 as an example).

3. Investigation of luminescence as it affects albedo and polarization in an effort to elucidate the material composition of the lunar surface.

4. Investigation of incremental color changes as an index of lunar landing area characteristics.

5. Investigation of the effect of simulated solar wind effects on the best contrived models.

6. Continuation of the theoretical work on Grumman models begun in Phase IV.

REFERENCES

1. Egan, W. G., _Polarimetry and the Lunar Surface_, (A Literature Survey) , Grumman Research Department Memorandum RM-271, April 1965.

2. Hapke, B., "A Theoretical Photometric Function for the Lunar Surface," _Journal of Geophysical Research_, 68, No. 15, August 1, 1963, pp. 4571-4586.

3. Hapke, B., _An Improved Theoretical Lunar Photometric Function_, 121st American Astronomical Society Meeting, Hampton, Virginia, March 28-31, 1966.

4. Gehrels T., Coffeen, T., and Owings, D., "Wavelength Dependence of Polarization, III, The Lunar Surface," _Astronomical Journal_, Vol. 69, December 1964, p. 826-852.

5. Halajian, J.D., _Photometric Measurements of Simulated Lunar Surfaces_, Second Interim Report on NASA Contract No. NAS 9-3182, Grumman Research Department Memorandum RM-262, January 1965.

6. Halajian, J.D., _Photometric Measurements of Simulated Lunar Surfaces_, Grumman Research Department Report RE-219, Interim Report on NASA Contract No. NAS 9-3182, July 1965.

7. Halajian, J.D., and Spagnolo, F.A., _Photometric Measurements of Simulated Lunar Surfaces_, Grumman Research Department Memorandum RM-308, Quarterly Progress Report on NASA Contract No. NAS 9-3182, January 1966.

8. Halajian, J.D., and Spagnolo, F.A., _Photometric Measurements of Simulated Lunar Surfaces_, Grumman Research Department Report; Final Contract Report on Contract No. NAS 9-3182 (in preparation).

9. Egan, W.G., _Search for a Lunar Surface Model (Volume II - Polarimetry)_, Grumman Research Department Memorandum RM-276, May 1965.

10. Egan, W.G. et al., _Search for a Lunar Surface Model - Appendix A: Analysis of Photometric and Polarimetric Equipment_, Grumman Research Department Memorandum (in preparation).

11. Irvine W.M., Pikoos, C., Charon, J., and Lecomte, G., "Effect of High Voltage on Spectral Sensitivity for two Photomultipliers," _Astrophysical Journal_, 140, Nov. 15, 1964, pp. 1629-1631.

12. Nagaraja Rao, C.R., "Polarization and Albedo," _Nature_, 204, No. 4955, October 17, 1964, pp. 277-278.

13. Lyot, B., "Research on the Polarization of Light from Planets and from Some Terrestrial Substances," Annales de l'Observatorie de Paris, Section de Meudon, Vol. VIII, No. 1, 1929, NASA Technical Translation: NASA TT F-187.

14. Dollfus, A., Study of the Planets by Means of the Polarization of Their Light, Thesis, University of Paris, May 21, 1955, NASA Technical Translation: NASA TT F-188.

15. Hapke B., Effects of a Simulated Solar Wind on the Photometric Properties of Rocks and Powders, Center for Radiophysics and Space Research, Cornell University, Report CRSR 169, June 1964.

16. Coffeen, D.L., "Wavelength Dependence of Polarization, IV, Volcanic Cinders and Particles," Astronomical Journal, 70, August 1965, pp. 403-413.

17. Dollfus, A., and Geake, J.E., "L'altération des Propriétés Polarimétriques du Sol Lunaire par l'action des Protons Solaires," Comptes Rendus Acad. Sci., 260, No. 19, May 10, 1965, pp. 4921-4923.

18. Wehner G.K., Rosenberg, D.L., and KenKnight, C.E., Investigation of Sputtering Effects on the Moon's Surface, Eighth Quarterly Status Report on Contract NASw-751, Report No. 2792, May 14, 1965, Applied Science Division, Litton Systems, Inc., Minneapolis, Minnesota.

19. Egan, W.G. and Smith L.L., Polarimetric Measurements of Simulated Lunar Surfaces, Grumman Research Department Memorandum RM-304, Interim Report on NASA Contract NAS 9-4942, December 1965.

20. Hapke, B., Some Comments on Gehrels' Model of the Lunar Surface, Center for Radiophysics and Space Research, Cornell University, Report CRSR 199, June 1965.

21. Halajian, J.D. and Reichman, J., Correlation of Mechanical and Thermal Properties of Extraterrestrial Materials, Grumman Research Department Memorandum RM-309, Second Quarterly Progress Report on Contract NAS 8-20084, February 1966.

22. "Moscow Releases 2 of Its Moon Photos," New York Times, February 6, 1966, p. 1.

23. Halajian, J.D., "The Case for a Cohesive Lunar Surface Model," Annals of the New York Academy of Sciences, 123, Art. 2, July 15, 1965, pp. 671-710.

24. Egan, W.G. and Smith, L.L., _Polarimetric Measurements of Simulated Lunar Surfaces (Phase II)_, Grumman Research Department Memorandum RM-312, Second Interim Report on NASA Contract NAS 9-4942, February 1966.

25. Binder, A.B., Cruikshank, D.P., and Hartmann, W.K., "Observations of the Moon and of the Terrestrial Rocks in the Infrared," _Icarus_, 4, No. 4, September 1965, pp. 415-420.

26. Clarke, D., "Studies in Astronomical Polarimetry, III, The Wavelength Dependence of the Polarization of Light Reflected by the Moon and Mars," _Monthly Notices Royal Astr. Soc._, 130, No. 1, 1965, pp. 83-94.

27. Halajian, J.D., _Photometric Measurements of Simulated Lunar Surfaces_, Grumman Research Department Memorandum RM-250, Interim Report on NASA Contract No. NASA 9-3182, Nov. 1964

28. Strom, R.G., Private Communication.

29. Van de Hulst, H.C., _Light Scattering by Small Particles_, John Wiley & Sons, Inc., New York, 1957.

30. Remy-Battiau, L., _Mie Scattering Functions for Spherical Particles of Refractive Index m=1.25_, Mem in 4° Soc R. Sc. Liege 2, fasc. 7, 1, 1962.

31. Lowan, A.N., _Tables of Scattering Functions for Spherical Particles_, Natl. Bur. Standards, Washington, D.C., Appl. Math. Series 4, 1948.

32. Deirmendjian, D., Clasen, R., and Viezee, W., "Mie Scattering with Complex Index of Refraction," _Journal of the Optical Society of America_, 51, No. 6, June 1961, pp. 620-633.

33. Wattson, R.B., and Danielson, R.E., The Infrared Spectrum of the Moon," _Astrophysical Journal_, 142, No. 1, July 1, 1965, pp. 16-22.

34. Epstein, L.C., _Sky and Telescope_, Vol. XXXI, No. 1, January 1966, p.30.

35. Hapke, B., and Van Horn, H., _Photometric Studies of Complex Surfaces With Applications to the Moon_, Journal of Geophysical Research, Vol. 68, p. 4545, 1963.

36. Beckmann, Petr, _Radar Backscatter from the Surface of the Moon_, Journal of Geophysical Research, Vol. 70, p. 2345, May 15, 1965.

37. Beckman, Petr, and Spizzichino, Andre, <u>The Scattering of Electromagnetic Waves from Rough Surfaces</u>, Pergamon Press, New York, 1963.

38. Fraiture, T., <u>Scattering of Electromagnetic Waves from Rough Surfaces</u>, Annales de la Societe Scientifique de Bruxelles, Vol. 7911, p. 144, 1965.

39. Hopfield, J.J., <u>Mechanism of Lunar Polarization</u>, Science, Vol. 151, p. 1380, March 18, 1966.

40. Ruffine, R.S., and de Wolfe, D.A., <u>Cross-Polarized Electromagnetic Backscatter from Turbulent Plasmas</u>, Journal of Geophysical Research, Vol. 70, p. 4313, September 1, 1965.

41. Hodge, D.B., and Schultz, F.V., <u>The Born Approximation Applied to Electromagnetic Scattering From a Finite Cone</u>, Purdue University, TR-EE64-18, September 1964.

42. Ivanov, A.P., and Toporets, A.S., <u>Investigation of Diffuse Reflection by Means of Polarized Light</u>, Soviet Physics - Technical Physics, Vol. 1, p. 598, 605, 1957.

43. Ruachev, V.P., and Polyanskii, V.K., <u>Passage of Polarized Light Through a Light Scattering Surface</u>, Optics and Spectroscopy, Vol. 18, p. 594, 1965.

44. McCoyd, G.C., <u>Polarization Properties of Single Dielectric Rough Surface Models</u>, Grumman Research Department Memorandum (in preparation).

45. Egan, W.G., and Smith, L.L., <u>Polarimetric Measurements of Simulated Lunar Surfaces, Phase III</u>, Grumman Research Department Memorandum RM-315, Third Interim Report on Contract NAS 9-4942, March 1966.

46. NASA - Ranger VII Photographs of the Moon, Parts I (Camera "A" Series), II (Camera "B" Series) and III (Camera "P" Series); NASA SP-61, NASA SP-62, and NASA SP-63, September 1964, February 1965, and August 1965.

47. Egan, W.G., and Hallock, H.B., <u>Polarimetry Signature of Terrestrial and Planetary Materials</u>, Proceedings of Fourth Symposium on Remote Sensing of Environment, University of Michigan, Ann Arbor, Michigan, April 12-14, 1966.

48. Steiger, W.R., Private Comminication, (also in Ref. 6 above).

49. <u>Handbook of Chemistry and Physics</u>, 32nd Edition, 1950-1951,
    Chemical Rubber Publishing Company.

50. Born, M., and Wolf, E., <u>Principles of Optics</u>, Macmillan (1959).

APPENDIX

TEST PROCEDURE

Percent Polarization

A reproduction of the tracing used to calculate the percent polarization in Phase I for Volcanic Ash No. 1 using the $0°$ photometer is presented in Fig. 120 as typical of the experimental procedure used throughout Phases I, II, and III. The abscissa measures the phase angle (the angle between the source and the photometer as viewed from the sample) and the ordinate measures the intensity of the signal in arbitrary units. The zero intensity level or dark current reference level is suppressed to reduce the size of the figure.

For a given phase angle the polaroid is placed in continuous rotation by means of a motor drive until the plane of transmission is normal to the plane of vision (the plane passing through the source, sample, and photometer). Referenced to the dark current, the intensity measured is I_1. The polaroid then continues $90°$, placing the transmission plane in the plane of vision and the intensity measured in this position is I_2. The initial reference position of the polaroid is shown by a pilot light indicator. The polaroid is moved through several rotations and the average values each of I_1 and I_2 are read from the tracing ($I_1 = 130.0$, $I_2 = 99.0$ for phase angle $68.2°$). The small arrows in the figure at each phase angle indicate the motion of the recording pen as the polaroid transmission plane is moved away from the normal to the plane of vision. The percent polarization is determined by

$$P(\%) = 100 \, \frac{I_1 - I_2}{I_1 + I_2} \, .$$

From Fig. 120, negative polarizations ($I_1 < I_2$) are observed for phase angles less than $21°$ and positive values ($I_1 > I_2$) for phase angles greater than $21°$. The phase angle at which zero polarization occurs (inversion angle) is determined from the two curves at the upper left of the figure. The polaroid is rotated to give I_1, with the phase angle greater than the

inversion angle and fixed in this position while the source arm is moved towards smaller phase angles. The polaroid is then rotated 90° to give I_2 and the arm is again moved. The angle of inversion can be determined from the position of the crossover point of the two curves.

A complete reduction of the data in Fig. 120 is given in Table 16 and is plotted in Fig. 14.

TABLE 16

Percent Polarization - Typical Calculation

Volcanic Ash No. 1   0° Photometer   10/26/65

PHASE ANGLE	I_1	I_2	P(%)
3.0°	129.2	132.1	- 1.1
7.5°	129.8	133.9	- 1.6
17.5°	129.6	130.6	- 0.4
21.3°	-----	-----	0
27.6°	129.6	124.2	+ 2.1
39.4°	129.8	116.9	+ 5.2
49.4°	129.8	110.2	+ 8.2
60.1°	129.0	103.0	+11.2
68.2°	130.0	99.0	+13.5

Plane of Polarization

Figure 121 is a reproduction of the tracing used to determine the position of the plane of polarization for aged silver chloride at 30° latitude as measured with the 60° photometer and typical of those used in Phases I and II. The abscissa measures the relative position of the polaroid as it is rotated through 360° at a fixed phase angle, while the ordinate gives the recorded intensity.

The maxima of the resulting sine curves correspond to I_1 (polaroid transmission plane normal to the plane of vision), and the minima to I_2 (transmission plane in the plane of vision)

in this case. However, with an inversion, the opposite occurs below the inversion angle. The positions of the maxima and minima were determined by folding the tracing and matching the two halves of the curves. The tick marks numbered 1 through 6 in the figure indicate voltage calibrations and these small corrections were applied to the observed data. For Phase I, measurements were made relative to the reading from a black aluminite metal plate at a phase angle of 128° with positive $\Delta\theta$ being taken arbitrarily to the left. The relative shifts of the plane of polarization $\Delta\theta$ were measured from the displacement of the maxima and minima from the reference curve for each sine curve, and averaged. The complete reduction of Fig. 121 is presented in Table 17. For Phase II, a secondary reference was substituted for the aluminite plate, and the $\Delta\theta$ became an absolute deviation.

TABLE 17

Plane of Polarization - Typical Calculation

Aged Silver Chloride   60° Photometer   11/15/65

30° Latitude

$\Delta\theta$ (degrees) referred to 128° Aluminite Reference

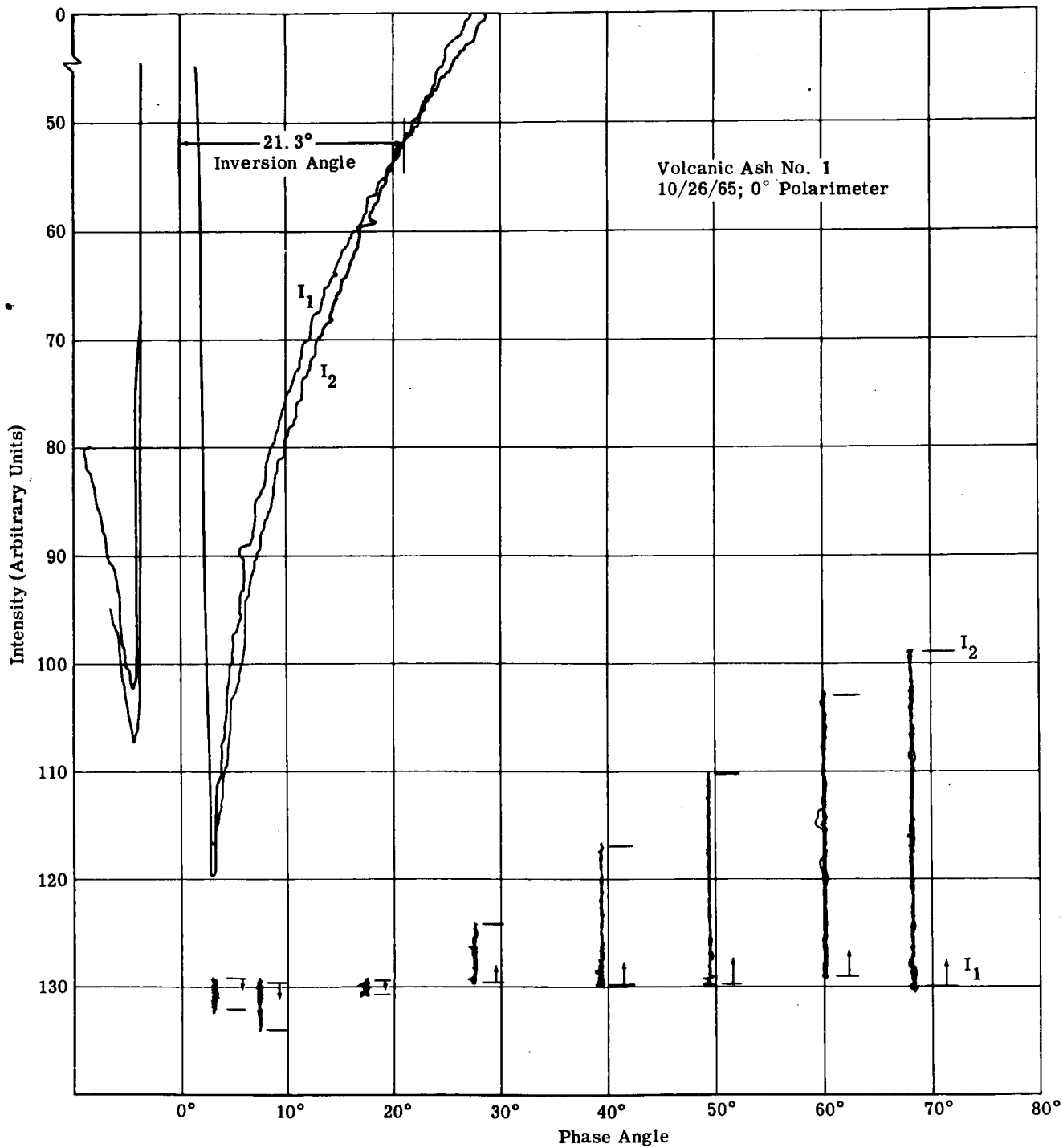| Phase Angle	128	95	68	35	5
Max.	+ 0.6	+ 0.2	+ 0.3	+ 2.5	+4.4
Min.	+ 0.2	+ 0.6	+ 0.6	+ 1.4	+4.2
Average	+ 0.4	+ 0.4	+ 0.5	+ 2.0	+4.3

Fig. 120   Volcanic Ash No. 1:   Reproduction of Tracing for
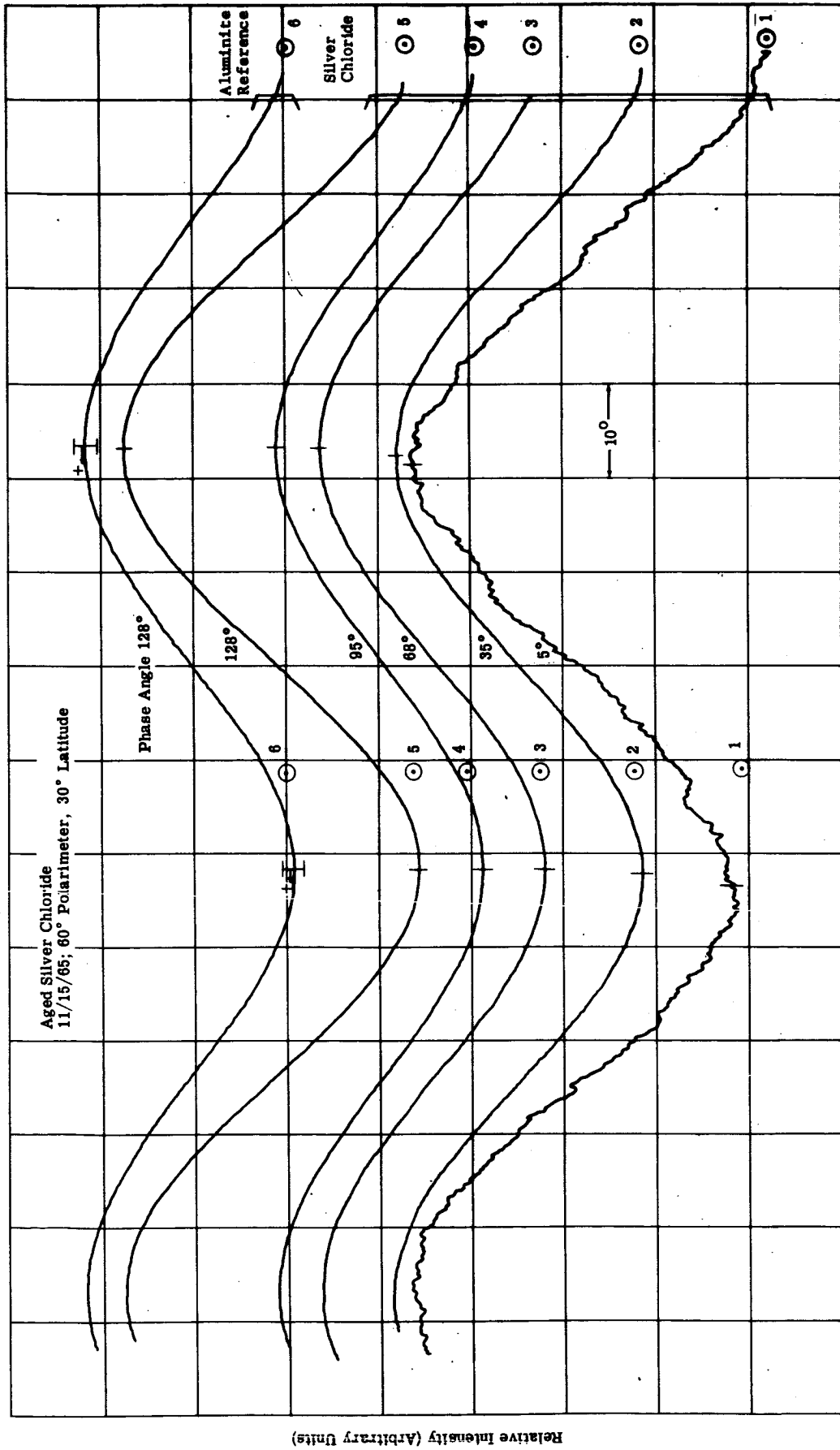Determination of Percent Polarization

Fig. 121 Aged Silver Chloride: Reproduction of Tracing for
Determination of Relative Position of Plane of Polarization

231

Grumman

GRUMMAN AIRCRAFT ENGINEERING CORPORATION
BETHPAGE, NEW YORK